Design and Additive Manufacturing of Cellular Solids for Lightweight Hybrid Sandwich Structures

Albert Forés Garriga

http://hdl.handle.net/10803/688729

Data de defensa: 04-07-2023

UNIVERSITAT RAMON LLULL

DOCTORAL THESIS

Title	Design and Additive Manufacturing of Cellular Solids for Lightweight Hybrid Sandwich Structures
Presented by	Albert Forés Garriga
Centre	IQS School of Engineering
Department	Department of Industrial Engineering
Directed by	Dr. Marco Antonio Pérez

"*The important thing is not to stop questioning.*
Curiosity has its own reason for existence."

Albert Einstein

This thesis has been funded with the support of the grant RTI2018-099754-A-I00 funded by MCIN/AEI/10.13039/501100011033 and by ERDF A way of making Europe (2018-2022), and from the RIS3CAT Llavor 3D Community co-financed by the Generalitat de Catalunya (ACCIÓ) through the project TRANSPORT COMRDI16-1-0010 (2017-2020).

ACCIÓ
Catalonia Trade & Investment

Generalitat de Catalunya

Project RTI2018-099754-A-I00 funded by:

MINISTERIO DE CIENCIA E INNOVACIÓN

UNIÓN EUROPEA
FONDO EUROPEO DE DESARROLLO REGIONAL
"Una manera de hacer Europa"

AGENCIA ESTATAL DE INVESTIGACIÓN

Acknowledgements

La primera pàgina d'aquesta tesi doctoral està dedicada a totes les persones que, sense l'ajuda i el suport de les quals, aquesta tesi no hauria estat possible. És per això que vull mostrar el meu agraïment a tothom qui durant aquests anys m'ha acompanyat, mostrant interès pel que feia i amb disposició d'ajudar-me. Vull remarcar que aquesta tesi és també fruit del seu suport.

En primer lloc vull agrair a l'Institut Químic de Sarrià (IQS) per tota la formació i acompanyament rebut des del primer dia que vaig començar els estudis de grau. Un record especial per aquella primera conversa amb el P. Alberto Barrera, SJ. L'equip humà de l'IQS m'ha ajudat a superar-me en coneixements i també com a persona. Sense cap dubte, avui escric el darrer pas de la meva tesi doctoral per haver coincidit amb l'IQS. Moltíssimes gràcies, i en especial al Dr. Pedro Regull, ex-director, i al Dr. Salvador Borrós, director actual de l'IQS, per la confiança atorgada per a la realització d'aquesta tesi doctoral.

Agrair particularment al meu director de tesi, el Dr. Marco A. Pérez. Com a professor, va confiar en mi i va saber il·lusionar-me mentre prenia la decisió d'iniciar els meus estudis de doctorat. Com a director, m'ha guiat, m'ha donat tot el seu suport i m'ha ajudat a avançar en la investigació dia a dia, aconseguint que gaudís, inclús en els moments difícils. Moltes gràcies pel teu compromís i complicitat.

Vull remarcar també el meu agraïment a tots els professors i professores de l'IQS que al llarg d'aquests deu anys m'han transmès no solament els seus coneixements sinó que cadascú amb el seu pòsit, m'ha esperonat a sortir de la meva zona de confort, a reflexionar i a esforçar-me per a créixer, actitud imprescindible per a enfrontar-te a una tesi doctoral i a la vida. En concret, als professors membres del Departament d'Enginyeria Industrial, Dra. Marisa Espasa, Dr. Joaquín Menacho, Dr. Pere Palacín, Dr. Josep Maria Puigoriol, Sra. Núria Llaverías, Sr. Ferran López, Sr. Juan Antonio Tormo i Sr. Sauro Yagüe. Moltíssimes gràcies a tots. I un agraïment particular als Dr. Andrés García, Dr. Guillermo Reyes, Sr. César Alquézar i Sra. Mercedes Peña per les seves tasques desenvolupades en el marc del projecte d'aquesta tesi i, en especial, al Dr. Giovanni Gómez pel seu suport i la seva col·laboració durant aquests anys de doctorat.

No pot faltar el meu agraïment molt especial a l'Ari i el Dani, amb qui he tingut la sort de compartir l'experiència del doctorat des del primer dia, així com a la resta de doctorands del *Applied Mechanics and Advanced Manufacturing Research Group* (GAM) i companys de l'IQS, Ferran, Guillermo, Héctor, Josep, Ricard, Adrià, Andrea, Daniel, Jan, Josep Maria, Júlia, Laia i Laura. Hem tingut la fortuna de conèixe'ns, hem compartit moments de tota mena, il·lusions i frustracions, ens hem ajudat, ens hem encoratjat i ens hem alegrat els uns pels altres fins a consolidar uns vincles que ja no es poden trencar.

Som alumni IQS i família de per vida! Ara, continuarem lluitant pels nostres somnis i ideals, tant de bo ens en sortim! No oblidem allò que diu «Tot està per fer i tot és possible!».

Gràcies també als alumnes de l'*Institut Catholique d'Arts et Métiers* (ICAM) amb qui he pogut col·laborar: Audrey, Jocelyn, John, Max, Michael, Sarah, Sophie, Thomas i Tanguy. Tots heu contribuït en la recerca desenvolupada pel grup d'investigació i alhora hem compartit bons moments. Moltes gràcies també a tos els alumnes que m'han patit a classe. De tots he après i en guardo bons records!

No puc descuidar el meu agraïment a la Núria per ser-hi, sense fer soroll, sense pressió, sabent escoltar i trobant sempre la paraula que més necessites en els moments delicats. Sobretot aquests darrers mesos que en podríem dir més difícils.

Per últim, agrair a la meva família, de manera molt especial als meus pares, per ser-hi sempre i de manera incondicional. Gràcies per fer-me sentir estimat, per l'educació que m'heu donat i pel vostre exemple.

Albert Forés i Garriga

Als meus pares, Margarita i Artur.

Abstract

The threatening, cross-cutting climate change and the problematic lack of resources have become increasingly evident over the last few years. To counter this challenging situation, engineers and scientists worldwide are struggling to bring more efficient and environmentally friendly alternatives, especially to industrial activities responsible for significant contamination levels, such as the automotive, aeronautic, aerospace, and maritime transportation sectors. Hence, improvements in these and other fields of the present and the future of engineering involve optimizing structures, thus achieving components with the desired performance while making more efficient and sustainable use of raw materials. For this purpose, hybrid configurations such as sandwich structures are highly competitive solutions that the industry has already adopted and consolidated during the last decades. In this sense, choosing the appropriate arrangement is critical for achieving the desired performance of a sandwich panel. In particular, the core's material and morphology play a fundamental role in the behavior of the structure since, apart from increasing its inertia by separating the two skins, it is responsible for supporting most of the shear stresses while decreasing the density of the whole panel. Consequently, its selection becomes a strategic decision.

The irruption of Additive Manufacturing (AM) technologies that occurred during the last years has revolutionized many industrial sectors, directly impacting manufacturing processes and components design. Taking advantage of its infinite advantages for fabricating high-complexity geometries compared to traditional manufacturing processes, this doctoral thesis aims to contribute to the design of more efficient hybrid sandwich structures using lightweight cellular cores manufactured by Fused Filament Fabrication (FFF).

To do so, this research has been developed by addressing three levels of study, in order to analyze the performance of the material, the cellular design, and the consolidated hybrid sandwich structure. The results presented in the different scientific contributions derived from this work have been validated analytically, numerically, and experimentally, and show the potential of the two- and three-dimensional patterns considered for the fabrication of fully functional sandwich structures, making better use of the materials. Furthermore, the numerical models and analytical equations provided, as well as the released open-source software for generating cellular designs, will be of help for conducting new studies in the field of structural efficiency optimization.

Finally, this thesis has shed light on some areas for improvement in the FFF technology, such as the presence of intra- and inter-layer filament joint inaccuracies in the manufacturing of thin-walled two-dimensional cellular designs and the current limitations in reducing the minimum thickness of those walls. However, with ongoing advancements and breakthroughs in the field, these drawbacks will soon be addressed, leading to even more impressive outcomes in the near future.

Resum

El canvi climàtic amenaçador i la problemàtica manca de recursos s'han fet cada vegada més evidents en els darrers anys. Per a contrarestar aquest desafiament, enginyers i científics de tot el món lluiten per a aportar alternatives més eficients i respectuoses amb el medi ambient, especialment en les activitats industrials responsables de nivells significatius de contaminació, com els sectors del transport automobilístic, aeronàutic, aeroespacial i marítim. Millores en aquests i altres camps del present i del futur de l'enginyeria impliquen optimitzar les estructures per tal d'aconseguir components amb el rendiment desitjat, mentre es fa un ús més eficient i sostenible de les matèries primeres. Per aquest propòsit, les configuracions híbrides, com les estructures tipus sandvitx, són solucions altament competitives que la indústria ja ha adoptat i consolidat durant les darreres dècades. En aquest sentit, l'elecció de la configuració adequada és crucial per a assolir el rendiment desitjat d'un panell sandvitx. En particular, el material i la morfologia del nucli juguen un paper fonamental en el comportament de l'estructura. Per tant, la seva selecció esdevé una decisió estratègica.

La irrupció de les tecnologies de Fabricació Additiva (AM) que ha tingut lloc durant els darrers anys ha revolucionat molts sectors industrials, impactant directament en els processos de fabricació i el disseny de components. Aprofitant els seus infinits avantatges per a fabricar geometries de gran complexitat en comparació amb els processos de fabricació tradicionals, aquesta tesi doctoral té com a objectiu contribuir al disseny d'estructures híbrides tipus sandvitx més eficients, utilitzant nuclis cel·lulars lleugers construïts per Fabricació per Filament Fos (FFF).

Per a fer-ho, aquesta investigació s'ha desenvolupat abordant tres nivells d'estudi per a analitzar el rendiment del material, el disseny cel·lular i l'estructura híbrida de sandvitx consolidada. Els resultats presentats en les diferents contribucions científiques derivades d'aquest treball s'han validat analíticament, numèricament i experimentalment, i mostren el potencial dels patrons bidimensionals i tridimensionals considerats per a la fabricació d'estructures de sandvitx totalment funcionals, fent un millor ús dels materials. A més, els models numèrics i les equacions analítiques proporcionades, així com el programari lliure publicat per a la generació de dissenys cel·lulars, seran d'utilitat per a la realització de nous estudis en el camp de l'optimització de l'eficiència estructural.

Finalment, aquesta tesi ha posat de manifest algunes àrees d'evolució en la tecnologia FFF, com ara la presència d'imprecisions en les juntes de filament intra-capa i inter-capa en la fabricació de dissenys cel·lulars bidimensionals de parets primes, i les limitacions actuals en la reducció del gruix mínim d'aquestes parets. No obstant això, amb els progressos i els avenços en curs en el camp, aviat s'abordaran aquests inconvenients, portant a resultats encara més impressionants en un futur pròxim.

Resumen

El cambio climático amenazante y la problemática falta de recursos se han hecho cada vez más evidentes en los últimos años. Con el fin de contrarrestar este desafío, ingenieros y científicos de todo el mundo están luchando para ofrecer alternativas más eficientes y respetuosas con el medio ambiente, especialmente en las actividades industriales responsables de niveles significativos de contaminación, como los sectores de transporte autmovilístico, aeronáutico, aeroespacial y marítimo. Mejoras en estos y otros campos de la ingeniería actual y futura implican optimizar las estructuras, logrando componentes con el rendimiento deseado, mientras se hace un uso más eficiente y sostenible de las materias primas. Para este propósito, las configuraciones híbridas como las estructuras sándwich son soluciones altamente competitivas que la industria ya ha adoptado y consolidado durante las últimas décadas. En este sentido, la elección de la configuración adecuada es crítica para lograr el rendimiento deseado de un panel sándwich. En particular, el material y la morfología del núcleo desempeñan un papel fundamental en el comportamiento de la estructura. Consecuentemente, su selección se convierte en una decisión estratégica.

La irrupción de las tecnologías de Fabricación Aditiva (AM) que ha tenido lugar durante los últimos años ha revolucionado muchos sectores industriales, impactando directamente en los procesos de fabricación y el diseño de componentes. Aprovechando sus infinitas ventajas para fabricar geometrías de alta complejidad en comparación con los procesos de fabricación tradicionales, esta tesis doctoral tiene como objetivo contribuir al diseño de estructuras híbridas sándwich más eficientes utilizando núcleos celulares ligeros construidos por Fabricación por Filamento Fundido (FFF).

Para lograrlo, esta investigación se ha desarrollado abordando tres niveles de estudio con el fin de analizar el rendimiento del material, el diseño celular y la estructura híbrida de sándwich consolidada. Los resultados presentados en las diferentes contribuciones científicas derivadas de este trabajo se han validado analítica, numérica y experimentalmente, y muestran el potencial de los patrones bidimensionales y tridimensionales considerados para la fabricación de estructuras de sándwich completamente funcionales, haciendo un uso más eficiente de los materiales. Además, los modelos numéricos y las ecuaciones analíticas proporcionadas, así como el software de código abierto liberado para generar diseños celulares, serán de ayuda para realizar nuevos estudios en el campo de la optimización de la eficiencia estructural.

Finalmente, esta tesis ha manifestado algunas áreas de mejora en la tecnología FFF, como la presencia de imprecisiones en las uniones de filamentos intra-capa e inter-capa en la fabricación de diseños celulares bidimensionales de paredes delgadas y las limitaciones actuales para reducir el espesor mínimo de esas paredes. Sin embargo, con los avances y las innovaciones continuas en el campo, estas desventajas pronto se abordarán, lo que conducirá a resultados aún más impresionantes en un futuro cercano.

Compendium of publications

The herein-presented thesis has led so far to a total of three publications in peer-reviewed journals and one pending submission, three communications at national conferences and three communications at international conferences. The compendium of published peer-reviewed scientific articles that constitute the pillars of this thesis consists of three publications, which are listed in the following lines. They will be referred to in the text by their Roman numerals.

Publication I

A. Forés-Garriga, M.A. Pérez, G. Gómez-Gras, G. Reyes-Pozo, Role of infill parameters on the mechanical performance and weight reduction of PEI Ultem processed by FFF, *Mater. Des.* **193**, 108810, JCR Impact factor 2020: 7.991 (Q1 in *Materials Science, Multidisciplinary*), doi: 10.1016/j.matdes.2020.108810 (2020).

Publication II

A. Forés-Garriga, G. Gómez-Gras, M.A. Pérez, Mechanical performance of additively manufactured lightweight cellular solids: Influence of cell pattern and relative density on the printing time and compression behavior, *Mater. Des.* **215**, 110474, JCR Impact factor 2021: 9.417 (Q1 in *Materials Science, Multidisciplinary*), doi: 10.1016/j.matdes.2022.110474 (2022).

Publication III

A. Forés-Garriga, G. Gómez-Gras, M.A. Pérez, Additively manufactured three-dimensional lightweight cellular solids: Experimental and numerical analysis, *Mater. Des.* **226**, 111641, JCR Impact factor 2021: 9.417 (Q1 in *Materials Science, Multidisciplinary*), doi: 10.1016/j.matdes.2023.111641 (2023).

Publication IV

A. Forés-Garriga, G. Gómez-Gras, M.A. Pérez, Lightweight hybrid composite sandwich structures with additively manufactured cellular cores, *Thin-Walled Struct.*, JCR Impact factor 2021: 5.881 (Q1 in *Mechanics, Engineering Mechanical, Engineering Civil*), Preprint submitted on May 29, 2023.

All the published papers derived from this thesis will be appended at the end of this document as they were published in *open-access*. The submitted preprint version of the latest publication is also included.

Comments on the author's contribution to the publications

The author of this thesis is the first author of all presented publications. Nonetheless, given that they have several authors, the specific contribution of the PhD candidate Albert Forés Garriga to each publication is outlined below.

Publication I

He planned the DOE and fabricated the tensile, flexural, and shear American Society for Testing and Materials (ASTM) standard specimens employing a full factorial design of the most relevant FFF parameters according to the state of the art. He was also responsible for planning and executing the corresponding experimental characterization, which included digital microscopy analysis and mechanical testing, as well as post-processing the digital image correlation (DIC) recorded data. Together with the other authors, he contributed to the interpretation and analysis of the results. He wrote the preliminary version of the manuscript and participated in the submission and review processes.

Publication II

He identified the most relevant two-dimensional cellular designs in line with the state of the art. He contributed to the creation of the Computer-Aided Design (CAD) of the geometries and the adjustment of the corresponding wall thickness to ensure the correct manufacturing of the samples employing the FFF technology. In addition, he developed the mathematical expression to analytically determine the relative density of each of the studied designs regarding their multiple dimensional variables. He was also responsible for planning and executing the corresponding experimental characterization, which included digital microscopy analysis and mechanical testing, as well as post-processing the DIC recorded data. Furthermore, he coordinated the development and refinement of a robust finite element (FE) numerical model capable of simulating the compression behavior of the two-dimensional cellular designs using invariant boundary conditions. Together with the other authors, he contributed to the interpretation and analysis of the results. He wrote the preliminary version of the manuscript and participated in the submission and review processes.

Publication III

He identified the most relevant three-dimensional cellular designs in line with the state of the art. He led the development and release of new free software for the creation of cellular structures. He contributed to the creation of the CAD design of the geometries and the manufacturing of the samples employing FFF technology. He supervised the removal of the support structures using a solvent developed by other members of the research group. He was also responsible for planning and executing the corresponding experimental characterization, which included digital microscopy analysis and mechanical testing, as well as post-processing the DIC recorded data. In addition, he quantified the degree of isotropy of the different cellular solids using a proposed novel index based on the graphical representation of

their stiffness tensor. Furthermore, he coordinated the development and refinement of two robust FE numerical models capable of simulating the compression behavior of the three-dimensional cellular designs using invariant boundary conditions. Together with the other authors, he contributed to the interpretation and analysis of the results. He wrote the preliminary version of the manuscript and participated in the submission and review processes.

Publication IV (Preprint submitted)

He conducted a numerical study using FE simulations to investigate the effect of the cellular core design (two- and three-dimensional morphologies) and density on the flexural stiffness of sandwich structures with carbon fiber reinforced polymer (CFRP) skins. Based on the obtained results, he also fabricated the most optimal core configurations using FFF, as well as cured the CFRP skins and consolidated the sandwich structures, in order to validate the numerical results with experimental tests. Together with the other authors, he contributed to the interpretation and analysis of the results. He wrote the preliminary version of the manuscript and participated in the submission and review processes.

Coherence between the compendium of publications

The four presented publications are aligned with a well-defined research project that aims to contribute to the development of new sandwich structures, leveraging the latest advancements in AM technologies to reproduce bio-inspired cellular cores that are lightweight and with high structural potential. To achieve this goal, this research has focused on determining the mechanical properties of the selected material (Ultem), as well as analyzing the behavior of different two-dimensional and three-dimensional cellular designs and their performance when they are used as functional cores in assembled sandwich structures, combining analytical, numerical, and experimental approaches.

Publication I focuses on studying the elastoplastic behavior of Ultem commercial filament after being processed by FFF, regarding the most relevant manufacturing parameters of this technology. For this purpose, standardized samples of the material were characterized in tension, bending, and shear stresses to determine the effect of the selected parameters on both the mechanical properties and the weight of the fabricated components. The main outcome of this work was the determination of the effective stiffness tensor of Ultem, which was required for addressing all the numerical approaches developed in this research.

Publications II and III are focused on the mechanical behavior of a wide range of two-dimensional and three-dimensional cellular designs fabricated with Ultem processed by FFF, respectively. On the one hand, Publication II presents the equations that, parameterized with the dimensions of the studied patterns, allow for the analytical calculation of the cellular structures' densities and stiffnesses. On the other hand, Publication III introduces a new and more robust index to determine the degree of anisotropy of cellular solids which can consider the inherent anisotropy of many current AM technologies as it is based on the graphical representation of the homogenized stiffness tensor. Additionally, the first

version of developed open-source software, called TPMSgen [1], was released for the parametric design of three-dimensional cellular solids. Finally, the experimental linear behavior of the analyzed cellular solids was validated in both cases with FE analyses. The provided results confirm that both the design and density of the cellular solids are two versatile parameters to adapt the mechanical properties and weight of the components to the final requirements.

Finally, Publication IV focuses on the implementation of two- and tri-dimensional cellular solids made of Ultem processed by FFF as cores in sandwich structures with CFRP skins, in order to determine the influence that both design and density have on the mechanical behavior of the composite panels. For this purpose, a numerical study using a FE analysis model has been presented, in order to reproduce the elastic behavior of a wide range of additively manufactured sandwich structures under bending stresses by parameterizing the dimensions of the core and skins, as well as the mechanical properties of the constituent materials. In addition, the configurations that obtained the optimal behavior for each considered cellular pattern were manufactured and experimentally tested to validate the numerical approach results. The outcomes of this investigation demonstrate the structural potential of the considered designs and highlight certain limitations of the selected fabrication technology based on its current level of maturity.

Other publications

Communications at international conferences

- M.A. Pérez, **A. Forés-Garriga**, G. Gómez-Gras, M.D. Abad, Análisis numérico y experimental del comportamiento mecánico de sólidos celulares tridimensionales obtenidos por fabricación por filamento fundido, XV Congreso Iberoamericano de Ingeniería Mecánica (CIBIM-2022), Madrid (Spain), November 22-24, 2022 (Oral presentation).
- **A. Forés-Garriga**, G. Gómez-Gras, G. Reyes-Pozo, M.D. Abad, A.A. García-Granada, J. Menacho, M.A. Pérez, Mechanical behavior and manufacturing analysis of 2D Cellular Solids manufactured by Fused Filament Fabrication, 1st Ibero-American Conference on Composite Materials (IAMaC-2021), Porto (Portugal), July 29-30, 2021 (Oral presentation).
- **A. Forés-Garriga**, G. Gómez-Gras, G. Reyes-Pozo, M.D. Abad, A.A. García-Granada, J. Menacho, M.A. Pérez, Bending performance of sandwich structures composed of 2D and 3D cellular cores manufactured with Fused Filament Fabrication and CFRP skins, 1st Ibero-American Conference on Composite Materials (IAMaC-2021), Porto (Portugal), July 29-30, 2021 (Oral presentation).

Communications at national conferences

- **A. Forés-Garriga**, G. Gómez-Gras, M.D. Abad, M.A. Pérez, Comportamiento a flexión de estructuras sándwich con núcleos celulares bio-inspirados elaborados por Fabricación por

Filamento Fundido, XXIV Congreso Nacional de Ingeniería Mecánica (CNIM-2023), Las Palmas de Gran Canaria (Spain), October 25-27, 2023 (Oral presentation).

- **A. Forés-Garriga**, A. Chueca de Bruijn, G. Gómez-Gras, M.A. Pérez, Nuevos desarrollos en estructura ligera tipo sándwich con núcleos bioinspirados impresos en 3D, XIV Congreso Nacional de Materiales Compuestos (MATCOMP-2021), Sevilla (Spain), June 21-23, 2022 (Oral presentation).
- **A. Forés-Garriga**, M.A. Pérez, G. Gómez-Gras, G. Reyes-Pozo, Impacto de la densidad de relleno en las propiedades mecánicas de elementos de ULTEM™ 9085 procesados por FFF, XXIII Congreso Nacional de Ingeniería Mecánica (CNIM-2020), Jaén (Spain), October 20-22, 2021 (Oral presentation).
- **A. Forés-Garriga**, G. Gómez-Gras, M.A. Pérez, New developments in Lightweight Composite Sandwich Panels with 3D printed cores, I Jornada de Doctorands IQS (JDIQS-2019), Barcelona (Spain), May 16-17, 2019 (Poster presentation).
- G. Gómez-Gras, M.A. Pérez, A. Chueca, **A. Forés-Garriga**, D. Munar, Estudio de núcleos celulares impresos en 3D para estrurcturas ligeras tipo sándwich, XXII Congreso Nacional de Ingeniería Mecánica (CNIM-2018), Madrid (Spain), September 19-21, 2018 (Oral presentation).

Contents

List of figures

List of tables

List of abbreviations

3D	**Three**-**D**imensional
AM	**A**dditive **M**anufacturing
ASTM	**A**merican **S**ociety for **T**esting and **M**aterials
CAD	**C**omputer-**A**ided **D**esign
CFRP	**C**arbon **F**iber **R**einforced **P**olymer
CMB	**C**oordinate **M**achine **B**inary
DIC	**D**igital **I**mage **C**orrelation
DOE	**D**esign **O**f **E**xperiments
FE	**F**inite **E**lement
FDM	**F**used **D**eposition **M**odelling
FF	**F**irst **F**ailure
FFF	**F**used **F**ilament **F**abrication
FST	**F**lame, **S**moke, and **T**oxicity
H-RVE	**H**omogenized - **R**epresentative **V**olume **E**lement
JCR	**J**ournal **C**itation **R**eports
PBF	**P**owder **B**ed **F**usion
PSF	**P**oly**S**ul**F**one
PTFE	**P**oly**T**etra**F**luoro**E**thylene
PE	**P**oly**E**thylene
PMI	**P**oly**M**ethacryl**I**mide
PS	**P**oly**S**tyrene
PUR	**P**oly**UR**ethane
PVC	**P**oly**V**inyl **C**hloride
SE	**S**olid **E**lements
STEP	**ST**andard for the **E**xchange of **P**roduct model data
STL	**ST**ereo**L**ithography
TPMS	**T**iply **P**eriodic **M**inimal **S**urface
Ultem	**ULTEM**™ 9085

List of symbols

Roman symbols		
E	elastic modulus	MPa
G	shear modulus	MPa
T_g	glass-transition temperature	°C
t	Sandwich face thickness	mm
c	Sandwich core thickness	mm
d	Sandwich total thickness	mm
f	Volume fraction occupied by the faces of a sandwich	(-)
A	Zener Ratio	(-)
A^U	Universal Anisotropy Index	(-)
A^V	Stiffness tensor volume-based anisotropy index	(-)
Greek symbols		
ν	Poisson's ratio	(-)
ρ	density	kg/m^3
σ_T	tensile stress	MPa
σ_C	compressive stress	MPa
τ	shear stress	MPa
Subscripts		
x	x-direction	(-)
y	y-direction	(-)
z	z-direction	(-)
Superscripts		
$*$	cellular solid property	(-)
s	solid infill property	(-)
sp	sparse infill property	(-)

1 Introduction

The opening chapter introduces the topic of this research and the motivation that encouraged the development of the present doctoral thesis. It also outlines the main research hypothesis and objectives, and briefly summarizes the structure of this dissertation to guide the reader throughout the whole document.

1.1 Motivation

Over the last decade, CO_2 emissions have become a major concern globally. The transport sector is responsible for 23% of the global energy-related CO_2 emissions, with road transport being the largest contributor [2]. The growing number of vehicles, the increase in global trade, and air traffic have led to a surge in CO_2 emissions from transportation. Despite various initiatives aimed at reducing emissions, such as the use of cleaner fuels, the adoption of electric vehicles, and the promotion of public transportation, the transport sector continues to produce high levels of greenhouse gases. Addressing this challenge requires continued efforts to develop sustainable and low-carbon transportation systems.

The weight of a vehicle directly influences the number of emissions it generates. Heavier vehicles typically require more energy to accelerate and brake, which further contributes to fuel consumption and the corresponding emissions to the atmosphere. Hence, manufacturers are increasingly exploring new ways to reduce their weight, such as the use of lightweight materials and redesigning components, to create lighter, more fuel-efficient vehicles.

In this regard, one of the most important advances in the last decades has been the implementation of sandwich structures for the manufacture of various types of transportation, especially in the naval, aeronautical, and aerospace sectors. These composite materials are composed of two outer layers of stiff and strong materials with a lightweight core in between. This configuration seeks to achieve an optimal arrangement of materials to obtain very efficient structures in terms of physical and mechanical properties, making better use of the available resources. In particular, one of the most outstanding aspects of sandwich structures is their exceptional strength-to-weight ratio. Hence, engineers can significantly reduce the weight of vehicles while maintaining their structural integrity and safety. Additionally, sandwich panels can offer excellent insulation properties that can reduce the energy required to heat or cool the vehicle's interior. Therefore, as the demand for sustainable transportation options continues to grow, the use of sandwich panels is likely to become increasingly common in the design and construction of vehicles, since they have the potential to create more fuel-efficient and environmentally friendly means of transportation.

The above-mentioned advantages of these structures depend to a large extent on the characteristics and properties of the core. So, its choice becomes a strategic decision. For many years, the feasibility of developing new core designs has undoubtedly been constrained by the technical limitations of traditional manufacturing methods such as confirmatory or subtractive. However, the rise of AM technologies, capable of manufacturing fully functional end components, constitutes a turning point in the feasibility of manufacturing new lightweight structures with almost no restrictions in terms of geometric complexity. Therefore, these technologies have attracted enormous attention from the scientific community and different industrial sectors, as it brings exceptional design flexibility, reduction of waste material and shorter production times. For all these reasons, the use of AM technologies is becoming increasingly popular, and will undoubtedly constitute one of the strategic pillars of the global transformation toward Industry 4.0 in the next decade.

In this regard, AM has enormous potential, and one of its most promising applications is the production of cellular solids. These materials are composed of a porous cellular structure formed by interconnected cells and voids. Until some years ago, cellular solids were only found in nature, such as in bones, wood, and plant stems, but advanced techniques such as AM have made it possible to replicate them. Furthermore, their physical and mechanical properties can be tailored by adjusting factors such as the size and shape of the cells, the material used, and the density of the structure. As a result, bioinspired cellular solids have been the focus of extensive research and development, intending to create more efficient and versatile materials for various applications, including aerospace, automotive, and biomedical industries.

Therefore, the implementation of additively manufactured cellular solids as cores in hybrid sandwich structures could lead to breakthroughs in the design and fabrication of very lightweight components to improve vehicle efficiency and reduce CO_2 emissions from the transportation sector. However, although several investigations have focused on analyzing the isolated behavior of novel cellular designs, their functionality in sandwich structures has hardly been considered. Thus, the motivation for the development of the present doctoral thesis arises from exploring in full depth the possibility of integrating core biomimetic core designs on sandwich panels to conform functional lightweight parts.

1.2 Hypothesis and research objectives

After analyzing the context that inspired this research, a set of initial hypothetical statements were formed, which are summarized in the following lines:

- Reducing the weight of transportation vehicles is a highly effective method for enhancing their efficiency, which leads to lower fuel consumption and a decrease in the amount of CO_2 emissions released into the atmosphere. Utilizing lightweight materials and cutting-edge structures makes it possible to face this challenge with guarantees.
- High-performance composite materials have demonstrated their effectiveness in reducing weight, but their high manufacturing costs limit their applicability. To overcome this challenge, the industry has embraced sandwich-structured compounds as a highly competitive solution. This optimized configuration can provide numerous additional advantages bringing added value to the structural solution.
- The selection of the core type in a sandwich structure is an important choice as it significantly impacts its structural behavior. Bioinspired cellular cores offer promising qualities for a variety of applications, such as their enhanced mechanical performance and lightweight capacity. However, the performance of these cores can vary depending on the cell geometry and density. Furthermore, the manufacturing of non-conventional geometries poses a technical challenge that must be addressed.

- Advances in AM have made it possible to replicate natural cellular patterns, which have evolved over thousands of years to provide optimal structural efficiency, at a macroscopic scale. Among the various AM technologies, FFF offers a unique opportunity for developing cellular cores for sandwich structures at a low cost, enabling new degrees of freedom in the geometric design of cells that have yet to be explored.
- It is widely recognized that the mechanical properties of the core significantly affect the performance of the whole sandwich structure. Additionally, given the inherent anisotropy resulting from the additive fabrication process, it is essential to consider the impact of FFF printing parameters on the mechanical behavior of cellular designs.
- Accurate numerical simulation models experimentally verified and validated can serve as a powerful tool for analyzing and optimizing new designs based on this structural solution, further customizing it for a wide range of engineering applications, which is expected to benefit the industry greatly.

Based on the initial hypotheses, the purpose of this thesis is to contribute to the development of sandwich structures consisting of CFRP skins and advanced bioinspired cores fabricated with FFF technology. Therefore, the objective is to investigate the feasibility of using cellular designs as core materials in sandwich panels to achieve high-performance hybrid structures. The focus is on examining the structural performance of these designs based on their geometry, density, and cell arrangement. Hence, this research aims to demonstrate the potential of AM technologies, specifically FFF, for creating sandwich panel cores that can provide new opportunities for creating lightweight structures and components in combination with advanced composite materials.

To this end, an analytical, experimental, and numerical approach will be used in this research. The experimental component will include a comprehensive analysis at three levels of operation: the FFF processed material, the cellular core designs, and the hybrid sandwich structures. On the other hand, the numerical approach will provide a mechanical analysis and optimization methodology to create new designs based on the proposed structural solution.

The ultimate objective is to develop a cost-effective and competitive structure that could provide substantial environmental benefits. The outcomes of this research will allow facing the challenge of reducing the weight of structural components with guarantees, thus arousing interest in its potential applicability in different industrial sectors.

The accomplishment of the above-stated goal relies on the attainment of various specific objectives, which can be summarized as follows:

1. Examine how the mechanical behavior and anisotropy of components produced by FFF are impacted by the primary printing parameters that influence the material deposition paths of this AM technology.

2. Design cellular cores employing two- and three-dimensional patterns, considering their manufacturing feasibility through FFF technology, and investigate how the mechanical behavior is affected by the geometry, density, and arrangement of the cells.

3. Develop a numerical model to simulate the compression and flexural behavior of the isolated cellular designs, as well as the bending performance of hybrid sandwich structures combining cellular cores with CFRP skins.

4. Manufacture sandwich structures consisting of two- and three-dimensional cellular cores produced using the FFF technology, along with CFRP skins, to experimentally characterize their mechanical behavior and validate the developed numerical model.

1.3 Thesis outline

This text is the culmination of five years of research focused on the development of hybrid sandwich structures exploiting the potential of the latest developments in AM technologies to fabricate lightweight and functional bio-inspired cores. The document consists of six chapters, which are structured as follows.

Chapter 1 encompasses the motivation, the hypothesis and research objectives, and the organization of the present thesis.

The state of the art is covered in **Chapter 2**, which is organized into four subsections. In the first one, the potential of sandwich structures for many of the most powerful engineering sectors is highlighted, as well as the materials that are most commonly used for their fabrication. The second section focuses on the design and fabrication through different AM technologies of bio-inspired cellular solids that draw inspiration from natural structures aiming to enhance material properties. Thirdly, the operating principle of the FFF technique is described, focusing on relevant aspects such as the anisotropy and mechanical properties of the manufactured parts to be able to approach the development of the proposed solution with guarantees. Finally, a recapitulation section outlines the essential points derived from the state of the art, which are crucial for comprehending and supporting the hypothesis and scope of this thesis.

Chapter 3 presents the methodology employed for the development of this research. In particular, the analytical, numerical and experimental procedures that were implemented to assess the studies of the FFF processed material, the two- and three-dimensional cellular cores, and the hybrid sandwich structures are detailed.

The main results of this research are highlighted and discussed in **Chapter 4** of this document.

Chapter 5 synthesizes in the form of conclusions the knowledge acquired with the development of the previous chapters in order to give concise answers to the hypotheses formulated at the beginning of this

research. This chapter also encompasses the principal scientific contributions and recommendations for future work to be conducted in line with the presented investigation.

To conclude, **Chapter 6** is a compilation of the four research papers published as part of this thesis in peer-reviewed scientific journals.

2

Literature review

This chapter contains an in-depth review of various topics relevant to hybrid structures, focusing on the design and performance analysis of sandwich structures. Aspects regarding faces and core material selection are addressed. In addition, the most relevant works in the field of cellular cores manufactured by AM technologies are presented. Finally, the FFF technology and the Ultem™ 9085 material used in this research are discussed in more detail.

2.1 Hybrid materials and design strategies

Hybrid materials are combinations of two or more materials assembled in such a way as to have attributes not offered by either one alone [3]. Thus, these compounds seek to incorporate the properties of different monolithic materials smartly in order to achieve the desired characteristics (*i.e.* physical, chemical, mechanical, electrical…).

In this sense, one of the most widely implemented strategies for the design of new hybrid materials with specific property profiles is based on the following four pillars:

1. **Components**: The choice of materials to be combined.
2. **Configuration**: The shape and connectivity of the components.
3. **Relative volumes**: The volume fraction of each component.
4. **Scale**: The length scale of the structural unit.

Particulate and fibrous composites are the main examples of hybrid materials. However, there are many others, such as sandwich structures, cellular structures, and more, which are all summarized in Figure 2.1.

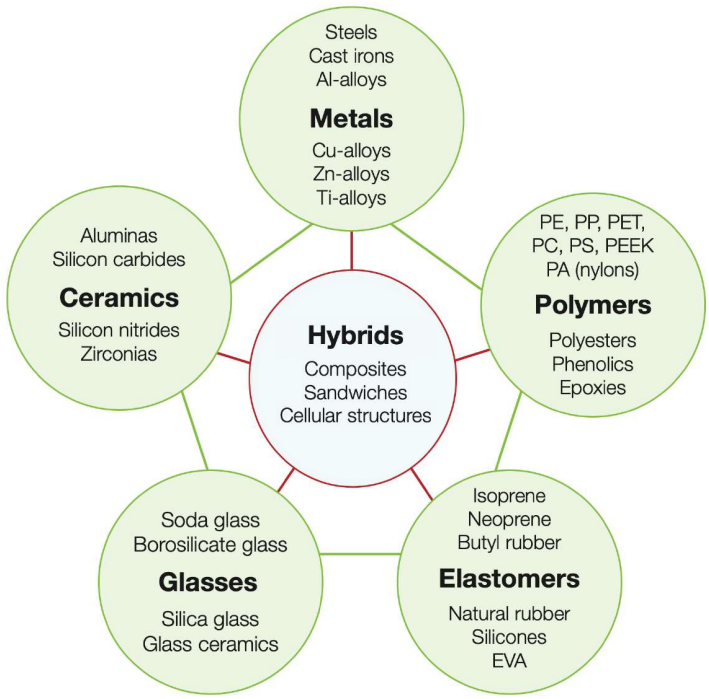

Figure 2.1: Examples of hybrid materials (*center*) and principal types of monolithic material employed for their consolidation (*corners*). Adapted from [3].

2.1.1 Composites

Composites combine two solid components, one (the reinforcement) as fibers or particles, contained in the other (the matrix) [3]. Theoretically, any two materials can be merged in order to obtain a composite. To do so, the mixture can be consolidated in different geometries and arrangements that determine whether the typology of the composite structure is unidirectional fibrous, laminated fiber, chopped fiber, or particulate (see Figure 2.2).

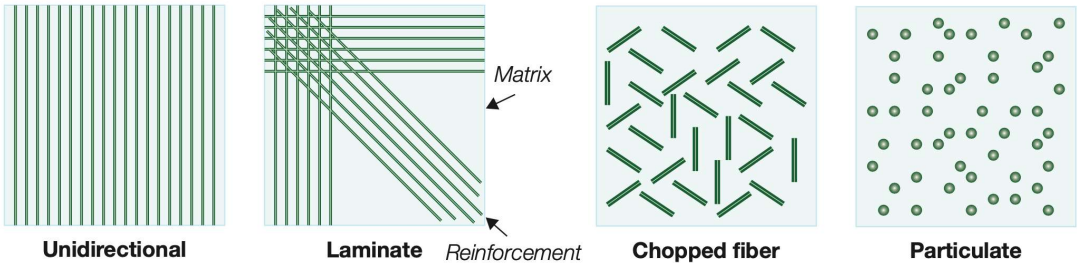

Figure 2.2: Schematic of hybrid materials of the composite type. Adapted from [3].

2.1.2 Sandwich structures

Sandwiches typically consist of two outer faces made of one material, which are bonded to a low-density material core of a different type that separates them. A sandwich works similarly to an I-beam, which is an efficient structural shape because as much as possible of the material is placed in the flanges situated farthest from the center of bending or neutral axis [4]. Hence, this arrangement (see Figure 2.3) efficiently increases the inertia of the panels and their section modulus at a very low weight cost, thus resulting in a flexural stiffness per unit weight that surpasses what either individual component could offer on its own, producing an excellent structure for resisting bending and buckling loads.

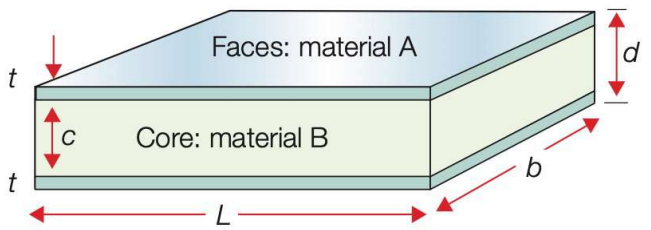

Figure 2.3: Schematic of a sandwich structure arrangement. Adapted from [3].

The faces bear the majority of the load and therefore need to be rigid and durable. Additionally, since they are the outer layer of the sandwich panel, the material employed for fabricating the faces must also be able to withstand the environmental conditions in which the panel will work. Meanwhile, the

core takes most of the volume of the whole sandwich structure. It needs to be lightweight and rigid, but also strong enough to support the shear stresses necessary to guarantee the functionality of the panel as a load-bearing unit.

Thanks to their outstanding properties, sandwich panels are widely used in various engineering fields. They are employed in walls, roofs, and floors to provide structural support and insulation in building constructions [5]. Furthermore, sandwich panels offer excellent solutions in the transportation industry for fabricating aircraft floors, walls, and ceilings, in order to reduce weight and improve fuel efficiency [6]. Moreover, they are also used in the marine industry for hulls and decks [7].

Interestingly, sandwich panels do exist in nature as well. Bones, for example, have a sandwich-like structure, with a core made of trabecular bone and two outer layers of compact bone. This structure provides bones with strength and flexibility, making them ideal for supporting and protecting the body [8]. In addition, sections through the wing of birds, and the stalk and leaves of many plants show a low-density foam-like core separating solid faces [9].

2.1.3 Cellular structures

Cellular structures are systems made up of interconnected pores or bars that form a unique structure with distinctive mechanical properties. The cells within the structure can be regular or irregular in shape, and their design and size can be adapted to meet the requisites of the desired application. The unique arrangement of cells provides a range of advantages such as a high strength-to-weight ratio, excellent energy absorption, and sound insulation properties. Moreover, the gas occupying the spaces of the porous structure can play a fundamental role in controlling properties such as thermal and electrical conductivity, as well as the mechanical compressibility of the cellular structure [3].

Foams are one of the most common types of cellular structures. They are made by expanding polymers, metals, ceramics, or glasses with a foaming agent or any other way of introducing a gas [10–12]. As a result, a porous structure is obtained, formed by solid cell walls or edges that confine the gas in the different hollow spaces that have been formed. Accordingly, the morphology of foams tends to be bending-dominated (see Figure 2.4), as the walls fold when they are loaded, thus compromising the stiffness of the whole structure.

During the 20^{th} century, several advances in materials science together with the development of new manufacturing processes made it possible to reproduce some basic two-dimensional designs present in nature, such as hexagonal panels [4]. Despite they are also porous cellular structures, the morphology of these extruded-like patterns exhibits a high rigidity in one direction, especially under buckling stresses, offering a much more stretch-dominated performance. Thus, the development of lightweight honeycombs made of advanced technical materials such as Nomex® or aluminum represented a paradigm shift for the fabrication of functional hybrid sandwich structures [13].

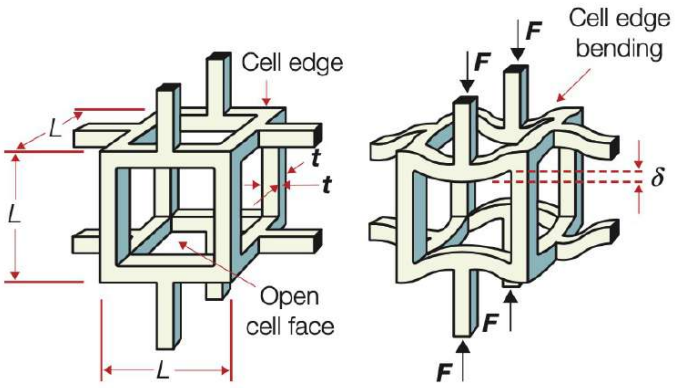

Figure 2.4: Deformation diagram of a bending-dominated cellular structure. Adapted from [3].

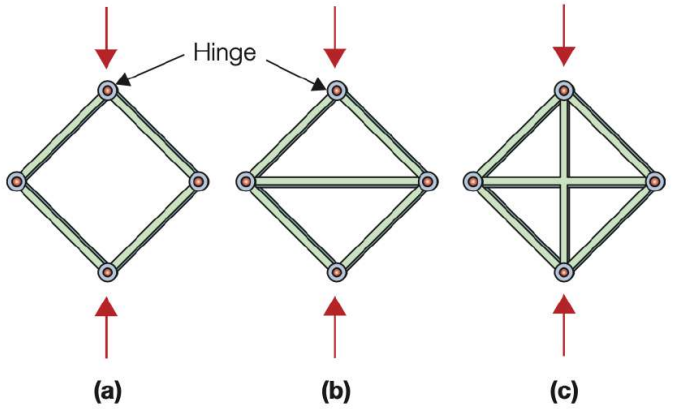

Figure 2.5: Schematic process for obtaining stretch-dominated designs. Adapted from [3].

Classical manufacturing processes such as casting, molding, and milling have limited the possibilities of fabricating other stretch-dominated patterns with highly complex geometries to explore the structural capabilities of cellular solids for a long time. However, the recent developments in the AM field have spread the horizons for fabricating endless cellular structures [14, 15]. In particular, the layer-by-layer fabrication process that characterizes these technologies allows for the creation of unique cellular solids with intricate shapes that were once impossible to produce using classical manufacturing processes. Consequently, they have opened up new opportunities in various industries, including aerospace, automotive, and medical, where mass optimization is often required [16].

Furthermore, AM has not only enabled the fabrication of improved two-dimensional designs with very interesting auxetic properties to withstand impact stresses [17] but also the direct production of entirely new three-dimensional arrangements, such as lattice and Triply Periodic Minimal Surface (TPMS) cellular solids. On the one hand, lattice structures are composed of a repeated pattern of interconnected beams, struts or bars, that form a stable three-dimensional (3D) framework reminiscent of trusses at both the micro and macro levels. On the other hand, TPMS structures, which were first described in

the mid-19th century by Joseph Plateau and further investigated in 1987 by Alan Schoen [18], offer a constant curvature that seeks to minimize the surface area of the structure employing mathematical expressions while maintaining its enclosure volume. Overall, AM technologies have made more accessible the possibilities to create structures that possess unique properties such as high porosity, tunable mechanical properties, and excellent heat and mass transfer capabilities, making them ideal for use in various applications [19–21].

2.1.4 The equivalent properties approach for hybridization

A material property chart, also known as a materials selection chart, is a visual tool to aid in the choice of materials for a particular application based on the desired properties (see Figure 2.6). By plotting multiple materials on the same chart, engineers and designers can quickly compare and contrast the strengths and weaknesses of different materials and identify the best candidate for their specific needs. The chart typically plots two or more material properties (*i.e.* physical, mechanical, price, environmental) against each other. Therefore, material property charts can be used to identify

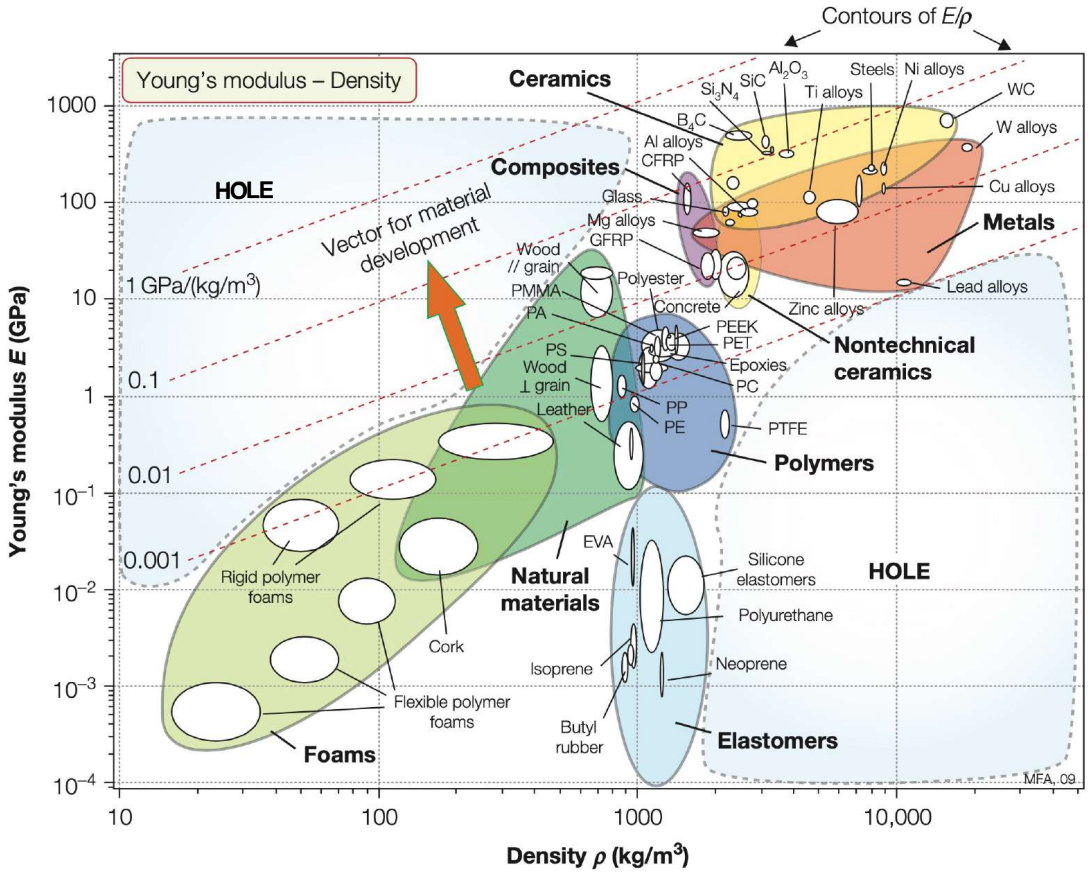

Figure 2.6: Material property chart that depicts holes in Young's modulus-density space. Adapted from [3].

trade-offs between different material properties. For example, a material with high strength may be more brittle and prone to fracture, while a material with high toughness may be less stiff.

Overall, any material property chart shows some parts that are populated with materials while others are not. The holes that appear belong to points that are inaccessible for fundamental reasons that relate to the size of atoms and the nature of the forces that bind them together. However, other parts are empty even though, in principle, they could be filled. The hybridization process (development of combinations of materials) can, in some cases, lead to the production of materials that lie exactly in these holes. Thus, the development of new hybrid structures in the direction of the vector for material development will enable lighter, stiffer structures to be made. For this purpose, it becomes very useful to evaluate the properties of the resulting hybrid structures as a whole material.

Furthermore, this approach offers several benefits over picking each constituent separately. Firstly, focusing on a macroscopic perspective of the hybrid structure allows for a more accurate prediction of the overall mechanical behavior of the structure under different loading conditions. Even though the literature contains many studies for comprehending how a particular architecture behaves [22–24], the precise calculation of its properties can be a demanding issue since the characteristics of each constituent material interact with each other in complex ways. Secondly, treating the hybrid structure as a homogeneous material with its own set of mechanical, thermal, electrical, and other properties enables the optimization of each constituent material to develop advanced materials with tailored properties for a specific application. This can favor obtaining hybrid structures with improved mechanical and physical properties, such as increased strength, stiffness, and toughness, as well as reduced weight and cost. Thirdly, this design approach makes it possible to identify potential failure mechanisms and improve the overall reliability and safety of the whole structure.

In addition, the determination of the effective properties of the hybrid structure will favor the comparison of its performance with the rest of existing monolithic materials more simply and fairly. In this sense, although other cases are possible, one of the following scenarios will be fulfilled in the hybridization process (see Figure 2.7) according to the type of hybrid to be designed, the employed combination of materials, and the inspected properties [3]:

- **"The best of both" scenario**: the optimal case in which the best properties of both materials are desired.
- **"The rule of mixtures"** scenario: the most commonly achievable result is often the arithmetic mean of the characteristics of the components, which are adjusted by the fraction of each component's volume.
- **"The weaker link dominates"** scenario: in some cases, a lesser compromise must be accepted and the hybrid properties tend to be lower than what is predicted by the rule of mixtures arithmetic mean and closer to a harmonic mean.
- **"The last of both" or weakest-link** scenario: sometimes it is not the greatest but the least of the properties that are desired.

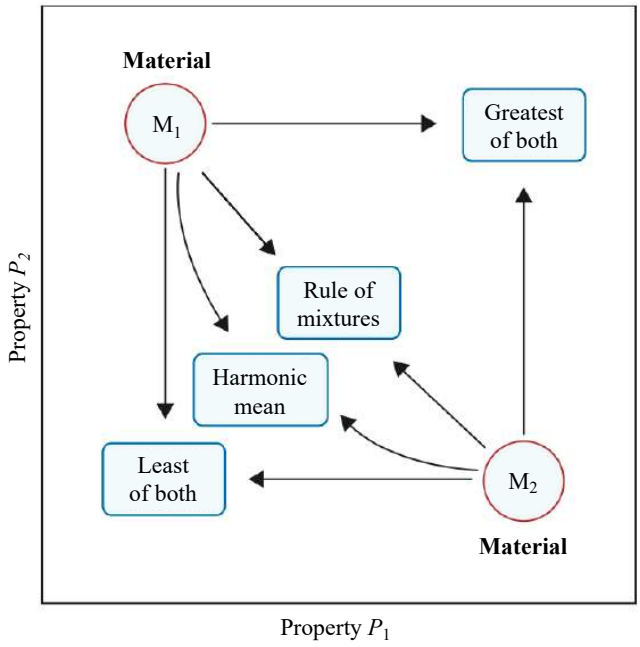

Figure 2.7: The possibilities of hybridization. Adapted from [3].

2.2 Sandwich panels design for structural applications

As previously introduced, sandwich structures consist of up to three or more constituents: the faces, the core, and the adhesive joints. In 1969, Allen [25] established the principles of sandwich design. Typically, the faces can be made of different materials depending on what is needed for the structure or the manufacturing process. The same applies to the employed adhesives. There is a wide variety of materials to choose from, and since the introduction of fiber composites, the range of face materials available has increased almost infinitely, each with its unique properties. Even the number of core possibilities has increased significantly in recent years thanks to the development of more and more competitive cellular plastics. Therefore, designing sandwich structures is both a materials selection and sizing problem [4].

Choosing the right materials from such a wide range of possibilities can appear to be a very complicated task. However, quite the contrary, it is one of the main features of using sandwich structures because it allows for the selection of the most appropriate materials for each specific application, and some disadvantages can be overcome through geometrical sizing. For example, some reinforced plastics may not have the same high stiffness as metals, but by increasing the core thickness, sufficient rigidity can still be achieved. Hence, materials are often chosen not for their mechanical properties, but for other reasons such as environmental resistance, surface finish, the use of a specific manufacturing method, cost, or wear resistance, among others.

2.2.1 Face materials

Almost any structural material which is available in the form of a thin sheet may be used to form the faces of a sandwich panel [25]. However, the most frequently used face materials can be classified into two primary categories: metallic and non-metallic materials [4]. The metallic group contains steel, stainless steel and aluminum alloys, providing a wide range of strength properties whereas the variation in stiffness is quite limited. Meanwhile, the non-metallic group is the largest one, which encompasses materials such as plywood, cement, veneer, reinforced plastic, and fiber composites. However, despite the wide range of possibilities, the general properties of primary interest for an appropriate faces choice in the design of sandwich structures are depicted in Figure 2.8:

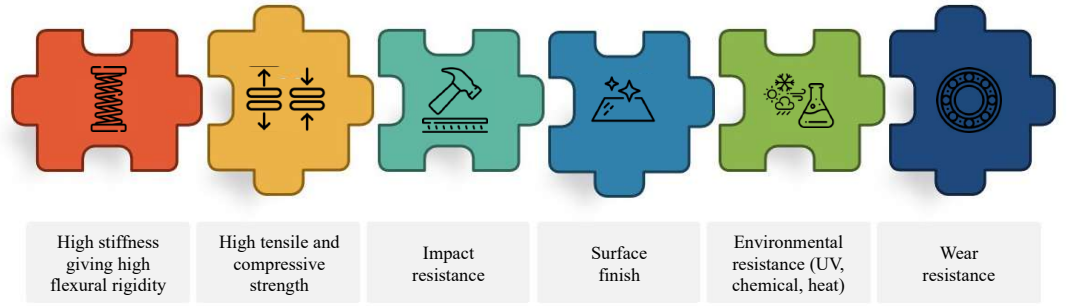

Figure 2.8: Properties of primary interest for the faces of sandwich structures.

In particular, the introduction of fiber composites had a significant impact on the use of sandwich structures. The reason for this is that most composites offer strength properties similar to, or even higher than those of metals, but their stiffness is often lower. Therefore, to achieve high rigidity, composites are often sandwiched with a lightweight core. In addition, their fabrication is much easier than manufacturing metal face sandwich structures.

A unique feature of fiber composites is their anisotropic behavior, meaning that they have different properties in different directions. This can be seen as an initial complexity that engineers might perceive as an obstacle. However, it is, in fact, an advantage as it provides the opportunity to tailor properties in conjunction with the applied loads. Hence, one can orient fibers to carry the load in any particular direction [26–28]. Therefore, not only are the material components stressed to their ultimate limit, but the component itself can also be utilized more efficiently.

2.2.2 Core materials

The core component is perhaps the most important part of the whole sandwich structure. First, it should be as light as possible so that its mass contribution has as little impact as possible on the weight of the entire structure. Secondly, although the transverse forces creating normal stresses perpendicular to the core are usually low, even a small decrease in core thickness would create a large decrease in bending stiffness. Hence, its stiffness along the direction perpendicular to the faces should be high

enough to prevent a decrease in the core thickness, which would compromise the flexural rigidity of the sandwich structure. The core is mainly subjected to shear, which generates core shear stresses and global deformations through core shear strains. Consequently, the selection of a core must ensure it can withstand the transverse load without failing and have a sufficiently high shear modulus to provide the necessary shear stiffness. Finally, Young's modulus and the shear modulus of the core are both factors that influence the critical wrinkling load. Meanwhile, the core material and its thickness primarily impact other functions of the sandwich, such as thermal and acoustical insulation. Figure 2.9 summarizes the most important characteristics for an appropriate core selection in the design of sandwich structures:

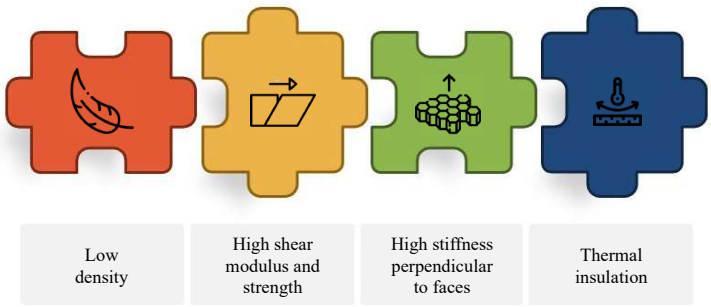

Figure 2.9: Properties of primary interest for the cores of sandwich structures.

Following is a brief description of the three types of cores most commonly used for the manufacture of sandwich structures [4]:

- **Balsa wood**: It was the first material used as cores in load-bearing sandwich structures. Despite being a type of wood, can be viewed as a closed-cell structure with an aspect ratio of around 1:25 when examined under a microscope (see Figure 2.10 *a*-*c*). Its properties are strongest in the direction of fiber growth but much weaker in other directions. Balsa is available in different qualities with densities ranging from 100 to 300 kg/m^3. However, since natural balsa blocks have varying densities, the design limit should be based on the piece with the lowest properties. Despite being limited to the minimum density, the mechanical properties of balsa appear to be quite good and higher than most cellular plastics.

- **Honeycombs**: They have mainly been developed and utilized in the aerospace industry and construction applications. They can be created using various cell shapes (see Figure 2.10 *d*-*h*), including the commonly used hexagonal design (*d*), square or rectangular shape (*e*), reinforced hexagonal (*f*), over-expanded hexagonal (*g*), and the flex-core (*h*). The latter two configurations are primarily used when the core needs to be curved during the manufacturing of the sandwich structure, as they reduce anticlastic bending and cell wall buckling. Aluminum alloy or impregnated glass or aramid fiber mats, such as Nomex®, are the most frequently used materials for creating honeycombs.

- **Cellular foams**: Despite having lower stiffness- and strength-to-weight ratios compared to honeycombs, foams are solid on a macroscopic level (see Figure 2.10 *i-k*), which makes the manufacturing of sandwich elements easier: it is easy to bond to the foam surface, it requires simple surface preparation and shaping, and the connections of core blocks can be performed through adhesive bonding. Additionally, cellular foams are often less expensive and offer high thermal insulation and acoustical damping. Another advantage is that the closed-cell structure of most foams ensures that the sandwich arrangement is buoyant and resistant to water penetration. Among the various possibilities, the most commonly used foam alternatives are polyurethane (PUR), polystyrene (PS), polyvinyl chloride (PVC), polyethylene (PE), and polymethacrylimide (PMI) foams.

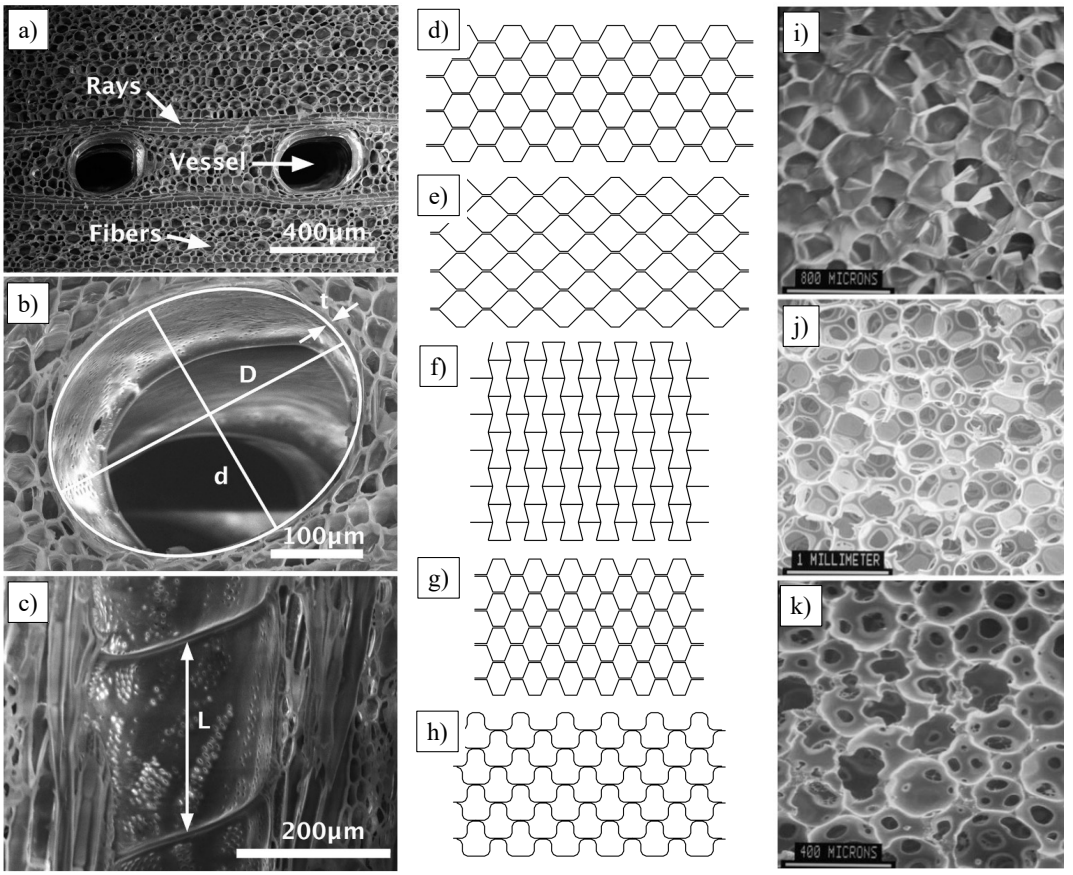

Figure 2.10: SEM micrograph of the cross-section of medium-density balsa (*a-c*), commonly used cell configurations for honeycomb core materials (*d-h*), and SEM images of a closed-cell low-density PE foam (*i*), an open-cell PUR foam (*j*), and a micro-porous PUR foam (*k*). Adapted from [4, 29, 30].

2.2.3 Adhesives

When selecting an adhesive appropriate for the sandwich structure, the main focus is on finding one that meets the mechanical requirements of the components and can create a strong bond in the

environment where the structure will work. Factors like fatigue, heat resistance, strength, aging, and creep are crucial considerations. Fortunately, there is a wide range of adhesives available that can create a strong bond between almost any combination of sandwich materials, being epoxy resins, modified epoxies, phenolics, polyurethanes, urethane acrylates, and polyester and vinyl ester resins the most commonly used types [4]. Additionally, the adhesive must be suitable for the specific environment where it will be used. Hence, other factors like health concerns, manufacturing methods, curing time, curing temperature, and tooling requisites will also play a significant role in determining the appropriate adhesive for the particular application and manufacturing environment. Ultimately, these requirements will have the greatest influence on the choice of the adhesive system.

2.2.4 Overview of the most commonly used materials

In view of the above, the design of hybrid sandwich structures has great potential to address the challenge of covering the holes that currently exist in material-property charts. Hence, choosing the most appropriate adhesive and materials for manufacturing the skins and the core, as well as correctly sizing their thickness and other dimensions, makes it possible to achieve structures with tailor-made properties that are specific to the desired application.

As an example, Figure 2.11 depicts a flexural modulus-density material-property chart. The areas occupied by monolithic materials like metals, polymers, ceramics, composites, and foams appear as labeled pale envelopes. The performance of a hybrid cantilever sandwich panel consisting of CFRP face sheets and high-performance foam core subjected to a structural load at its far, unsupported end, is overlapping them. Every point of the highlighted trend belongs to a different sandwich arrangement labeled with the corresponding f ratio value (see Eq. 2.1), which is calculated as the division between the thickness of each skin (t) and the total thickness of the sandwich structure (d), ranging from 0 (all core, no faces) to 1 (no core, all faces).

$$f = 2t/d \tag{2.1}$$

As can be seen, some configurations of the CFRP-foam sandwiches considered in this example can achieve stiffness and density values that occupy certain areas of the material-property chart that were previously uncovered, thus proving the potential of the hybridization approach. In particular, using the index $E^{1/3}/\rho$ for a light, stiff panel as a criterion of excellence, those sandwich arrangements with $0.01 < f < 0.2$ rank as the most optimal candidates from a stiffness per unit weight perspective, as they are the closest to the tangency with the straight line.

The use of aluminum and Nomex® honeycombs and cellular foams as core materials in sandwich structures has been widely studied, as is evidenced by the large number of scientific publications of the last decade [31, 32].

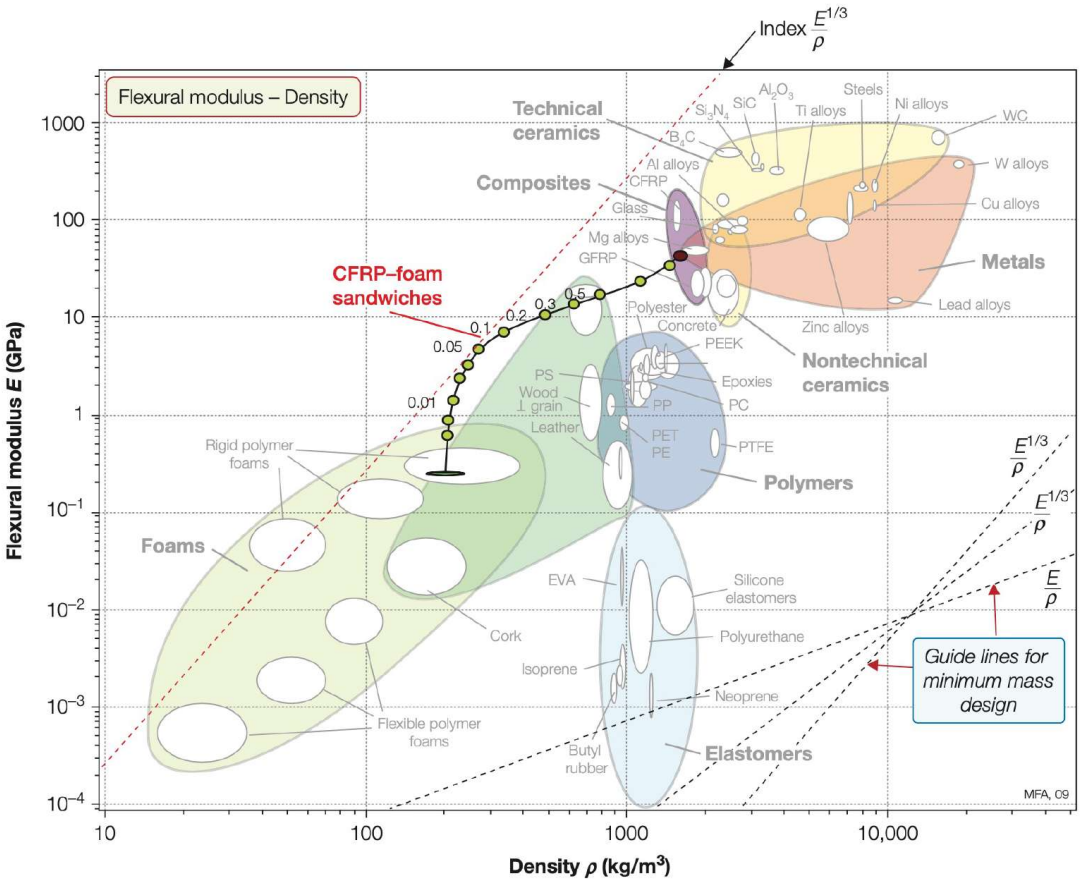

Figure 2.11: Equivalent strength and density of a CFRP-foam sandwich compared with those of monolithic materials. Adapted from [3].

Some works focused on analyzing the machining process of Nomex® and aluminum panels prior to their assembly into sandwich structures [33, 34]. Others focused on characterizing the honeycombs statically and dynamically. Thus, taking into account aspects such as material, cell size and wall thickness, static tests were performed and numerical models were presented to simulate the mechanical behavior and deformation cinematics of the cellular cores under compressive [35, 36], bending [37], and impact stresses [38–40]. At the same time, the design and mechanical analysis of new foam compositions was also addressed [41–43]. Furthermore, the impact on the integrity and resistance of the sandwich structure as well as the uncontrolled fracture propagation that can be originated from the presence of defects in the cores were experimentally and numerically quantified by some authors [44, 45].

Based on the results published so far (see Figure 2.12), some recent investigations filled lattice and honeycomb cores with foams to improve the performance of sandwich structures [46–48]. Despite achieving their objective, the traditional processes used to manufacture those cellular cores significantly limit the creation of new designs that could allow this line of research to be explored in more depth.

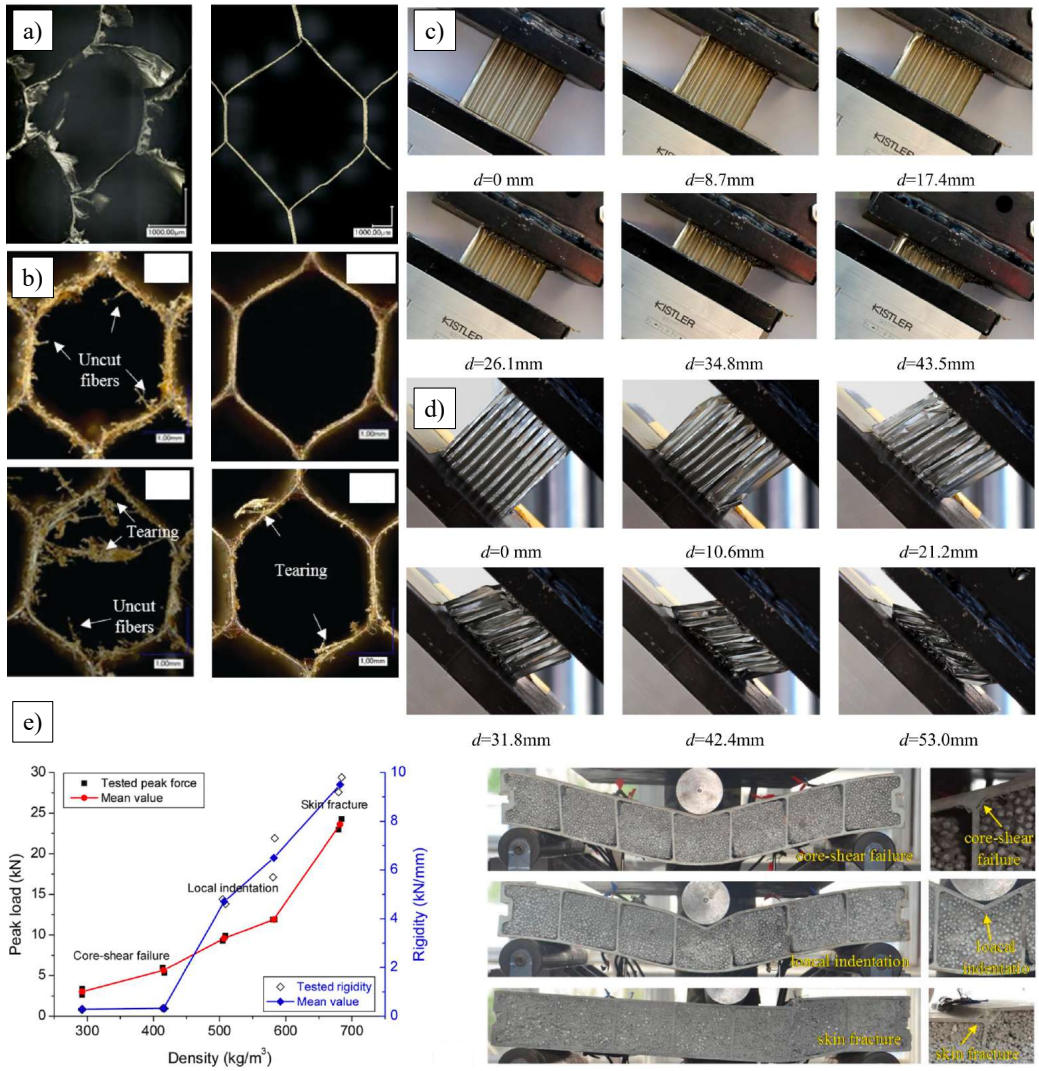

Figure 2.12: Representative results of machining (*a-b*) and quasi-static compression-shear crushing (*c-d*) of honeycombs, and mechanical improvements achieved with the foam infill approach (*e*). Adapted from [33–35, 47].

2.2.5 Additive manufacturing and sandwich structures

AM technologies have revolutionized the design and fabrication of core materials for sandwich structures. They offer the ability to produce complex geometries and internal structures with high accuracy and repeatability, which are challenging to achieve using traditional manufacturing methods. The implementation of AM technologies in the design of core materials for sandwich structures has brought new opportunities for fabricating high-performance structures with customized properties, leading to the development of new lightweight two- and three-dimensional geometries that can withstand impact and bending loads more efficiently, and therefore offer an improved performance [49–52].

Most of the studies have opted for FFF technology, as it is one of the most economical alternatives, as well as user-friendly and compatible with a wide range of materials. Thus, a significant number of publications have explored the structural capacities under compression [53], flexural [54–58] and impact [59–61] load cases of sandwich panels manufactured by this technology (see Figure 2.13). However, due to the current maturity of this AM technology, such research has been limited by the difficulties in combining different materials. Thus, they have focused on the study of sandwich structures made with cellular cores and skins of the same material, usually polymeric [62–67].

However, some researchers have successfully achieved the direct fabrication of sandwich structures combining two materials through FFF technology. This novel approach eliminates the assembly and consolidation stages when fabricating the sandwich structure. Therefore, the whole panel can be

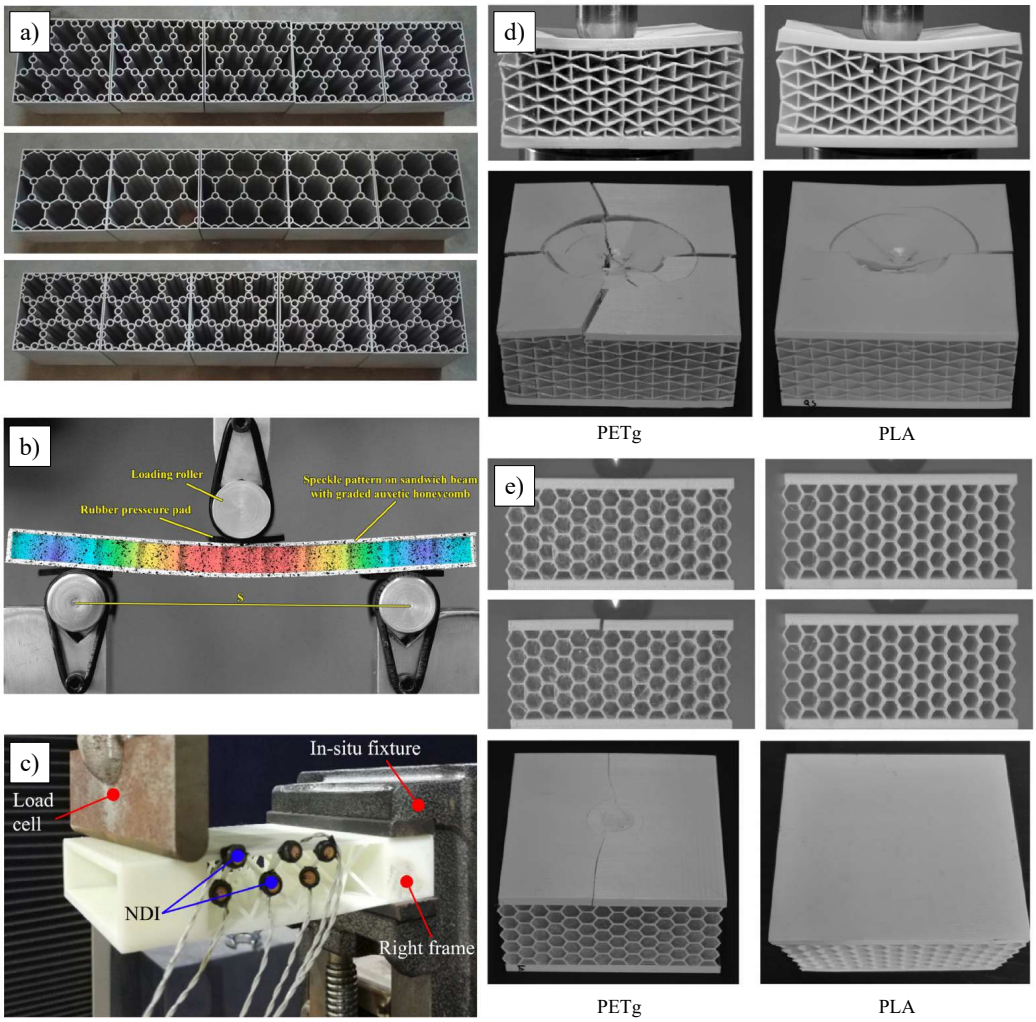

Figure 2.13: Examples of two-dimensional patterns manufactured by FFF (*a*), flexural analysis of sandwiches with two- (*b*) and three-dimensional (*c*) cellular cores, and impact deformations of an auxetic core (*d*) versus a standard hexagonal design (*e*). Adapted from [49, 56, 59, 66].

additively manufactured using the same equipment, which can suppose significant savings in time and costs as it simplifies the production process. These few studies have focused on analyzing the quality of the bond between the faces and the core [68]. The preliminary results of the bending performance of these samples are further proof of the efficiency of the hybridization process for optimizing structures [69, 70].

In the meantime, other authors prefer to let the technology evolve at its own pace while focusing on exploring the real potential of cellular cores made by FFF. To this end, their approach is based on bonding these lightweight designs with composite skins that provide increased stiffness and strength to the hybrid sandwich structure (see Figure 2.14). However, the limited work published to date has focused on the flexural and impact mechanical performance of a short number of two-dimensional and lattice core designs [71–73].

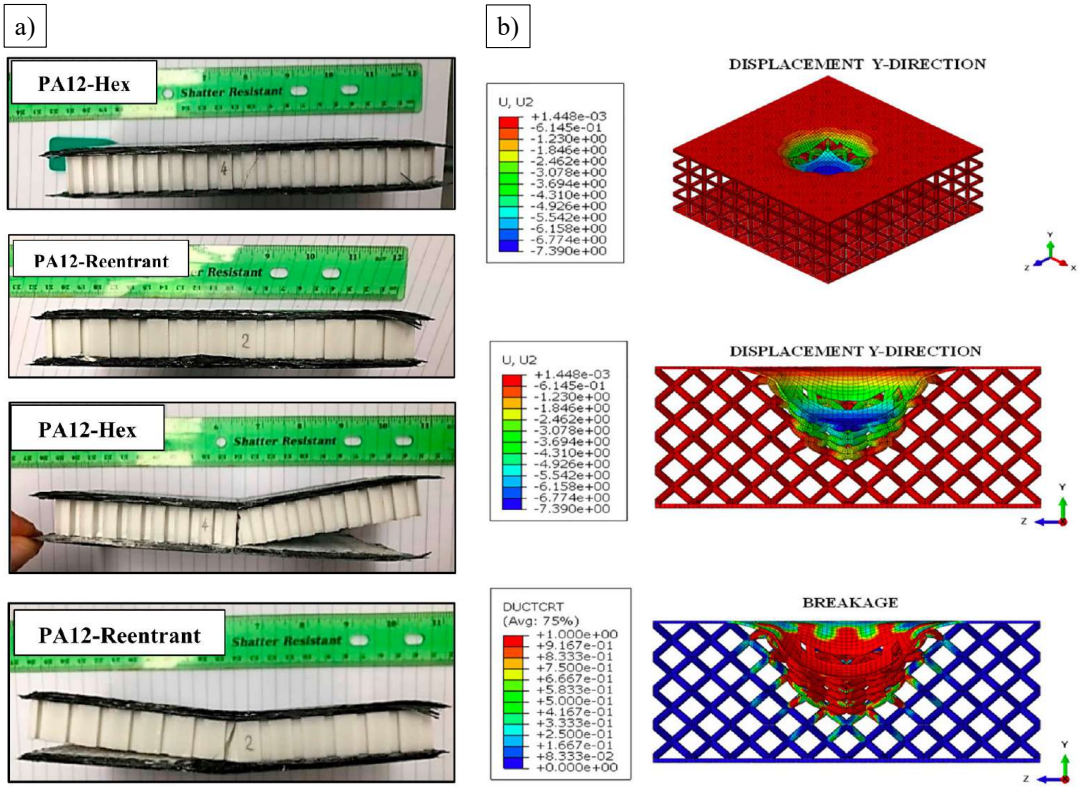

Figure 2.14: Experimental (*a*) and numerical (*b*) approaches on the mechanical performance of hybrid sandwich structures employing FFF cellular cores. Adapted from [71, 72].

Regarding the literature review on the sandwich structures analysis, Table2.1 presents a selection of the most relevant scientific publications focusing on foams, Nomex®, and aluminum honeycomb cores implementation, as well as lightweight additively manufactured alternatives.

Table 2.1: Referenecs on the analysis of sandwich structures.
Light gray: Use of AM cellular cores. *White:* Use of other core materials.

Reference	Aim of study
Murugan & Friswell, 2013 [26]	Fiber orientation effects in composites (practical application)
Mohamed & Abdelbary, 2023 [27]	Fiber orientation effects in composites (analytical + mechanical testing)
Hassan *et al.*, 2022 [28]	Fiber orientation effects in composites (experimental)
Borrega *et al.*, 2015 [29]	Analysis of natural core materials (balsa)
Petel *et al.*, 2013 [30]	Impact analysis (foams)
Kausar *et al.*, 2023 [31]	Review on applications of sandwich structures
Kueh *et al.*, 2023 [32]	Review on impact testing of sandwich structures
Jaafar *et al.*, 2017 [33]	Machining of Nomex® honeycomb cores
Makich *et al.*, 2022 [34]	Machining of aluminum honeycomb cores
Zhang *et al.*, 2019 [35]	Compression analysis of aluminum honeycomb cores
Giglio *et al.*, 2011 [36]	Compression analysis of Nomex® honeycomb cores
Sun *et al.*, 2017 [37]	Bending analysis of sandwich structures with aluminum honeycomb cores
Hu & Yu, 2013 [38]	Impact analysis of honeycomb cores (analytical approach)
Li *et al.*, 2020 [39]	Impact analysis of aluminum honeycomb cores
Duan *et al.*, 2022 [40]	Impact analysis of sandwich structures with honeycomb cores (aluminum)
Zhang *et al.*, 2023 [41]	Bending analysis of foam cores
Tang *et al.*, 2020 [42]	Impact analysis of sandwich structures with foam cores
Balaban & Toygar, 2022 [43]	Compression analysis of sandwich structures with foam cores
Wang *et al.*, 2017 [44]	Compression analysis of aluminum honeycomb cores with holes
Miao *et al.*, 2021 [45]	Fracture analysis of foam cores
Wang *et al.*, 2022 [46]	Impact analysis of foam-filled sandwich structures
Li & Fan, 2021 [47]	Bending analysis of foam-filled sandwich structures
Pietras *et al.*, 2020 [48]	Compression analysis of foam-filled sandwich structures
Xia *et al.*, 2023 [49]	Impact analysis of two-dimensional cores
Novak *et al.*, 2022 [50]	Impact analysis of three-dimensional cores
Ambekar *et al.*, 2021 [51]	Bending analysis of three-dimensional cores
Ejeh *et al.*, 2022 [52]	Bending analysis of three-dimensional cores
Zhang *et al.*, 2020 [53]	Compression analysis of sandwich structures with cellular cores (single material)
Paczos *et al.*, 2018 [54]	Bending analysis of sandwich structures with cellular cores (single material)
Essassi *et al.*, 2020 [55]	Bending analysis of sandwich structures with cellular cores (single material)
Meng *et al.*, 2020 [56]	Bending analysis of sandwich structures with cellular cores (single material)
Brischetto & Torre, 2020 [57]	Bending analysis of sandwich structures with cellular cores (single material)
Essassi *et al.*, 2020 [58]	Bending analysis of sandwich structures with cellular cores (single material)
Santos *et al.*, 2021 [59]	Impact analysis of sandwich structures with cellular cores (single material)
Sun *et al.*, 2021 [60]	Impact analysis of sandwich structures with cellular cores (single material)
Yazdani Sarvestani *et al.*, 2018 [61]	Impact analysis of sandwich structures with cellular cores (single material)
Indreș *et al.*, 2021 [62]	Bending analysis of sandwich structures with cellular cores (single material)
Peng *et al.*, 2021 [63]	Bending analysis of sandwich structures with cellular cores (single material)
Spahic *et al.*, 2021 [64]	Bending analysis of sandwich structures with cellular cores (single material)
Ghannadpour *et al.*, 2022 [65]	Bending analysis of sandwich structures with cellular cores (single material)
Zamani *et al.*, 2022 [66]	Bending analysis of sandwich structures with cellular cores (single material)
Kanani & Kennedy, 2023 [67]	Bending analysis of sandwich structures with cellular cores (single material)
Bonthu *et al.*, 2020 [68]	Manufacturing defects analysis

Continued on next page

Table 2.1 – continued from previous page

Reference	Aim of study
Bharath *et al.*, 2021 [69]	Bending analysis of sandwich structures with cellular cores (hybrid)
Brischetto *et al.*, 2018 [70]	Bending analysis of sandwich structures with cellular cores (hybrid)
Acanfora *et al.*, 2021 [71]	Impact analysis of sandwich structures with cellular cores (hybrid)
Harland *et al.*, 2019 [72]	Bending analysis of sandwich structures with cellular cores (hybrid)
Li & Wang, 2017 [73]	Bending analysis of sandwich structures with cellular cores (hybrid)

2.3 Additively manufactured cellular solids

Cellular structures can be first classified into two main categories according to the morphology of the cells that constitute them: two-dimensional and three-dimensional [74]. Two-dimensional cellular solids, also known as planar or sheet-like structures, are characterized by a flat array of cells arranged in a regular pattern, thus obtaining a body that appears to have a direction of extrusion. In contrast, three-dimensional cellular solids consist of a 3D network of interconnected struts, bars, plates, and surfaces, packed together to fill space.

A second classification results from analyzing the connectivity of the cells. Cellular solids can be divided into open-celled and closed-celled designs [75]. The former have cellular units whose material is arranged only on the edges, thus leaving their interior space connected, whereas the faces of the latter are solid and each cell is sealed off from its neighbors. This feature is of utmost importance for the design of cellular structures, not only because of its direct impact on the mechanical properties of the lightweight solid but also because the availability of interconnected cells conditions their functionality and application. Thus, open-celled designs can be implemented, for example, for manufacturing advanced heat exchangers, in which a forced flow of fluid is circulated inside [76].

One of the key approaches in designing cellular solids is to identify the optimal geometry of the cells and the thickness of the cell walls [77, 78]. By carefully selecting these parameters, the mechanical and physical properties of the material can be tailored to meet specific requirements, such as stiffness, strength, and energy absorption [79–83]. Although researchers have been studying cellular solids for a long time, trying to understand their unique properties, it has been especially during the last decade that the interest in exploring novel designs has grown exponentially thanks to the advent of AM technologies and the use of sophisticated computational models [84–86]. Therefore, it has become possible to fabricate cellular solids with complex geometries and microstructures, opening up new possibilities for the design and development of advanced materials [87–89].

Properties of a cellular solid depend, above all else, on its relative density (ρ^*/ρ^s). This single most important feature can be estimated as the density of the cellular material (ρ^*) divided by that of the solid from which is made (ρ^s). Accordingly, as the relative density increases, the cell walls thicken and the pore space shrinks. Then, when the relative density of the structure is above 0.3 [74], there is a transition from a cellular structure to one which is better thought of as a solid containing isolated pores (see Figure 2.15).

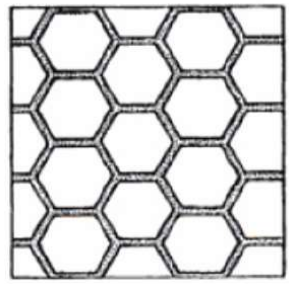

Cellular solid

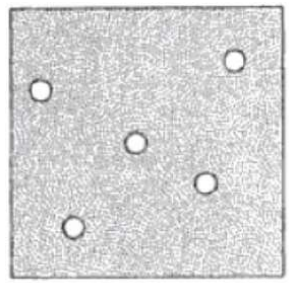

Porous material

Figure 2.15: Comparison between a cellular solid (*top*) and a solid with isolated pores (*bottom*). Adapted from [74].

Due to the importance of this parameter for the design and fabrication of functional cellular structures, the authors presented a set of mathematical models based on power-law expressions to simplify the analytical calculation of the relative density, such as those presented below in a general way:

$$\text{For all two-dimensional designs:} \quad \frac{\rho^*}{\rho^s} = C_1 \frac{t}{l} \tag{2.2}$$

$$\text{For open-celled three-dimensional designs:} \quad \frac{\rho^*}{\rho^s} = C_2 \left(\frac{t}{l}\right)^2 \tag{2.3}$$

$$\text{For closed-celled three-dimensional designs:} \quad \frac{\rho^*}{\rho^s} = C_3 \frac{t}{l} \tag{2.4}$$

where: l is the length of the edge/face

t is the cell-wall thickness

C_1, C_2, and C_3 are numerical constants, near unity, that depend on the cell shape

To implement these equations, it is essential to determine the value of the constant C beforehand for each particular design with experimental measurements. Once calibrated, the mathematical models presented in Table 2.2 allow the relative density of the corresponding cellular design to be parametrically predicted with sufficient accuracy.

Table 2.2: Power-law expressions for predicting the relative density of different cellular structures. Adapted from [74]

Two-dimensional designs	
Equilateral triangles	
$(Z_e = 6, n = 3$ or $Z_e = 4, n = 4)$	$\frac{\rho^*}{\rho^s} = 2\sqrt{3}\frac{t}{l}\left(1 - \frac{\sqrt{3}}{2}\frac{t}{l}\right)$
Squares	
$(Z_e = 4, n = 4$ or $Z_e = 3, n = 6)$	$\frac{\rho^*}{\rho^s} = 2\frac{t}{l}\left(1 - \frac{1}{2}\frac{t}{l}\right)$
Regular hexagons	
$(Z_e = 3, n = 6)$	$\frac{\rho^*}{\rho^s} = \frac{2}{\sqrt{3}}\frac{t}{l}\left(1 - \frac{1}{2\sqrt{3}}\frac{t}{l}\right)$
Open-celled three-dimensional designs	
Triangular prisms	
$(Z_e = 8, Z_f = 4.5, \widetilde{n} = 3.6, \widetilde{f} = 5)$	$\frac{\rho^*}{\rho^s} = \frac{2}{\sqrt{3}}\frac{t^2}{l^2}\left(1 + \frac{3}{A_r}\right)$
Square prisms	
$(Z_e = 6, Z_f = 4, \widetilde{n} = 4, \widetilde{f} = 6)$	$\frac{\rho^*}{\rho^s} = \frac{t^2}{l^2}\left(1 + \frac{2}{A_r}\right)$
Hexagonal prisms	
$(Z_e = 5, Z_f = 3.6, \widetilde{n} = 4.5, \widetilde{f} = 8)$	$\frac{\rho^*}{\rho^s} = \frac{4}{3\sqrt{3}}\frac{t^2}{l^2}\left(1 + \frac{3}{2A_r}\right)$
Rhombic dodecahedra	
$(Z_e = 5.33, Z_f = 3, \widetilde{n} = 4, \widetilde{f} = 12)$	$\frac{\rho^*}{\rho^s} = 2.87\frac{t^2}{l^2}$
Tetrakaidecahedra	
$(Z_e = 4, Z_f = 3, \widetilde{n} = 5.14, \widetilde{f} = 14)$	$\frac{\rho^*}{\rho^s} = 1.06\frac{t^2}{l^2}$
Closed-celled three-dimensional designs	
Triangular prisms	
$(Z_e = 8, Z_f = 4.5, \widetilde{n} = 3.6, \widetilde{f} = 5)$	$\frac{\rho^*}{\rho^s} = 2\sqrt{3}\frac{t}{l}\left(1 + \frac{1}{2\sqrt{3}A_r}\right)$
Square prisms	
$(Z_e = 6, Z_f = 4, \widetilde{n} = 4, \widetilde{f} = 6)$	$\frac{\rho^*}{\rho^s} = 2\frac{t}{l}\left(1 + \frac{1}{2A_r}\right)$
Hexagonal prisms	
$(Z_e = 5, Z_f = 3.6, \widetilde{n} = 4.5, \widetilde{f} = 8)$	$\frac{\rho^*}{\rho^s} = \frac{2}{\sqrt{3}\frac{t}{l}\left(1 + \frac{\sqrt{3}}{2A_r}\right)}$
Rhombic dodecahedra	
$(Z_e = 5.33, Z_f = 3, \widetilde{n} = 4, \widetilde{f} = 12)$	$\frac{\rho^*}{\rho^s} = 1.90\frac{t}{l}$
Tetrakaidecahedra	
$(Z_e = 4, Z_f = 3, \widetilde{n} = 5.14, \widetilde{f} = 14)$	$\frac{\rho^*}{\rho^s} = 1.18\frac{t}{l}$

Z_e is the edge-connectivity (number of edges that meet at a vertex)
Z_f is the face-connectivity (number of faces which meet at an edge)
n is the number of edges per unit cell ($\widetilde{n}$ stands for the average value)
f is the number of faces per unit cell ($\widetilde{f}$ stands for the average value)
$A_r = h/l$ is the aspect ratio of the unit cell in three-dimensional designs
h is the height of the unit cell

Although the use of power-law expressions has significant potential for estimating the relative density of cellular solids prior to their manufacturing, this approach has several disadvantages that must be considered. First, as previously mentioned, the C value must be experimentally calibrated for each specific structure, which can be time-consuming and costly. Additionally, the power-law expression may not accurately capture the complex geometries of certain cellular solids, leading to errors in the calculation of relative density. Hence, deducting parametric equations directly from the dimensions of the unit cell could bring significant advantages to calculate the relative density of cellular structures more precisely.

The potential of new human-made cellular designs attracted the attention of researchers and engineers, who focused on evaluating the printability of different designs and their mechanical properties, combining numerical simulations with validation tests to optimize the structures for appropriate manufacturing considering all the available AM technologies. On the one hand, the extruded-like design of two-dimensional patterns requires no use of support structures during fabrication, as geometries can stand by themselves while they are printed. This fact directly benefits manufacturing time and material consumption, making better use of resources. Therefore, studies employing extrusion-based technologies, such as FFF, generally deal with cellular geometries composed of shell-like walls, as the vertical overlapping of the deposited rasters favors the construction of honeycomb-like designs [90–92]. On the other hand, specific AM technologies are better suited for manufacturing certain typologies of three-dimensional cellular solids. In particular, printing lattice-type arrangements often requires intensive use of support structures. In this sense, opting for powder bed technologies simplifies the fabrication of supports, since the whole powder volume sustains the layer in construction, and the surplus can be reused for future constructions [93–100]. Therefore, Powder Bed Fusion (PBF) is the most used technique for manufacturing truss-like cellular solids [101–107].

However, one of the most promising developments in the design of three-dimensional cellular solids for lightweight applications was the discovery of the TPMS [108, 109]. These geometries are mathematically created to minimize the surface area for a given volume, having no self-intersecting or enveloping surfaces. Moreover, the lack of nodes and discontinuities in their curvature reduces stress concentration, thus improving their mechanical performance [110, 111]. In addition, the average curvature at each point of the geometry is zero, hence making them self-supporting and able to be fabricated by extrusion-based AM technologies without requiring support structures [112–116]. The charts presented in Figure 2.16 show some representative results of the printability analysis of different lattice (*a*) and Gyroid Shell-TPMS (*b*) cellular solids, fabricated with powder-bed fusion and extrusion-based metal AM technologies, respectively. The presented curves indicate the limiting dimensions that allow the correct printing of each of the three-dimensional designs considered. In addition, the results published by Saleh *et al.* [117] demonstrate the accuracy of FFF equipment in reproducing these types of cellular structures by comparing the dimensions of the printed part with those of the original CAD design (see Figure 2.17).

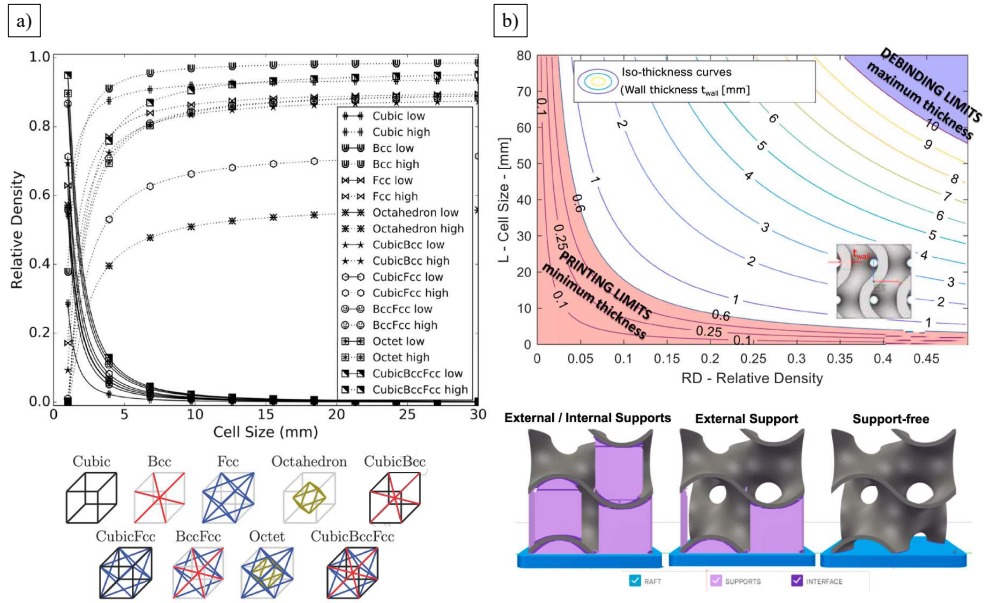

Figure 2.16: Printability analysis of lattice (*a*) and Gyroid Shell-TPMS (*b*) cellular solids employing powder-bed fusion and extrusion-based metal AM technologies, respectively. Adapted from [118].

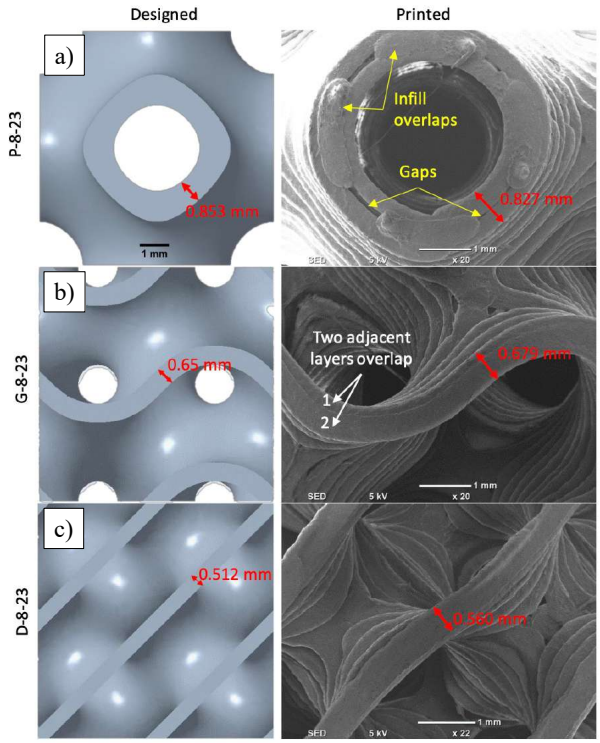

Figure 2.17: CAD design and FFF manufactured Primitive (*a*), Gyroid (*b*), and Diamond (*c*) Shell-TPMS cellular solids. Adapted from [117].

Preliminary investigations revealed the potential of both two- and three-dimensional cellular structures for weight reduction purposes without sacrificing strength or stability. Consequently, manufacturers of AM equipment responded by quickly incorporating some designs as advanced infill methods for prototyping applications [119]. But, while its use can be very effective in saving material costs and reducing printing time, quantifying the impact of the selected infill design and its density on the mechanical properties of the produced components becomes essential in totally functional end-part manufacturing purposes. For example, when the cells are equiaxed, the properties are isotropic, but when the cells are even slightly elongated or flattened, the properties depend on the direction, presenting an orthotropic or even an auxetic behavior (see Figure 2.18) [84, 85, 90, 120–133]. Hence, if such parts are to be used in load-bearing components, understanding their mechanics is of utmost importance for an optimal design [120, 134–141]. Therefore, an advanced design of cellular solids demands tight control of the kinematics of their deformation to achieve the desired microstructure properties to satisfy specific design requirements [142, 143].

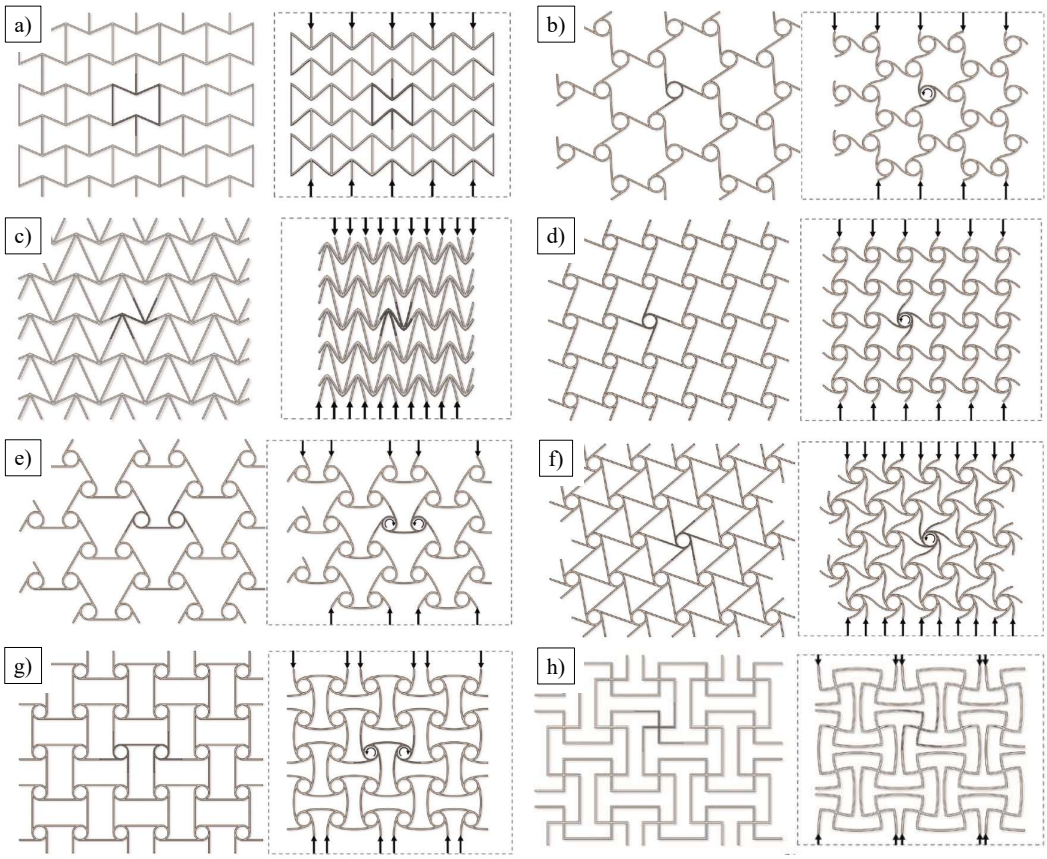

Figure 2.18: Examples of re-entrant hexagonal (*a*), trichiral (*b*), double arrowhead (*c*), tetrachiral (*d*), anti-trichiral (*e*), hexachiral (*f*), anti-tetrachiral (*g*), and square grids (*h*) auxetic honeycombs before and after uniaxial compressive deformation. Adapted from [144].

Accordingly, many publications of the last five years have focused on achieving a better understanding of a wide range of cellular structures, aiming to produce components with completely tailored functional characteristics and tight control of their performance [115, 145, 146]. Hence, with the ambition of providing solutions to multiple engineering fields, most of the conducted studies have focused on exploring the potential of the different cellular designs for very specific applications, whether structural, energy absorption or thermal and acoustic insulation [145, 147–153]. Overall, the different works mainly investigate the performance of cellular structures through a combination of numerical simulation models with a few experimental validation tests, in order to quantify aspects such as stiffness, strength, energy absorption capacity, or weight savings that different cellular patterns can achieve. Figure 2.20 presents some real cases where the implementation of cellular solids has allowed the optimization of fluid dynamics, heat transfer efficiency, and weight reduction, as well as successful in *in-vivo* tests of body implants.

In addition, some authors, such as Fu *et al.* [143] and Liu *et al.* [80], have gone a step further by tackling the optimization of the design morphology to maximize the degree of isotropy of the cellular structures (see Figure 2.19). To this end, the anisotropy has been quantified with existing methods, such as the Zener Ratio [154], an index widely used in the analysis of cubic crystals. However, parallel research in other fields of science has shown the instability of this indicator for comparative purposes, concluding that the Zener Ratio lacks universality [155]. Despite the efforts made to obtain a more robust quantitative method, the definition of an indicator that considers certain important details such as the anisotropy inherent to the AM process could significantly contribute to the development of new designs that offer the desired degree of isotropy.

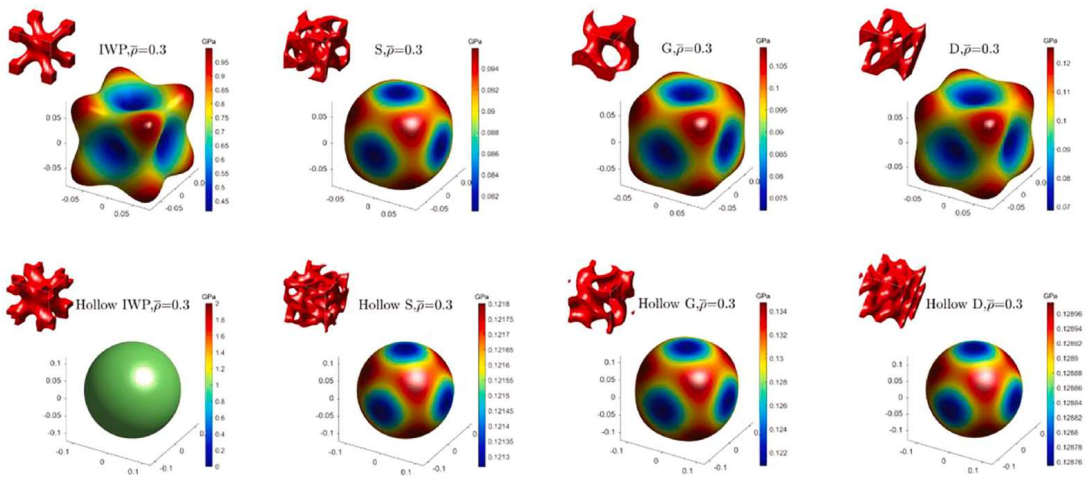

Figure 2.19: Qualitative analysis of the anisotropy of cellular solids employing the graphical representation of their stiffness tensor: original (*top*) and homogenized designs (*bottom*). Adapted from [143].

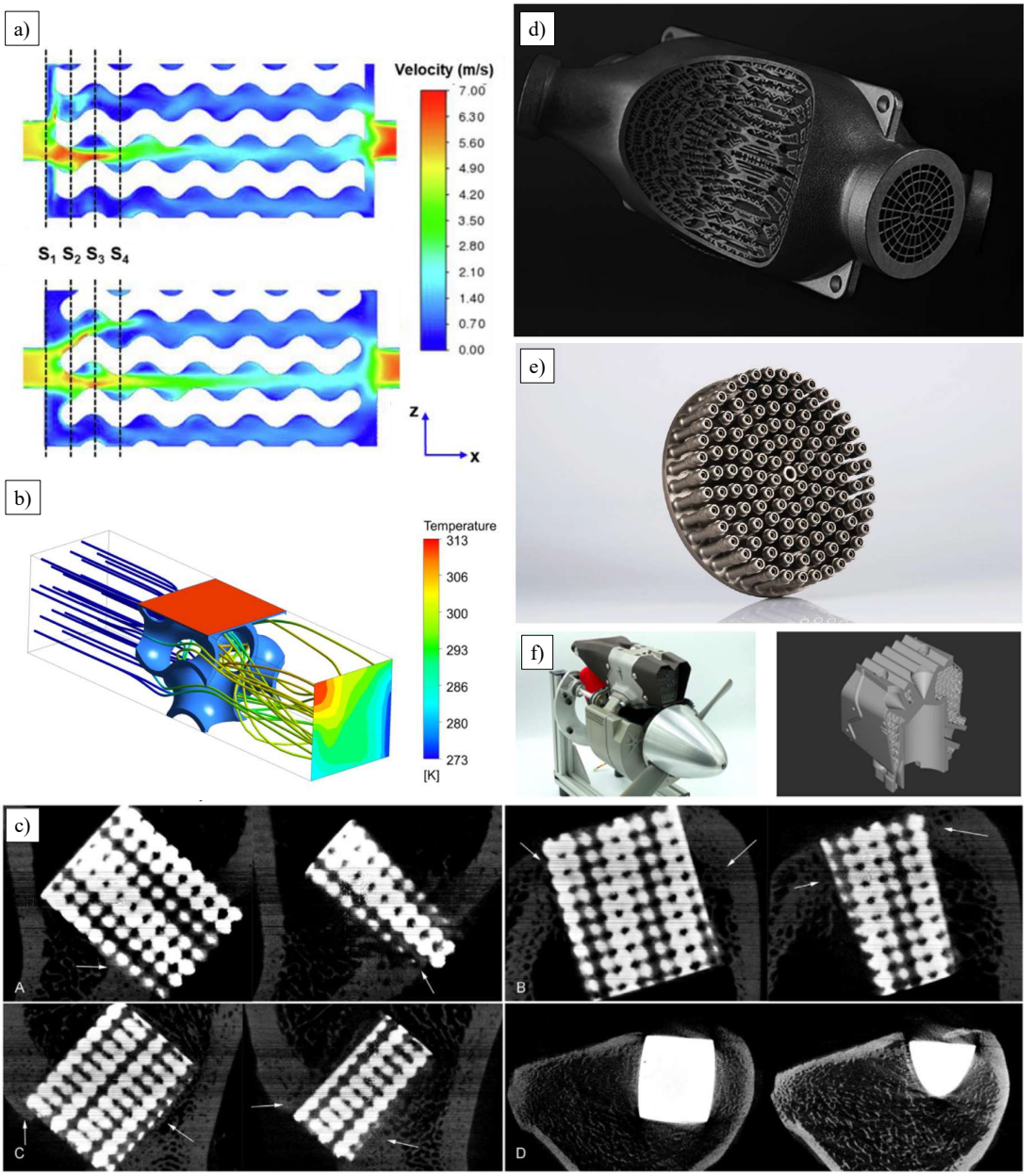

Figure 2.20: Real cases of improvements in fluid dynamics (*a*), heat transfer efficiency (*b*), *in-vivo* tests of body implants (*c*), and weight reduction in F1 heat exchangers (*d*), rocket nozzles (*e*), and UAV engines (*f*), thanks to the implementation of AM cellular solids. Adapted from [156–159].

Regarding the literature review on the cellular solids analysis, Table 2.3 presents a selection of the most relevant studies focusing on additively manufactured two- and three-dimensional designs.

Table 2.3: Referenecs on additively manufactured cellular solids.
Light gray: Use of FFF technology. *White:* Use of other AM technologies.

Reference	Cellular morphology	Aim of study
Seharing *et al.*, 2020 [75]	2D + 3D	Review on applications of AM cellular solids
Kaur & Singh, 2021 [76]	3D	Review on applications of AM cellular solids
Lubombo & Huneault, 2018 [77]	2D	Mechanical characterization (tensile + flexural)
Kumar *et al.*, 2019 [78]	2D	Mechanical characterization (compressive)
Refai *et al.*, 2020 [79]	3D	Unit cell homogenization (numerical)
Liu *et al.*, 2021 [80]	3D	Mechanical characterization (flexural)
Cheng *et al.*, 2019 [81]	3D	AM cellular design optimization (experimental + numerical)
Feng *et al.*, 2022 [82]	3D	AM cellular design optimization (experimental + numerical)
Yang *et al.*, 2022 [83]	3D	AM cellular design optimization (experimental + numerical)
Liu & Hu, 2010 [84]	2D + 3D	Review on auxetic cellular solids
Álvarez-Elipe & Díaz-Lantada, 2012 [85]	2D + 3D	Review on auxetic cellular solids
Fleck *et al.*, 2010 [86]	2D + 3D	Mechanical characterization (analytical)
du Plessis *et al.*, 2022 [87]	3D	Review on applications of AM cellular solids
Lin *et al.*, 2022 [88]	3D	Sound insulation capacity
Zeng & Wang, 2022 [89]	3D	Heat transfer capacity
Andrew *et al.*, 2021 [90]	2D	Mechanical characterization (impact)
Zaharia *et al.*, 2020 [91]	2D	Mechanical characterization (tensile + compressive + flexural + impact)
Tao *et al.*, 2019 [92]	2D	AM cellular design optimization (experimental + numerical)
Yang *et al.*, 2022 [93]	A	
Jones *et al.*, 2022 [94]	3D	AM cellular design optimization (experimental + numerical)
Alomar & Concli, 2021 [95]	3D	Mechanical characterization (compressive)
Ding *et al.*, 2020 [96]	3D	Mechanical characterization (compressive)
Li *et al.*, 2018 [97]	3D	Mechanical characterization (compressive)
Xiao *et al.*, 2018 [98]	3D	AM cellular design optimization (experimental + numerical)
Cao *et al.*, 2018 [99]	3D	Mechanical characterization (compressive)
Gümrük *et al.*, 2013 [100]	3D	Mechanical characterization (tensile + compression + shear)
Alberdi *et al.*, 2020 [101]	3D	Mechanical characterization (compressive)
Li *et al.*, 2020 [102]	3D	Mechanical characterization (compressive)
Maconachie *et al.*, 2019 [103]	3D	Review on applications of AM cellular solids
Torres *et al.*, 2019 [104]	3D	Mechanical characterization (fatigue)
Habib *et al.*, 2018 [105]	3D	Mechanical characterization (compressive)
Leary *et al.*, 2018 [106]	3D	Mechanical characterization (compressive)
Yang *et al.*, 2015 [107]	3D	AM cellular design optimization (experimental + numerical)
Sreedhar *et al.*, 2018 [108]	3D	Filtration capacity
Al-Ketan *et al.*, 2018 [109]	3D	Mechanical characterization (compressive)
Al-Ketan *et al.*, 2020 [110]	3D	Mechanical characterization (compressive)
Sathishkumar *et al.*, 2020 [111]	3D	Mechanical characterization (compressive)

Continued on next page

Table 2.3 – continued from previous page

Reference	Cellular morphology	Aim of study
Kumar *et al.*, 2020 [112]	3D	Printability + mechanical characterization (compressive)
Jia *et al.*, 2020 [113]	3D	Mechanical characterization (compressive)
Kumar *et al.*, 2020 [114]	2D + 3D	Printability + mechanical characterization (compressive)
Downing *et al.*, 2021 [115]	3D	Mechanical characterization (compressive)
Maskery *et al.*, 2017 [116]	3D	Mechanical characterization (compressive)
Saleh *et al.*, 2022 [117]	3D	Mechanical characterization (compressive)
Tanlak *et al.*, 2017 [118]	3D	Printability
Gopsill *et al.*, 2018 [119]	2D	AM cellular design optimization (numerical)
Bates *et al.*, 2016 [120]	2D	Mechanical characterization (compressive)
Bates *et al.*, 2019 [121]	2D	Mechanical characterization (compressive)
Caccese *et al.*, 2013 [122]	2D	Mechanical characterization (impact)
Ma *et al.*, 2020 [123]	2D	Mechanical characterization (compressive)
Alderson *et al.*, 2010 [124]	2D	Mechanical characterization (compressive)
Scarpa *et al.*, 2007 [125]	2D	Mechanical characterization (compressive)
Hu *et al.*, 2018 [126]	2D	Mechanical characterization (compressive)
Hou *et al.*, 2018 [127]	2D	Mechanical characterization (impact)
Mir *et al.*, 2014 [128]	2D	Review on auxetic cellular solids
Prawoto, 2012 [129]	2D + 3D	Review on auxetic cellular solids
Grima *et al.*, 2008 [130]	2D	Review on auxetic cellular solids
Gaspar *et al.*, 2005 [131]	2D	Review on auxetic cellular solids
Whitty *et al.*, 2003 [132]	2D	AM cellular design optimization (numerical)
Scarpa *et al.*, 2007 [133]	2D	Mechanical characterization (compressive)
Ufodike *et al.*, 2021 [134]	2D	Mechanical characterization (compressive)
Bai *et al.*, 2021 [135]	3D	Mechanical characterization (compressive)
Ye *et al.*, 2020 [136]	3D	Mechanical characterization (compressive)
Arjunan *et al.*, 2020 [137]	3D	Mechanical characterization (compressive)
Bahrami Babamiri *et al.*, 2020 [138]	3D	Mechanical characterization (compressive)
Azzouz *et al.*, 2019 [139]	3D	Mechanical characterization (compressive + flexural + shear)
Zhang *et al.*, 2018 [140]	3D	Mechanical characterization (compressive)
Yap & Yeong, 2015 [141]	2D	Mechanical characterization (compressive)
Chen *et al.*, 2022 [142]	3D	Mechanical characterization (compressive)
Fu *et al.*, 2022 [143]	3D	AM cellular design optimization (experimental + numerical)
Montgomery-Liljeroth *et al.*, 2023 [144]	2D	Review on auxetic cellular solids
Wei *et al.*, 2021 [145]	2D	Thermal expansion capacity
Sun *et al.*, 2021 [146]	3D	Mechanical characterization (compressive)
Pramanik *et al.*, 2022 [147]	2D	Mechanical characterization (compressive)
Lee *et al.*, 2022 [148]	3D	Enhanced flow performance
Novak *et al.*, 2022 [149]	3D	Mechanical characterization (compressive)
Tee *et al.*, 2021 [150]	3D	Mechanical characterization (compressive)
Ouda *et al.*, 2020 [151]	3D	Enhanced flow performance
Yang & Li, 2020 [152]	3D	Mechanical characterization (compressive)
Xu *et al.*, 2019 [153]	3D	Mechanical characterization (compressive + dynamic)

Continued on next page

Table 2.3 – continued from previous page

Reference	Cellular morphology	Aim of study
Zener & Siegel, 1949 [154]	-	Anisotropy index calculation
Ranganathan & Ostoja-Starzewski, 2008 [155]	-	Anisotropy index calculation
Lee *et al.*, 2022 [156]	3D	Enhanced flow performance
Dong & Zhao, 2021 [157]	3D	Bone regeneration capacity
Attarzadeh *et al.*, 2022 [158]	3D	Heat transfer capacity
Blakey-Milner *et al.*, 2021 [159]	2D + 3D	Review on applications of AM cellular solids

2.4 The Fused Filament Fabrication technology

2.4.1 Operating principle

Extrusion-based technologies have gained widespread popularity due to their straightforward operational mechanism and efficient performance at a lower cost compared to other AM alternatives. The most common extrusion-based technology is FFF, also known as Fused Deposition Modeling (FDM) because of the trademark registered by Stratasys Ltd in 1991, which excels mainly due to its versatility, since it is suitable for working with a wide range of materials.

In this 3D printing technology (see Figure 2.21), a thermoplastic material is deposited in thin layers by an extrusion head that moves according to the building trajectories. To do so, a filament feedstock is pushed using a stepper motor into the extrusion system. Once it reaches the liquefier, the filament is heated a few degrees above its glass transition temperature. Then, the melted material is extruded

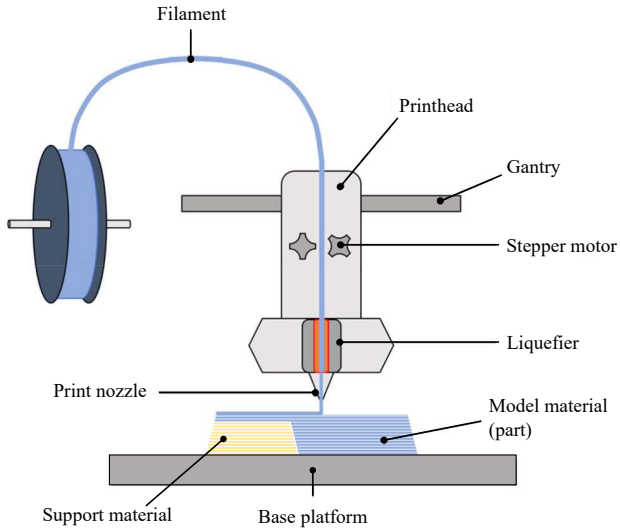

Figure 2.21: Schematic of the FFF process. Adapted from [160].

through the print nozzle and deposited on the layer under production. The temperature difference that appears when contacting the environment of the printing chamber and the already manufactured volume causes an almost instantaneous solidification. Thus, the new layer adheres to the adjacent one, and the volume of the whole part gets constructed. In addition, if the degree of inclination of certain areas of the design exceeds the established limits, the FFF technology requires the construction of additional support structures to hold those overhangs, which will be later removed manually or by dissolution processes once the printing is finished.

The FFF manufacturing process starts with a 3D model of the desired part that can be prepared using CAD software. Then, the surface of the design is typically exported into stereolithography (STL) file format as a series of small, triangular facets, which approximate the shape of the object being modeled. The geometry is processed in an FFF slicing software, where a wide range of process parameters (see

Table 2.4: FFF process parameters. Adapted from [161]

Category	Parameter	Brief description
Slicing parameters	Layer thickness/height	The thickness of each deposited layer in the building platform
	Raster width	The width of deposited beads
	Flow rate	The volume of filament extruded through the nozzle per unit of time
	Print speed	The distance that the extruder travels per unit of time during the printing process
	Infill density	The percentage of the volume of the internal structure to be filled with filament material
	Raster orientation/angle	The direction of a raster relative to the x-axis of the building platform
	Infill pattern	The pattern followed by the extruder to fill the space between two contours within a layer
	Air gaps	The gap between two adjacent rasters within a layer. If overlapped, this value is said to be negative
	Contour width	The width of the material bead used for contours
Orientation	Build orientation	The orientation of the part on the building platform based on the Cartesian coordinate system
Temperature conditions	Extrusion temperature	The temperature at which the filament is heated in a liquefier during the FFF process
	Building platform temperature	The temperature of building platform
	Ambient temperature	The surrounding temperature where the FFF deposition process occurs. It may impact moisture content, warping, or cooling rate

Table 2.4) can be adjusted. As a result, a G-Code file is automatically generated, which contains the set of instructions that the printer requires for manufacturing the part according to the chosen parameters.

Therefore, properly setting the printing parameters is crucial for achieving functional end-parts using FFF technology. If not set correctly, it can result in many issues, such as poor surface finish, weak mechanical properties, or even a complete print failure [162]. Additionally, the optimal settings can vary depending on the selected material, the design of the part, and the specific equipment being used. Thus, a thorough understanding of the printing process and proper calibration of the parameters is essential for achieving consistent, high-quality components.

2.4.2 PEI Ultem™ 9085

One of the most significant advantages of FFF technology compared to other AM technologies is its compatibility with a wide range of materials, including pure thermoplastics, composites, and bioplastics [161, 163]. The scheme presented in Figure 2.22 shows a FFF materials classification according to their typology, providing the principal examples for each class.

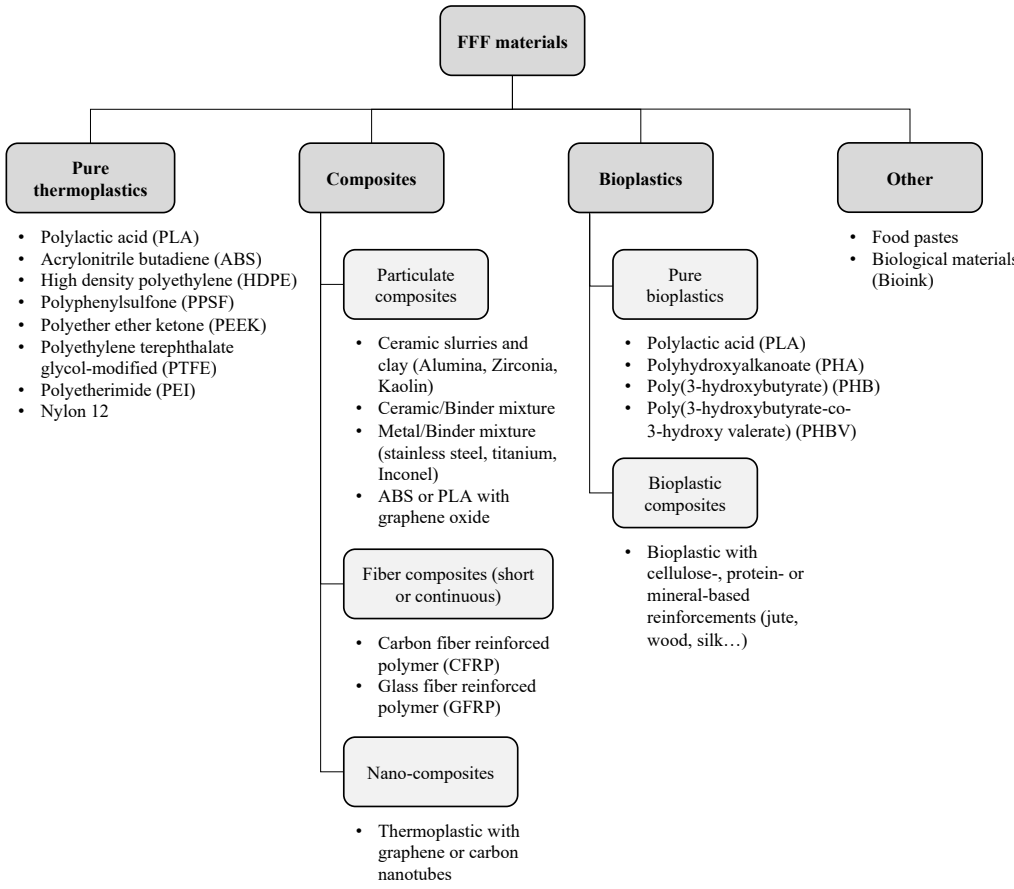

Figure 2.22: FFF materials classification according to their typology with examples. Adapted from [161] and [163].

Among all of them, PEI is a group of amorphous thermoplastics that offer excellent characteristics, including good processability and the ability to withstand exposure to high temperatures. These thermoplastics were obtained by the polycondensation reaction in the presence of three monomers such as bisphenol A, phthalimide anhydride halogen and diamine [164]. The repeating structure of ether and imide functional groups in their monomers contributes to their thermal stability as evidenced by their high glass-transition temperature (T_g) of around 200°C. In comparison to other thermoplastics with relatively low T_g values, such as ABS (110°C to 125°C) or PLA (50°C to 80°C), PEI is a better candidate for high-temperature applications. Additionally, PEI has superior mechanical strength, ductility, chemical resistance, and high dielectric strength. The demand for stricter regulations for smoke evolution and flame resistance, energy efficiency, and electronics miniaturization has opened up new market opportunities for PEI. Furthermore, its resistance to lubricants, coolants, and fuels makes it an attractive material for the aerospace and automotive industries, among others [165, 166].

Ultem™ (see Figure 2.23), the trade name formally announced by General Electric Company in 1982, refers to a family of PEI thermoplastics that were developed by J.G. Wirth's research group [167]. Despite its exact formulation not being disclosed, it is known to be a blend of PEI and PC copolymer to enhance flowability [168, 169]. These high-performance engineering thermoplastics have a balance of qualities characteristic of amorphous polymers while also approaching the performance of some crystalline and thermoset resins, which results in a very attractive combination [170].

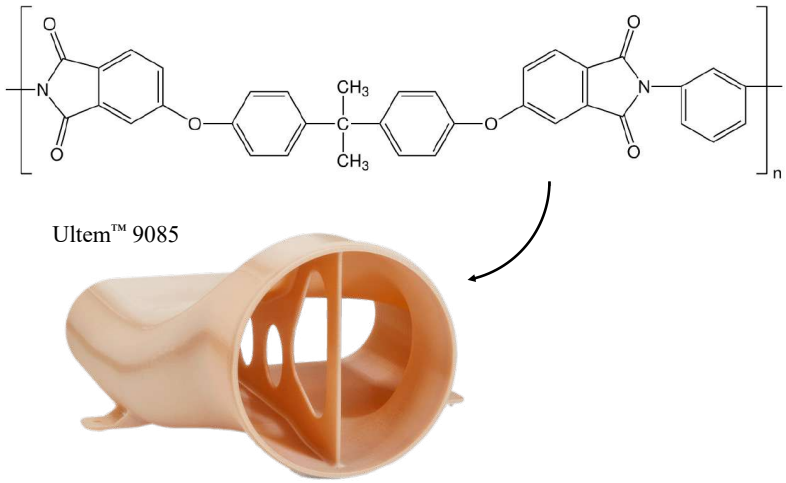

Figure 2.23: PEI's monomeric unit, Ultem™ 9085's main component.

Currently, there are two types of commercially available Ultem™ filaments for FFF manufacturing: Ultem™ 1010 and Ultem™ 9085. Both materials have exceptional heat and chemical resistance, as well as a high strength-to-weight ratio. On the one hand, Ultem™ 1010 has the lowest coefficient of thermal expansion among the wide range of FFF materials, complies with NSF 51 food safety requirements, and is certified for ISO 10993 and USP Class VI biocompatibility, making it ideal for medical and

food-related applications [171, 172]. However, for manufacturing components that require toughness, high strength, ductility, low mass, and compliance with low out-gassing and flame, smoke, and toxicity (FST) regulations, Ultem™ 9085 (Ultem from now on) is the best choice [173]. This FFF material meets strict test criteria and retains the traceability required by the aerospace industry, making it a popular choice for fabricating aircraft and helicopter interior fittings and air ducts, as well as in the rail transport, automotive, and energy industries [165, 174, 175]. Furthermore, it has also proven to exhibit superior mechanical performance compared to other common thermoplastics [176, 177]. Given the above, Ultem™ 9085 is an excellent candidate for exploring the capabilities of AM-fabricated cellular cores for hybrid sandwich structures.

2.4.3 Mechanical performance of FFF parts

The FFF technology has progressed exponentially in recent years, thanks to expanding the range of materials available and producing more robust and reliable professional equipment that allows to increase production speeds and reduce manufacturing costs. With such developments, FFF technology has been increasingly utilized for end-use part manufacturing in many engineering sectors, like aerospace, automotive, and medical devices [178].

The mechanical performance of these components is an important factor to ensure the success of the final product. Therefore, understanding the influence of printing parameters on the performance of FFF parts is of paramount importance for many applications where ensuring safety and reliability is essential. Therefore, optimizing these parameters can lead to significant improvements in the mechanical properties.

In this sense, published scientific contributions have been mostly focused on the mechanical analysis of the inherent anisotropy induced by the FFF technology in solid configurations [162, 179, 180]. For instance, extensive studies of the behavior of ABS parts under tensile, flexural, and compression states were conducted [181, 182], as well as under fatigue test conditions [183]. These results awakened the interest to model the processed material with numerical approaches [184]. Furthermore, PLA was also investigated with the same purpose [185–187], and the influence of printing parameters on fatigue life was also evaluated [188]. The same analyses were attempted with PC [189], whose results provided a stiffness matrix that described the performance of this material depending on the manufacturing parameters [190]. Other investigations conducted employing the same material delved into its fracture behavior [191, 192] and the creep effect [193]. Simultaneously, other authors offered a numerical approach to simulate its performance under fatigue loads [194].

In the case of more advanced materials that have aroused interest in recent years, such as Ultem in particular, the available information in this regard is still limited. For example, its tensile behavior has been documented [195–198], as well as its response to flexural and compression tests [166, 199, 200], and its fatigue strength compared with other thermoplastics [176]. In addition, the consequences of moisture absorption in the Ultem filament before printing [201] and its impact resistance [177] have also been investigated. Meanwhile, the chemical similarities between Ultem and the corresponding

polysulfone (PSF) support material pose particular challenges for the elimination of the second one. For this reason, other authors focused their work on developing novel solvents and support-removal methodologies [202, 203].

However, the benefits associated with the influence of the rasters separation in terms of weight decrease, as well as material and manufacturing time savings are yet not fully addressed. Further, the optimization of mechanical performance by just modifying the infill configuration can be crucial to bringing the FFF technology to the forefront of industrial manufacturing. In addition, having a numerical model to simulate the mechanical behavior of this material that has been experimentally validated would allow the design of new, more efficient components to be approached with guarantees of success.

Regarding the literature review on the performance of FFF components, Table 2.5 presents a selection of the most relevant studies focusing on the mechanical characterization of parts manufactured using this AM technology under different load cases.

Table 2.5: Referenecs on the mechanical characterization of FFF parts under different load cases. *Light gray:* Use of Ultem. *White:* Use of other materials.

Reference	Aim of study
Sola *et al.*, 2023 [160]	Tensile testing
Dey *et al.*, 2021 [161]	Review on FFF materials
Popescu *et al.*, 2018 [162]	Review on FFF process parameters
Jandyal *et al.*, 2022 [163]	Review on FFF materials and applications
Hsissou *et al.*, 2021 [164]	Review on FFF materials
Ceruti *et al.*, 2019 [165]	Review on FFF applications
Byberg *et al.*, 2018 [166]	Tensile + flexural + compressive testing
Melton *et al.*, 2011 [167]	Review on FFF materials
Blanco *et al.*, 2018 [168]	Thermodynamic properties
Luchinsky *et al.*, 2018 [169]	Thermodynamic properties + shear viscosity
Lau, 2014 [170]	Review on FFF materials
Stratasys, 2021 [171]	Technical datasheet
Hooper *et al.*, 2019 [172]	Review on FFF applications
Stratasys, 2021 [173]	Technical datasheet
Najmon *et al.*, 2019 [174]	Review on FFF applications
Wu *et al.*, 2018 [175]	Review on FFF applications
Fard & Hashemi, 2020 [176]	Fatigue testing
Roberson *et al.*, 2015 [177]	Process comparison (building vs machining)
Dilberoglu *et al.*, 2017 [178]	Review on FFF applications
Dizon *et al.*, 2018 [179]	Anisotropy analysis
Gabor *et al.*, 2019 [180]	Anisotropy analysis
McLouth *et al.*, 2017 [181]	Fracture toughness analysis
Sood *et al.*, 2010 [182]	Tensile + flexural + impact testing
Ziemian & Ziemian, 2019 [183]	Fatigue testing
Ahn *et al.*, 2002 [184]	Anisotropy analysis

Continued on next page

Table 2.5 – continued from previous page

Reference	Aim of study
Wittbrodt & Pearce, 2015 [185]	Material color influence on mechanical properties
Lee & Liu, 2019 [186]	Tensile testing
Chacón *et al.*, 2017 [187]	Tensile + flexural testing
Gomez-Gras *et al.*, 2018 [188]	Fatigue testing
Smith & Dean, 2013 [189]	Tensile testing
Domingo-Espin *et al.*, 2015 [190]	Anisotropy analisis
Sedighi *et al.*, 2020 [191]	Tensile + flexural + mode I fracture testing
Bahrami *et al.*, 2020 [192]	Mixed-mode I-II fracture testing
Salazar-Martín *et al.*, 2018 [193]	Creep testing
Puigoriol-Forcada *et al.*, 2018 [194]	Fatigue testing
Zaldivar *et al.*, 2017 [195]	Tensile testing + dynamic mechanical analysis + thermal mechanical analysis
Bagsik & Schöppner, 2011 [196]	Tensile testing
Bagsik *et al.*, 2010 [197]	Tensile + compressive testing
Gebisa & Lemu, 2019 [198]	Tensile testing
Motaparti, 2016 [199]	Flexural + compressive testing
Gebisa & Lemu, 2018 [200]	Flexural testing
Zaldivar *et al.*, 2018 [201]	Tensile testing + dynamic mechanical analysis
Chueca de Bruijn *et al.*, 2022 [202]	Solvent removal for support structures
Chueca de Bruijn *et al.*, 2020 [203]	Solvent removal for support structures

2.5 Literature gaps

The trends presented in Figure 2.24 demonstrate the growing interest in recent years in the main topics detailed earlier in this chapter of the thesis. However, at the time of this thesis, there are still many

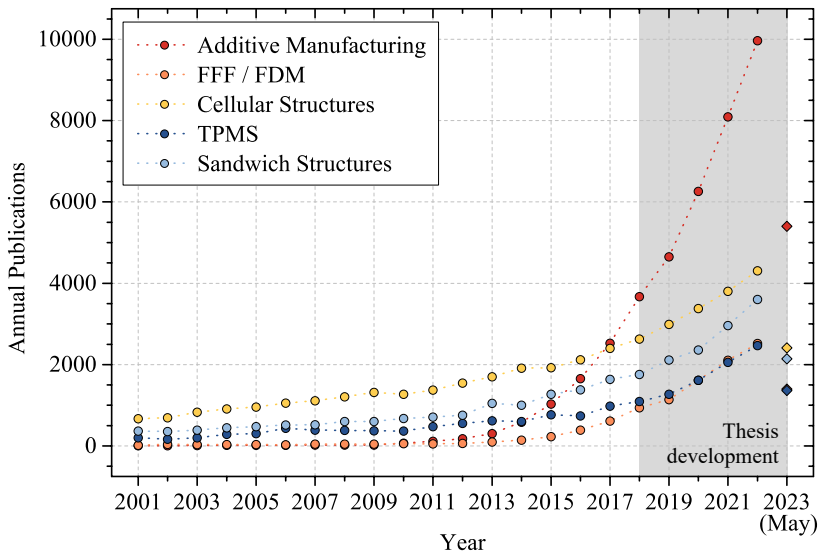

Figure 2.24: Evolution of the number of annual publications registered in ScienceDirect since 2001 that deal with any of the topics related to this research.

gaps in the literature to be explored. These unknowns, which are listed below, form the basis of this work and highlight the key areas in which this research contributes to the design and AM of cellular solids for lightweight hybrid sandwich structures.

- **To conduct a complete study of the mechanical properties of Ultem in order to approach the FE simulation of components manufactured by FFF considering the different printing parameters**: Previous investigations into the performance of FFF specimens have primarily focused on identifying the printing parameters that influence their mechanical properties. However, when it comes to the design and manufacturing of fully functional end parts, absolute control of these parameters becomes essential in order to produce parts with consistent and predictable mechanical behavior. For this reason, a comprehensive analysis of the tensile, flexural, and shear performance of FFF specimens is required. This analysis should allow the calculation of the entire stiffness tensor and determine the yield and strength points of the printed parts while taking into account multiple infill configurations. By doing so, it will be possible to optimize the printing process and ensure that the final products meet the required mechanical specifications.

- **To quantify the impact of using the Sparse infill on the equivalent mechanical properties of the material**: Although this infill type is one of the most widely used in FFF technology due to its significant savings in material and manufacturing time, it compromises the structural capacity of the manufactured components. However, its optimized design could become a strategic advantage for the manufacture of lightweight components. To this end, it is necessary to quantify the effect of this infill configuration on the mechanical properties of FFF samples, comparing them with those of the corresponding solid configuration.

- **To explore the impact of cellular design, density, and arrangement on the equivalent material properties in order to tailor its performance to the application requirements**: Many studies have focused on assessing the mechanical behavior of different cellular solids mainly under compressive, bending and impact loading states combining numerical and experimental approaches. However, the disparity of methodologies and materials implemented makes a fair comparison of the published results difficult. Thus, analyzing the performance of a wide range of two- and three-dimensional cellular designs employing the same test conditions would allow achieving the necessary data to adjust the equivalent properties of a material by controlling the design, the density and the arrangement of the cells.

- **To provide new analytical methodologies that further contribute to the design of cellular solids**: There has been a recent trend in research towards exploring the mechanical performance of cellular solids using a combination of numerical and experimental approaches. While this has proven to be an effective method for understanding the behavior of these materials, there is also a need for analytical calculations. Providing analytical calculations would have several advantages for the design of lightweight components with tailored performance. Firstly, it would allow for a more efficient and cost-effective approach to designing and manufacturing cellular solids.

Analytical models can be used to predict the mechanical behavior of these materials without the need for extensive experimental testing. Additionally, analytical calculations can provide insight into the relationship between the structure and properties of cellular solids, allowing designers to optimize their performance based on specific requirements. This would enable the creation of more customized and specialized cellular solids for a wide range of applications.

- **To validate a robust numerical methodology for both the simulation of the compression and flexural behavior of cellular cores, as well as the bending of hybrid sandwich structures**: In recent years, there has been a significant increase in the use of numerical approaches to simulate the mechanical behavior of cellular solids. However, the majority of the published numerical approaches tend to focus on reproducing the exact behavior of a particular case, rather than considering more versatile models that employ generic boundary conditions. The development of these models would allow for the simulation of multiple cellular designs, making it possible to explore a wider range of structures and properties. This approach would also facilitate the optimization of cellular solids for specific applications by allowing researchers to investigate how changes in design parameters affect mechanical behavior. Furthermore, by using generic boundary conditions, researchers can develop more transferable numerical models that can be applied across a range of materials and scales. This would not only provide a deeper understanding of the underlying mechanics of cellular solids but also enable the development of more efficient and sustainable materials for a variety of engineering applications.

- **To deeply explore the potential of additively manufactured cellular cores for obtaining more efficient hybrid sandwich structures**: The maturity of FFF technology limits the possibility of manufacturing hybrid sandwich structures in a single process. Despite these limitations, the full potential of cellular cores in hybrid sandwich structures should be explored through further investigation. By considering a wider range of cellular designs and densities, it may be possible to identify new opportunities for the integration of different materials and manufacturing methods. This could lead to the development of new hybrid sandwich structures with enhanced mechanical properties and multifunctional capabilities. Additionally, further investigation into the mechanical behavior of cellular cores in hybrid sandwich structures could provide insights to optimize their design and performance for a wide range of applications.

3

Methodology

This chapter presents the different approaches to investigate the mechanical performance at three levels of detail: material, cellular core design, and sandwich structure. In each case, the analytical, numerical and/or experimental approaches that have been combined to validate the outcomes of this research are described.

In order to address the objectives defined in this doctoral thesis, this research was structured in three distinct stages. Firstly, a complete study of the role that the FFF technology printing parameters play on the elastoplastic behavior of the material selected for this research (Ultem) was conducted. Then, the second stage focused on exploring the structural capabilities of a wide range of two- and three-dimensional cellular designs under compressive stresses. Finally, considering the mechanical behavior of Ultem processed by FFF and the potential of the considered cellular cores, it was possible to determine with certainty the structural efficiency of multiple hybrid sandwich structures during the third stage of the present investigation.

To address this challenge and validate the raised hypotheses, analytical, experimental and numerical methods were combined to validate the results of each stage. The following sections of this chapter detail the methodology implemented in each of these approaches, considering theoretical calculations, mechanical fabrication and experimentation, digital microscopy and DIC analyses, and FE modeling.

3.1 Material characterization

3.1.1 Design of experiments

To identify the role that the FFF printing parameters played on the mechanical performance and weight reduction of Ultem parts, tensile (ASTM D638 [204]), flexural (ASTM D790 [205]), and shear (ASTM D5379 [206]) loading tests were conducted. In particular, the three parameters evaluated were:

a) **Sample orientation**: Sets the position of the design to be fabricated on the printing bed.

b) **Raster angle**: Determines the angle of the filaments' intra-layer orientation relative to the x-axis of the printing bed.

c) **Raster-to-raster air gap**: Indicates the physical separation between two intra-layer contiguous rasters.

An accurate combination of these factors is essential for controlling the material deposition and the internal design of the FFF parts. Accordingly, the printed parts were categorized into two main configurations: solid (air gap = 0 mm) and sparse (air gap > 0 mm).

To evaluate the effect of the filament's intra-layer direction on the mechanical performance of solid specimens, 3 different raster angles were studied: 0°, 90°, and $\pm 45^{\circ}$. However, it should be noted that some of these raster angle values may not be useful in combination with the sparse infill configurations for structural applications. In particular, unidirectional sparse configurations would dramatically reduce the consistency of these low-density parts in some testing directions, as this infill type eliminates the intra-layer raster connections. Therefore, only the raster angle of $\pm 45^{\circ}$ was considered appropriate for testing the sparse configuration. In this case, and regarding the dimensions of the ASTM specimens, the inspected raster-to-raster air gap values were 0.25 mm, 0.50 mm, and 0.75 mm.

Material deposition rasters directly depend on the arrangement of the part on the building bed (Flat or Edge) due to the shape of the ASTM specimens. Moreover, the possible anisotropic properties of the material had to be evaluated for every raster angle and part arrangement, especially when a unidirectional infill pattern was used (0° or 90°). Hence, each solid and sparse configuration was characterized in all three cartesian orientations (x, y, and z) as shown in Figure 3.1.

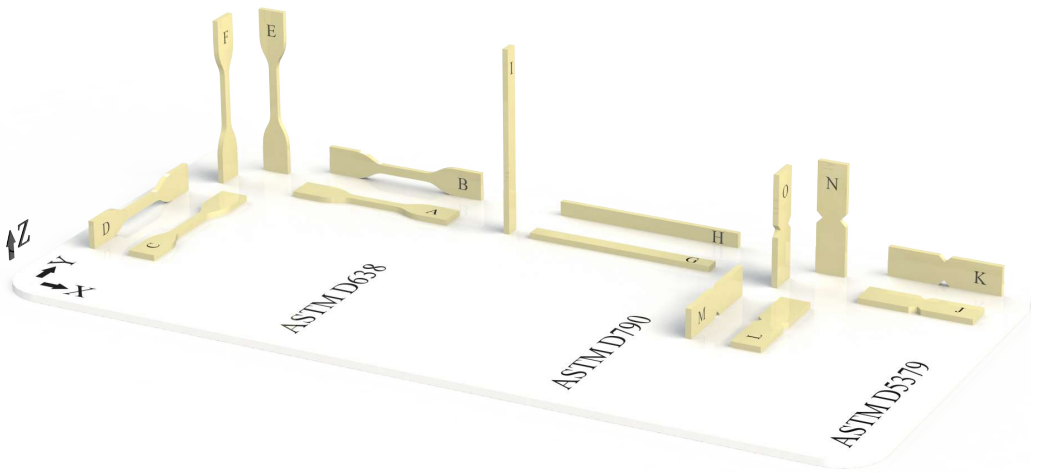

Figure 3.1: Printing orientations of all the manufactured test samples. ASTM D638: x-Flat (A), x-Edge (B), y-Flat (C), y-Edge (D), z-Flat (E), and z-Edge (F); ASTM D790: x-Flat (G), x-Edge (H), and z-Edge (I); ASTM D5379: x-Flat (J), x-Edge (K), y-Flat (L), y-Edge (M), z-Flat (N), and z-Edge (O).

On the one hand, tensile tests were performed along the global x, y, and z axes of the printing bed, to determine any degree of isotropy in each solid configuration, and particularly to confirm the expected orthotropy of the $\pm 45°$ samples. The preliminary results obtained from samples of this configuration demonstrated an equivalent behavior between specimens rotated 90° around the z-axis on the printing bed. Consequently, the analysis of the part orientations x-Flat, x-Edge, and z-Edge was considered enough for the complete evaluation of the tensile mechanical performance of the sparse configuration.

On the other hand, flexural tests were conducted in all configurations to study the differences between intra-layer and inter-layer bending properties. To do so, specimens were fabricated and evaluated in x-Flat, x-Edge, and z-Edge part orientations for both solid and sparse configurations, considering again the previous equivalence of samples.

Additionally, a full factorial design of experiments (DOE) was followed for conducting the shear experiments, with identical part orientations tested in both solid and sparse configurations.

Finally, a minimum of 3 specimens per infill configuration were tested for each part orientation depicted in Figure 3.1 to verify the repeatability of all experiments. This led to a total of 277 tested specimens[1].

[1]Tensile testing: 115 samples (70 solid and 45 sparse). Flexural testing: 54 samples (27 solid and 27 sparse). Shear testing: 108 samples (54 solid and 54 sparse).

The previously described factors and their respective different levels considered in this DOE are summarized in Tables 3.1 and 3.2.

Table 3.1: Design factors and levels considered for analyzing the solid configuration.

Solid configuration			
ASTM test standard	Air gap (mm)	Raster angle (°)	Part orientation
D638 [204]	0.00	0 90 ±45	x-Flat / x-Edge y-Flat / y-Edge z-Flat / z-Edge
D790 [205]	0.00	0 90 ±45	x-Flat / x-Edge z-Edge
D5379 [206]	0.00	0 90 ±45	x-Flat / x-Edge y-Flat / y-Edge z-Flat / z-Edge

Table 3.2: Design factors and levels considered for analyzing the sparse configuration.

Sparse configuration			
ASTM test standard	Air gap (mm)	Raster angle (°)	Part orientation
D638 [204]	0.25 0.50 0.75	±45	x-Flat / x-Edge z-Edge
D790 [205]	0.50 0.50 0.75	±45	x-Flat / x-Edge z-Edge
D5379 [206]	0.75 0.50 0.75	±45	x-Flat / x-Edge y-Flat / y-Edge z-Flat / z-Edge

3.1.2 Sample manufacturing

Each specimen geometry, exported into STL format, was processed using Stratasys' official slicer software (Insight) to generate a Coordinate Machine Binary (CMB) file that contains the necessary information to fabricate every sample according to the proposed DOE. The slice height value was set to 0.254 mm, while both contour and infill raster widths were set at 0.508 mm. Samples were built with one external contour to emphasize the impact of each infill configuration on their mechanical performance. Seam control options were adjusted to ensure that any contour joint did not occur within the gauge section and/or the transition radius region of the specimen. In all cases, the parallel

offset part rasters feature was activated to prevent the unwanted appearance of a continuous defect along the part's height in those solid infill trajectories of 0º or 90º that present unidirectional rasters (see Figure 3.2). Sparse configurations were created by increasing the distance between contiguous filaments with the raster-to-raster air gap value.

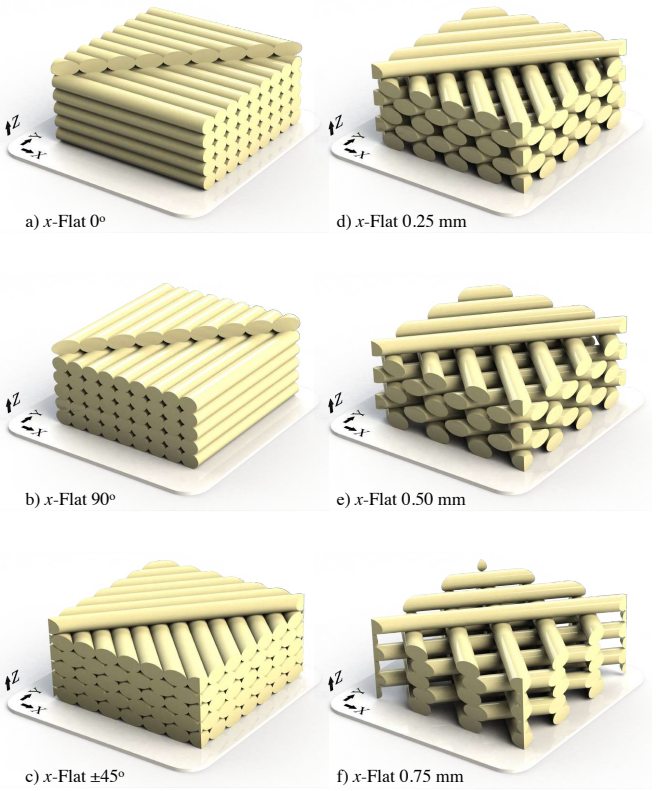

Figure 3.2: Representation of the cross-sectional area of samples in *x*-Flat 0º (*a*), *x*-Flat 90º (*b*), and *x*-Flat ±45º (*c*) solid configurations, and *x*-Flat 0.25 mm (*d*), *x*-Flat 0.50 mm (*e*), and *x*-Flat 0.75 mm (*f*) sparse configurations.

Samples were fabricated with a Stratasys Fortus 400mc professional FFF printer. This equipment has a heated chamber to ensure a controlled temperature during the whole printing process. This monitored environment is essential for guaranteeing the quality of the produced parts since it improves the inter-layer cohesion between consecutive layers. The Stratasys recommended working conditions for depositing Ultem FFF filament included an oven temperature of 195ºC. The model material (Ultem) was extruded at 380ºC and the support material (PSF) at 421ºC. After printing, the support structures were manually removed, and the mass and dimensions of each sample were measured.

3.1.3 Digital microscopy analyses

Once printed, samples were examined using a high-resolution Olympus DSX1000 digital microscope equipped with x5/x20 lenses in order to assess the quality investigation of the FFF manufacturing process and identify possible defects. In particular, the taken images allowed a detailed observation

of the consolidation of both intra-layer and inter-layer filament bonds and helped to determine their impact on the mechanical properties of the Ultem processed by this AM technology.

3.1.4 Digital image correlation

The inherent surface roughness of parts produced by FFF compromises the use of gauges for strain analysis. For this reason, DIC technology has been implemented in this research as an alternative.

DIC is a non-contact, full-field measurement technique that allows for the accurate quantification of deformation and strain fields on the surface of materials and structures. It involves analyzing a series of digital images taken before and after deformation to extract surface displacement and strain fields using algorithms. DIC has become a powerful tool for material and structural characterization, enabling researchers to analyze the mechanical behavior of materials and structures under various loading conditions. The technique is widely used in fields such as materials science, biomechanics, civil engineering, and aerospace engineering. DIC technology has rapidly advanced in recent years, leading to increased accuracy, speed, and versatility of the technique, making it an essential tool for researchers and engineers alike.

In particular, a 3D DIC setup was integrated for the investigation of full-field deformation during experimental tests when necessary. To do so, specimens were previously sprayed with a black-and-white stochastic pattern (see Figure 3.3). Then, 2 Allied Vision GigE MAKO G-507B cameras with APO-Xenoplan 1.4/23-0903 lens separated at an angle of approximately 23 degrees were used for recording the displacements on the surface of the samples. The whole system was calibrated with a GOM Correlate CP20/MV55x44 panel. Finally, the recorded video sequences were post-processed with GOM Correlate Professional software to analyze the full-field deformation of the samples.

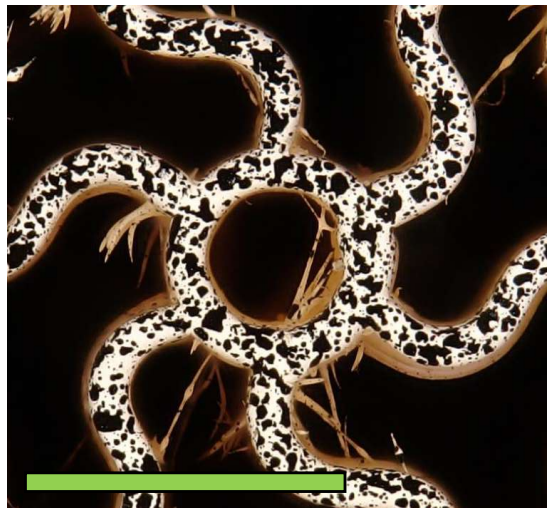

Figure 3.3: Example of a black-and-white stochastic pattern sprayed on the surface of a two-dimensional cellular solid design fabricated with FFF. The scale bar corresponds to 5 mm.

3.1.5 Tensile testing

Tensile tests were performed according to the ASTM D638 standard [204] using ZwickRoell Z030 30 kN equipment (see Figure 3.4). Type IV specimens with a thickness of 4 mm were selected for testing. The yield point was determined using an offset method of 0.1% strain. Two DIC extensometers placed perpendicularly in the center of the gauge section of each specimen were used to calculate the Poisson's coefficients within the elastic region. Results for tensile modulus, yield stress, yield strain, tensile strength, and strain at tensile strength were reported.

Figure 3.4: Experimental setup for ASTM D638 tensile test standard with DIC equipment.

3.1.6 Flexural testing

ASTM D790 standard [205] three-point flexural tests were conducted on specimens with a thickness of 4 mm using ZwickRoell Z030 30 kN equipment (see Figure 3.5). According to a 64 mm support span, the width and length dimensions of the samples were set to 10 mm and 127 mm, respectively, as specified by the test standard. The resulting rate of crosshead displacement was 1.71 mm/min under these conditions. The yield point was determined using an offset method of 0.1% strain. Although the ASTM D790 standard recommends ending the test when a 5% strain is reached, all of the samples were tested until failure occurred. Results for flexural modulus, yield stress, yield strain, flexural strength, and strain at flexural strength were reported.

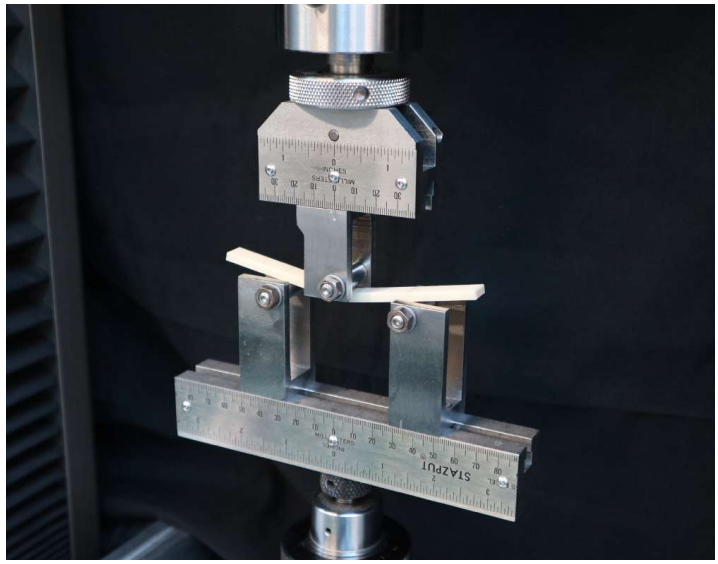

Figure 3.5: Experimental setup for ASTM D790 flexural test standard.

3.1.7 Shear testing

Shear tests were conducted using ZwickRoell Z030 30 kN equipment following the ASTM D5379 standard [206], again with specimens of 4 mm thickness (see Figure 3.6). No twisting effect was observed during the test, so there was no need to use additional tabs. DIC equipment was used to measure the shear strain at the center of the specimen. While the test standard recommends stopping the test at a strain of 5%, the shear tests were continued until failure occurred. The yield point was estimated using the offset method with a strain of 0.2%. Results for shear modulus, yield point data, shear strength, and strain at shear strength were reported.

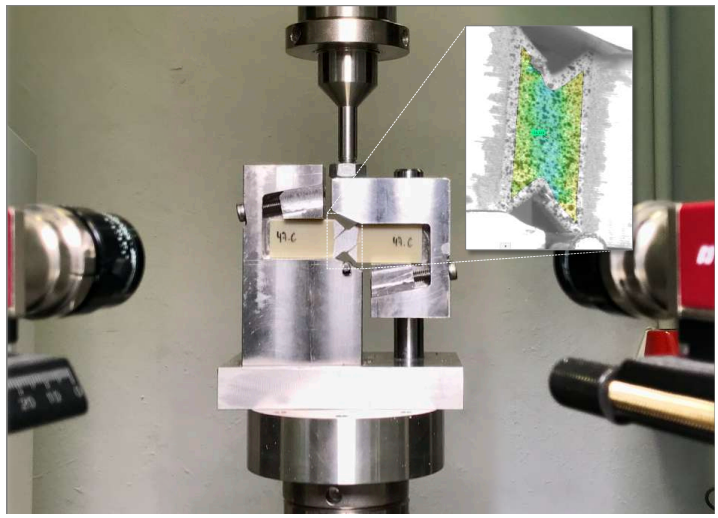

Figure 3.6: Experimental setup for ASTM D5379 shear test standard with DIC equipment.

3.2 Cellular solids characterization

Having analyzed the anisotropic behavior of Ultem and obtained the compliance matrices for different infill configurations, the second stage consisted of characterizing the cellular designs fabricated by FFF to evaluate their structural capacities.

3.2.1 Design of experiments

Thirteen two-dimensional (see Figure 3.7) and twenty three-dimensional (see Figure 3.8) cellular solids were selected to assess the role that the pattern's design, cell size, and density play on the mechanical performance and weight reduction of lightweight structures. To this end, their compression behavior was examined and validated through analytical, numerical and experimental approaches.

In particular, the analysis encompasses the two-dimensional cellular geometries Antitetrachiral, Circular, Hexachiral, Hexagon, Re-Entrant Hexagon (types I and II), Lozenge Grids, Rotachiral, Sinusoidal Ligaments, Square Grids, SrCuBO, and Tetrachiral. Moreover, the Sparse infill, classically used in FFF printing strategies, was also included for comparison. Three different density levels were considered in all cases, except for the Sparse pattern, for which six air gap values were considered, thus providing a total of 42 different infill configurations. Only tests in x and z-directions were conducted with the symmetrical cellular designs[2], considering the equivalence of in-plane x and y-directions.

[2]Symmetrical two-dimensional cellular patterns: Antitetrachiral, Lozenge Grids, Rotachiral, Sinusoidal Ligaments, Square Grids, SrCuBO, Tetrachiral, and Sparse.

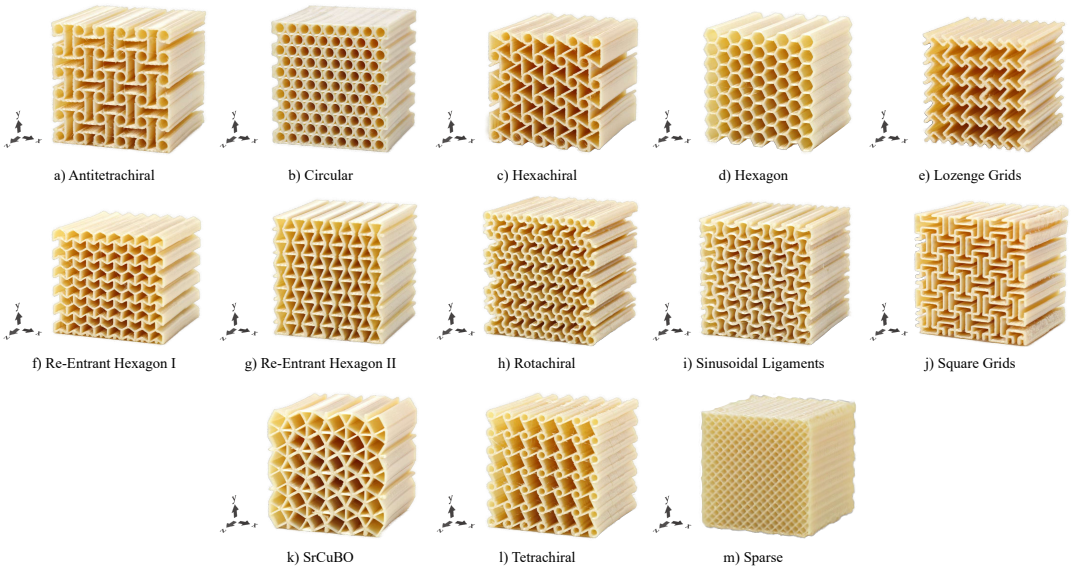

Figure 3.7: FFF manufactured sample of each two-dimensional cellular solid assessed.

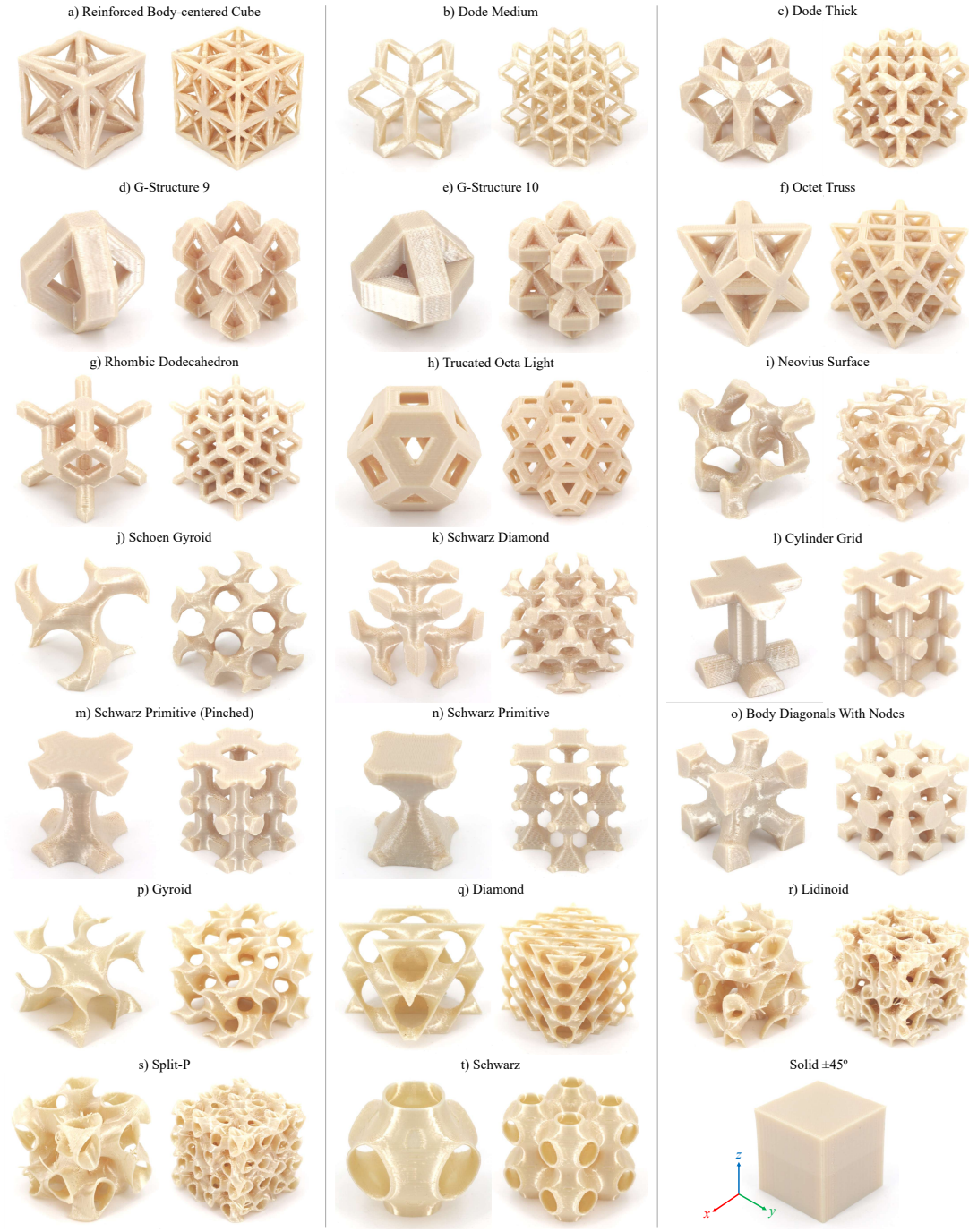

Figure 3.8: FFF manufactured sample of each three-dimensional cellular solid assessed.

Regarding the three-dimensional cellular solids, the study included eight lattices, seven Skeletal-TPMS, and five Shell-TPMS designs:

a) **Lattice designs**: Reinforced body-centered cube, Dode medium, Dode thick, G-Structure 9, G-Structure 10, Octet truss, Rhombic dodecahedron, and Truncated octa light.

b) **Skeletal-TPMS designs**: Neovius surface, Schoen gyroid, Schwarz diamond, Cylinder grid, Schwarz primitive (pinched), Schwarz primitive, and Body diagonals with nodes.

c) **Shell-TPMS designs**: Gyroid, Diamond, Lidinoid, Split-P, and Schwarz.

2 different unit cell sizes were considered in each case, thus resulting in samples made of a single cell and others of eight cells. In addition, two infill densities (solid and sparse) were implemented when possible. Samples were only tested in z-direction considering the spatial symmetry of three-dimensional designs.

Finally, the mechanical behavior of the two and three-dimensional cellular solids was also compared with the compressive performance of a solid cube with nominal dimensions equivalent to the fabricated specimens ($40 \times 40 \times 40$ mm). In order to test the repeatability of all the experiments, 2 specimens per cellular pattern and test orientation were analyzed. This led to a total of 340 tested specimens[3].

3.2.2 Analytical approach

One of the parameters that better describe the physical and mechanical characteristics of a cellular solid is its relative density. It is calculated by dividing the density of the cellular solid (ρ^*) by the density of the solid material (ρ^s) it is made of. Furthermore, the relative density also corresponds to the ratio between the effective elastic modulus in the z-direction (E_z^*) and the one corresponding solid material (E_z^s) for two-dimensional patterns:

$$\frac{E_z^*}{E_z^s} = \frac{\rho^*}{\rho^s} \tag{3.1}$$

In addition, the effective in-plane elastic moduli (E_x^* and E_y^*) and strengths (σ_x^* and σ_y^*) of two-dimensional cellular patterns can be estimated with the following power-law expressions, which also require the values of sample's relative density and solid material's elastic modulus:

$$\begin{aligned} \frac{E_x^*}{E_x^s} &= B_x \left(\frac{\rho^*}{\rho^s}\right)^b \qquad \frac{E_y^*}{E_y^s} = B_y \left(\frac{\rho^*}{\rho^s}\right)^b \\ \frac{E_x^*}{E_x^s} &= C_x \left(\frac{\rho^*}{\rho^s}\right)^c \qquad \frac{E_y^*}{E_y^s} = C_y \left(\frac{\rho^*}{\rho^s}\right)^c \end{aligned} \tag{3.2}$$

[3] 198 two-dimensional and 142 three-dimensional cellular solids

where: $b = 1$ and $c = 1$ for stretch-dominated structures

$b = 3$ and $c = 2$ for bending-dominated structures

B_x, B_y, C_x, and C_y are experimental coefficients that depend on the cell geometry

Hence, given the relevance of the relative density of the two-dimensional patterns, the dimensions of each cell design that was considered in this work were parameterized as displayed in Figure 3.9. Moreover, the modification of these design parameters allows the fabrication of multiple cellular solids with different densities using the same cell morphology. Therefore, the following analytical equations were determined to calculate the relative density of the two-dimensional patterns prior to fabrication.

a) Antitetrachiral

$$\frac{\rho^*}{\rho^s} = \frac{2}{b^2}\left[t\left(a\pi + b\right) + \frac{\sqrt{2}}{2}\left(2a - t\right)\sqrt{at} - \left(a + \frac{t}{2}\right)^2 \arccos\left(\frac{2a - t}{2a + t}\right)\right] \tag{3.3}$$

b) Circular

$$\frac{\rho^*}{\rho^s} = \frac{4}{\sqrt{3}}\frac{at\pi}{\left(2a + t\right)^2} \tag{3.4}$$

c) Hexachiral

$$\frac{\rho^*}{\rho^s} = 1 - \frac{1}{b^2}\left[\frac{2\pi}{\sqrt{3}}\left(a - \frac{t}{2}\right)^2 + \left(\sqrt{b^2 - 4a^2} - t\sqrt{3}\right)^2\right] \tag{3.5}$$

d) Hexagon

$$\frac{\rho^*}{\rho^s} = \frac{t\sqrt{3}}{9a^2}\left(6a - t\sqrt{3}\right) \tag{3.6}$$

f) Lozenge Grids

$$\frac{\rho^*}{\rho^s} = \frac{8a - t}{8a^2}t \tag{3.7}$$

f) Re-Entrant Hexagon I

$$\frac{\rho^*}{\rho^s} = 1 - \frac{\left(a\sin\theta - \frac{t}{2}\right)\left(b - \frac{t}{\sin\theta}\right)}{ab\sin\theta} \tag{3.8}$$

g) Re-Entrant Hexagon II

$$\frac{\rho^*}{\rho^s} = \frac{2t\left[a + \frac{1}{\sin\theta}\left(b - t\right) - \frac{t^2}{2\tan\theta}\right]}{b\left(2a - \frac{b}{\tan\theta}\right)} \tag{3.9}$$

h) Rotachiral

$$\frac{\rho^*}{\rho^s} = \frac{\pi t\,(3b-2a)}{\sqrt{3}b^2} + \frac{\sqrt{3at\,(b-2a)\,(2a+b+2t)}}{\sqrt{2}b^2} - \\ - \frac{2\sqrt{3}}{b^2}\left(\frac{b}{4} - \frac{a}{2} + \frac{t}{2}\right)^2 \arccos\left(\frac{b^2+2bt-4a^2-12at}{[b+2\,(t-a)]\,(2a+b)}\right) - \\ - \frac{2\sqrt{3}}{b^2}\left(a + \frac{t}{2}\right)^2 \arccos\left(\frac{6at+2ab+4a^2-bt}{(2a+t)\,(2a+b)}\right) \tag{3.10}$$

i) Sinusoidal Ligaments

$$\frac{\rho^*}{\rho^s} = \frac{4}{a^2}\left[\left(b-\frac{t}{2}\right)^2 + \left(b-\frac{t}{2}+\Psi\right)\left(\frac{a}{2}-b+\frac{t}{2}\right) + \left(\frac{a}{2}-\Psi\right)\left(\Omega-b+\frac{t}{2}\right)\right] + \\ + \frac{2}{a^2}\left[\left(\frac{a^2}{8b}+\frac{b}{2}+\frac{t}{2}\right)^2 (2\gamma - \sin(2\gamma)) - \left(\frac{a^2}{8b}+\frac{b}{2}-\frac{t}{2}\right)^2 (2\delta - \sin(2\delta))\right] \tag{3.11}$$

where:

$$\alpha = \arcsin\left(\frac{\sqrt{2}\left(a^2-4b^2-4ab\right)}{2\,(4b^2+a^2)}\right)$$

$$\beta = \arccos\left(-\frac{\sqrt{2}\left(-16b^4-32tb^3-8a^2b^2-8bta^2-a^4\right)}{2\,(4b\,(b+t)+a^2)\,(4b^2+a^2)}\right)$$

$$\gamma = \arcsin\left(\frac{\frac{a}{2}-\Psi}{\frac{a^2}{8b}+\frac{b}{2}+\frac{t}{2}}\right)$$

$$\delta = \arcsin\left(\frac{\frac{a}{2}-\Omega}{\frac{a^2}{8b}+\frac{b}{2}-\frac{t}{2}}\right)$$

$$\Psi = \frac{a}{2} - \left(\frac{a^2}{8b}+\frac{b+t}{2}\right)\cos\left(\frac{\pi}{2}+\alpha-\beta\right)$$

$$\Omega = -\frac{a^2}{8b}+\frac{b}{2}+\left(\frac{a^2}{8b}+\frac{b+t}{2}\right)\sin\left(\frac{\pi}{2}+\alpha-\beta\right)$$

j) Square Grids

$$\frac{\rho^*}{\rho^s} = \frac{10a-t}{9a^2}t \tag{3.12}$$

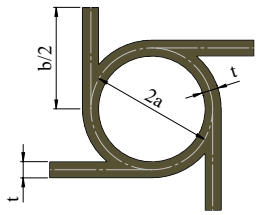

a) Antitetrachiral

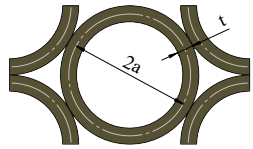

b) Circular

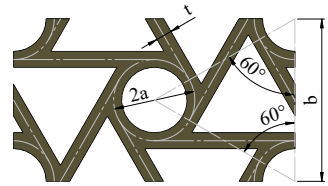

c) Hexachiral

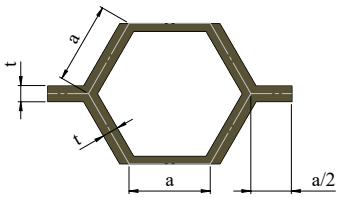

d) Hexagon

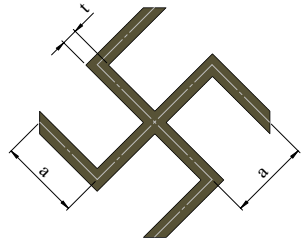

e) Lozenge Grids

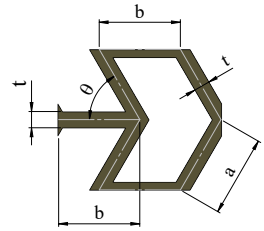

f) Re-Entrant Hexagon I

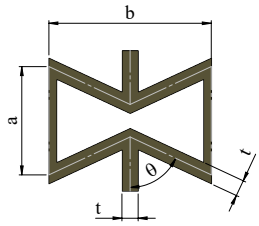

g) Re-Entrant Hexagon II

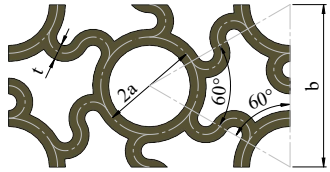

h) Rotachiral

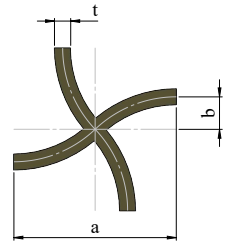

i) Sinusoidal Ligaments

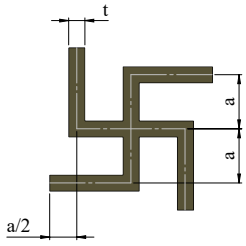

j) Square Grids

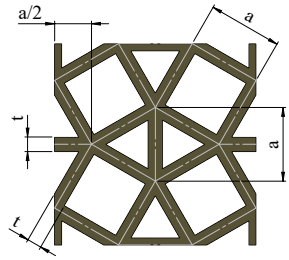

k) SrCuBO

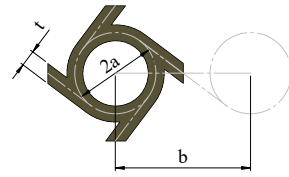

l) Tetrachiral

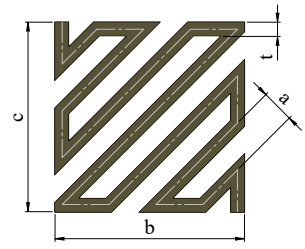

m) Sparse

Figure 3.9: Design parameters considered for the fabrication of the two-dimensional cellular solids assessed.

k) SrCuBO

$$\frac{\rho^*}{\rho^s} = \frac{20at - t^2\left(4 + 6\sqrt{3}\right)}{a^2\left(4 + 2\sqrt{3}\right)} \tag{3.13}$$

l) Tetrachiral

$$\frac{\rho^*}{\rho^s} = \frac{2}{b^2}\left[t\left(a\pi + 2\sqrt{\left(\frac{b}{2}\right)^2 - a^2}\right) - \left(a + \frac{t}{2}\right)^2 \arccos\left(\frac{2a - t}{2a + t}\right)\right] + \\ + \frac{\sqrt{2}}{b^2}\left(2a - t\right)\sqrt{at} \tag{3.14}$$

m) Sparse

$$\frac{\rho^*}{\rho^s} = \frac{bc + a\left(b + c - t\right)}{bc\left(t + a\right)}t \tag{3.15}$$

3.2.3 Manufacturing of the samples

Most of the cellular solids were designed using SolidWorks software. However, a self-developed open-source software, named TPMSgen [1], was employed for generating the CAD files of the TPMS structures, directly from their mathematical expressions:

a) Schoen gyroid

$$\sin x \cos y + \sin y \cos z + \sin z \cos x = 1 \tag{3.16}$$

b) Schwarz diamond

$$\cos x \cos y \cos z + \sin x \sin y \sin z = \frac{1}{2} \tag{3.17}$$

c) Schwarz primitive (pinched)

$$\cos x \cos y \cos z = \frac{1}{2.5} \tag{3.18}$$

d) Schwarz primitive

$$\cos x \cos y \cos z = \frac{1}{1.5} \tag{3.19}$$

e) Body diagonals with nodes

$$2\left(\cos x \cos y + \cos y \cos z + \cos z \cos x\right) - \left(\cos 2x + \cos 2y + \cos 2z\right) = 1 \tag{3.20}$$

f) Gyroid

$$\sin x \cos y + \sin y \cos z + \sin z \cos x = 0 \tag{3.21}$$

g) Diamond

$$\sin x \sin y \sin z + \sin x \cos y \cos z + \cos x \sin y \cos z + \cos x \cos y \sin z = 0 \tag{3.22}$$

h) Lidinoid

$$\sin 2x \cos y \sin z + \sin x \sin 2y \cos z + \cos x \sin y \sin 2z - \\ - \cos 2x \cos 2y - \cos 2y \cos 2z - \cos 2z \cos 2x + 0.3 = 0 \tag{3.23}$$

i) Split-P

$$1.1\,(\sin 2x \cos y \sin z + \sin x \sin 2y \cos z + \cos x \sin y \sin 2z) - \\ - 0.2\,(\cos 2x \cos 2y + \cos 2y \cos 2z + \cos 2z \cos 2x) - \\ - 0.4\,(\cos 2x + \cos 2y + \cos 2z) = 0 \tag{3.24}$$

j) Schwarz

$$\cos x + \cos y + \cos z = 0 \tag{3.25}$$

Samples for conducting the experimental tests were fabricated in a Stratasys Fortus 400mc FFF professional equipment with Ultem material, following the optimum operating conditions suggested by the printer manufacturer (see Section 3.1.2). The official Insight slicer software was used for the generation of the CMB files, which contain the corresponding G-code for printing the specimens. All samples were built with a slice height of 0.254 mm.

Two-dimensional patterns were fabricated according to the design dimensions specified in Table 3.3 and with a nominal wall-thickness t of one contour (0.508 mm). This fact reduced the required material for building each cell pattern and its manufacturing time. Meanwhile, the Sparse pattern was directly created by controlling the intra-layer separation between filaments with the raster-to-raster air gap parameter on a cubic part design. Specimens were manufactured in the upright orientation to take advantage of the extruded-like shape of the two-dimensional patterns. Consequently, no support material was required as geometries can stand by themselves while building, which directly benefits the manufacturing time and material consumption.

Table 3.3: Dimensions used for the fabrication of two-dimensional patterns.

Pattern	Density level	a (mm)	b (mm)	θ (°)
Antitetrachiral	I	1.30	4.00	-
	II	2.00	7.00	
	III	2.75	10.00	

Continued on next page

Table 3.3 – continued from previous page

Pattern	Density level	a (mm)	b (mm)	θ (°)
Circular	I	1.70	-	-
	II	2.20		
	III	3.20		
Hexachiral	I	1.30	5.20	-
	II	1.90	7.50	
	III	2.50	10.00	
Hexagon	I	2.35	-	-
	II	2.85		
	III	3.85		
Lozenge Grids	I	1.70	-	-
	II	2.20		
	III	2.70		
Re-Entrant Hexagon I	I	2.35	2.69	60
	II	2.85	3.19	60
	III	4.35	4.69	60
Re-Entrant Hexagon II	I	3.80	5.80	65
	II	4.80	7.30	65
	III	5.80	8.30	65
Rotachiral	I	1.25	6.00	-
	II	1.55	7.50	
	III	2.05	10.00	
Sinusoidal Ligaments	I	3.00	1.00	-
	II	4.00	1.00	
	III	6.00	1.00	
Square Grids	I	1.80	-	-
	II	2.30		
	III	3.10		
SrCuBO	I	3.50	-	-
	II	5.00		
	III	7.00		
Tetrachiral	I	1.30	5.00	-
	II	1.50	6.00	
	III	2.00	8.00	
Sparse	I	0.25	-	-
	II	0.50		
	III	0.75		
	IV	1.50		
	V	3.00		
	VI	6.00		

To exploit the maximum capabilities of the FFF technology in terms of weight reduction, different infill configurations were compared when possible in the case of three-dimensional designs. Hence, both solid and sparse (with a raster-to-raster air gap of 0.25 mm) infill configurations could be employed for the fabrication of the lattice and Skeletal-TPMS samples, as they present larger cross-sectional areas that allow the incorporation of intra-layer separations between filaments. However, the constant and thin thickness of Shell-TPMS patterns precludes this comparison. Therefore, these designs were printed using solid walls of 2 contours (1.016 mm), as it was the minimum thickness that guaranteed their proper fabrication, aiming to evaluate the potential of FFF technology to produce structures as light as possible. In contrast to two-dimensional designs, the intricate geometry of the three-dimensional patterns included several areas with overhangs that sometimes required the use of PSF as support material for their construction (see Figure 3.10). Thus, an optimized procedure employing a solvent of 20% v/v aniline in toluene dissolution was used for removing all support structures [202, 203].

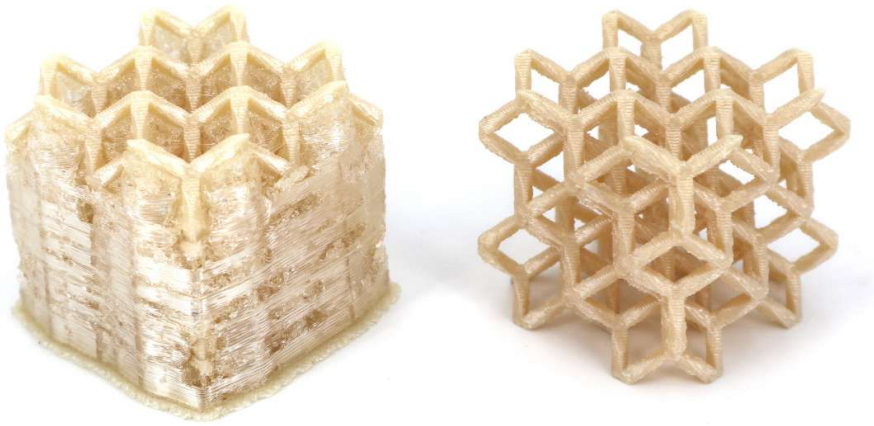

Figure 3.10: Appearance of a three-dimensional FFF cellular solid (Dode medium 8-cells) with the required support structures for its fabrication (*left*) and after the cleaning treatment with the 20% v/v aniline in toluene solution (*right*).

3.2.4 Compression testing

The two- and three-dimensional cellular designs were tested in compression on a ZwickRoell Z030 30 kN equipment, following the ASTM C365 standard [207] (see Figure 3.11). A crosshead rate of 3 mm/min was employed, which ensured that failure occurred within 3 to 6 minutes in all cases. The results for elastic modulus, maximum stress prior to FF, and the corresponding absorbed energy were reported, considering the specimen's nominal external dimensions for stress calculations. Experimental elastic moduli were extracted from test data between 0.1% and 0.3% of compressive strain through linear regression. The energy absorption efficiency was determined by dividing the area under the load-displacement curve by the material volume used for the fabrication of each three-dimensional cellular design.

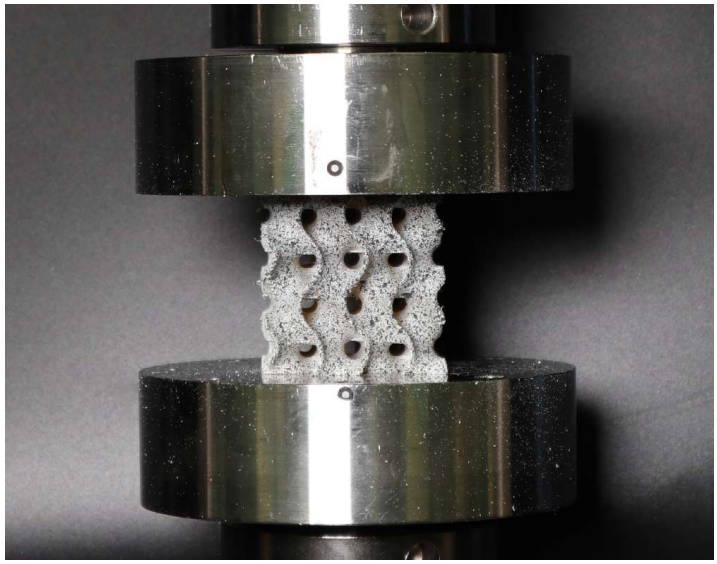

Figure 3.11: Experimental setup for conducting the compression tests of the cellular patterns, corresponding to the Gyroid 8-cells sample.

Two-dimensional patterns were tested in the in-plane x and y-directions, as well as the out-of-plane z-direction. However, for symmetrical cells such as Antitetrachiral, Lozenge Grids, Rotachiral, Sinusoidal Ligaments, Square Grids, SrCuBO, Tetrachiral, and Sparse patterns, tests were only performed in the x and z-directions due to the equivalence of x and y-directions. The nominal external dimensions were measured on each sample, and the in-plane Poisson's ratios were determined using DIC extensometers.

Compression tests on the fabricated three-dimensional cellular solids were only conducted perpendicularly to the printing plane (z-direction). In this case, and due to the difficulties to measure the nominal external dimensions of the printed specimens, CAD dimensions of $40 \times 40 \times 40$ mm were employed for effective stress and strain calculations. Again, DIC technology was integrated for the inspection of full-field displacements during testing.

3.2.5 Numerical approaches

The compression behavior of the tested samples was also validated with different FE models, employing the two main approaches to simulate cellular solids according to the state of the art: Solid Elements (SE) and Homogenized - Representative Volume Element (H-RVE). To do so, an implicit analysis employing the static structural module of Ansys software was conducted for each case to accurately reproduce the lineal behavior of any design.

The SE model is based on the real shape of the specimen. As a result, it allows capturing the deformation kinematics of the entire structure as well as identifying possible local effects, at the cost of higher mesh complexity and significantly longer computational times. On the other hand, the H-RVE approach is

a cost-effective alternative that employs a simplification of the equivalent volume occupied by the cellular structure and its corresponding effective properties obtained from numerical homogenization. Therefore, the CAD geometry of the sample was imported in the standard for the exchange of product model data (STEP) format or a 40 × 40 × 40 mm cubic part was directly created according to the chosen FE approach. Figure 3.12 depicts an example of each FE model.

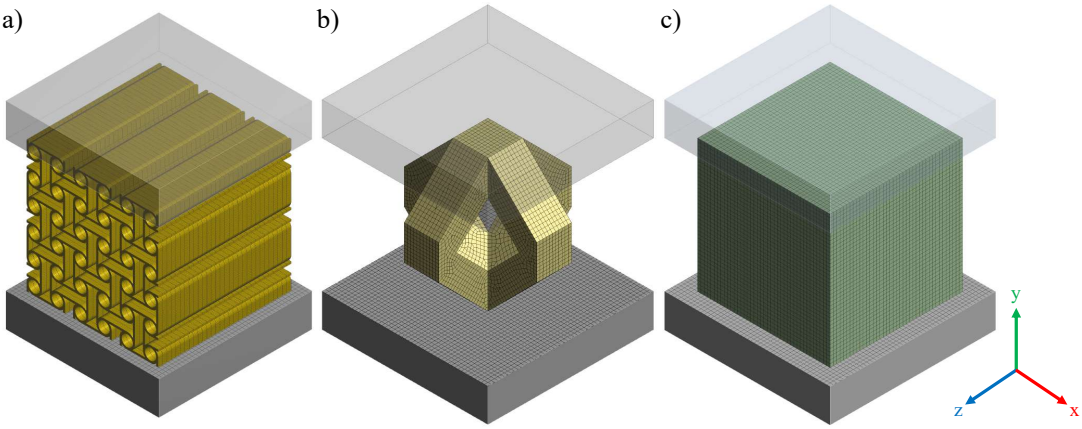

Figure 3.12: SE model developed for the simulation of the two- (*left*) and three-dimensional (*center*) cellular solids, and H-RVE model simplification employing effective properties (*right*).

According to the desired test axis for conducting the analysis, two parallel rigid bodies were created in touch with the top and bottom faces of the cellular design, respectively, that behaved as the compression test plates. All displacements and rotations were blocked to completely fix the bottom plate, while a 0.1 mm compression displacement was imposed on the upper plate in the corresponding testing direction.

Higher-order 3D 20-node SOLID186 element type was employed for generating the mesh of both the compression plates and the part. Concerning the SE models, the two-dimensional cellular designs were meshed using 30 divisions along the z-direction, whereas the side length of the resulting elements in the building plane was set to 0.15 mm. On the other hand, a body mesh method with elements of 0.50 mm of side length was implemented in three-dimensional patterns. Meanwhile, the equivalent cube which was employed for the H-RVE approach was also meshed using a body mesh method with elements of 1.00 mm.

Regarding the definition of the materials, Structural Steel was selected for modeling the compression plates, which was directly imported from the Engineering Data library available in Ansys. For the additively manufactured cores with solid layers, the experimental values obtained from the previous material characterization tests (Section 3.1) were employed. To do so, the Ultem $\pm 45°$ infill configuration results [208] were selected for developing three different scenarios considering multiple degrees of anisotropy for model simplification: orthotropic, quasi-isotropic, and isotropic. The corresponding Ultem properties are summarized in Table 3.4.

Table 3.4: Ultem elastic properties and stress limits used in the FE models.

Ultem elastic properties				
Property	Symbol	Orthotropic	Quasi-isotropic	Isotropic
Young's modulus *x*-direction (MPa)	E_x^s	2092	2121	2123
Young's modulus *y*-direction (MPa)	E_y^s	2150	2121	2123
Young's modulus *z*-direction (MPa)	E_z^s	2126	2126	2123
Poisson's ratio *xy*	ν_{xy}^s	0.344	0.344	0.368
Poisson's ratio *yz*	ν_{yz}^s	0.392	0.392	0.368
Poisson's ratio *xz*	ν_{xz}^s	0.392	0.392	0.368
Shear modulus *xy* (MPa)	G_{xy}^s	630	630	704
Shear modulus *yz* (MPa)	G_{yz}^s	745	741	704
Shear modulus *xz* (MPa)	G_{xz}^s	737	741	704
Ultem stress limits				
Property	Symbol	Orthotropic	Quasi-isotropic	Isotropic
Tensile *x*-direction (MPa)	$\sigma_{T,x}^s$	26.50	24.45	24.46
Tensile *y*-direction (MPa)	$\sigma_{T,y}^s$	22.40	24.45	24.46
Tensile *z*-direction (MPa)	$\sigma_{T,z}^s$	24.48	24.48	24.46
Compressive *x*-direction (MPa)	$\sigma_{C,x}^s$	-26.50	-24.45	-24.46
Compressive *y*-direction (MPa)	$\sigma_{C,y}^s$	-22.40	-24.45	-24.46
Compressive *z*-direction (MPa)	$\sigma_{C,z}^s$	-24.48	-24.48	-24.46
Shear *xy* (MPa)	τ_{xy}^s	25.72	25.72	25.86
Shear *yz* (MPa)	τ_{yz}^s	27.37	25.93	25.86
Shear *xz* (MPa)	τ_{xz}^s	24.48	25.93	25.86

Based on the above data and the experimental results from the compression tests of the two-dimensional sparse pattern, Eqs. 3.26 were analytically derived to determine the properties of this infill configuration that could be implemented in the numerical models.

$$
\begin{aligned}
E_x^{sp} &= \eta_2 \cdot E_x^s & E_y^{sp} &= \eta_2 \cdot E_y^s & E_z^{sp} &= \eta_3 \cdot E_z^s \\
\nu_{xy}^{sp} &= \eta_1 \cdot \nu_{xy}^s & \nu_{yz}^{sp} &= \eta_1 \cdot \nu_{yz}^s & \nu_{xz}^{sp} &= \eta_1 \cdot \nu_{xz}^s \\
G_{xy}^{sp} &= \eta_2 \cdot G_{xy}^s & G_{yz}^{sp} &= \eta_3 \cdot G_{yz}^s & G_{xz}^{sp} &= \eta_3 \cdot G_{xz}^s \\
\sigma_{T,x}^{sp} &= \eta_1 \cdot \sigma_{T,x}^s & \sigma_{T,y}^{sp} &= \eta_1 \cdot \sigma_{T,y}^s & \sigma_{T,z}^{sp} &= \eta_1 \cdot \sigma_{T,z}^s \\
\sigma_{C,x}^{sp} &= \eta_1 \cdot \sigma_{C,x}^s & \sigma_{C,y}^{sp} &= \eta_1 \cdot \sigma_{C,y}^s & \sigma_{C,z}^{sp} &= \eta_1 \cdot \sigma_{C,z}^s \\
\tau_{xy}^{sp} &= \eta_1 \cdot \tau_{xy}^s & \tau_{yz}^{sp} &= \eta_1 \cdot \tau_{yz}^s & \tau_{xz}^{sp} &= \eta_1 \cdot \tau_{xz}^s
\end{aligned}
\tag{3.26}
$$

$$\text{where:} \quad \eta_1 = \frac{\rho^*}{\rho^s} = \frac{bc + a\,(b + c - t)}{bc\,(t + a)} t$$
$$\eta_2 = \frac{E_x^*}{E_x^s} = \frac{E_y^*}{E_y^s} = \frac{2t^3}{a^3 + 3ta^2 + 4at^2 + 2t^3}$$
$$\eta_3 = \frac{E_z^*}{E_z^s} = \frac{t^2}{(a + t)^2}$$

The type of contact between the compression plates and the part was configured to accurately reproduce the boundary conditions of the test. To do so, frictional contacts with asymmetric behavior were introduced. The friction coefficient was set to 0.42. The Augmented Lagrange formulation with a penetration tolerance of 0.1 mm was activated, permitting ramped effects.

Several authors [209, 210] have demonstrated the role that the bonds appearing between consecutive FFF rasters play on the elastic asymmetry of the printed parts. Accordingly, the tensile and shear properties that were introduced in the FE model needed to be corrected to successfully reproduce the compression behavior. Hence, the Normal Stiffness Factor (FKN) was adjusted in the contacts' definition in order to consider the elastic asymmetry phenomenon. In particular, FKN factors of 0.215 and 0.050 were calibrated with the experimental elastic moduli results obtained by the Solid $\pm 45^{\circ}$ cube for the in-plane (x and y-directions) and the out-of-plane (z-direction) tests, respectively.

Finally, the reaction force was determined on the bottom compression plate in order to evaluate the stiffness of each two-dimensional and three-dimensional cellular pattern.

3.2.6 Degree of anisotropy

In the study of cellular solids, it is common to treat the resulting non-homogeneous structure fabricated with its constituent material (Ultem) as a new metamaterial. In this sense, it is interesting to analyze the degree of anisotropy of the obtained configuration to confirm its applicability and functionality. This parameter allows quantifying the uniformity of the mechanical properties of the material in any direction of the 3D space.

Scientists have compared the different anisotropy indices published to date to provide the most suitable method for each application to qualify this property in the most robust and reliable possible way [155]. Most of these methods, such as the Zener Ratio (A) and the Universal Anisotropy Index (A^U), focus on the stiffness tensor of the material and quantify the degree of anisotropy by calculating a ratio between some of its coefficients.

However, multiple works in the field of AM have noted the significantly high orthotropy of the processed material in some technologies, such as FFF [184]. Thus, the existing anisotropy indices may not capture such orthotropy if it is not specifically reflected in the stiffness tensor coefficients that are strictly used for their calculation, which could alter the comparison of the degree of anisotropy of cellular solids fabricated by different additive technologies.

Accordingly, a novel degree of anisotropy index A^V was proposed in this thesis to address this issue. It is based on the ratio between the volumes of the graphical representation $\Psi(x, y, z)$ of the whole stiffness tensor coefficients, which can be directly computed employing numerical integration methods, and the corresponding isotropy circumscribed sphere (see Figure 3.13):

$$A^V = \frac{\iiint_V \Psi(x, y, z)\, dx\, dy\, dz}{\frac{4}{3}\pi \max(f(x, y, z))^3} \tag{3.27}$$

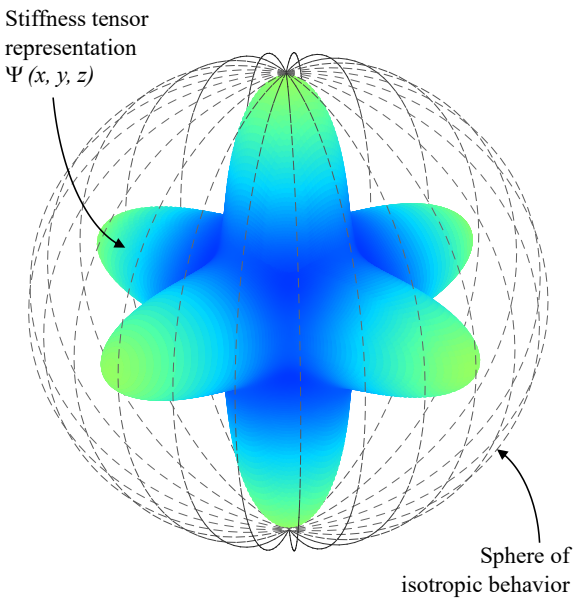

Figure 3.13: Volumetric representation of the RVE stiffness tensor of the Schwarz primitive (pinched) cellular solid, and the corresponding isotropic circumscribed sphere. The ratio of these two volumes is the A^V anisotropy index.

Therefore, the A^V index can only handle values from 0 to 1, being $A^V = 1$ a perfectly isotropic cellular solid.

The following lines describe the steps to obtain the graphical representation $\Psi(x, y, z)$ of the stiffness tensor ($\boldsymbol{C^H}$) of the RVE of a cellular solid, expressed in Voigt notation and referenced to the global *XYZ* coordinate system.

First, the generalized Hooke's law for continuous media can be expressed as:

$$\boldsymbol{\sigma} = \boldsymbol{C^H} \times \boldsymbol{\varepsilon} \tag{3.28}$$

where: $\boldsymbol{\sigma}$ is the stress tensor referenced to the global *XYZ* coordinates

$\boldsymbol{\varepsilon}$ is the strain tensor referenced to the global *XYZ* coordinates

Then, a rotation of $\boldsymbol{C^H}$ around the *x*-axis (α), *y*-axis (β), and z-axis (γ) can be introduced to evaluate the stress and strain tensors $\boldsymbol{\sigma_{\alpha\beta\gamma}}$ and $\boldsymbol{\varepsilon_{\alpha\beta\gamma}}$ as:

$$\begin{aligned} \boldsymbol{\sigma_{\alpha\beta\gamma}} &= \boldsymbol{L^{\sigma}_{\alpha\beta\gamma}} \times \boldsymbol{\sigma} \\ \boldsymbol{\varepsilon_{\alpha\beta\gamma}} &= \boldsymbol{L^{\varepsilon}_{\alpha\beta\gamma}} \times \boldsymbol{\varepsilon} \end{aligned} \tag{3.29}$$

where: $\boldsymbol{L^{\sigma}_{\alpha\beta\gamma}}$ and $\boldsymbol{L^{\varepsilon}_{\alpha\beta\gamma}}$ are the bond-stress and strains transformation matrices, which are determined from the rotation matrix $\boldsymbol{Q}$ and classical rotation matrices $\boldsymbol{R_x}$, $\boldsymbol{R_y}$, and $\boldsymbol{R_z}$, as detailed in Eq. 3.30

$$\begin{aligned} \boldsymbol{L^{\sigma}_{\alpha\beta\gamma}} &= \begin{bmatrix} Q_{11}^2 & Q_{12}^2 & Q_{13}^2 & 2Q_{12}Q_{13} & 2Q_{11}Q_{13} & 2Q_{11}Q_{12} \\ Q_{21}^2 & Q_{22}^2 & Q_{23}^2 & 2Q_{22}Q_{23} & 2Q_{21}Q_{23} & 2Q_{21}Q_{22} \\ Q_{31}^2 & Q_{31}^2 & Q_{33}^2 & 2Q_{31}Q_{33} & 2Q_{31}Q_{33} & 2Q_{31}Q_{31} \\ Q_{21}Q_{31} & Q_{22}Q_{31} & Q_{23}Q_{33} & Q_{22}Q_{33}+Q_{23}Q_{31} & Q_{21}Q_{33}+Q_{23}Q_{31} & Q_{21}Q_{31}+Q_{22}Q_{31} \\ Q_{11}Q_{31} & Q_{12}Q_{31} & Q_{13}Q_{33} & Q_{12}Q_{33}+Q_{13}Q_{31} & Q_{11}Q_{33}+Q_{13}Q_{31} & Q_{11}Q_{31}+Q_{12}Q_{31} \\ Q_{11}Q_{21} & Q_{12}Q_{22} & Q_{13}Q_{23} & Q_{12}Q_{23}+Q_{13}Q_{22} & Q_{11}Q_{23}+Q_{13}Q_{21} & Q_{11}Q_{22}+Q_{12}Q_{21} \end{bmatrix} \\ \boldsymbol{L^{\varepsilon}_{\alpha\beta\gamma}} &= \begin{bmatrix} Q_{11}^2 & Q_{12}^2 & Q_{13}^2 & Q_{12}Q_{13} & Q_{11}Q_{13} & Q_{11}Q_{12} \\ Q_{21}^2 & Q_{22}^2 & Q_{23}^2 & Q_{22}Q_{23} & Q_{21}Q_{23} & Q_{21}Q_{22} \\ Q_{31}^2 & Q_{31}^2 & Q_{33}^2 & Q_{31}Q_{33} & Q_{31}Q_{33} & Q_{31}Q_{31} \\ 2Q_{21}Q_{31} & 2Q_{22}Q_{31} & 2Q_{23}Q_{33} & Q_{22}Q_{33}+Q_{23}Q_{31} & Q_{21}Q_{33}+Q_{23}Q_{31} & Q_{21}Q_{31}+Q_{22}Q_{31} \\ 2Q_{11}Q_{31} & 2Q_{12}Q_{31} & 2Q_{13}Q_{33} & Q_{12}Q_{33}+Q_{13}Q_{31} & Q_{11}Q_{33}+Q_{13}Q_{31} & Q_{11}Q_{31}+Q_{12}Q_{31} \\ 2Q_{11}Q_{21} & 2Q_{12}Q_{22} & 2Q_{13}Q_{23} & Q_{12}Q_{23}+Q_{13}Q_{22} & Q_{11}Q_{23}+Q_{13}Q_{21} & Q_{11}Q_{22}+Q_{12}Q_{21} \end{bmatrix} \end{aligned} \tag{3.30}$$

where: $\boldsymbol{Q_{ij}}$ corresponds to the element located in row *i* and column *j* in $\boldsymbol{Q}$

$$\boldsymbol{Q} = \boldsymbol{R_x} \times \boldsymbol{R_y} \times \boldsymbol{R_z}$$

$$\boldsymbol{R_x}(\alpha) = \begin{bmatrix} 1 & 0 & 0 \\ 0 & \cos(\alpha) & -\sin(\alpha) \\ 0 & \sin(\alpha) & \cos(\alpha) \end{bmatrix} \quad \boldsymbol{R_y}(\beta) = \begin{bmatrix} \cos(\beta) & 0 & \sin(\beta) \\ 0 & 1 & 0 \\ -\sin(\beta) & 0 & \cos(\beta) \end{bmatrix}$$

$$\boldsymbol{R_z}(\gamma) = \begin{bmatrix} \cos(\gamma) & -\sin(\gamma) & 0 \\ \sin(\gamma) & \cos(\gamma) & 0 \\ 0 & 0 & 1 \end{bmatrix}$$

Substituting Eqs. 3.29 into Eq. 3.28, the following expression Eq. 3.31 is obtained:

$$\boldsymbol{\sigma_{\alpha\beta\gamma}} = \boldsymbol{L^{\sigma}_{\alpha\beta\gamma}} \times \boldsymbol{C^H} \times \boldsymbol{L^{\varepsilon}_{\alpha\beta\gamma}}^{-1} \times \boldsymbol{\varepsilon_{\alpha\beta\gamma}} \tag{3.31}$$

Then, the effective stiffness tensor in a specific orientation ($\boldsymbol{C^H_{\alpha\beta\gamma}}$) can be determined as:

$$\boldsymbol{C^H_{\alpha\beta\gamma}} = \boldsymbol{L^{\sigma}_{\alpha\beta\gamma}} \times \boldsymbol{C^H} \times \boldsymbol{L^{\varepsilon}_{\alpha\beta\gamma}}^{-1} \tag{3.32}$$

At this point, the corresponding compliance tensor $\boldsymbol{S^H_{\alpha\beta\gamma}}$ can be directly calculated by inverting $\boldsymbol{C^H_{\alpha\beta\gamma}}$. Thus, for example, taking abc the global *x*-axis reference, the effective elastic modulus $E_{\alpha\beta\gamma}$ is:

$$E_{\alpha\beta\gamma} = \frac{1}{S^H_{\alpha\beta\gamma_{11}}} \tag{3.33}$$

where: $S^H_{\alpha\beta\gamma_{11}}$ is the first term of the effective compliance tensor $\boldsymbol{S^H_{\alpha\beta\gamma}}$

Finally, the graphical representation $\Psi(x, y, z)$ of the homogenized stiffness tensor can be plotted with the sequential computation of different rotation angles α, β, and γ. Each combination will rotate the tensor and evaluate the effective stiffness in a particular examined direction $d_{\alpha\beta\gamma}$:

$$\boldsymbol{d_{\alpha\beta\gamma}} = \boldsymbol{Q} \times \begin{bmatrix} 1 \\ 0 \\ 0 \end{bmatrix} \tag{3.34}$$

Accordingly, given an orientation $\boldsymbol{d_{\alpha\beta\gamma}}$ and the corresponding effective elastic modulus $E_{\alpha\beta\gamma}$, the coordinates *x*, *y*, and *z* of a point in the graphical representation of the stiffness tensor are obtained as:

$$\begin{cases} x = E_{\alpha\beta\gamma} \cdot d_{\alpha\beta\gamma_1} \\ y = E_{\alpha\beta\gamma} \cdot d_{\alpha\beta\gamma_2} \\ z = E_{\alpha\beta\gamma} \cdot d_{\alpha\beta\gamma_3} \end{cases} \tag{3.35}$$

where: $d_{\alpha\beta\gamma_1}$, $d_{\alpha\beta\gamma_2}$, and $d_{\alpha\beta\gamma_3}$ are the first, second, and third terms of the particular examined direction $d_{\alpha\beta\gamma}$

3.3 Sandwich panels characterization

3.3.1 Design of experiments

To conclude this research, the two- and three-dimensional cellular patterns with the highest structural potential were implemented for the fabrication of lightweight cores for sandwich structures. Specifically, the effect of the cellular design and density on the flexural performance of hybrid panels, combining

additively manufactured cellular cores made of Ultem processed by FFF and CFRP skins, was analyzed following the ASTM C393 standard [211] (see Figure 3.14).

For this purpose, the potential of each cellular design was first numerically simulated considering 14 combinations of core thickness and skins, keeping a constant total thickness of the sandwich panel, and accounting for 6 different core density levels between 5% to 30% of relative density. Therefore, a total of 1596 FE models were solved to investigate the structural capabilities of each considered cellular pattern.

According to the results of the numerical approach, the optimal configurations of each cellular design were fabricated in order to experimentally validate the mechanical behavior of the hybrid sandwich structures. In order to test the repeatability of the experiments, two specimens per cellular design and density were experimentally tested, thus resulting in a total of 86 analyzed specimens.

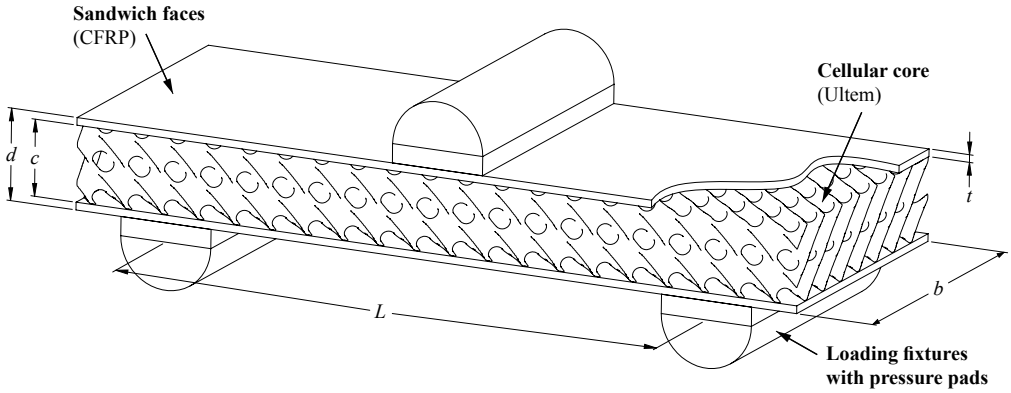

Figure 3.14: Arrangement and dimension parameters of a hybrid sandwich panel specimen for 3-point bending testing according to ASTM C393 standard.

3.3.2 Numerical approach

A FE implicit model was developed to evaluate the bending performance of the cellular hybrid sandwich structures in Ansys. Regarding the geometrical complexity of the considered core designs, an RVE approach was employed in order to simplify the generation of the mesh as well as reduce computation resources.

First, the unit cell of each considered two- and three-dimensional patterns (see Figure 3.15) was numerically homogenized employing the Ansys Material Designer module. To do so, periodic boundary conditions were imposed in x, y, and z axes. Hence, the effective orthotropic properties of the RVE of each cellular design were obtained. On the other hand, the mechanical properties for sandwich faces (see Table 3.5) were directly obtained from the CFRP material's technical data sheet provided by its manufacturer [212].

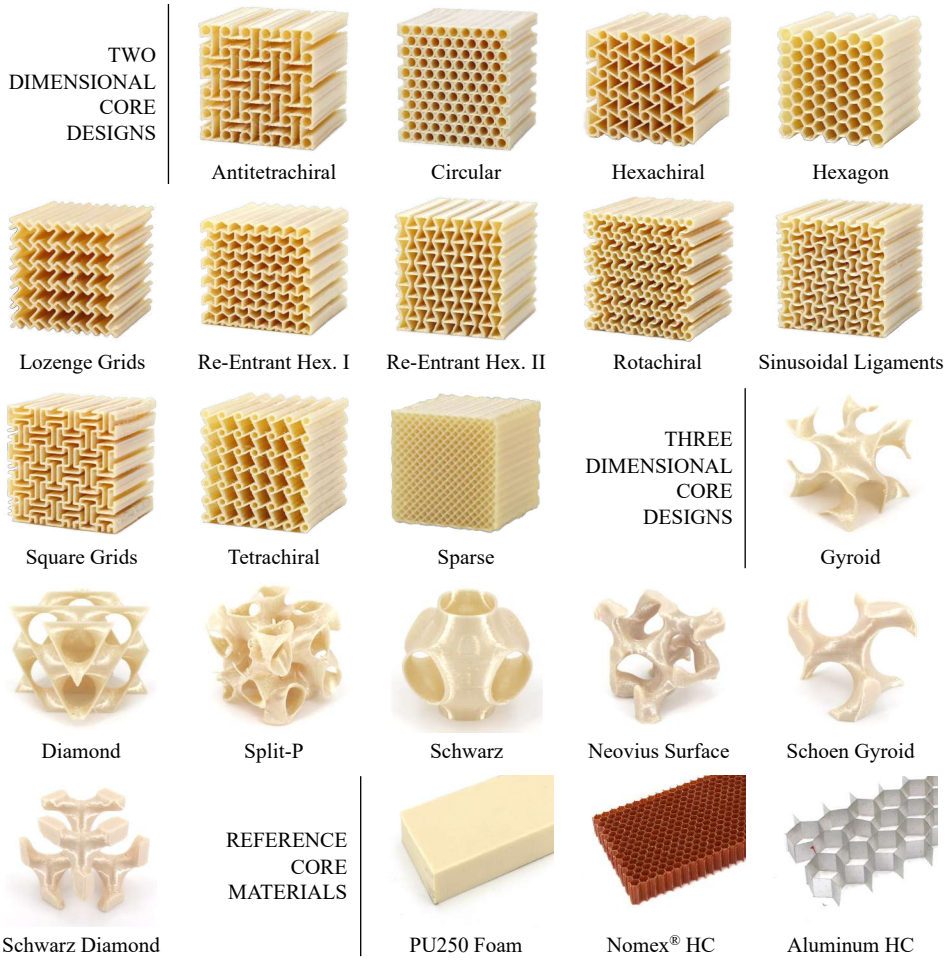

Figure 3.15: FFF two- and three-dimensional cellular core designs considered for the consolidation of the hybrid sandwich panels. Classical core materials were included as reference configurations.

A parametric static structural analysis was developed to assess the role of the additively manufactured core design and density on the three-point bending performance of hybrid sandwich structures, considering multiple combinations of core (c) and face (t) thicknesses. In all cases, the total height of the panel (d) and the bending span (L) were kept fixed at 20.572 mm and 150 mm, respectively.

The FE model was simplified into a quarter of the panel to reduce calculation time and computation resource consumption. To do so, two frictionless support boundary conditions were defined in order to designate the xz and yz symmetry planes. SOLID186 element type was employed to generate the mesh of the whole sandwich panel. In particular, both the core and the skins were each divided into 50, 8, and 8 elements along the x, y, and z-axis, respectively.

Finally, a remote displacement of 1 mm was applied at the center of the top CFRP skin of the sandwich panel, coinciding with the yz-symmetry plane. Then, the z-axis reaction force that appeared on this boundary condition was determined to evaluate the stiffness of each sandwich structure.

Table 3.5: CFRP elastic properties used in the FE model. [212]

CFRP elastic properties		
Property	Symbol	Value
Young's modulus *x*-direction (MPa)	E_{f_x}	119300
Young's modulus *y*-direction (MPa)	E_{f_y}	8200
Young's modulus *z*-direction (MPa)	E_{z_z}	8200
Poisson's ratio *xy*	$\nu_{f}^{s}{}_{xy}$	0.1
Poisson's ratio *yz*	$\nu_{f}^{s}{}_{yz}$	0.34
Poisson's ratio *xz*	$\nu_{f}^{s}{}_{xz}$	0.1
Shear modulus *xy* (MPa)	$G_{f}^{s}{}_{xy}$	59059
Shear modulus *yz* (MPa)	$G_{f}^{s}{}_{yz}$	3600
Shear modulus *xz* (MPa)	$G_{f}^{s}{}_{xz}$	59059

In order to validate the accuracy of the developed FE model, the analytical expression (Eq. 3.36) proposed by Ashby [3] was employed to evaluate the equivalent flexural modulus ($\tilde{E}_{flex}$) of sandwich panels. Accordingly, a perfectly bonded contact was assumed between the sandwich faces and core, and round bending test supports were employed, with a frictionless contact between them and the bottom sandwich CFRP face. The Augmented Lagrange formulation was activated with a penetration tolerance of 1E-5 mm and an FKN value of 0.01, as it is recommended for bending test simulations.

$$\frac{1}{\tilde{E}_{flex}} = \frac{1}{E_f\left[\left(1-(1-f)^3\right)+\dfrac{E_c}{E_f}(1-f)^3\right]} + \frac{B_1}{B_2}\left(\frac{d}{L}\right)^2\frac{(1-f)}{12G_c} \tag{3.36}$$

where: $B_1 = 48$ and $B_2 = 4$ for three-point bending with central load configuration

$f = 2t/d$ is the volume fraction of the nominal cross-section occupied by its faces

E_f is the elastic modulus of the sandwich faces considered isotropic

E_c and G_c are the elastic and shear moduli of the sandwich cores considered isotropic

3.3.3 Manufacturing of the cellular core designs

The optimal configurations of each simulated cellular design were fabricated to experimentally validate the bending performance of the hybrid sandwich structures. In order to obtain a total height of the sandwich panels (d) of 20.572 mm, and regarding the dimensions of a standard specimen according to ASTM C393 [211] and the thickness (t) of the cured CFRP prepreg material selected for fabricating the CFRP skins (see Section 3.3.4), the resulting core dimensions were $200 \times 75 \times 20.5$ mm. Cellular cores were designed, using SolidWorks and TPMSgen software [1], considering three different densities for each two-dimensional and three-dimensional pattern selected (see Figure 3.15).

The experimental test specimens were produced using Ultem material in a Stratasys Fortus 400mc FFF professional equipment, following the recommended operating conditions provided by the manufacturer (see Section 3.1.2). G-code was automatically generated employing the official Insight slicer software provided by the printer's manufacturer. Employing the same printing configuration that was used in the second stage of this research where the performance of the cellular solids was addressed, the slice height for fabricating all the core samples was set at 0.254 mm.

Two-dimensional cellular patterns were created with a nominal wall-thickness of just one contour (0.508 mm) aiming to exploit the possibilities of the FFF technology to fabricate cores as light as possible. On the other hand, just the Solid $\pm 45^{o}$ infill configuration was considered this time to fabricate the three-dimensional cellular designs except for Shell-TPMS designs, which were manufactured with a constant wall thickness of 2 contours (1.016 mm).

3.3.4 Curing of skins and sandiwch consolidation

Unidirectional MTC510 carbon fiber prepreg (MTC510-UD300-HS-33%RW 24K) was used for the fabrication of the sandwich panel skins. For this purpose, the coil of the original material was cut according to the core dimensions set for the study (200×75 mm) using an aluminum plate as a cutting template. In all cases, and according to the results of the numerical approach, the skins were manufactured using a single layer of fiber. Then, the CFRP prepreg offcuts were placed on a 1000×340 mm glass tray in order to be cured in different batches, whose surface was previously treated with a cleaning agent [213], a sealant [214] and a release agent [215] before each batch.

Up to 18 skins could be placed in each tray at a time. These were covered with a bleed film and an absorption blanket. The set was placed in a vacuum bag. The back pressure applied to the bag (-0.90 bar) was achieved with a vacuum pump. Removing the air from inside the bag, it compresses the skins against the glass to achieve a mirror finish, and against the blanket on the other side.

After verifying that the vacuum method worked properly, the set was introduced in an OV301 Precision Benchtop Curing oven. This temperature-controlled equipment was implemented to cure the CFRP skins, following the curing ramp recommended by the prepreg manufacturer (see Table 3.6 and Figure 3.16). Once the curing process was completed, the sandwich skins could be easily separated from the glass surface.

Table 3.6: Sandwich prepreg curing ramp.

Prepreg curing ramp						
	Start	Heating	Curing	Post-curing	Cooling	Total
Stage time (min)	-	33.3	60	60	40	193.3
Set point (°C)	20	120	120	120	20	-
Temperature slope (°C/min)	-	3	-	-	-2.5	-

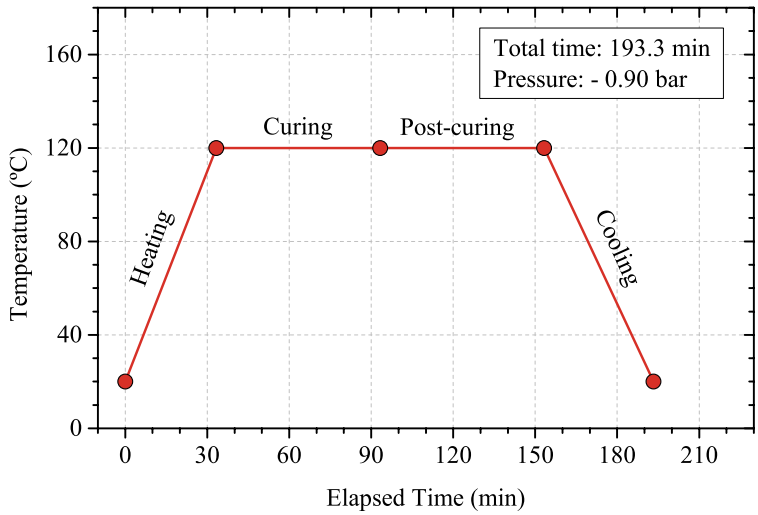

Figure 3.16: Graphical representation of the sandwich prepreg curing ramp.

Finally, the assembly of the additively manufactured cellular cores and the CFRP skins was completed with the consolidation of the sandwich structures. For this, the selected adhesive film MTFA500[216] was cut according to specimen dimensions, following the same procedure detailed above for the CFRP prepreg. Then, the assemblies were prepared by placing a sheet of adhesive between each skin and the cellular core.

With the purpose of consolidating the union between faces and core, the adhesive had to be properly cured by applying the required pressure (-0.45 bar) and temperature (see Table 3.7 and Figure 3.17) provided by the manufacturer. Again, the same glass tray was used to cure a total of 18 samples at a time. In this case, a rectangular polytetrafluoroethylene (PTFE) plate of slightly larger dimensions than the specimen ones was placed over each of the sandwich panels in order to apply uniform compression on each sample and, at the same time, prevent the CFRP skins from puncturing the vacuum bag. When the curing curve was completed, the samples were removed from the oven, and the consolidated hybrid sandwich structures were obtained.

Table 3.7: Sandwich adhesive curing ramp.

Adhesive curing ramp						
	Start	Heating	Curing	Post-curing	Cooling	Total
Stage time (min)	-	50	60	60	40	210
Set point (°C)	20	120	120	120	20	-
Temperature slope (°C/min)	-	2	-	-	-2.5	-

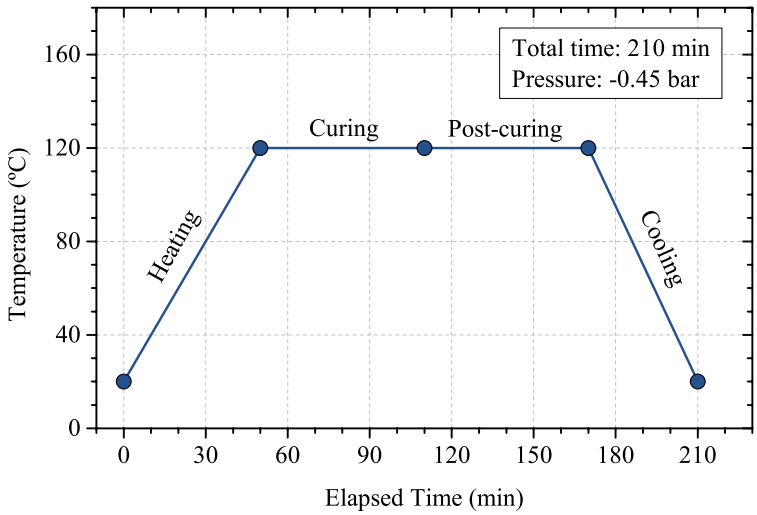

Figure 3.17: Graphical representation of the sandwich adhesive curing ramp.

Figure 3.18 depicts a perspective view of a consolidated sample of a sandwich panel with two outer skins made of CFRP and an additively manufactured cellular lightweight core fabricated using FFF technology. In this case, the employed core design corresponds to the Schwarz three-dimensional pattern.

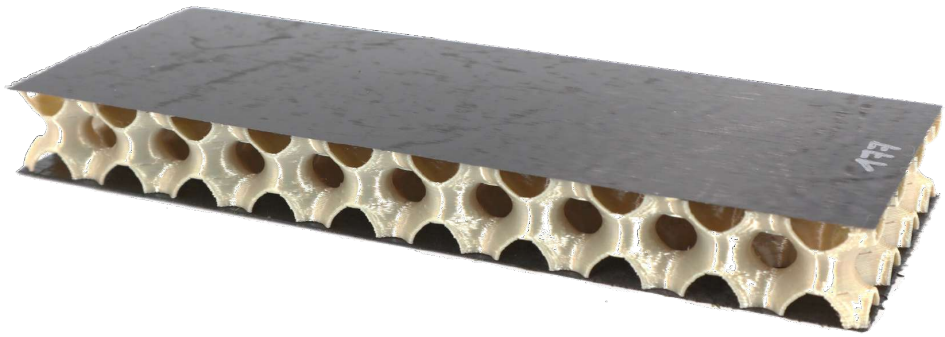

Figure 3.18: Representative sample of a consolidated sandwich panel composed of CFRP skins and an additively manufactured cellular core, corresponding to the Schwarz three-dimensional pattern.

3.3.5 Three-point bending testing

The bending performance of the optimum sandwich panels was experimentally validated. To do so, three-point bending tests were conducted using a ZwickRoell Z030 30 kN equipment. According to the ASTM C393 standard [211] and employing the midspan loading configuration, the distance between the centerlines of the testing support bars (L) was adjusted to 150 mm. A crosshead rate of 6 mm/min was employed, which ensured that failure occurred within 3 to 6 minutes in all cases. The deflection

at the center of the specimen was measured with a laser displacement sensor. The results for elastic modulus and maximum stress prior to first failure (FF) were reported, considering the specimen's nominal external dimensions for stress calculations. Experimental elastic moduli were extracted from test data between 0.1% and 0.3% of bending strain through linear regression. Furthermore, the ultimate failure mode was reported for each test according to the standard identification codes presented in Table 3.8:

Table 3.8: Ultimate failure modes for sandwich panels tested under three-point bending.

Failure identification codes					
First character		Second character		Third character	
Failure Type	Code	Failure Type	Code	Failure Type	Code
Core crushing	C	At load bar	A	Core	C
Skin to core delamination	D	Gage	G	Core-facing bond	A
Facing failure	F	Multiple areas	M	Bottom facing	B
Multi-mode	M(xyz)	Outside gage	O	Top facing	T
Transverse shear	S	Various	V	Both facings	F
Explosive	X	Unknown	U	Various	V
Other	O			Unknown	U

Finally, Figure 3.19 depicts the employed setup for conducting the three-point bending tests of the hybrid sandwich panels. As can be seen, rubber pads were added between the tooling supports and the CFRP faces of the specimen to avoid undesired failure modes.

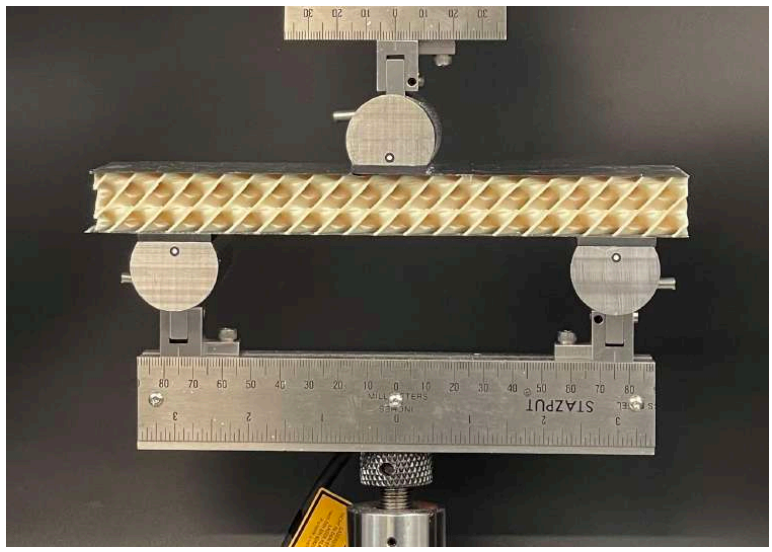

Figure 3.19: Experimental setup for conducting the bending tests of the sandwich structures, corresponding to the sample with the Diamond three-dimensional core design.

4

Results and discussion

This chapter includes a general discussion of the main results derived from the research plan that has been designed and explained throughout the previous pages, regarding the characterization of material processed by FFF technology, cellular solids and hybrid sandwich structures. The chapter culminates with a summary and an overview of the most relevant results of the thesis.

This thesis aims to provide a highly efficient structural solution, based on the advances that the discovery of sandwich structures has made during the last decades, by exploiting the potential of bio-inspired cellular solids, whose fabrication is now feasible through the use of advanced AM technologies.

To analyze the developed solution in detail and ensure its functionality, this challenge has been addressed at three different levels. Firstly, a complete characterization study of the high-performance material (Ultem) processed by FFF has been carried out, taking into account the impact of the main printing parameters of this technology on the degree of anisotropy of the manufactured components. Secondly, the mechanical behavior under compression of thirteen two-dimensional and twenty three-dimensional cellular designs has been validated analytically, numerically and experimentally. Finally, the potential of bio-inspired cellular solids as lightweight cores for the fabrication of efficient hybrid sandwich structures has been demonstrated, while pointing out some limitations of the AM technology used.

The results of each issue addressed are presented as a separate subsection in the following pages.

4.1 Material characterization

In order to determine the mechanical properties of the material selected for the present investigation (Ultem) once processed by FFF, a total of three solid and three sparse infill configurations have been analyzed. Regarding the former, the classic solid $\pm 45^{\circ}$ infill was considered, as well as two completely unidirectional configurations: 0°, with rasters aligned along the x-axis; and 90°, with rasters aligned along the y-axis. As for the latter, the three air gap levels selected for this research were 0.25 mm, 0.50 mm, and 0.75 mm.

Figure 4.1 demonstrates the impact of implementing the sparse infill configuration on the total manufacturing time and material volume, estimated by the official slicer Insight software, required for the fabrication of a cube of side length c. According to the calculated results, the implementation of the sparse pattern would allow savings of up to 60% in lead time and material costs compared to the reference solid infill configurations.

However, the fabrication of functional parts, such as the ones to be achieved at the end of the present thesis, requires comprehending the mechanical performance of the deposited material. Therefore, knowing the advantages that the sparse infill can bring from a manufacturing standpoint, it is essential to quantify the impact it has on the mechanical performance of the fabricated parts. In this sense, the mechanical behavior and structural efficiency of the chosen FFF infill configuration will be conditioned by the orientation of the printed rasters, the quantity and quality of the existing material bonds, and the amount of material used.

In order to analyze all these aspects, which directly depend on the printing parameters employed, standardized Ultem specimens were manufactured and characterized under tensile, bending and shear stresses, considering the six described solid and sparse infill configurations. Images depicted in

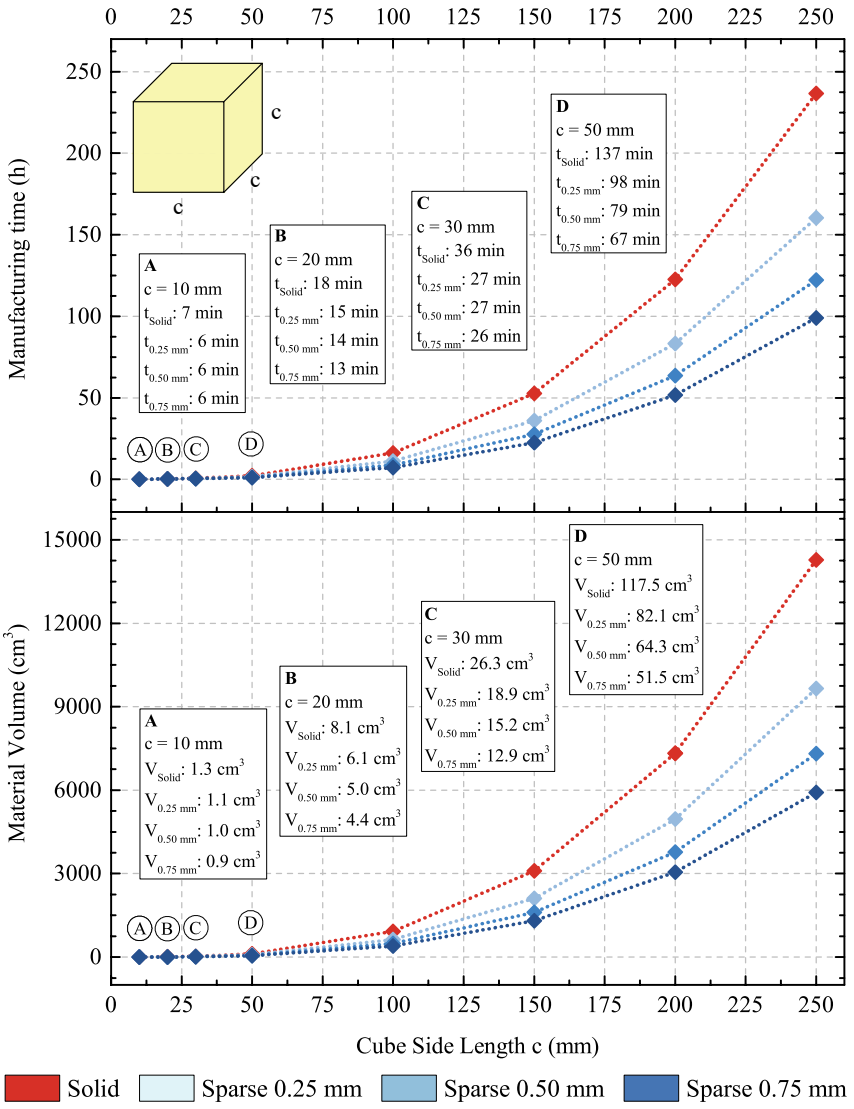

Figure 4.1: Impact of the raster-to-raster air gap parameter on the manufacturing time (*top*) and the material volume (*bottom*) of a FFF Ultem cube part, depending on its side length.

Figure 4.2, which were obtained from the digital image analysis of the tensile test samples, exemplify how the resistant cross-section (6×4 mm^2) of the fabricated specimens is in some cases significantly reduced with the use of high air gap values. This effect is minor in Flat printed samples, as their effective cross-section is orientated perpendicularly to the building direction of the sparse structure.

The stress-strain curves shown in Figure 4.3 are representative data extracted from all the experimental tests conducted (see Table 4.1). Confirming the above, these results are clear evidence of the impact that both the printing orientation and the infill configuration selected for the fabrication of the samples have on the elastoplastic properties of Ultem FFF parts.

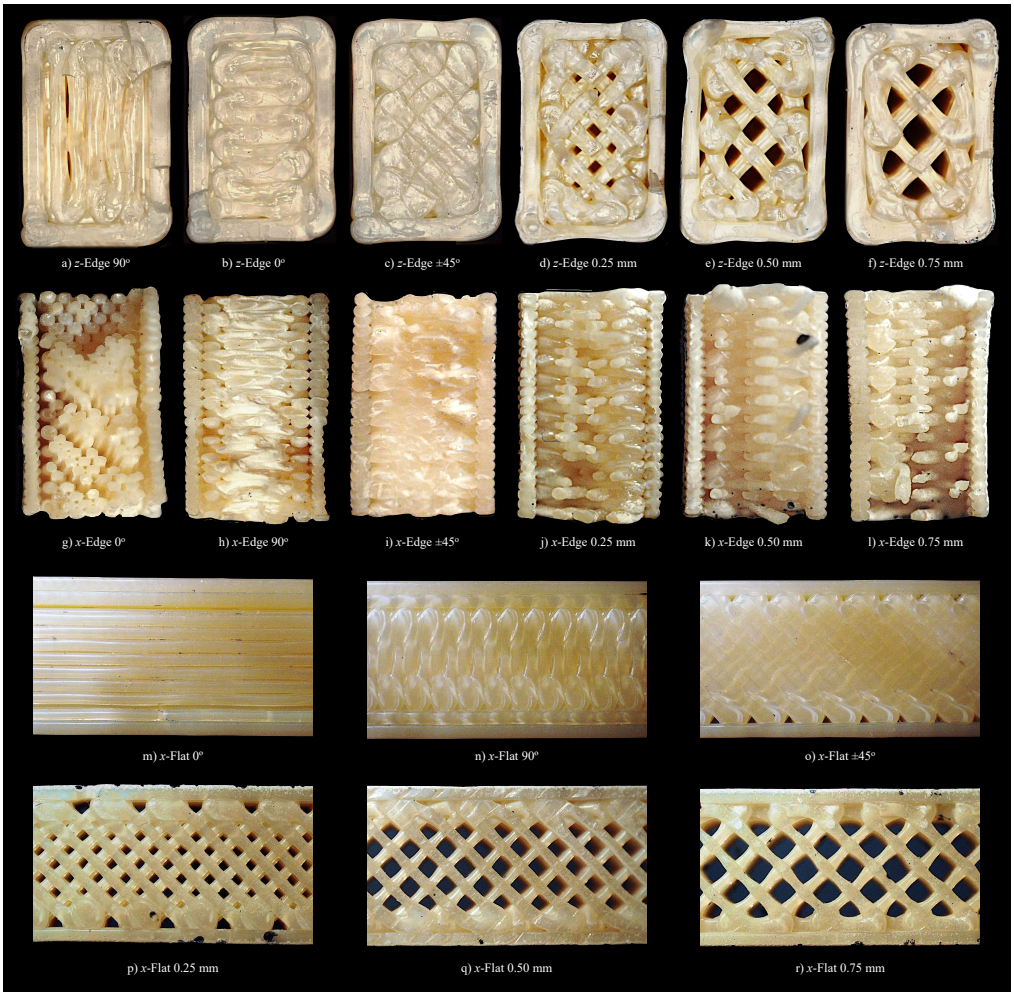

Figure 4.2: Effective cross-sectional area (6 mm × 4 mm) (*a-l*) and front surface (*m-r*) of tensile samples employing solid and sparse infill configurations.

The employed professional FFF printer is equipped with a thermal chamber that aims to reduce the temperature gradient between the filament being deposited and the built part to strengthen raster bonds, improve mechanical performance, and reduce orthotropy. However, experimental results presented in Table 4.1 demonstrate that a certain degree of anisotropy in the elastic properties of the material exists. To understand the reason for this phenomenon, the deposited material rasters together with the presence and orientation of filament bonds within each layer (intra-layer) and between adjacent layers (inter-layer) should be considered. The results of this part of the thesis confirm that the maximum stiffness can be achieved by depositing the material filaments aligned with the stress direction, as expected. Moreover, the cohesion of the inter-layer bonds is much weaker than that of the intra-layer ones, since the elapsed time for the formation of the former is much longer than that of the latter, causing a greater cooling of the last built layer, which deteriorates the quality of the bond that is formed (see Figure 4.4).

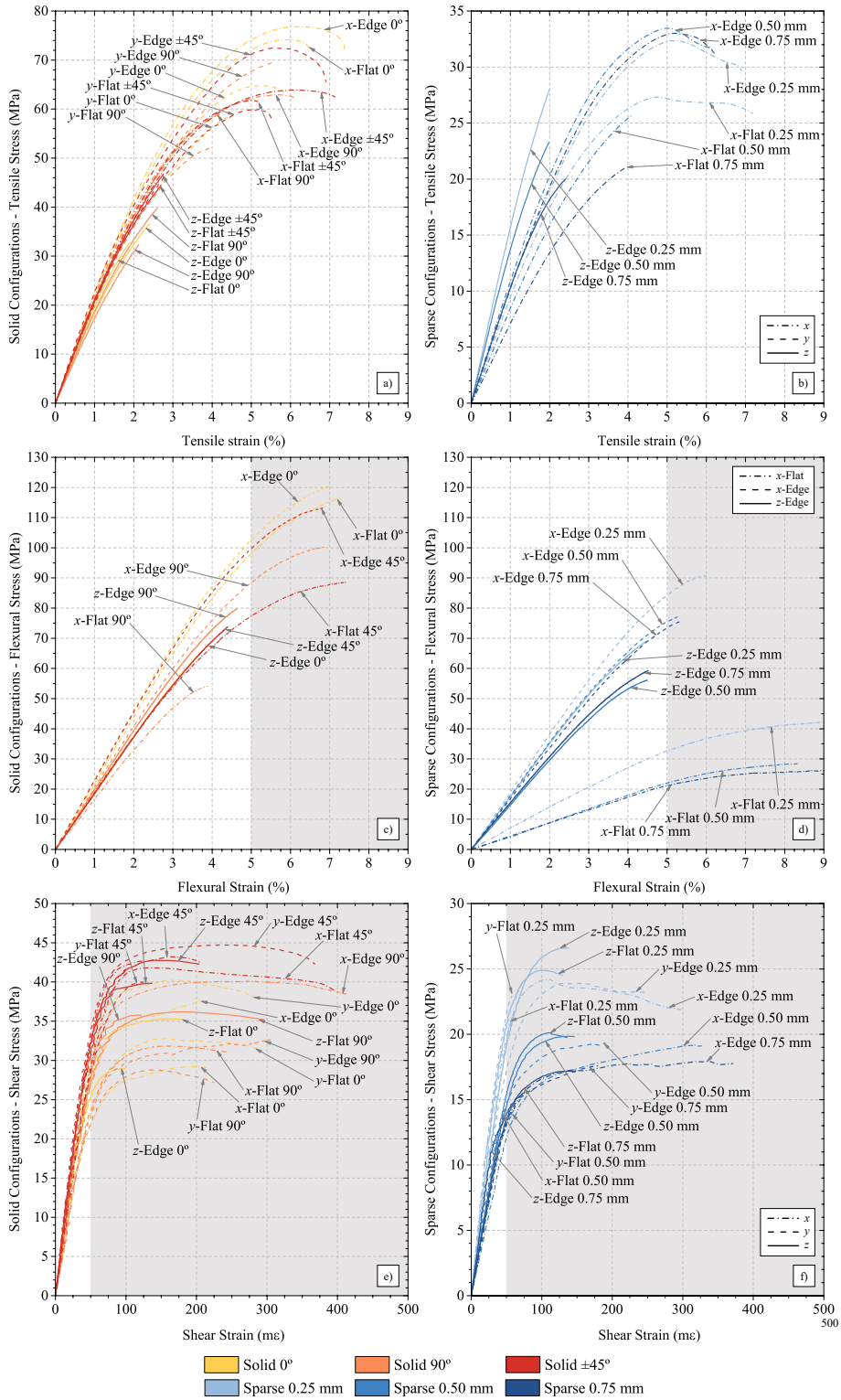

Figure 4.3: Representative stress-strain data from the tensile (*a-b*), flexural (*c-d*), and shear (*e-f*) tests of solid (*left*) and sparse (*right*) infill configurations according to the considered printing orientations.

Table 4.1: Engineering constants of Ultem processed by FFF regarding the chosen infill configuration.

Test	Engineering constant	Solid configuration			Sparse configuration		
		0°	90°	±45°	0.25 mm	0.50 mm	0.75 mm
Tensile	E_x (MPa)	2242 ±79	2100 ±160	2092 ±108	978 ±48	969 ±119	870 ±183
	E_y (MPa)	2069 ±168	2113 ±74	2150 ±198	(978) (±48)	(969) (±119)	(870) (±183)
	E_z (MPa)	1935 ±67	1879 ±133	2126 ±61	1612 ±159	1329 ±65	1056 ±73
	ν_{xy}	0.351 ±0.037	0.328 ±0.047	0.344 ±0.007	0.436 ±0.024	0.546 ±0.085	0.505 ±0.071
	ν_{yx}	N/A	N/A	N/A	N/A	N/A	N/A
	ν_{xz}	0.367 ±0.042	0.387 ±0.053	0.392 ±0.002	0.289 ±0.044	0.388 ±0.087	0.363 ±0.017
	ν_{zx}	0.297 ±0.008	0.083 ±0.083	0.348 ±0.029	N/A	N/A	N/A
	ν_{yz}	N/A	0.352 ±0.029	N/A	N/A	N/A	N/A
	ν_{zy}	N/A	N/A	N/A	0.281 ±0.056	0.276 ±0.023	0.241 ±0.076
Flexural	E_{x-Flat} (MPa)	2260 ±7	1847 ±16	1942 ±3	726 ±11	487 ±4	468 ±4
	E_{x-Edge} (MPa)	2360 ±10	2112 ±10	2299 ±13	1809 ±143	1788 ±12	1548 ±57
	E_{z-Edge} (MPa)	1950 ±49	2073 ±7	1979 ±22	1809 ±22	1512 ±30	1554 ±16
Shear	G_{xy} (MPa)	529 ±41	551 ±76	630 ±81	452 ±18	310 ±10	N/A
	G_{xz} (MPa)	652 ±47	646 ±84	737 ±92	403 ±35	284 ±12	266 ±45
	G_{yz} (MPa)	629 ±29	566 ±44	745 ±89	397 ±38	291 ±31	260 ±20

Furthermore, reducing the weight of FFF components by implementing the sparse infill configuration also leads to a significant decrease in their stiffness, especially when the parts are subjected to tensile or shear stresses. However, there is a possibility that such configurations may be more efficient than the solid ones when the achieved mass reduction is considered in each case. To answer this question, the specific mechanical properties have been determined, by calculating the ratio between the corresponding value over the mass of each tested specimen. Hence, the following Figures 4.5 and 4.6 depict the specific properties determined with the tensile, flexural, and shear characterization tests of the Ultem samples, whose average value has been calculated considering each printing orientation and infill configuration, as well as the associated standard deviation.

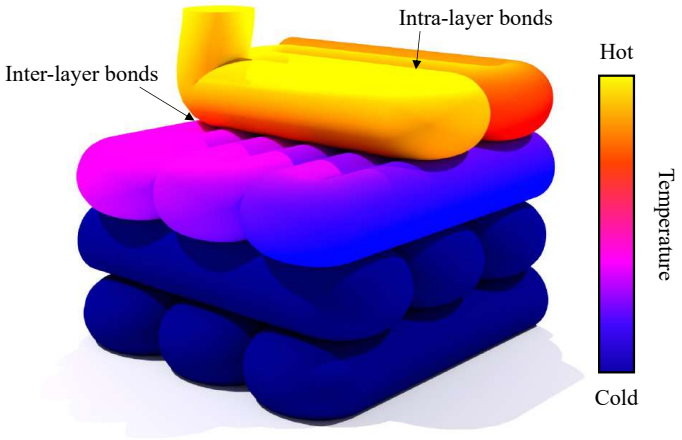

Figure 4.4: Representation of the temperature state of the deposited filament and the formation of intra- and inter-layer bonds during the FFF printing process.

On the one hand, the specific results of tensile, flexural and shear moduli prove that the solid configurations are slightly more efficient than the sparse ones in terms of stiffness since the former reached higher values in the majority of testing orientations. However, the performance of both infill configurations is very similar in terms of specific yield stress and maximum strength, being slightly favorable for the latter. In any case, the specific elongations presented by the sparse infill configurations are significantly larger, as the elimination of the intra-layer bonds allows greater movement and stretching of the filament rasters before yielding and failure.

All of the above results are empirical evidence of how the primary printing parameters, which influence the material deposition paths of FFF, impact the mechanical behavior and anisotropy of the components produced by this AM technology. Finally, the orthotropic compliance matrix S corresponding to each of the 6 infill configurations analyzed is provided in Figure 4.7, whose coefficients were calculated from the engineering constants presented in Table 4.1 as follows:

$$\boldsymbol{\varepsilon} = \boldsymbol{S} \cdot \boldsymbol{\sigma}$$

$$\begin{bmatrix} \varepsilon_x \\ \varepsilon_y \\ \varepsilon_z \\ \gamma_{yz} \\ \gamma_{xz} \\ \gamma_{xy} \end{bmatrix} = \begin{bmatrix} \frac{1}{E_x} & -\frac{\nu_{yx}}{E_y} & -\frac{\nu_{zx}}{E_z} & 0 & 0 & 0 \\ -\frac{\nu_{xy}}{E_x} & \frac{1}{E_y} & -\frac{\nu_{zy}}{E_z} & 0 & 0 & 0 \\ -\frac{\nu_{xz}}{E_x} & -\frac{\nu_{yz}}{E_y} & \frac{1}{E_z} & 0 & 0 & 0 \\ 0 & 0 & 0 & \frac{1}{G_{yz}} & 0 & 0 \\ 0 & 0 & 0 & 0 & \frac{1}{G_{xz}} & 0 \\ 0 & 0 & 0 & 0 & 0 & \frac{1}{G_{xy}} \end{bmatrix} \cdot \begin{bmatrix} \sigma_x \\ \sigma_y \\ \sigma_z \\ \tau_{yz} \\ \tau_{xz} \\ \tau_{xy} \end{bmatrix} \tag{4.1}$$

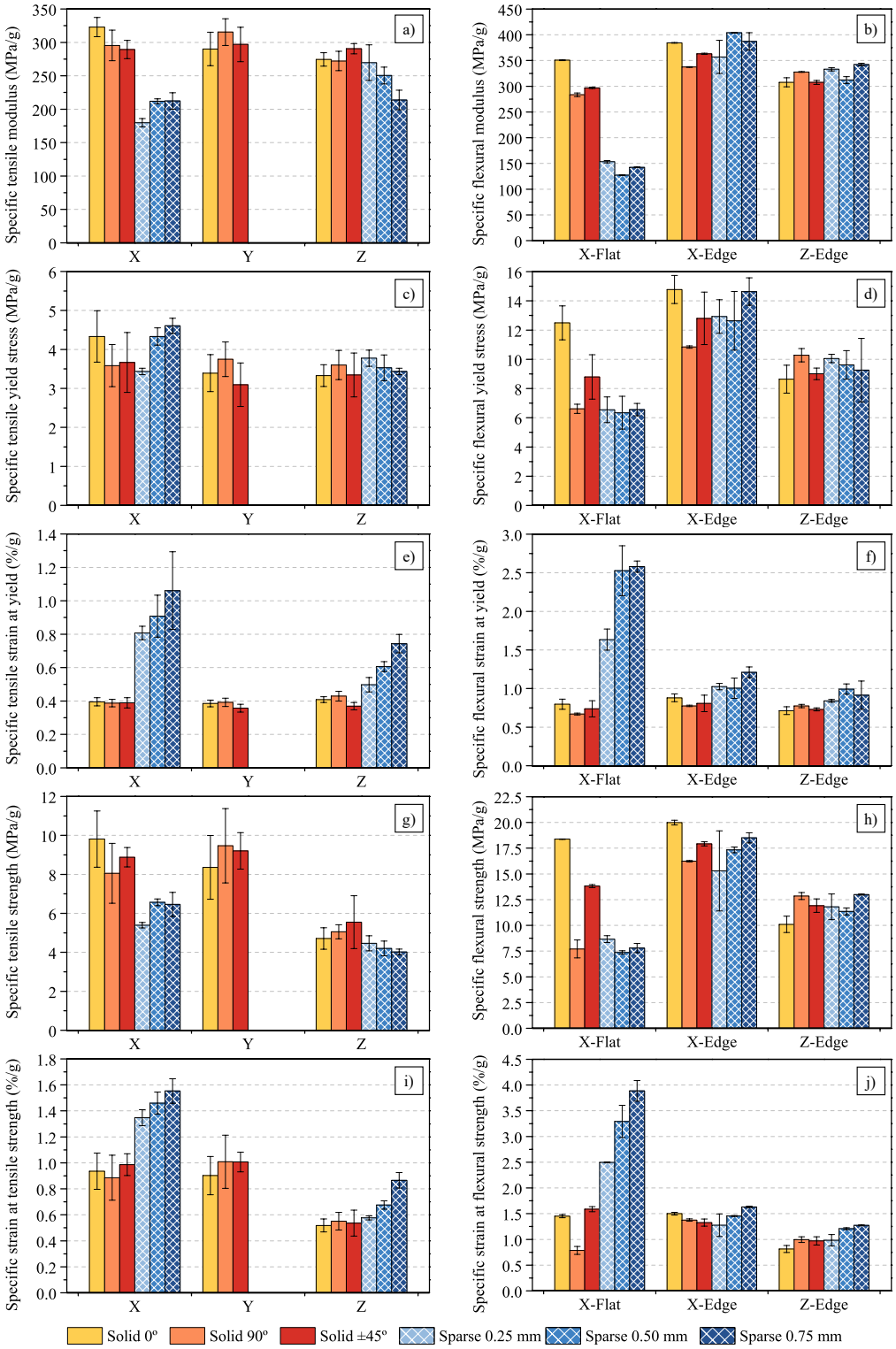

Figure 4.5: Specific tensile/flexural test results comparison between solid and sparse infill configurations: modulus (*a*/*b*), yield stress (*c*/*d*), strain at yield (*e*/*f*), strength (*g*/*h*), and strain at strength (*i*/*j*).

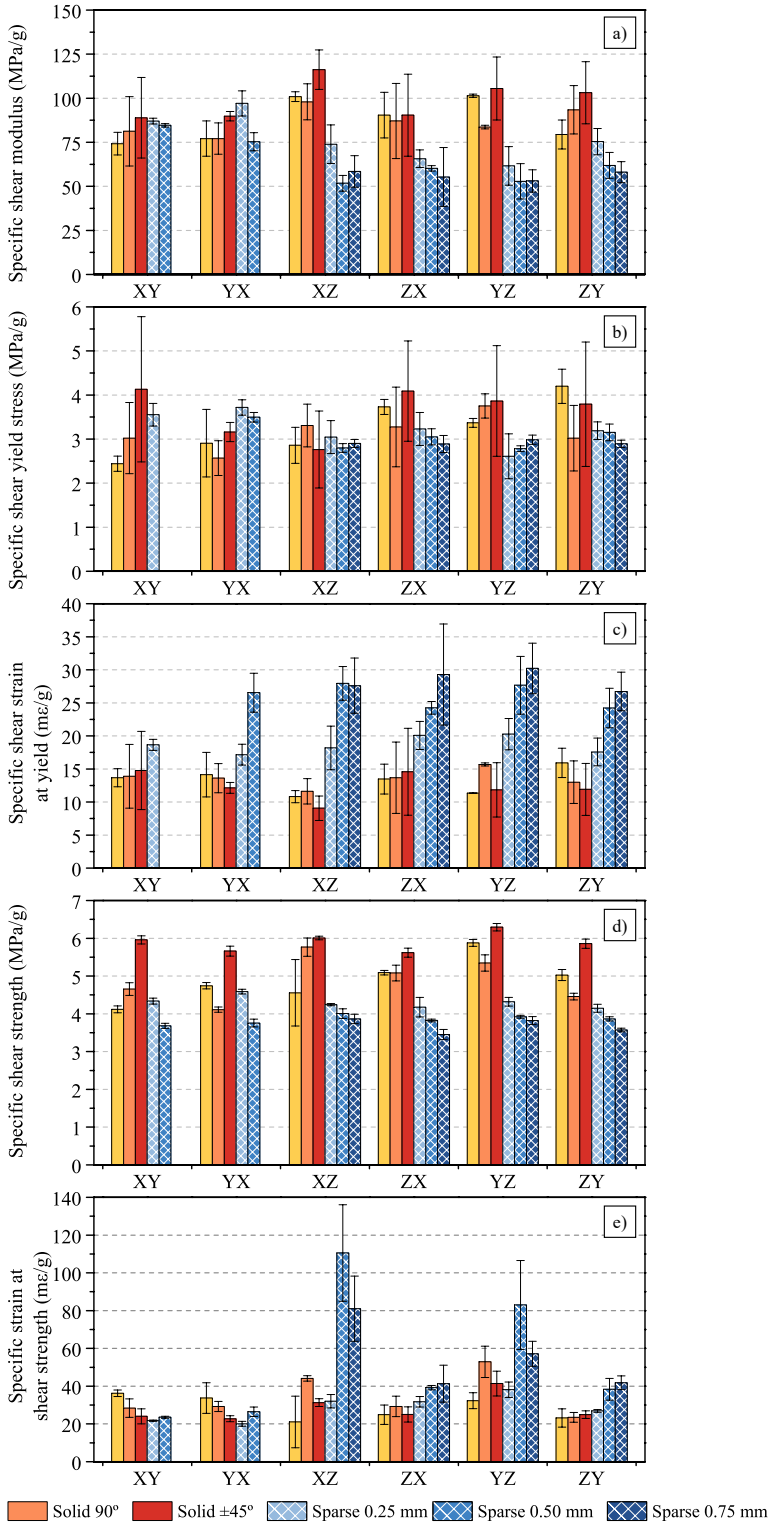

Figure 4.6: Specific shear test results comparison between solid and sparse infill configurations: shear modulus (*a*), shear yield stress (*b*), shear strain at yield (*c*), shear strength (*d*), and strain at shear strength (*e*).

Compliance matrix S in GPa^{-1} for solid 0° configuration

$$\begin{bmatrix} 0.446 \pm 0.016 & -0.156 \pm 0.018 & -0.158 \pm 0.020 & 0 & 0 & 0 \\ & 0.483 \pm 0.039 & \text{N/A} & 0 & 0 & 0 \\ & & 0.517 \pm 0.018 & 0 & 0 & 0 \\ & & & 1.589 \pm 0.073 & 0 & 0 \\ & \text{Sym.} & & & 1.534 \pm 0.109 & 0 \\ & & & & & 1.891 \pm 0.148 \end{bmatrix}$$

Compliance matrix S in GPa^{-1} for sparse 0.25 mm configuration

$$\begin{bmatrix} 1.023 \pm 0.050 & -0.446 \pm 0.033 & -0.305 \pm 0.048 & 0 & 0 & 0 \\ & 1.023 \pm 0.050 & -0.174 \pm 0.039 & 0 & 0 & 0 \\ & & 0.621 \pm 0.061 & 0 & 0 & 0 \\ & & & 2.521 \pm 0.240 & 0 & 0 \\ & \text{Sym.} & & & 2.479 \pm 0.214 & 0 \\ & & & & & 2.212 \pm 0.089 \end{bmatrix}$$

Compliance matrix S in GPa^{-1} for solid 90° configuration

$$\begin{bmatrix} 0.476 \pm 0.036 & -0.156 \pm 0.025 & -0.196 \pm 0.043 & 0 & 0 & 0 \\ & 0.473 \pm 0.017 & -0.167 \pm 0.015 & 0 & 0 & 0 \\ & & 0.532 \pm 0.038 & 0 & 0 & 0 \\ & & & 1.768 \pm 0.136 & 0 & 0 \\ & \text{Sym.} & & & 1.549 \pm 0.203 & 0 \\ & & & & & 1.816 \pm 0.251 \end{bmatrix}$$

Compliance matrix S in GPa^{-1} for sparse 0.50 mm configuration

$$\begin{bmatrix} 1.032 \pm 0.127 & -0.582 \pm 0.113 & -0.401 \pm 0.102 & 0 & 0 & 0 \\ & 1.032 \pm 0.127 & -0.208 \pm 0.020 & 0 & 0 & 0 \\ & & 0.753 \pm 0.037 & 0 & 0 & 0 \\ & & & 3.432 \pm 0.369 & 0 & 0 \\ & \text{Sym.} & & & 3.522 \pm 0.147 & 0 \\ & & & & & 3.224 \pm 0.108 \end{bmatrix}$$

Compliance matrix S in GPa^{-1} for solid ±45° configuration

$$\begin{bmatrix} 0.478 \pm 0.025 & -0.164 \pm 0.009 & -0.175 \pm 0.017 & 0 & 0 & 0 \\ & 0.465 \pm 0.043 & \text{N/A} & 0 & 0 & 0 \\ & & 0.470 \pm 0.013 & 0 & 0 & 0 \\ & & & 1.342 \pm 0.160 & 0 & 0 \\ & \text{Sym.} & & & 1.356 \pm 0.169 & 0 \\ & & & & & 1.587 \pm 0.203 \end{bmatrix}$$

Compliance matrix S in GPa^{-1} for sparse 0.75 mm configuration

$$\begin{bmatrix} 1.149 \pm 0.242 & -0.581 \pm 0.147 & -0.418 \pm 0.090 & 0 & 0 & 0 \\ & 1.149 \pm 0.242 & -0.228 \pm 0.074 & 0 & 0 & 0 \\ & & 0.947 \pm 0.065 & 0 & 0 & 0 \\ & & & 3.845 \pm 0.299 & 0 & 0 \\ & \text{Sym.} & & & 3.764 \pm 0.636 & 0 \\ & & & & & \text{N/A} \end{bmatrix}$$

Figure 4.7: Compliance matrices describing the orthotropic elastic behavior of Ultem processed by FFF with solid 0°, 90°, and ±45° and sparse 0.25 mm, 0.50 mm, and 0.75 mm infill configurations.

As will be demonstrated in the following sections, the experimentally determined compliance matrices with different FFF infill configurations are very valuable, as they can be directly implemented in FE models that aim to reproduce the orthotropic elastic behavior of Ultem components. Moreover, the standard methodology used and validated could be replicated to characterize any other polymeric, metallic or ceramic material processed by any AM technology, and implement the obtained results for the validation of forthcoming numerical models.

4.2 Cellular solids characterization

The aim of the second stage of the present investigation was to address the analysis of the mechanical performance of thirteen two-dimensional and twenty three-dimensional cellular solids fabricated with the same AM technology, focusing on how it is affected by the geometry, density, and arrangement of the cells. To this end, different analytical, numerical and experimental approaches were combined to validate the results presented.

4.2.1 Mechanical performance

Figure 4.8 summarizes the experimental results of elastic moduli, compression strength at FF, and energy absorption efficiency at FF obtained from the compression tests conducted with the two- and three-dimensional cellular solids. Specifically, charts *a*, *b* and *c* located in the left column of the panel depict the correlation between the mechanical properties exhibited by each design and its corresponding relative density. The same experimental values are compared to the amount of time required for the fabrication of each cellular specimen, whose nominal dimensions were $40 \times 40 \times 40$ mm, in graphs *d*, *e* and *f* on the right side of the figure. In each case, the designs belonging to the same cellular typology and testing direction have been bubble-wrapped in order to facilitate the comprehension and analysis of the data depicted.

Two-dimensional cellular solids display higher elastic moduli when tested perpendicularly to the building plane (out-of-plane) than the rest of the evaluated designs at the same values of relative density and manufacturing time, as expected. However, the in-plane stiffness is significantly compromised by their morphology. At the same time, the elastic moduli of the three-dimensional cellular solids cover the range between the above results, which positions them as an intermediate solution independent of the testing direction thanks to the symmetry in the 3D space that these designs exhibit.

Regarding the resulting dispersion when the experimental values from two-dimensional designs are plotted against the required manufacturing time, it proves that certain geometries compromise the feasibility of FFF technology. This aspect is caused by the fact that their cellular designs make it impossible to deposit the material in continuous trajectories on most occasions, requiring them to be built cell by cell. Although this phenomenon does not occur during the construction of the three-dimensional cellular solids, the depicted results show that the Shell-TPMS typologies are the most optimal to be fabricated by FFF since they did not require the incorporation of support structures, followed by the Skeletal-TPMS and the lattice.

Finally, the three-dimensional cellular designs considerably outperform the two-dimensional ones in terms of compression strength and energy absorption efficiency at FF. This aspect is directly related to the fragility of the latter caused by the large number of intra- and inter-layer bonds with limited quality that they possess, which can be analyzed in greater detail with the digital microscopy images presented in Figure 4.9.

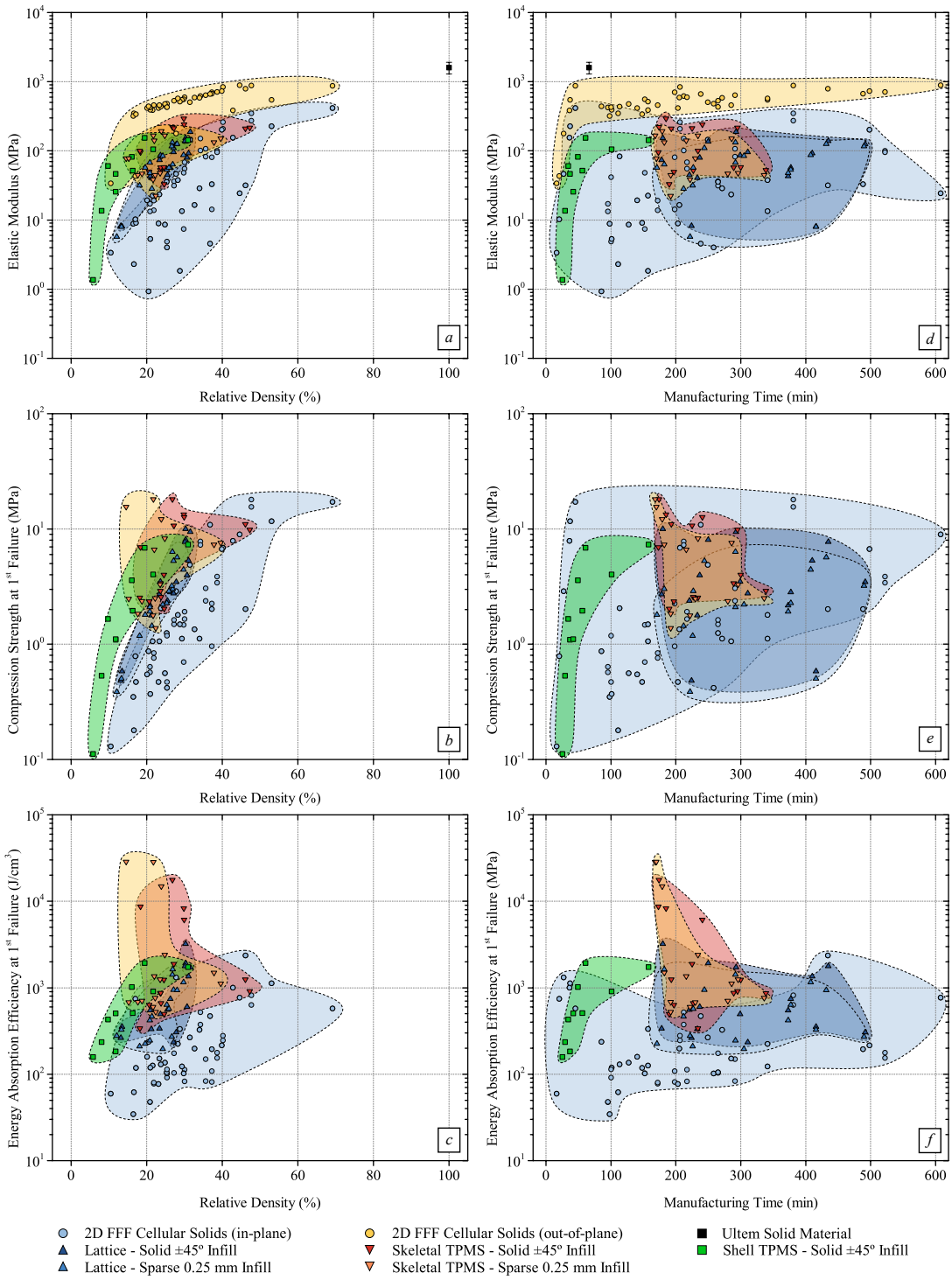

Figure 4.8: Experimental results of the elastic modulus (*a*, *d*), compression strength (*b*, *e*), and energy absorption efficiency (*c*, *f*) in terms of relative density and manufacturing time for each cellular solid.

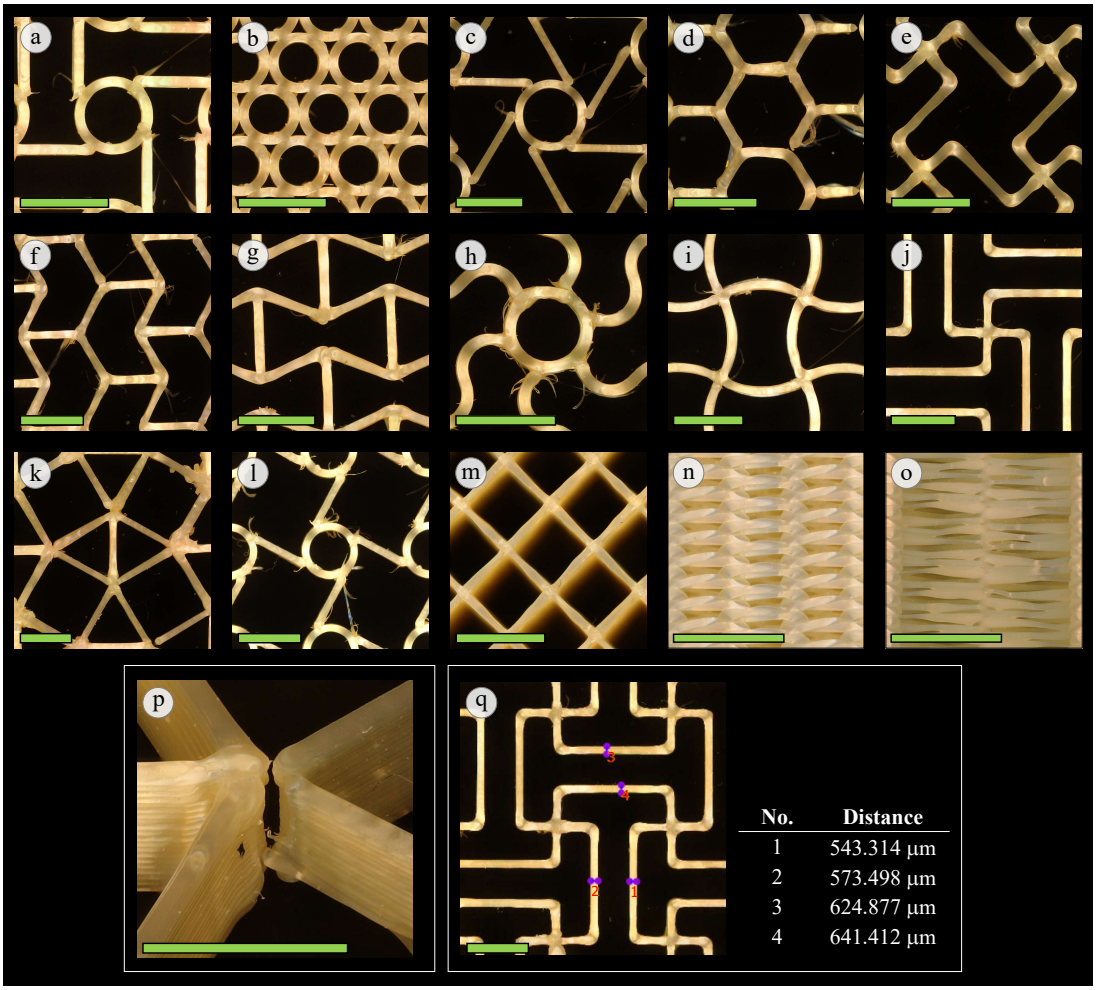

Figure 4.9: Microscopic detail of the intra-layer joints of Antitetrachiral (*a*), Circular (*b*), Hexachiral (*c*), Hexagon (*d*), Lozenge Grids (*e*), Re-Entrant Hexagon I (*f*), Re-Entrant Hexagon II (*g*), Rotachiral (*h*), Sinusoidal Ligaments (*i*), Square Grids (*j*), SrCuBO (*k*), Tetrachiral (*l*), Sparse in-plane (*m*) and out-of-plane (*n*-*o*) cellular solids, FFF inter-layer defects (*p*), and measurements of the thickness of the deposited rasters (*q*). The scale bar corresponds to 5 mm.

Images *a*-*m* depict the intra-layer bonds of the thirteen two-dimensional designs evaluated. As can be noticed, and despite using professional FFF equipment, the quality of both the deposited rasters and the filament bonds depends on the trajectories that were needed for the construction of the patterns. In cases where circles appear, the extruder head starts by creating the circles and then the bars that link them (see images *a*, *c*, *h*, and *l*). Consequently, the seam that occurs when closing each circumference is hardly noticeable, whereas the finish of the connections of the different cells is significantly worse.

Intra-layer bond imperfections are even more visible in patterns formed by rectilinear trajectories since they force the extruder head to repeatedly pass over the same point to build the whole pattern while leading to various material blobs (see image *k*). Additionally, the abrupt changes in the nozzle's direction or the end of the trajectory cause flaws in the bonding between cells, which directly compromises the

mechanical performance of the specimen. Conversely, the pattern's quality is substantially improved in those cases that benefit from optimized deposition paths, which favor the reduction of the amount of intra-layer connections as in the case of the Sparse design (see image *m*).

In addition, when successive in-plane imperfections arise in the same location for contiguous layers, an inter-layer defect emerges, as depicted in images *n-p*. This discontinuity has proved to dramatically impact the mechanical performance of the two-dimensional cellular design when it is tested in any of the in-plane directions, especially its compression strength and the corresponding energy absorption efficiency at FF. Finally, the inconsistent thickness of the deposited rasters (see image *q*) is also an important point to consider, as it would have a direct impact on the calculation of real stresses in lightweight samples manufactured with walls as thin as those analyzed.

The graphs in Figure 4.10 allow comparing the experimental results of elastic modulus (*top*) and strength (*bottom*) achieved by the two- and three-dimensional cellular solids tested (see Tables 4.2, 4.3, and 4.4) with the rest of the materials included in the Ansys GRANTA EduPack database considering their density. To simplify their analysis, the depicted points have been bubble-wrapped into 5 different categories according to the cellular typology and test orientation: Two-dimensional (in-plane and out-of-plane), Shell-TPMS, Skeletal-TPMS, and Lattice. Furthermore, the experimental results obtained from the mechanical characterization of Ultem specimens processed through FFF with the solid $\pm 45°$ infill configuration (100% of relative density) have also been represented in black square dots.

The performance of cellular solids fabricated in Ultem is contained in the range of foams and natural materials. Focusing on the top chart, both two- and three-dimensional designs display lower elastic modulus than the solid material reference as expected, attending to the fact that less material is used. Regarding the wide spectrum of the achieved results, the cellular design directly impacts the mechanical performance and density of the lightweight structure, as it was intended to demonstrate. In fact, starting from a solid material, and therefore a single point on the graph, these factors provide a way to control the mechanical and physical properties to cover a much larger area and suit the needs of each structural application. In addition, when two- and three-dimensional samples with similar densities are compared, the latter exhibit stiffnesses that place them between the in-plane and out-of-plane behaviors of the former. Specifically, while their elastic moduli are similar to the optimal out-of-plane orientation of two-dimensional cellular solids, their in-plane performance is improved by up to two orders of magnitude, being Shell-TPMS designs the most efficient patterns.

As can be noticed from the strength results presented in the bottom graph, the compression strength of three-dimensional designs is significantly higher than the in-plane strength of two-dimensional cellular solids at resembling values of density. This result can be explained by the fact that the three-dimensional geometries are mostly stretch-dominated, while the two-dimensional cellular solids tend to be bending-dominated. Additionally, the manufacturing imperfections that were previously reported in Figure 4.9 create discontinuities in the cell-wall bonds, which have dramatic consequences on the performance of two-dimensional cellular solids. In contrast, three-dimensional cell patterns are less susceptible to these manufacturing defects.

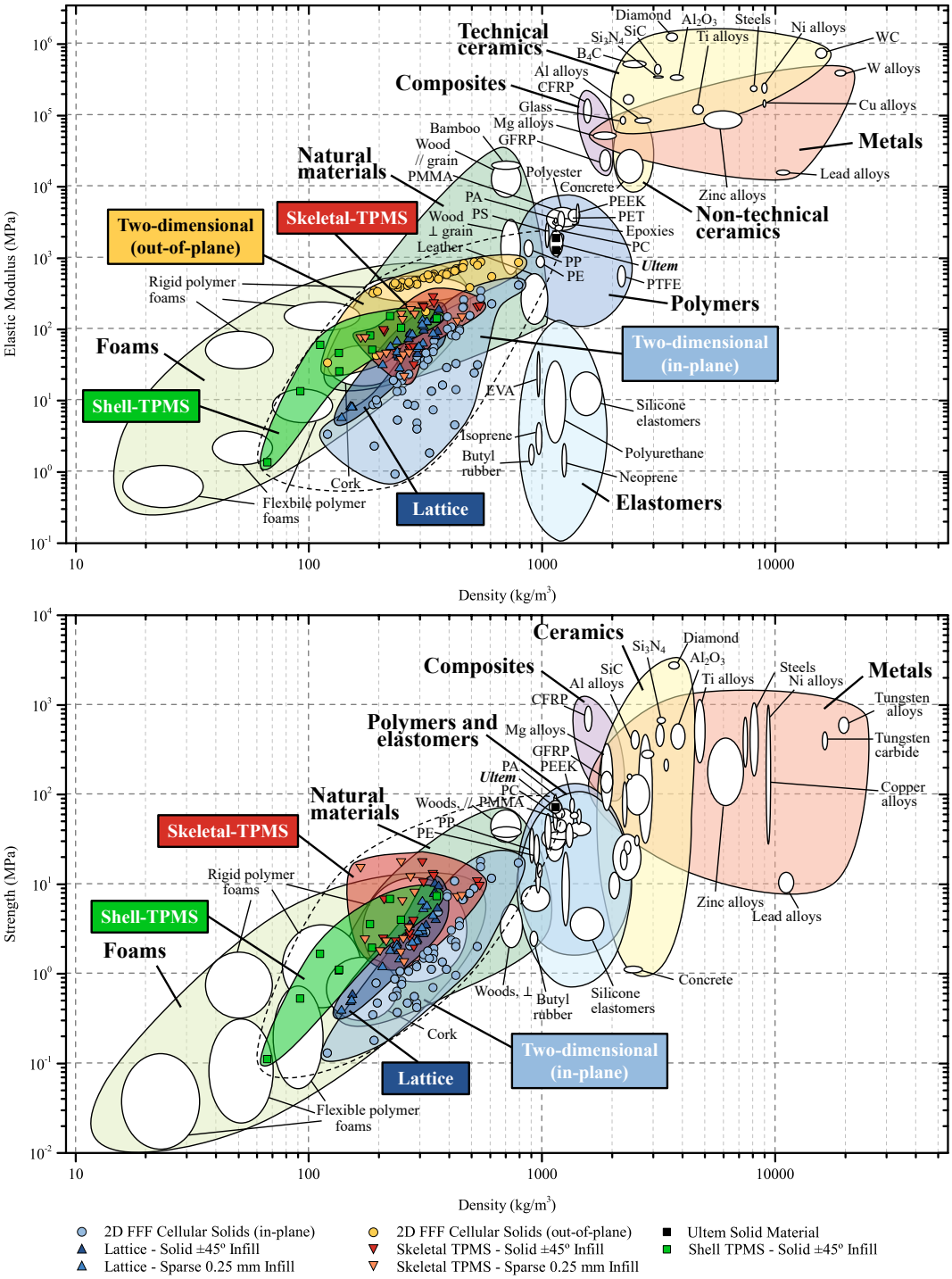

Figure 4.10: Comparison of the experimental performance of the two- and three-dimensional FFF cellular solids with materials database adapted from CES EduPack 2019, ANSYS Granta©2020 Granta Design, with permission.

Table 4.2: Compressive experimental elastic moduli and 1st peak stresses exhibited by each two-dimensional cellular solid for different levels of relative density.

Cellular design	Core relative density (%)	Elastic modulus (MPa)			1st peak stress (MPa)	
		E_x	E_y	E_x	$\sigma_x^{1^{st}}$	$\sigma_y^{1^{st}}$
Antitetrachiral	44.58	24±9	Sym.	888±5	8.99±2.44	Sym.
	25.32	4±0		484±5	0.42±0.00	
	16.60	2±0		350±2	0.18±0.02	
Circular	47.64	348±19	274±38	882±63	18.02±1.07	15.58±0.38
	40.18	262±23	209±55	842±42	6.90±1.85	6.86±0.64
	34.21	151±3	101±16	624±2	7.79±0.68	7.19±0.61
Hexachiral	38.61	101±3	96±9	716±64	3.86±0.31	3.42±0.25
	27.18	36±1	32±0	532±17	1.49±0.07	1.63±0.05
	21.81	19±2	14±0	457±34	0.84±0.06	0.76±0.13
Hexagon	25.25	36±2	Sym.	434±3	1.25±0.30	Sym.
	21.50	23±1		390±7	1.06±0.10	
	16.44	9±1		320±3	0.35±0.02	
Lozenge Grids	32.60	17±2	Sym.	593±10	1.35±0.00	Sym.
	24.76	9±1		480±12	0.56±0.02	
	20.90	5±0		394±0	0.37±0.00	
Re-Entrant Hexagon I	35.59	107±7	83±7	640±21	3.06±0.03	2.38±0.18
	30.02	69±0	56±0	597±23	1.92±0.05	1.66±0.09
	20.81	17±1	13±1	423±24	0.64±0.07	0.57±0.02
Re-Entrant Hexagon II	37.17	14±1	81±1	705±0	0.96±0.01	2.26±0.00
	29.76	7±0	48±4	559±7	0.70±0.03	1.47±0.04
	25.33	5±0	42±1	430±78	0.47±0.06	1.19±0.05
Rotachiral	37.22	33±4	Sym.	672±25	2.02±0.20	Sym.
	29.26	14±1		547±8	1.12±0.07	
	23.06	9±1		415±24	0.55±0.04	
Sinusoidal Ligaments	46.15	32±6	Sym.	793±11	10.87±0.28	Sym.
	33.92	29±9		589±7	3.10±0.31	
	20.05	19±1		416±10	1.13±0.04	
Square Grids	36.73	5±1	Sym	665±9	2.71±0.43	Sym.
	28.72	2±0		515±31	1.49±0.22	
	20.42	1±0		443±4	0.87±0.08	
SrCuBO	39.83	203±13	Sym.	733±37	6.72±1.30	Sym.
	31.38	145±20		507±5	4.90±0.80	
	23.68	83±4		437±6	2.06±0.20	
Tetrachiral	28.23	38±6	Sym.	577±6	1.80±0.07	Sym.
	23.34	24±0		458±7	1.06±0.08	
	17.15	9±0		338±8	0.47±0.02	
Sparse	69.13	418±3	Sym.	577±6	17.22±0.00	Sym.
	53.02	228±18		548±13	11.68±0.02	
	42.76	155±2		385±3	7.89±0.09	
	27.71	46±0		178±1	2.89±0.03	
	16.93	10±1		43±0	0.79±0.02	
	10.46	3±0		34±1	0.13±0.01	

Table 4.3: Compressive energy absorption efficiency and Poisson's ratio exhibited by each two-dimensional cellular solid for different levels of relative density.

Cellular design	Core relative density (%)	Energy abs. efficiency (J/cm^3)		Poisson's ratio	
		W_x	W_y	ν_{xy}	ν_{yx}
Antitetrachiral	44.58	1011±394	Sym.	-1.081±0.001	Sym.
	25.32	129±2		-0.431±0.026	
	16.60	78±19		-0.785±0.009	
Circular	47.64	1011±299	782±29	0.324±0.007	0.298±0.010
	40.18	314±240	356±183	0.362±0.009	0.198±0.002
	34.21	697±48	501±75	0.465±0.006	0.350±0.011
Hexachiral	38.61	234±35	204±56	-0.068±0.002	-0.188±0.001
	27.18	131±5	222±41	-0.130±0.003	-0.219±0.005
	21.81	101±18	104±33	-0.531±0.001	-0.320±0.003
Hexagon	25.25	138±100	Sym.	0.823±0.015	Sym.
	21.50	170±28		0.672±0.002	
	16.44	45±8		0.757±0.006	
Lozenge Grids	32.60	258±28	Sym.	-0.007±0.002	Sym.
	24.76	168±21		-0.035±0.003	
	20.90	145±15		-0.021±0.007	
Re-Entrant Hexagon I	35.59	194±19	108±25	-0.147±0.013	-0.110±0.003
	30.02	144±8	105±2	-0.139±0.004	-0.251±0.010
	20.81	76±21	76±3	-0.132±0.016	-0.306±0.006
Re-Entrant Hexagon II	37.17	108±5	144±1	-0.334±0.001	-2.076±0.010
	29.76	142±15	140±8	-0.264±0.006	-2.511±0.008
	25.33	102±29	126±10	-0.147±0.043	-2.483±0.014
Rotachiral	37.22	250±71	Sym.	-0.080±0.002	Sym.
	29.26	156±22		-0.020±0.007	
	23.06	98±14		-0.024±0.003	
Sinusoidal Ligaments	46.15	3060±32	Sym.	-0.029±0.019	Sym.
	33.92	446±77		-0.116±0.040	
	20.05	201±5		-0.118±0.028	
Square Grids	36.73	642±186	Sym	-0.105±0.031	Sym.
	28.72	431±75		-0.056±0.019	
	20.42	312±3		-0.028±0.008	
SrCuBO	39.83	281±117	Sym.	0.223±0.004	Sym.
	31.38	369±26		0.200±0.002	
	23.68	172±2		0.194±0.002	
Tetrachiral	28.23	294±3	Sym.	0.102±0.002	Sym.
	23.34	194±10		0.056±0.003	
	17.15	147±1		0.039±0.001	
Sparse	69.13	727±18	Sym.	0.614±0.067	Sym.
	53.02	1425±57		0.151±0.042	
	42.76	1270±8		0.268±0.030	
	27.71	1663±50		1.031±0.113	
	16.93	937±77		0.814±0.077	
	10.46	75±10		1.327±0.101	

Table 4.4: Compressive experimental elastic moduli, strength at FF, and energy absorption efficiency exhibited by each three-dimensional cellular solid for different unit cell sizes.

Cellular design	Core relative density (%)	Elastic modulus (MPa)	Compression strength at FF (MPa)	Energy absorption efficiency at FF (J/cm^3)
Reinforced Body-centered Cube	27.1 27.8	96±12 124±2	2.8±0.1 3.5±0.2	234±34 305±34
Dode medium	13.2 13.4	8±0 8±0	0.5±0.0 0.6±0.0	263±5 352±5
Dode thick	21.3 26.3	45±0 57±0	2.4±0.1 2.8±0.0	554±18 741±31
G-Structure 9	18.4 18.2	73±4 86±1	2.7±0.1 3.5±0.2	337±13 493±94
G-Structure 10	30.3 31.5	152±3 188±21	10.0±0.1 9.4±1.2	3209±55 1722±598
Octet Truss	30.3 30.2	136±1 138±4	8.0±0.1 7.7±0.2	1924±77 1775±67
Rhombic Dodecahedron	30.7 31.0	80±4 92±2	4.0±0.3 5.3±0.2	601±134 1350±26
Trucated Octa Light	20.9 25.5	40±1 43±1	1.8±0.0 2.2±0.0	331±5 545±103
Neovius Surface	23.7 23.6	52±1 53±1	2.6±0.2 2.9±0.2	664±103 863±28
Schoen Gyroid	20.7 23.7	50±2 58±0	2.4±0.1 3.4±0.3	635±143 873±95
Schwarz Diamond	24.6 24.6	33±3 58±0	2.0±0.4 4.0±0.0	496±164 1243±34
Cylinder Grid	23.4 23.6	221±19 212±3	18.1±0.0 10.7±0.1	17764±690 1887±51
Schwarz Primitive (Pinched)	29.8 29.9	293±1 240±12	13.3±1.5 12.7±0.4	8302±1451 6125±257
Schwarz Primitive	26.8 27.2	95±3 101±3	6.9±0.3 2.5±0.0	8710±1477 339±17
Body Diagonals With Nodes	46.1 47.3	211±6 216±32	11.0±0.6 9.9±1.6	1252±182 914±163
Gyroid	8.0 16.0	14±4 82±2	0.5±0.1 3.6±0.1	235±15 1019±60
Diamond	9.8 19.4	61±5 154±2	1.7±0.0 6.9±0.1	429±2 1927±12
Lidinoid	16.3 30.9	52±2 143±1	2.0±0.1 7.3±0.1	511±3 1733±28
Split-P	11.7 21.7	47±3 105±0	1.1±0.0 4.0±0.0	184±5 908±8
Schwarz	5.8 11.8	1±0 26±0	0.1±0.0 1.1±0.0	158±46 507±28

4.2.2 Anisotropy degree

Given the differences between the in-plane and out-of-plane behavior of the two-dimensional cellular designs, the quantification of the degree of anisotropy of the analyzed cellular solids was addressed. For this purpose, the unit cell of each design was taken as RVE for subsequent numerical homogenization considering periodic boundary conditions. As a result, their equivalent engineering constants[1] were obtained, which are useful for the calculation of the compliance matrix S^H of the cellular solids as presented above in Eq. 4.1. At this point, the homogenized stiffness tensor C^H of each cellular design was directly determined as the inverse of the homogenized compliance matrix, *i.e.* $\boldsymbol{C^H = S^{H^{-1}}}$.

Then, the mathematical procedure detailed from Eq. 3.28 in Section 3.2.6 of Chapter 3 in this thesis was used to rotate the homogenized stiffness tensor of each cellular solid about the three global coordinate axes in order to obtain its graphical representation. Figure 4.11 shows the resulting graphs for the two- (*top*) and three-dimensional (*bottom*) designs. These graphs allow the visualization of the effective elastic modulus in each direction of the space that the pattern exhibits. Thus, the more spherical this representation is, the more isotropic the cellular solid behaves.

Significant differences arise when the shapes of the stiffness tensors' graphical representations of both cellular arrangements are compared. The extruded-like geometry of the two-dimensional designs provides them with a high out-of-plane elastic modulus, while the rigidity in the other in-plane directions is compromised. On the contrary, the three-dimensional designs provide a more balanced stiffness in all the orthogonal directions, as can be observed in their graphical representation which is less direction-dependent on most occasions.

The results presented in Table 4.5 quantify the degree of anisotropy of the different cellular solids studied employing the novel A^V index proposed in this thesis, which is calculated as the ratio between the volumes of the graphical representation of the stiffness tensor and the corresponding isotropy circumscribed sphere (see Eq. 3.27 and Figure 3.13 in Section 3.2.6 of Chapter 3). The equivalent values calculated with the Zener index (A) and the Universal anisotropy index (A^U) are included to facilitate the comparison of the different approaches [155].

Table 4.5: Degree of anisotropy of the two- and three-dimensional cellular solids.

Pattern	Relative density (%)	A^V	A	A^U	Pattern	Relative density (%)	A^V	A	A^U
	44.58	0.034	0.136	6.566		47.64	0.077	0.104	9.233
Antitetrachiral	25.32	0.023	0.045	24.23	Circular	40.18	0.066	0.062	16.938
	16.60	0.017	0.028	40.226		34.21	0.052	0.036	31.202
	38.61	0.101	1.015	0.000		25.25	0.106	0.970	0.001
Hexachiral	27.18	0.074	1.007	0.000	Hexagon	21.50	0.092	0.974	0.001
	21.81	0.060	1.003	0.000		16.44	0.073	0.978	0.001

Continued on next page

[1]Homogenized engineering constants: tensile moduli (E_x, E_y, and E_z), Poisson's ration (ν_{xy}, ν_{xz}, and ν_{yz}), and shear moduli (G_{xy}, G_{xz}, and G_{yz})

Table 4.5 – continued from previous page

Pattern	Relative density (%)	A^V	A	A^U	Pattern	Relative density (%)	A^V	A	A^U
Lozenge Grids	32.60	0.029	0.255	2.618	Re-Entrant Hexagon I	35.59	0.074	0.233	3.036
	24.76	0.025	0.251	2.679		30.02	0.062	0.158	5.378
	20.90	0.022	0.250	2.709		20.81	0.046	0.069	15.147
Re-Entrant Hexagon II	37.17	0.039	0.051	21.093	Rotachiral	37.22	0.053	0.954	0.003
	29.76	0.032	0.028	39.763		29.26	0.045	0.999	0.000
	25.33	0.030	0.019	60.789		23.06	0.037	1.000	0.000
Sinusoidal Ligaments	46.15	0.041	0.110	8.668	Square Grids	36.73	0.015	0.066	15.912
	33.92	0.045	0.070	14.812		28.72	0.013	0.066	15.927
	20.05	0.045	0.034	32.455		20.42	0.010	0.066	15.989
SrCuBO	39.83	0.153	0.583	0.359	Tetrachiral	28.23	0.069	0.644	0.237
	31.38	0.124	0.363	1.340		23.34	0.057	0.547	0.450
	23.68	0.106	0.209	3.590		17.15	0.043	0.541	0.469
Reinforced Body-centered Cube	27.11	0.611	0.709	0.144	Dode medium	13.16	0.494	2.656	1.239
	27.83	0.610	0.709	0.143		13.44	0.491	2.597	1.179
Dode thick	25.51	0.523	2.294	0.876	G-Structure 9	23.35	0.365	0.124	7.415
	26.29	0.521	2.347	0.927		23.62	0.385	0.126	7.285
G-Structure 10	30.33	0.827	1.207	0.042	Octet Truss	30.32	0.632	1.641	0.301
	31.52	0.829	1.204	0.041		30.16	0.631	1.633	0.294
Rhombic Dodecahedron	30.65	0.548	2.070	0.664	Truncated Octa Light	21.25	0.523	2.411	0.991
	31.05	0.547	2.101	0.693		20.94	0.524	2.419	0.998
Neovius Surface	23.75	0.606	1.653	0.310	Schoen Gyroid	20.68	0.585	1.812	0.437
	23.63	0.605	1.639	0.299		23.69	0.508	1.791	0.419
Schwarz Diamond	24.63	0.519	2.327	0.908	Cylinder Grid	26.77	0.360	0.181	4.443
	24.57	0.520	2.313	0.894		27.16	0.360	0.182	4.413
Schwarz Primitive (Pinched)	29.81	0.392	0.290	2.091	Schwarz Primitive	18.38	0.365	0.184	4.351
	29.93	0.391	0.289	2.103		18.22	0.364	0.184	4.351
Body Diagonals With Nodes	46.13	0.590	1.843	0.463	Gyroid	8.01	0.950	1.051	0.003
	47.26	0.589	1.852	0.470		15.99	0.911	1.087	0.008
Diamond	9.75	0.508	0.590	0.342	Lidinoid	16.29	0.820	1.220	0.047
	19.45	0.570	0.682	0.178		30.88	0.876	1.141	0.021
Split-P	11.74	0.966	1.030	0.001	Schwarz	5.79	0.473	3.271	1.892
	21.66	0.997	0.999	0.000		11.78	0.503	2.611	1.193

As can be seen, the use of the new A^V index makes it possible to compare the anisotropy of the cellular designs more easily than the other alternatives thanks to its limited range between 0 and 1. Furthermore, when analyzing in greater detail the anisotropy of certain two-dimensional designs, such as the Hexachiral, Hexagon or Rotachiral patterns, the values calculated by employing the Zener index (A) and the Universal anisotropy index (A^U) indicate almost perfect isotropy, while both the corresponding stiffness tensor representation depicted in Figure 4.11 and the numerical and

experimental results of this research verify the anisotropic behavior of these cellular designs, thus proving the inaccuracy of these methods for the case of study.

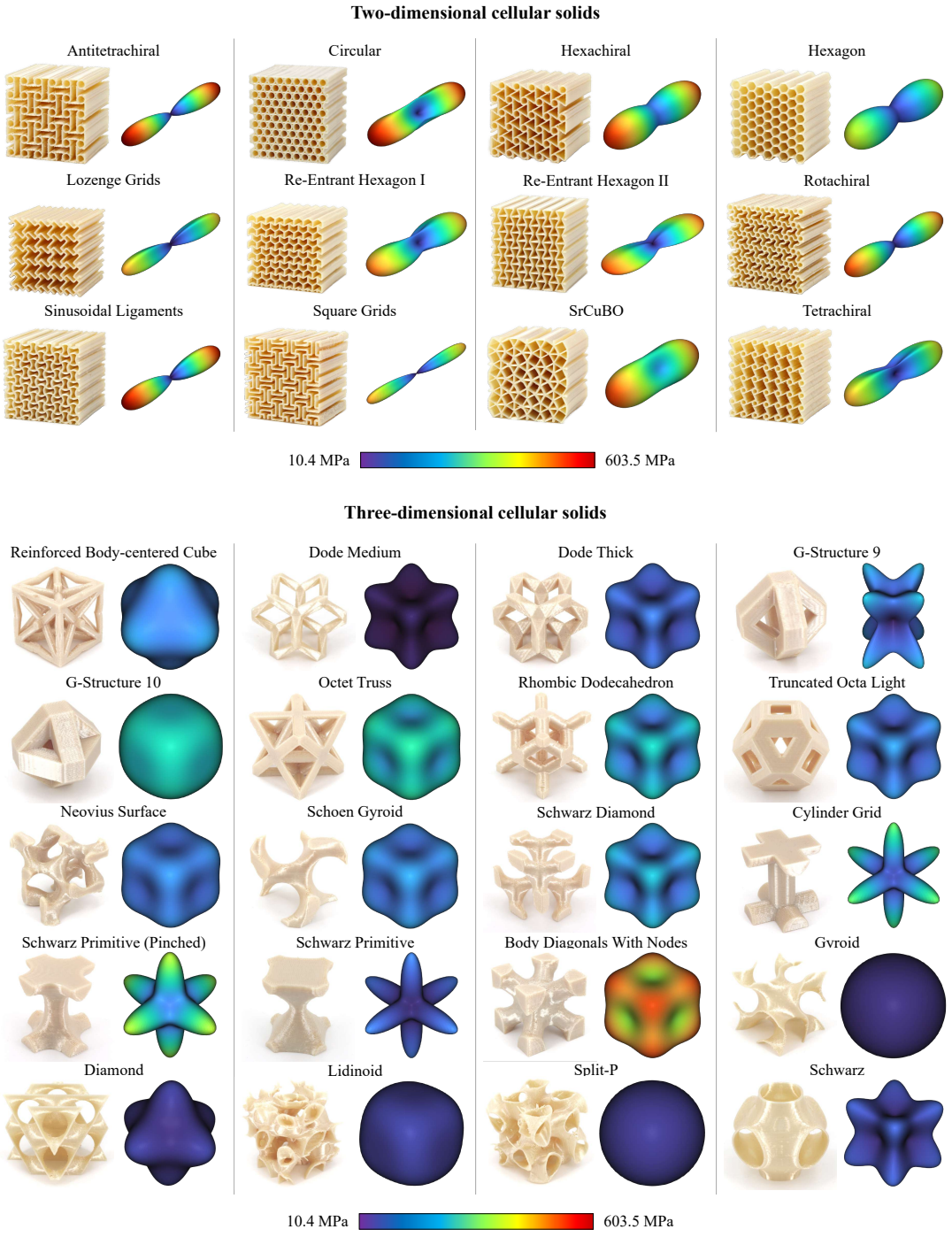

Figure 4.11: Homogenized stiffness tensor graphical representation for each of the studied two- (*top*) and three-dimensional (*bottom*) cellular solids.

The charts presented in Figure 4.12 relate the specific experimental results of elastic modulus (*top*) and compressive strength at FF (*bottom*) of the different cellular solids with their corresponding degree of anisotropy, which was calculated with the novel volume-based anisotropy index A presented in this thesis. Regarding both graphs, three-dimensional designs present a much more homogeneous behavior in 3D space than the two-dimensional ones, being the Shell-TPMS the most efficient cellular structure in that sense.

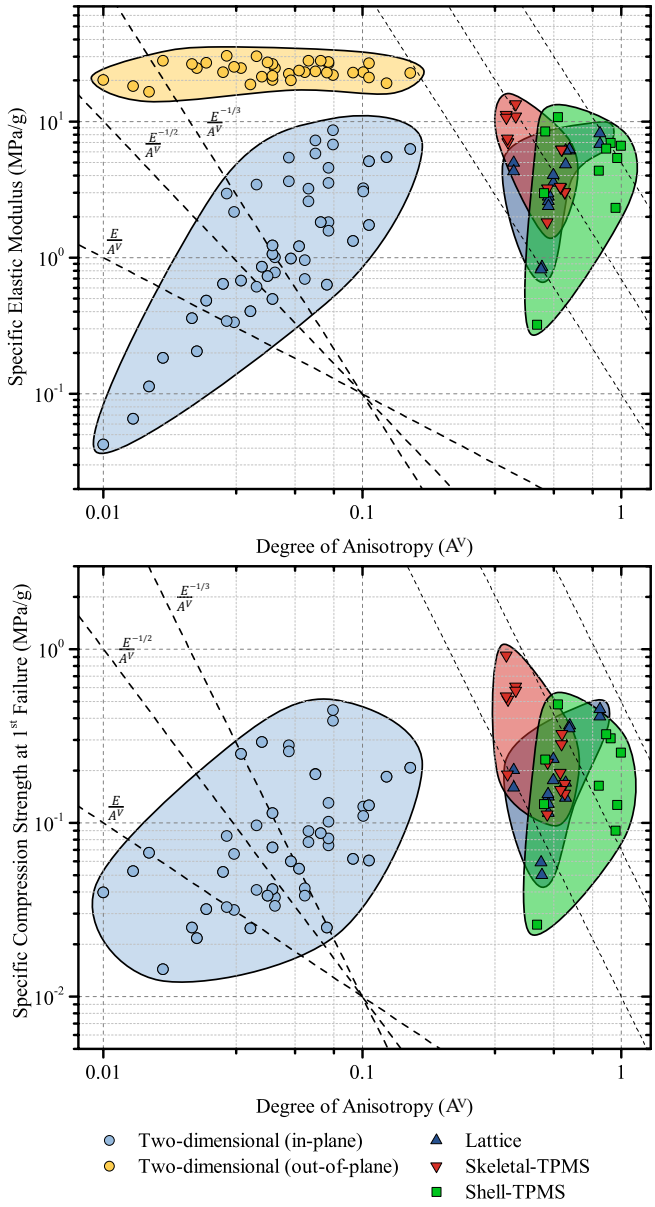

Figure 4.12: Representation of the experimental results of specific elastic modulus and compression strength of each two- and three-dimensional cellular design against the corresponding degree of anisotropy calculated with the novel A^V index proposed in this thesis.

4.2.3 Numerical approach

In parallel, the compressive behavior of the tested cellular solids was modeled using two FE numerical approaches: SE and H-RVE. This comparison aims to verify the potential of both alternatives for the simulation of cellular structures, taking into account aspects such as the accuracy of the results and the consumption of computational resources.

The main differences between the considered numerical approaches are due to the complexity of the CAD model and the material properties employed for the simulation. The SE method directly implements the exact geometry of the part whose performance is to be simulated and the mechanical properties of the material used for its manufacture. Meanwhile, the H-RVE model is developed using an enveloping body according to the maximum dimensions of the original geometry and introducing its effective mechanical properties, which can be obtained from the numerical homogenization of an RVE of the cellular structure as presented above.

Three possible levels of anisotropy were considered to ease the definition of the SE model material, based on the results from the experimental tests of standardized Ultem specimens processed by FFF that were previously presented in this chapter: orthotropic, quasi-isotropic, and isotropic (see Table 3.4 in Section 3.2.5 of Chapter 3). In addition, the numerical results were compared with the obtained experimental values using different wall-thicknesses (0.508 mm, 0.577 mm, and 0.60 mm), accounting for the imperfections that occur during the fabrication of two-dimensional cellular solids by this AM technology (see Figure 4.9).

The boxplots presented in Figure 4.13 show the deviation between numerical and experimental results. As can be seen by comparing the size of the boxes, simplifying the mechanical behavior of the material by considering a fully isotopic approach leads to a considerable loss of accuracy. On the other hand, the differences between the quasi-isotopic and orthotropic models were minimal. Therefore, the quasi-isotropic approach was selected for the numerical simulation of all the cellular solids, employing a wall-thickness of 0.577 mm for the case of two-dimensional designs as it was the configuration that showed the highest accuracy overall.

Figures 4.14 and 4.15 depict some representative results obtained from the simulation of the compressive mechanical behavior of two-dimensional and three-dimensional cellular solids, respectively, employing the SE numerical approach. The images in the left column of the first one show a comparison between the simulated deformed shape and the recorded images using DIC technology of the Antitetrachiral and Square Grids patterns at different strain stages. Both sequences correspond samples of density level III (see Table 3.4 in Section 3.2.5 of Chapter 3) tested along the x-direction. The employed colormap corresponds to the Von Mises stress results. This qualitative comparison shows a kinematic correspondence between the numerical and experimental results, with a marked auxetic behavior of both patterns.

Furthermore, the cross-section of each analyzed two-dimensional design is shown on the right side of Figure 4.15, colored with Von Misses stress before FF or any internal contact was detected. As can

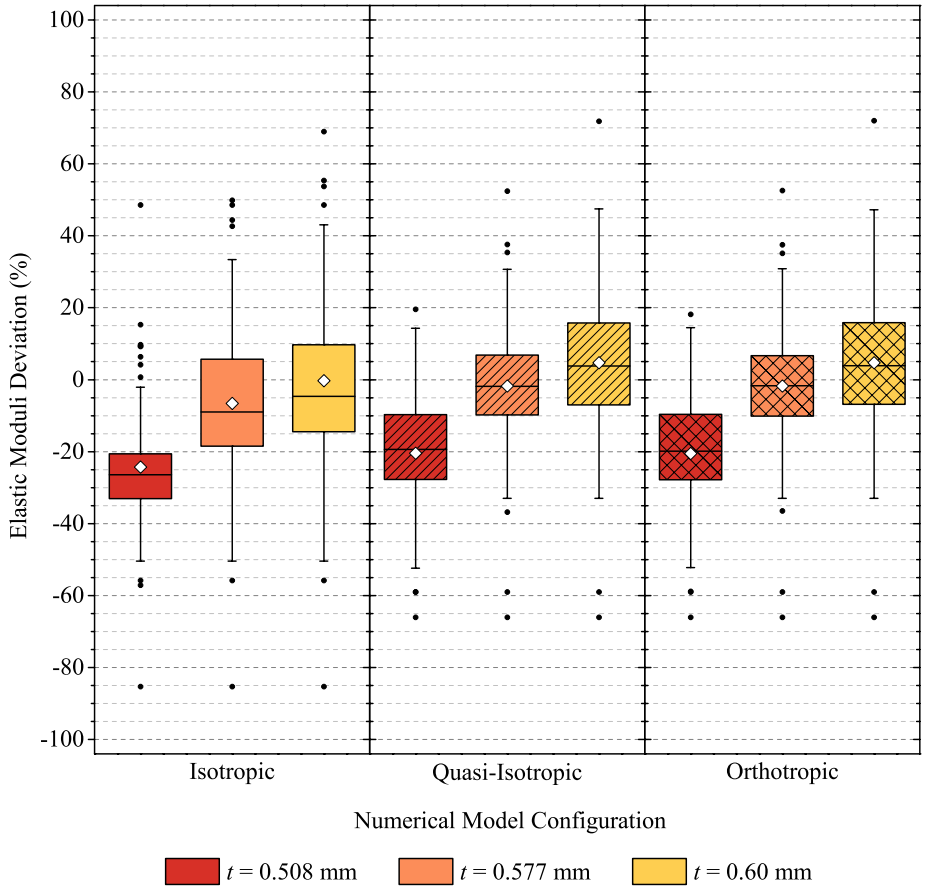

Figure 4.13: Boxplot diagrams depicting the deviation of the elastic moduli between the SE numerical model results and the experimental data for different material models and cell wall-thicknesses.

be seen, the deformed shape of most patterns is bending-dominated. It can also be noticed that some cellular geometries exhibit the maximum stress values at the connection points between unit cells. This fact verifies the experimental results, which revealed that failure occurs mainly in these areas due to bond weaknesses and other reported manufacturing issues. Therefore, this evidence highlights the importance of reducing FFF defects in intra-layer filament bonds to prevent premature failure, especially in two-dimensional designs. Hence, the importance of optimizing the printing toolpaths to make them more continuous is justified, as it would reduce the amount of intra-layer bonds.

Additionally, Figure 4.15 compares the numerical and experimental data of ten representative three-dimensional cellular solids tested under compression load. The images in the 1st and 4th rows correspond to the experimental displacement field calculated through DIC analysis for a 1 mm compression displacement (2.5% of strain). The deficiencies observed in the displacement field are due to limitations in recognizing the stochastic pattern sprayed on the surface of the samples, particularly on regions that are not visible to one of the DIC cameras (see Gyroid and Diamond specimens). The 2nd and 5th rows are the analogous numerical displacement fields, while the images in 3rd and 6th ones

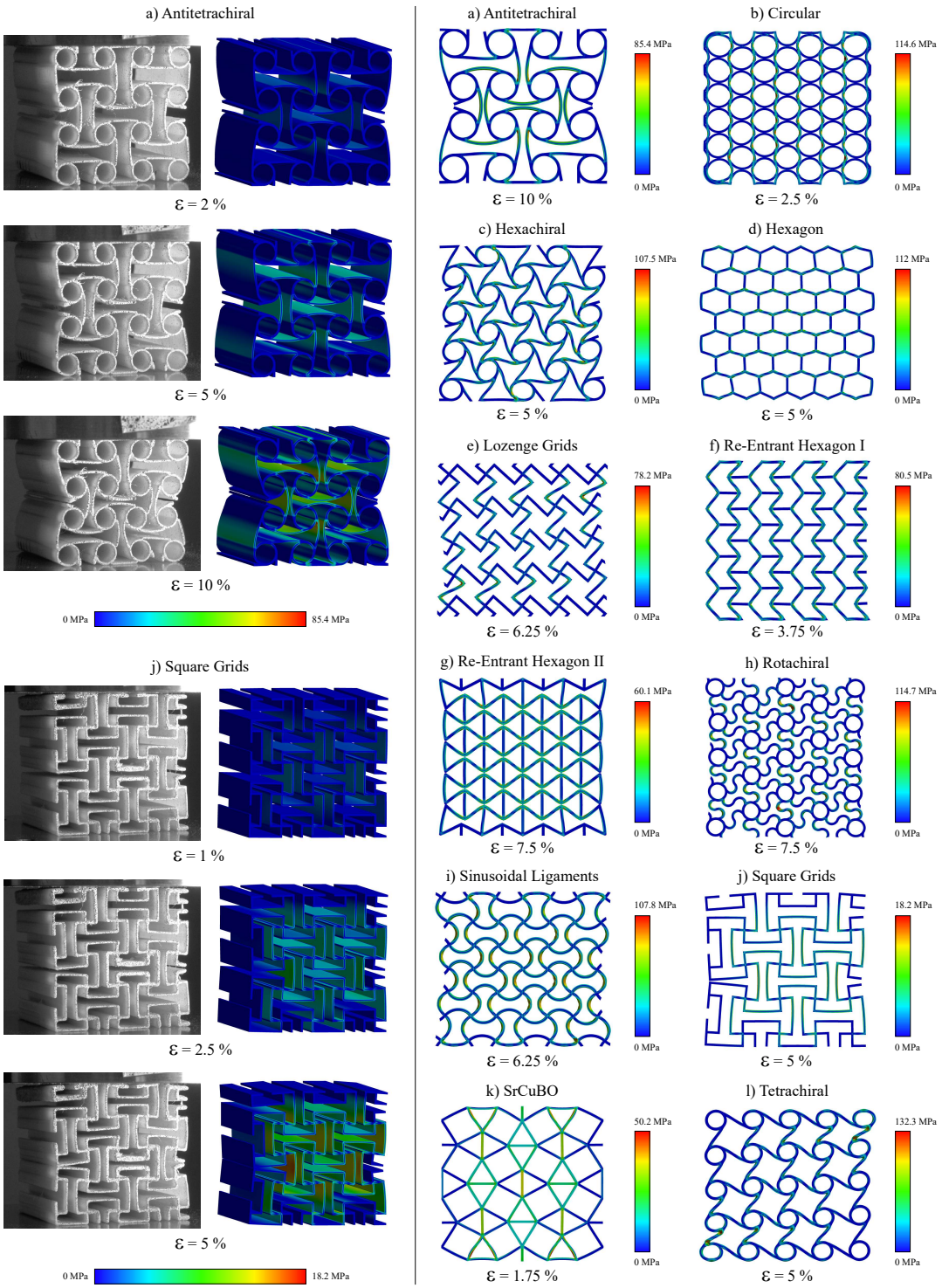

Figure 4.14: Comparison of the experimental and SE numerical deformed shape sequences of the Antitetrachiral and Square Grids patterns (*left*). Cross-section view of each two-dimensional design before FF or any internal contact was detected (*right*). Colormap stands for Von Mises stress.

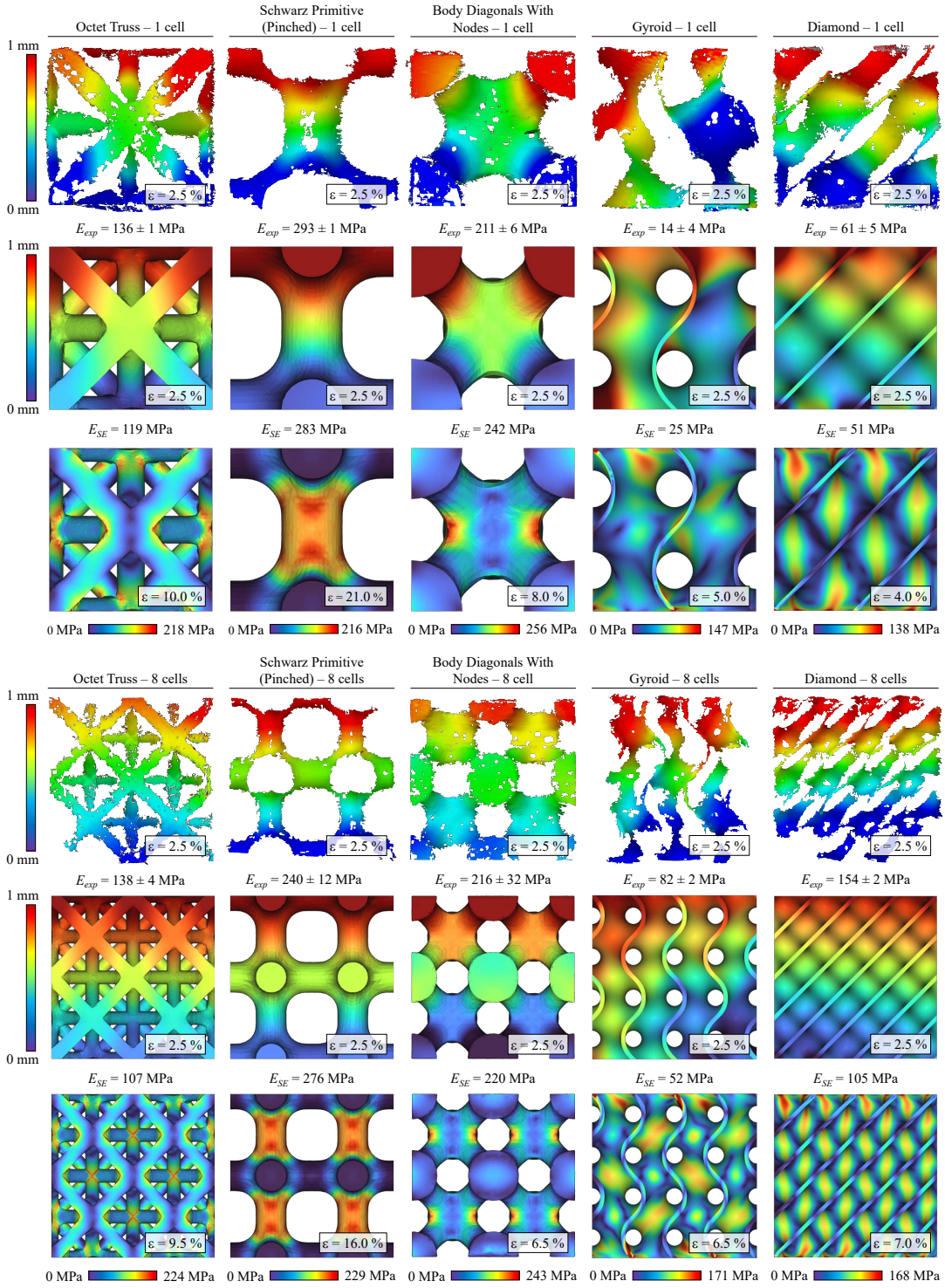

Figure 4.15: Numerical SE model results and experimental data of ten representative three-dimensional cellular solids tested under compression load. The first and fourth rows correspond to the experimental displacement field obtained through DIC analysis. The second and fifth rows are the analogous numerical displacement fields, while the third and sixth rows display the numerical Von Mises stress before FF occurred.

display the numerical Von Mises stress before FF. In general, the elastic moduli numerical results agree with experimental values, both indicated below each image, thus validating the SE numerical model. Furthermore, Von Mises stresses show different trends between three-dimensional cellular typologies, particularly on Shell-TPMS designs (see Gyroid and Diamond specimens). Overall, the identified areas of stress concentration match the experimental failure regions of the cellular solids. Note that walls in Shell-TPMS designs are not self-intersecting surfaces, hence avoiding joints and discontinuities in filament deposition. This fact favors the stress distribution and improves the mechanical performance of the cellular structure, thus confirming the experimental evidence.

However, the geometrical complexity that characterizes cellular solids, complicates the generation of the mesh that has to implement a large number of very small elements to completely adapt to the surface of the sample, especially in the case of three-dimensional designs. For this reason, and despite the quality and accuracy of the results calculated with the SE numerical model, the potential of this approach for simulating larger cellular structures may be limited by the computational resources it requires.

At this point, a much more computationally efficient alternative can be the implementation of the H-RVE model. The simplicity of this numerical approach makes it remarkably robust for the simulation of cellular solids regardless of their geometrical complexity, density, and cell dimensions while reducing the meshing process complexity considerably. However, its implementation is only suitable for uniform periodic geometries, as the effective RVE properties are supposed to be constant throughout the volume of the part. Moreover, the H-RVE approach requires computing more steps since a homogenization of the unit cell has to be performed before addressing the simulation of the whole design. In addition, this numerical analysis tends to be less accurate than the SE method because neither edge effects nor stress concentrations are considered due to the simplification of the model.

For all these reasons, the accuracy of both numerical methods is presented in Figure 4.16, where the values of the estimated elastic moduli of each cellular solid are compared with the experimentally determined ones. A regression line is fitted to each numerical approach, and the coefficient R^2 is provided to quantify the degree of correlation. As can be seen, both numerical models tend to underpredict the stiffness of the cellular structure, but the best fit corresponds to the SE model, even though the H-RVE model led to huge computational time savings.

Finally, in order to validate and compare both numerical approaches, the bending performance of a two-dimensional pattern (Hexachiral) and a three-dimensional Shell-TPMS design (Diamond) were experimentally and numerically evaluated under a centered 3-point bending load case. The obtained results are presented in Figure 4.17, which were evaluated when FF occurred. Total displacement and Von Mises stresses were numerically calculated employing the SE and the H-RVE models. In addition, the experimental stiffness of each pattern is included together with the values calculated using both FE methods for comparison. Lastly, other FE model details including the computational time and size are provided.

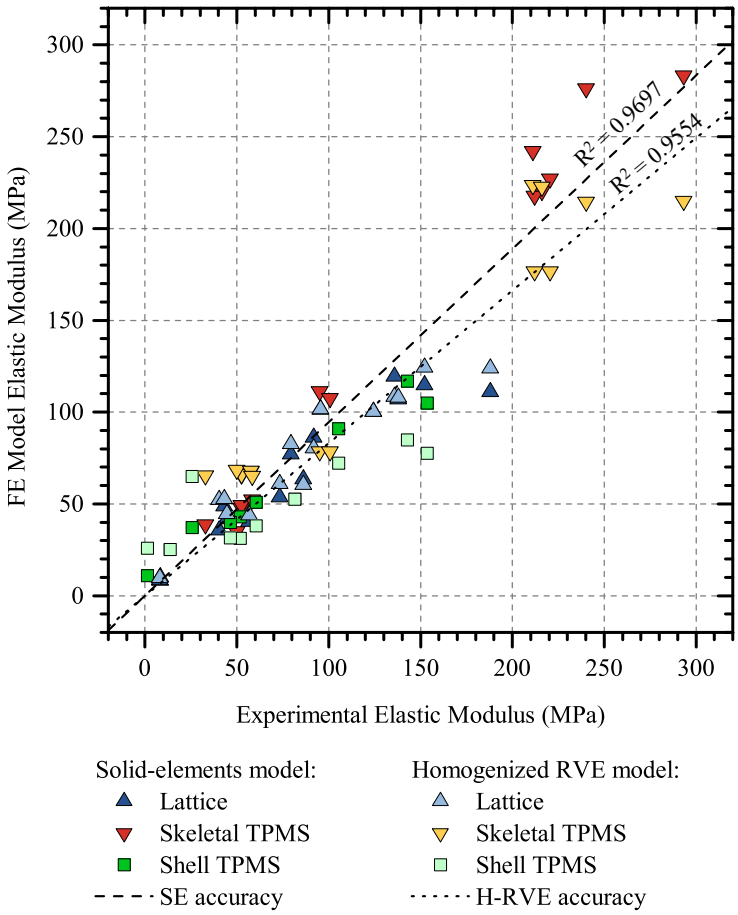

Figure 4.16: Accuracy of the SE and H-RVE numerical models in contrast to experimental data.

The numerical stiffness values agree with the experimental results from both types of cellular solids. The higher divergence is observed in the H-RVE approach, which is attributed to the simplification of the homogenized model. Furthermore, the displacement results from the Hexachiral pattern analysis are satisfactory. However, the bending-torsion coupling effect observed in the Diamond pattern is not identified by the H-RVE approach (note the slightly different stress field on the surrounding area of supports). Similarly, as displayed on the Von Mises stress plots, the stress concentrators are not captured in the homogenized model. Therefore, only effective stress values can be determined if this approach is implemented (note the difference between the maximum Von Mises stresses results obtained with the H-RVE and SE methods). Nevertheless, despite these points, the agreement of all the numerical results confirms the capability of both approaches to reproduce the elastic behavior of cellular solids with adequate confidence.

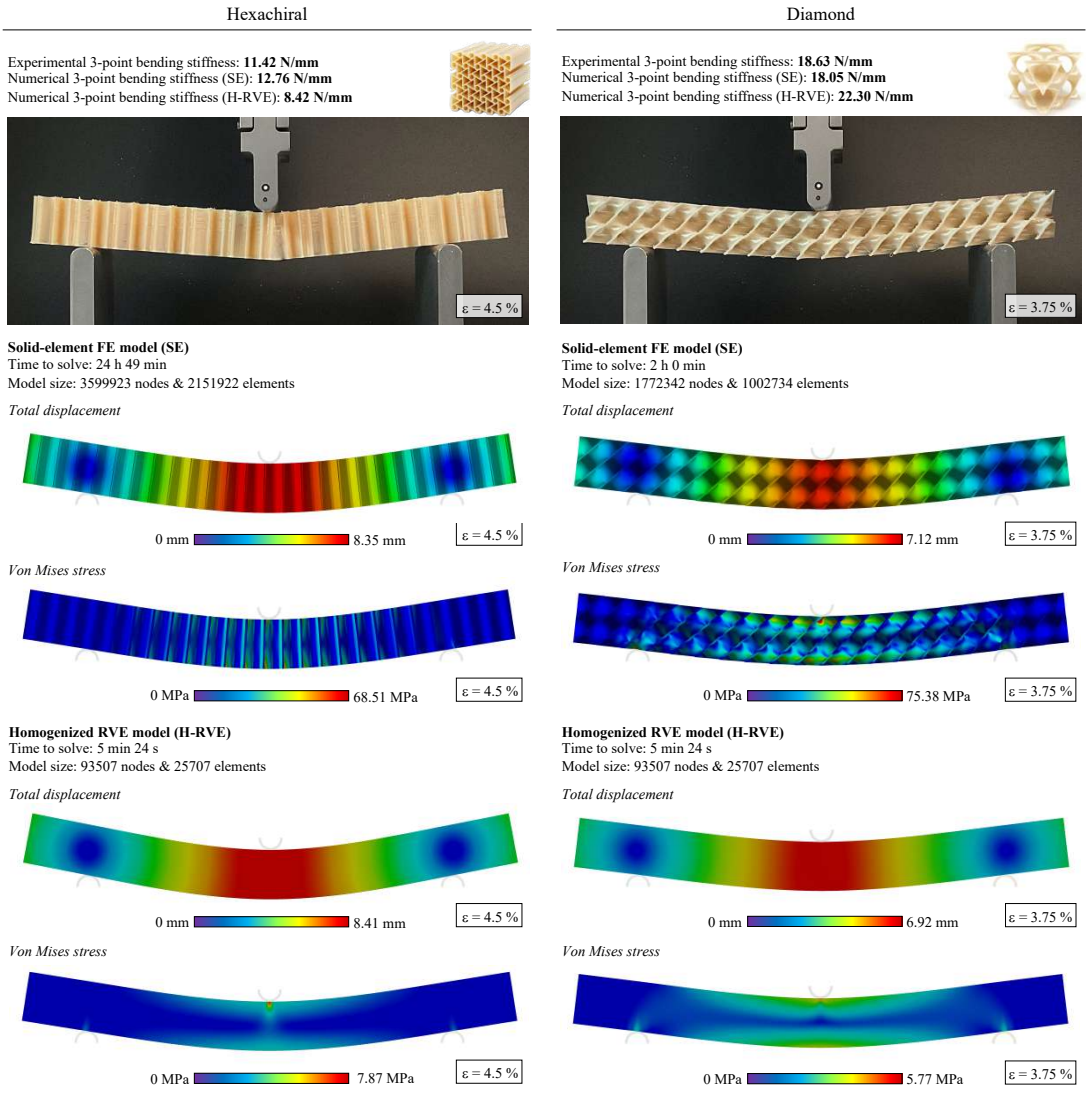

Figure 4.17: Validation results of SE and H-RVE numerical models for reproducing the flexural behavior of the two-dimensional Hexachical pattern (*left*) and the three-dimensional Diamond cellular design (*right*).

4.3 Sandwich panels characterization

After completing the first and second phases of this research, the third and final stage consisted of the study of the performance of hybrid sandwich structures employing two- and three-dimensional cellular cores manufactured by FFF. Specifically, the analysis focused on determining the flexural mechanical behavior of sandwich panels under a 3-point bending load case, combining analytical, numerical and experimental methodologies to verify the obtained results.

Figure 4.18 depicts a comparison of the simulated flexural moduli results with the values obtained from the analytical expression Eq. 3.36 presented by Ashby [3] for a solid continuous Ultem core

processed by FFF with the ±45° infill configuration. To do so, a parametric FE model was adjusted to adequately predict the bending performance of sandwich panels employing different values of skin and core thicknesses and implementing the H-RVE model that was previously developed for simulating the flexural behavior of the cellular cores (see Figure 4.17). The obtained curves show excellent agreement between the analytical and simulated bending stiffness values for 14 different sandwich arrangements which are indicated by the corresponding f value, starting from an isolated core and finishing with a full CFRP panel while keeping a constant total height of the panel $d = 20.572$ mm. Therefore, these results verify the computational capability of the developed numerical model to simulate the multiple FFF cellular core designs considered, employing their RVE homogenized properties.

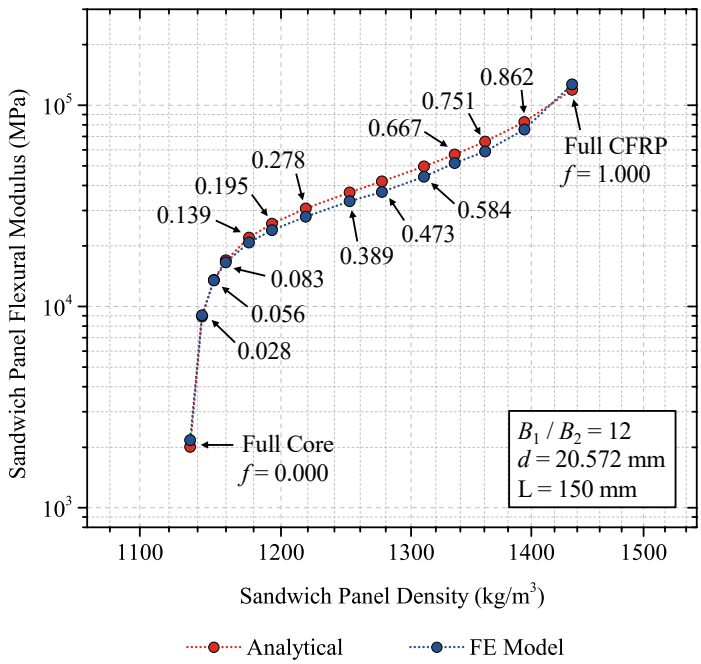

Figure 4.18: Accuracy of the FE model developed to simulate the flexural modulus of hybrid sandwich panels. The values of the volume fraction of the nominal cross-section occupied by its faces (f) are included for each considered sandwich arrangement.

Then, the flexural performance of the nineteen selected cellular cores was addressed, employing the calibrated FE model. The results are depicted in Figure 4.19, where the simulated flexural moduli of the considered cellular designs are analyzed for different relative densities. As can be seen, the flexural stiffness of the three-dimensional designs (*right*) is significantly higher than that exhibited by the two-dimensional patterns (*left*) for the same range of relative density. These differences become more evident at very low-density values, where the former can exhibit stiffness up to three orders of magnitude superior to the latter. Furthermore, the trends presented by the three-dimensional designs confirm that the Shell-TPMS patterns (Gyroid, Diamond, Split-P, and Schwarz) are more efficient than the Skeletal-TPMS ones (Neovius Surface, Schoen Gyroid, and Schwarz Diamond), as previously observed in core compression tests.

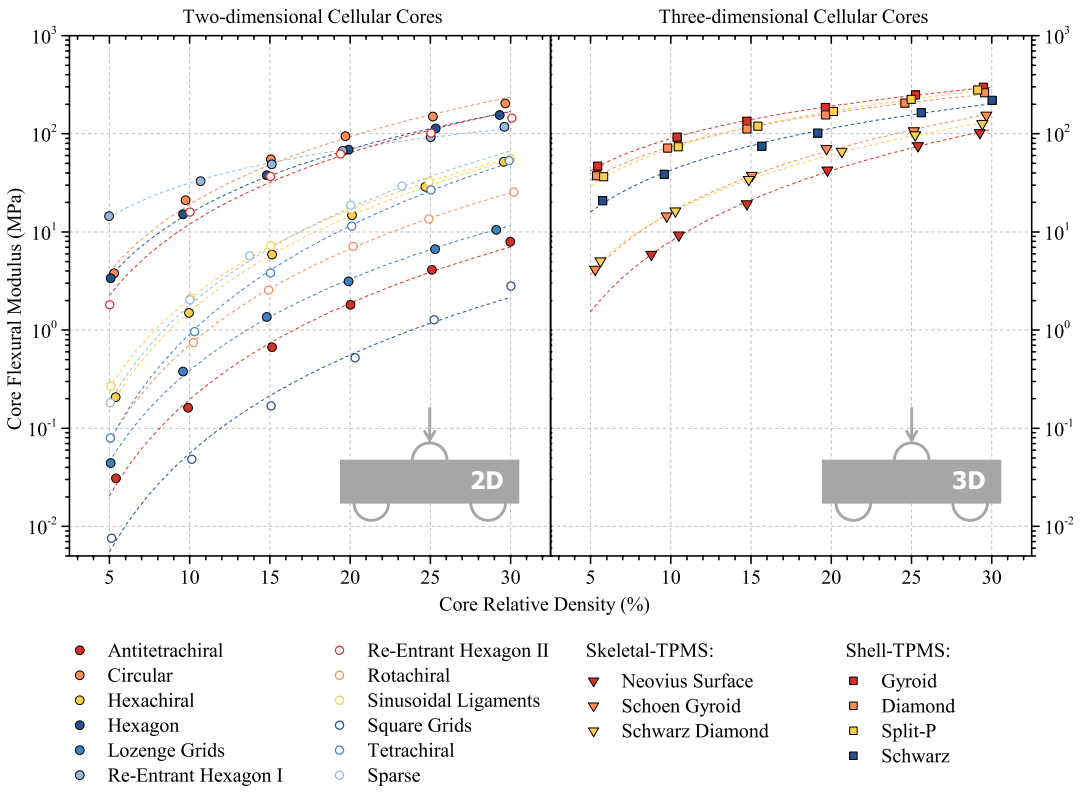

Figure 4.19: Flexural moduli results of two- (*left*) and three-dimensional (*right*) cellular core designs at different values of relative density obtained by FE numerical simulation.

Following the same procedure, the bending stiffnesses of multiple hybrid sandwich structures combining the inspected cellular core designs were simulated, considering in each case a total of twelve sandwich arrangements keeping the same total height of the panel. Figures 4.20 and 4.21 depict the numerical results of the flexural moduli of the hybrid sandwich panels employing two- and three-dimensional cellular cores, respectively. In all cases, the simulated arrangements are indicated by the corresponding f value and the flexural modulus of the CFRP Prepreg material is also included ($f = 1.000$).

The presented results demonstrate the importance of the cellular design employed as a lightweight core in the flexural performance of hybrid sandwich structures. In particular, the two-dimensional Circular, Hexachiral, Hexagon, Re-Entrant Hexagon II, and Sinusoidal Ligaments designs, as well as the three-dimensional Shell-TPMS designs, seem to be the most efficient in terms of stiffness and weight. Meanwhile, some cellular cores, such as Skeletal-TPMS or some two-dimensional designs, appear to compromise the stiffness of the assembly to a greater extent when very low-density patterns are used. In addition, the sandwich arrangement composed of CFRP skins made of a 0.286 mm single ply ($f = 0.028$) proves to be optimal in all cases.

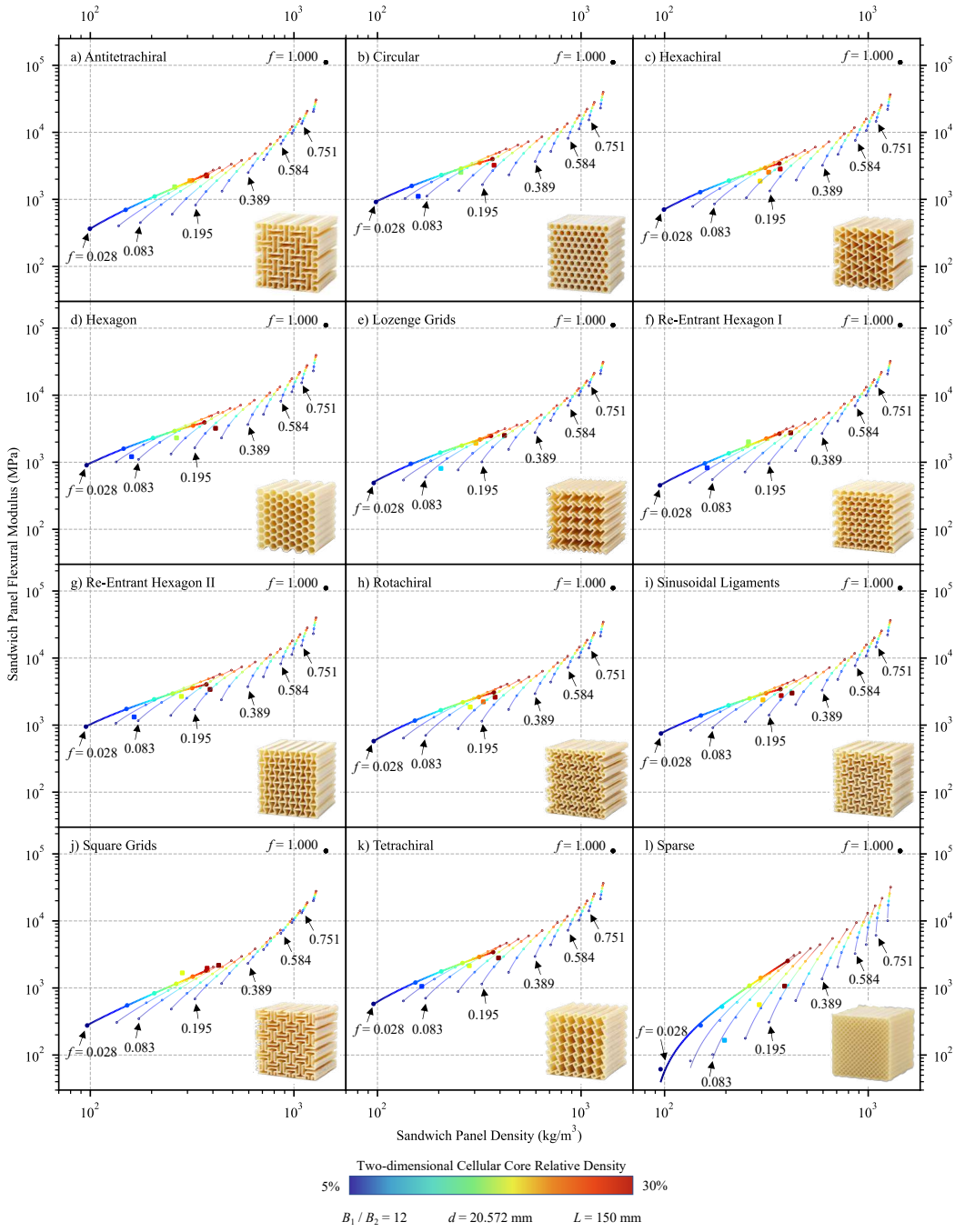

Figure 4.20: Numerically simulated flexural moduli of hybrid sandwich panels with two-dimensional FFF cellular cores considering multiple sandwich arrangements and core densities.

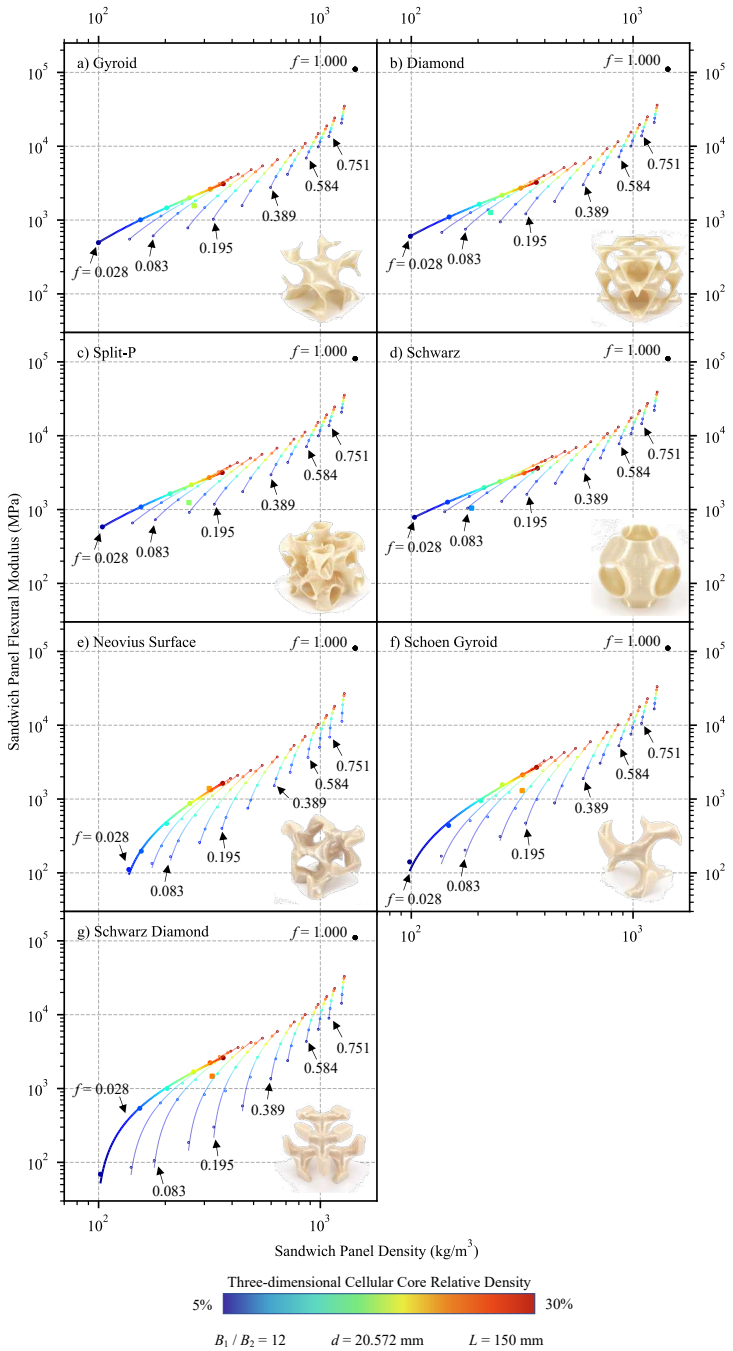

Figure 4.21: Numerically simulated flexural moduli of hybrid sandwich panels with three-dimensional FFF cellular cores considering multiple sandwich arrangements and core densities.

Furthermore, the experimental results of flexural moduli of the most optimal configurations of each two- and three-dimensional cellular core design are overlapped with the simulated trends in Figures 4.20 and 4.21, respectively. In particular, the single CFRP ply per sandwich skin arrangement was selected for the experimental validation tests, considering 3 different core density levels in each case. Depicted results confirm the accuracy of the developed FE model for the simulation of the bending performance of hybrid sandwich structures using different typologies of cellular solids as core material and unidirectional CFRP skins.

Finally, all the experimental flexural moduli and strength values, which are detailed in Table 4.6, are compared with the rest of the materials included in the Ansys GRANTA EduPack database in Figure 4.22. In addition, the values corresponding to reference cores[2] have been included.

The use of hybrid sandwich structures allows covering a very interesting area in both charts of Figure 4.22. As can be seen, the cellular cores manufactured by FFF improve the performance of foam-core sandwich structures, but their mechanical properties are slightly lower than the values obtained using the reference Aluminum and Nomex® honeycomb materials. This fact is due to the manufacturing methods used for the fabrication of the latter, which can obtain patterns with very thin walls compared to the employed AM technology. Therefore, commercial honeycombs have density values up to an order of magnitude lower than the printed cellular solids (see Figure 4.10).

All things considered, the results of this research demonstrate that there are more efficient cell designs than the hexagonal pattern used in commercial alternatives. Therefore, the advancement of existing AM technologies and the development of new methods to reduce the minimum wall width would help to increase the efficiency of sandwich structures using cellular cores.

Table 4.6: Results obtained from the experimental tests of hybrid sandwich panels under 3-point bending loads.

Core design	Core rel. density (%)	$\tilde{E}_{flex}$ (MPa)	$\tilde{\sigma}_{flex}$ (MPa)	Failure code	Core design	Core rel. density (%)	$\tilde{E}_{flex}$ (MPa)	$\tilde{\sigma}_{flex}$ (MPa)	Failure code
Antitetrachiral	28.75	2235 ±6	16.9 ±3.1	DAC	Circular	28.73	3233 ±140	25.5 ±0.4	FAT
	22.99	1894 ±10	13.7 ±2.6	DAC		18.10	2526 ±0	17.8 ±1.1	FAT
	18.39	1541 ±11	12.5 ±1.8	DAC		9.14	1112 ±67	8.3 ±0.2	FAT
Hexachiral	28.50	2841 ±145	31.9 ±0.5	FAT	Hexagon	32.42	3207 ±79	24.3 ±7.2	DAC
	24.45	2540 ±117	23.1 ±0.5	FAT		18.94	2308 ±58	15.1 ±2.7	DAC
	21.71	1875 ±140	15.1 ±3.0	FAT		9.37	1211 ±5	10.3 ±0.6	DAC

Continued on next page

[2]Considered reference cores: Aluminium honeycombs, Nomex® honeycomb, and foam (see Figure 3.15 in Section 3.3.2 of Chapter 3).

Table 4.6 – continued from previous page

Core design	Core rel. density (%)	$\tilde{E}_{flex}$ (MPa)	$\tilde{\sigma}_{flex}$ (MPa)	Failure code	Core design	Core rel. density (%)	$\tilde{E}_{flex}$ (MPa)	$\tilde{\sigma}_{flex}$ (MPa)	Failure code
Lozenge Grids	33.16	2511 ±251	21.5 ±4.4	FAT	Re-Entrant Hexagon I	32.74	2748 ±45	21.9 ±1.2	DAA
	22.56	1922 ±191	20.6 ±5.4	FAT		18.39	2013 ±21	22.5 ±0.4	DAC
	13.49	808 ±17	8.2 ±3.1	DAC		9.46	825 ±7	9.6 ±1.0	DAC
Re-Entrant Hexagon II	30.14	3407 ±126	30.4 ±22.9	FAT	Rotachiral	29.31	2610 ±155	34.3 ±0.1	FAT
	20.29	2682 ±79	23.2 ±5.1	FAT		25.05	2225 ±134	21.0 ±13.7	DAC
	9.64	1323 ±14	9.6 ±0.3	DAA		20.79	1862 ±98	16.5 ±8.4	DAC
Sinusoidal Ligaments	33.35	3003 ±421	20.4 ±9.3	FAT	Square Grids	33.90	2177 ±10	17.7 ±0.3	DAA
	28.84	2755 ±73	18.9 ±1.8	FAT		28.92	1969 ±79	19.7 ±0.2	FAT
	22.56	2380 ±168	25.8 ±13.2	DAC		20.56	1679 ±82	14.0 ±0.0	DAC
Tetrachiral	30.56	2804 ±89	30.1 ±2.9	FAT	Sparse	30.19	1066 ±12	23.8 ±0.1	FAT
	20.51	2148 ±71	19.8 ±2.1	FAT		21.26	563 ±11	13.0 ±0.8	SAC
	9.68	1057 ±12	11.0 ±1.1	FAT		12.54	166 ±2	3.8 ±1.1	SAC
Gyroid	15.56	1266 ±5	11.1 ±0.6	FAT	Diamond	19.30	1564 ±15	15.6 ±0.3	FAT
Split-P	18.05	1242 ±4	15.0 ±1.1	FAT	Scwharz	11.84	1045 ±6	6.8 ±0.2	DAA
Neovius Surface	23.52	1389 ±14	10.8 ±0.3	FAT	Schoen Gyroid	23.64	1302 ±18	9.0 ±2.2	DAA
Schwarz Diamond	24.39	1468 ±7	10.9 ±3.6	DAA					
PU250 Foam	20.55	1475 ±171	14.9 ±0.8	FAT	Nomex® honeycomb	4.40	5320 ±17	24.8 ±1.6	CAC
Aluminum honeycomb	6.46	13097 ±132	40.5 ±2.3	CAC					
	2.19	5549 ±3	9.4 ±0.8	CAC					

4.4 Summary and outlook

In summary, the feasibility of hybrid sandwich structures fabricated with CFRP skins and additively manufactured lightweight cellular cores produced by FFF has been addressed by combining different analytical, experimental, and numerical approaches at three levels of detail: material, cellular core design, and sandwich structure.

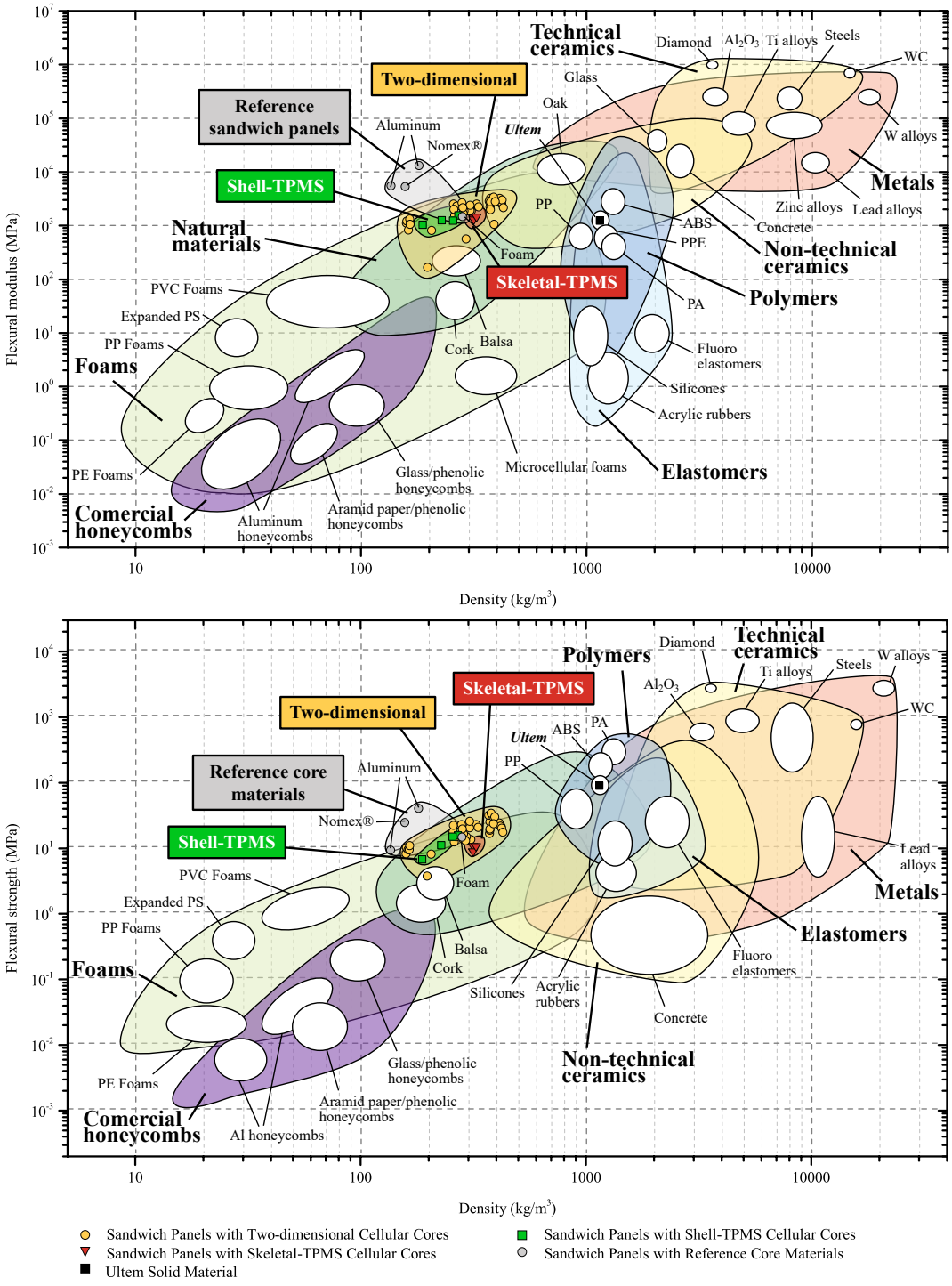

Figure 4.22: Comparison of the experimental performance of hybrid sandwich panels composed of two- and three-dimensional FFF cellular cores with materials database adapted from CES EduPack 2019, ANSYS Granta©2020 Granta Design, with permission.

First, the characterization of Ultem processed by FFF revealed the orthotropy of the produced components inherent to the layer-by-layer fabrication process. In addition, the use of porous infills, such as the Sparse pattern, significantly reduces fabrication time while favoring material savings, and its impact on the mechanical performance of the printed pars has been quantified.

Secondly, the analysis of the wide range of two- and three-dimensional cellular solids considered in this work has confirmed the advantages of three-dimensional Shell-TPMS designs over Skeletal-TPMS and two-dimensional patterns from the standpoint of fabrication and structural efficiency. In particular, their morphology can be fabricated by FFF without requiring additional support structures and employing continuous deposition paths, which favors the reduction of intra-layer and inter-layer joints, thus improving the strength of the cellular structure. In addition, the periodicity and homogeneity of Shell-TPMS samples in the 3D space provide them with a much higher degree of isotropy than the rest of the designs analyzed, which has been quantified with the new A^V Anisotropy index based on the volume of the graphical representation of the unit cell's stiffness tensor, proposed in this thesis.

Finally, the results obtained by implementing the studied cellular solids as cores in hybrid sandwich panels verified the potential of these designs to manufacture lightweight, functional, and very efficient structures. The findings of this research confirm that patterns of higher geometrical complexity than the hexagon, such as Shell-TPMS designs, whose manufacturing is unfeasible by other fabrication methods, offer better performance for the same density. Moreover, forthcoming developments in the FFF technology, as well as the use of other AM methods, could allow the fabrication of two- and three-dimensional cellular cores with thinner walls and improved quality, which could be a decisive advantage to differentiate them from the reference core materials.

5

Conclusions and future work

This chapter summarizes the most relevant insights of the present research, focused on the analysis of hybrid sandwich structures combining CFRP skins and additively manufactured lightweight cellular cores. After presenting the overall conclusions, the main contributions of this investigation are also summarized. Additionally, recommendations on how this study could be further expanded are provided, based on the implications of the obtained results.

5.1 General conclusions

The objective of this thesis was to assess the design and fabrication of cellular solids for lightweight hybrid sandwich structures using FFF technology. To do so, the constituent material properties, cellular design performance, and flexural behavior of the composite assembly were analyzed to establish a robust framework for the creation of high-performance structures for multiple engineering applications. Based on the results analyzed so far, the following conclusions can be drawn:

- An accurate control of FFF printing parameters, such as part orientation, raster angle, and raster-to-raster air gap, allows tailoring the mechanical properties and the degree of anisotropy of the manufactured components to the requirements of each application. In addition, they allow optimizing the weight of the manufactured parts in order to achieve more efficient structures. The obtained tensile and flexural moduli results ranged between 1935 and 2360 MPa for all solid configurations, being specimens manufactured with an orientation perpendicular to the printing plane the less rigid ones. Major differences were noticed in both the stress and strain values at yield (17-90 MPa, 1.1-6.7%) and break (20-122 MPa, 2.0-10.3%), where the mechanical properties of the flexural specimens were up to three times higher than the ones achieved by the tensile samples. Thus, according to the wide range of recorded values, appropriate control of all the evaluated design parameters would allow the fabrication of functional end parts with improved mechanical performance.

- Deposition paths, as well as both the intra-layer and the inter-layer filament bonds, directly impact the stiffness, strength, and type of failure of the printed parts. In particular, the obtained results confirm that the rigidity along the direction of the extruded filament is greater than the one of the intra-layer unions between contiguous rasters, while the stiffness of the inter-layer cohesion of adjacent layers is the lowest one. This phenomenon is due to the temperature gradient between the deposited filament and the last layer built that occurs. In this sense, the use of a thermal chamber during the whole manufacturing process helps to reduce the temperature difference produced by the cooling of the part, which strengthens material unions, improves mechanical performance, and decreases anisotropy.

- The introduction of a raster-to-raster air gap in the infill configuration leads to an up to 60% reduction of the manufacturing costs associated with material use and printing time, while the specific mechanical properties are comparable to those achieved with the solid configurations or even superior, particularly in the strain range.

- Overall, the calculated compliance matrices verify the inherent orthotropy of components produced by FFF technology and are valuable for the validation of forthcoming numerical models addressing different infill configurations.

- The outcomes of this investigation provide comprehensive research on the FFF technology's possibilities to achieve a wide spectrum of specific stiffnesses and strengths starting from the intrinsic properties of a single solid material, depending on the selected cellular geometry and

size. Hence, an accurate adjustment of the unit cell shape can lead to structures of metamaterials with equivalent densities but with very contrasting mechanical performances.

- In particular, the results obtained from the study of additively manufactured cellular solids verify that three-dimensional designs have a slight advantage over two-dimensional ones in terms of manufacturability, mechanical performance and structural efficiency. The extruded-like geometry of two-dimensional designs makes it impossible to fabricate them using continuous FFF deposition paths, which significantly increases the printing time. In addition, digital microscopic analysis revealed different manufacturing defects and highlighted the importance of optimizing printing trajectories.

- Intra-layer defects tend to occur mostly in certain types of these designs depending on their shape, either due to imperfections between cell connections or due to excessive deposition of material at filament's intersection points. Further, inter-layer defects are caused by inappropriate wall connectivity, which dramatically impacts the pattern's mechanical behavior when it is evaluated in the in-plane directions. Meanwhile, the smooth curvature of Shell-TPMS designs avoids the use of support structures during manufacturing, requiring less than half the fabrication time of the other three-dimensional cellular solids.

- The elastic modulus, compression strength, and energy absorption efficiency of three-dimensional designs are superior to that exhibited by two-dimensional patterns in the in-plane cell's orientation for equivalent relative densities. In particular, Shell-TPMS designs stood as the most efficient cellular solids, followed by the Skeletal-TPMS and lattice configurations. However, the highest stiffnesses were registered in the out-of-plane tests of two-dimensional patterns, whose values can now be calculated employing the parametric equations developed in this thesis prior to manufacturing.

- Two validated strategies for simulating the elastic behavior of cellular solids have also been presented, comparing their accuracy and computational requirements. In short, the H-RVE approach has computational advantages (uses 90% less time) but does not allow the simulation of local effects on the cell walls. In contrast, the SE model can reproduce the elastic behavior satisfactorily, including those local effects, but at a higher computational cost. In particular, this second approach successfully identified the stress concentration regions of the lattice and Skeletal-TPMS designs where the experimental failure occurred. In addition, the obtained results proved that the morphology of Shell-TPMS designs favors a more homogeneous stress distribution, which improves the mechanical performance of the cellular structure.

- A novel anisotropy index A^V based on the graphical representation of the homogenized stiffness tensor was proposed. It allows the comparison of the degree of anisotropy of the cellular solids more robustly, regarding important aspects such as the inherent anisotropy of the FFF manufacturing process. To this end, the expected higher degree of isotropy that the three-dimensional designs exhibit thanks to their geometric homogeneity in the 3D space in comparison to the two-dimensional patterns was verified and successfully quantified.

- The results achieved when implementing the cellular solids as lightweight cores in hybrid sandwich panels together with CFRP skins confirm the importance of the design and density in the flexural performance of the structure. In particular, the two-dimensional Circular, Hexachiral, Hexagon, Re-Entrant Hexagon II, and Sinusoidal Ligaments designs, as well as the three-dimensional Shell-TPMS morphologies, are the most efficient in terms of stiffness and weight. However, Skeletal-TPMS designs and the rest of the two-dimensional patterns seem to compromise the stiffness of the assembly to a greater extent when reducing core density. In all cases, the optimum manufacturing of the sandwich panels according to the employed test conditions is to set the fraction of the nominal cross-section occupied by its faces f at 0.028.

- The mechanical behavior of the analyzed structures confirms the potential of cellular designs of high geometric complexity for the fabrication of more efficient lightweight components, taking advantage of the latest advances in AM technologies such as the one used in this research. However, the current state of development of FFF still presents certain technical shortcomings, such as the minimum thickness of the deposited filament and maximum printing speed. Thus, these aspects now limit the feasibility of manufacturing lighter cellular solids, which could stand out from the reference core materials.

- The provided numerical approach for simulating the bending performance of hybrid sandwich panels using different typologies of cellular solids as core material and CFRP skins is a powerful tool to further contribute to the development of efficient structures while waiting for the appropriate level of technological maturity.

5.2 Research contributions

The results achieved during this thesis contribute to the following scientific findings:

- A comprehensive study of the anisotropy of Ultem processed by FFF under different loading states and considering six different infill configurations has been provided.

- A wide range of two- and three-dimensional cellular designs have been analyzed using the same material, printing technology and testing methodology, in order to evaluate their efficiency and manufacturing feasibility while investigating how the mechanical behavior is affected by the geometry, density, and arrangement of the cells.

- A set of verified mathematical equations have been provided to predict the density and stiffness of two-dimensional cellular solids according to their parametric dimensions and the mechanical properties of the material to be used for their fabrication.

- Different numerical models have been validated to simulate both the compression and the flexural behavior of the isolated cellular designs, as well as the flexural response of hybrid sandwich structures combining cellular cores with CFRP skins, contrasting their accuracy and the corresponding computational cost.

- An open-source software called TPMSgen has been developed and released. It is specific for the parametrical design of three-dimensional cellular structures and was employed for the generation of some of the samples tested in this research.
- A large number of experimental evidence have been provided to verify the analytical and numerical results obtained from this research, which are useful to further contribute to the development of new lightweight structures taking advantage of the disruptive capabilities of AM technologies.
- The structural feasibility of implementing two- and three-dimensional cellular solids produced using FFF technology as core materials in composite sandwich structures together with CFRP skins has been verified, thus validating the potential of these advanced designs for fabricating more efficient structures.

5.3 Future research perspectives

Based on the aforementioned conclusions, future studies could focus on:

- To evaluate the mechanical capabilities of the different two-dimensional and three-dimensional cellular designs under dynamic stresses, such as fatigue and impact tests. These conditions could enhance the structural potential of those patterns that exhibit an auxetic behavior, which was especially identified in some of the two-dimensional designs considered in this research.
- Optimizing material deposition paths to reduce the presence of defects in filament bonds, which could result to be very interesting to enhance the structural capabilities of two-dimensional designs, especially in the in-plane directions. Furthermore, the development of smaller diameter FFF extruders that guarantee a correct material flow would allow the fabrication of much lighter cellular solids at a very low cost, and reach the levels of density of reference core materials.
- Studying the feasibility of implementing FFF equipment with more than one extrusion head for single-stage fabrication of hybrid sandwich structures, using continuous carbon fiber extruders. This advanced manufacturing process could increase the strength of the composite panels by achieving a better adhesion between the core and the skins as well as significantly reduce production costs, making better use of materials and resources and avoiding waste generation.
- Exploring new bio-inspired lightweight designs, contemplating the use of other materials and different AM technologies. Among other aspects, it would be interesting to compare the behavior of periodic cells, such as those of the present research, with cores of heterogeneous density, or even consider the possibility of implementing topological optimization procedures. In addition, making the leap to other materials, such as metals, would allow starting from significantly superior mechanical properties, thus obtaining sandwich panels with very different performances from the ones achieved.

- Investigating and optimizing material recovery and recycling processes to make them suitable to treat the developed hybrid sandwich panels, aiming to be prepared to treat the waste generated when these structures reach their end of life and lose their structural functionality.

6

Appended publications

Publication I:

Role of infill parameters on the mechanical performance and weight reduction of PEI Ultem processed by FFF

10.1016/j.matdes.2020.108810

Materials and Design 193 (2020) 108810

Contents lists available at ScienceDirect

Materials and Design

journal homepage: www.elsevier.com/locate/matdes

Role of infill parameters on the mechanical performance and weight reduction of PEI Ultem processed by FFF

Albert Forés-Garriga, Marco A. Pérez *, Giovanni Gómez-Gras, Guillermo Reyes-Pozo

IQS School of Engineering, Universitat Ramon Llull, Via Augusta 390, 08017 Barcelona, Spain

HIGHLIGHTS

- The role of infill parameters and printing direction on the strength and elastic properties of PEI samples is investigated.
- Experimental data allows quantifying the impact on the stiffness, resilience, maximum stress, and type of failure.
- The temperature chamber strengthens inter-layer unions improving mechanical performance and diminishes the orthotropy.
- Three-dimensional compliance matrices for six different solid and sparse configurations are provided and discussed.

GRAPHICAL ABSTRACT

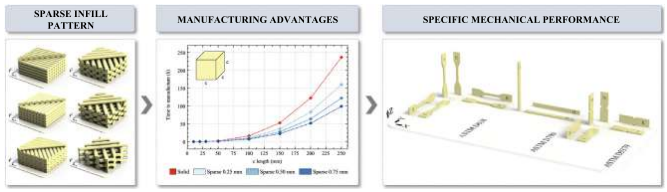

ARTICLE INFO

Article history:
Received 30 March 2020
Received in revised form 13 May 2020
Accepted 13 May 2020
Available online 20 May 2020

Keywords:
Additive manufacturing
Fused filament fabrication
PEI Ultem
Infill
Mechanical properties
Constitutive matrix

ABSTRACT

In comparison with conventional manufacturing technologies, Fused Filament Fabrication (FFF) offers countless benefits. It broadens the horizons of the design of structural components with high geometrical complexity, and lighter elements can be obtained by optimizing the infill of the part. The infill density stands as a manufacturing parameter that plays a significant part in weight reduction purposes. This fact provides FFF with an outstanding competitive advantage as compared to the rest of the additive manufacturing technologies. This work aims to investigate the role of infill parameters on the mechanical performance and weight reduction of ULTEM™ 9085 samples processed by FFF, under tensile, flexural, and shear loading conditions in six different orientations with several solid and sparse configurations. Regarding the effect of the part orientation and the infill settings, the experimental results permit to draw conclusions on stiffness, resilience, maximum stress, and type of failure of the printed parts. Three-dimensional compliance matrices for each infill configuration are provided. The analysis of the results correlates the infill configuration with the mechanical performance considering the intra-layer and inter-layer unions. Finally, this research provides experimental evidence to contribute to the definition of novel design-for-manufacturing strategies for obtaining functional structural elements by FFF.

1. Introduction

A new age of digital manufacturing has transformed the way things are produced. Under the name of Industry 4.0 revolution, numerous developments are occurring at the same time in multiple fields. Additive Manufacturing (AM) is at the forefront of these transformations. In the last decade, this continually evolving technology has widened the horizons of the fabrication possibilities. This fact has led to a complete change of the way how parts are designed and produced in a wide range of sectors, including automotive, energy, aerospace, and biomedical [1]. Among the many techniques encompassed by AM [2,3], Fused Filament

* Corresponding author.
E-mail address: marcoantonio.perez@iqs.edu (M.A. Pérez).

https://doi.org/10.1016/j.matdes.2020.108810

Fabrication (FFF) rises above the others. This technology, also commercially known as Fused Deposition Modelling (FDM), excels mainly due to its versatility, since it is suitable for working with a wide range of materials. The evolution of FFF has positioned it as a potential candidate for the industrial sector as it allows to construct components with a high geometrical complexity that can be produced neither at low costs nor in a short time with conventional manufacturing technologies.

In this 3D printing technology, a thermoplastic filament is deposited in thin layers by an extrusion head that moves according to the building toolpaths. The material is heated a few degrees above its glass transition temperature, which causes an almost instantaneous solidification when it comes into contact with the last manufactured layer. The new layer is adhered to the adjacent one, while the volume of the whole part gets constructed. The main setting parameters are sample orientation, layer thickness, raster angle, and raster-to-raster air gap.

One remarkable feature of the FFF is its feasibility to fabricate lighter structures by optimizing the infill of the part. The infill density stands as a manufacturing parameter that plays a significant role in the strategy to reduce weight, which provides FFF with an outstanding competitive advantage as compared to the rest of AM technologies [4]. This fact, together with the development of high-performance polymeric materials with remarkable specific strength and stiffness, allows the obtention of functional structural elements. As an illustrative example, Fig. 1 depicts the role of the air gap parameter on the manufacturing time and required material volume for the production of cubes of different sizes. Data of time to manufacture in minutes and material volume in cubic centimeters is added in text boxes to notice the remarkable differences between curves when a short side length is evaluated. Each curve corresponds to a different air gap setting, as indicated in the legend.

Accordingly, the study of the mechanical performance of structures with a low infill density is of great interest to the AM community. Published contributions have been mostly focused on the mechanical analysis of the inherent anisotropy induced by the technique in solid configurations [5–7]. For instance, extensive studies of the behavior of acrylonitrile butadiene styrene (ABS) FFF parts under tensile, flexural, and compression states were conducted [8,9], as well as in fatigue conditions [10]. These results awakened the interest towards a numerical approach of the processed material [11]. Polylactic acid (PLA) was also investigated with the same purpose [12–14], and the influences of building parameters on the fatigue life were also evaluated [15]. The same analyses were attempted with polycarbonate (PC) [16], whose results provided a stiffness matrix that described the performance of this material depending on the manufacturing parameters [17]. Other investigations with the same material deepened in its fracture behavior [18,19] and the creep effect [20]. Simultaneously, other authors offered a numerical approach of its performance in fatigue conditions [21].

Among the range of thermoplastic materials analyzed in recent years, ULTEM^{TM} 9085 (PEI Ultem) [22–24] soars above the rest. This high-performance polyetherimide (PEI) offers outstanding properties for multiple industrial purposes. It features a remarkable strength-to-weight ratio and impact strength with excellent heat resistance, as well as flame-retardant capacity, and promising flame-smoke-toxicity (FST) characteristics. For all these reasons, PEI Ultem becomes especially outstanding for applications in the transport and aerospace sectors [25,26]. Thanks to applications like these, the interest in PEI Ultem keeps growing, but many areas of study are still needed to be explored. For example, its tensile behavior has been documented [27–30], as well as its response to flexural and compression tests [31–33], and its fatigue strength compared with other thermoplastics [34]. The consequences of moisture absorption in the PEI Ultem filament before printing [35] and its impact resistance [36] have also been investigated. Meanwhile, the chemical similarities between PEI Ultem and its support material pose particular challenges for the elimination of the second one. For this reason, other authors focused their work on developing a novel solvent support-removal methodology [37].

However, to the knowledge of the authors, the benefits associated with the influence of the rasters separation in terms of weight decrease, reduction of material consumption, and production time are yet not fully understood. Further, the optimization of mechanical performance by just modifying the infill configuration can be crucial to bringing this technology to the forefront of industrial manufacturing.

Accordingly, the purpose of this work is to investigate the role that the infill parameters play in the mechanical performance and weight reduction of PEI Ultem processed by FFF under multiple load conditions. This study aims to provide experimental evidence to contribute further to the definition of novel design-for-manufacturing strategies with an in-deep analysis of accurate data related to the performance of PEI Ultem. Thus, the mechanical behavior of this material is evaluated regarding the benefits of structural weight reduction, material savings, and shorter time to manufacture.

2. Methodology

2.1. Design of experiments

Tensile, flexural, and shear loading tests were conducted to identify the role that the FFF building parameters play on mechanical performance and weight reduction. The building parameters chosen for this study were sample orientation, raster angle, and raster-to-raster air gap. These parameters were used for changing the internal design of the parts. The intra-layer orientation of the filaments was set with the raster angle value. The air gap refers to the separation between two parallel rasters. Thus, the manufactured parts can be grouped into two main configurations: solid (air gap = 0 mm) and sparse (air gap > 0 mm). The design of experiments is shown in Table 1, and the manufactured part orientations are represented in Fig. 2.

In order to identify the effect of the direction of the deposited filaments on the mechanical performance of solid specimens, three

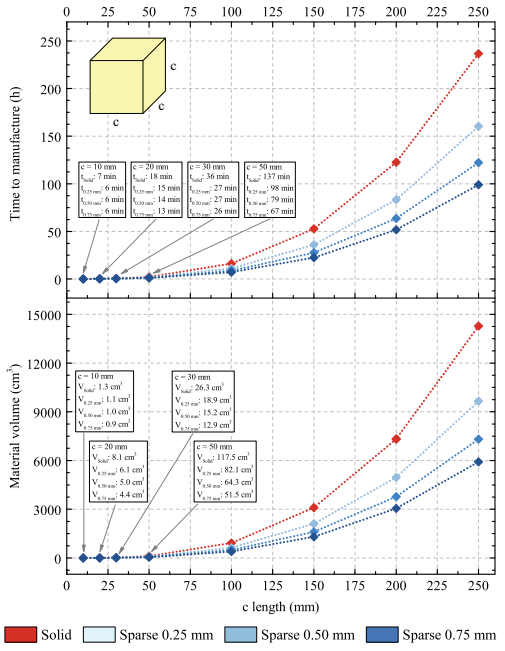

Fig. 1. Impact of the raster-to-raster air gap on the time to manufacture (top) and the material volume (bottom) of a PEI Ultem solid cube part, depending on its side length.

Table 1
Set of samples' orientations for each infill tested configuration.

ASTM test standard	Solid configuration			Sparse configuration		
	Air gap	Raster angle	Part orientation	Air gap	Raster angle	Part orientation
D638 [38]	0.00 mm	0° 90° ±45°	X-Flat/Edge Y-Flat/Edge Z-Flat/Edge	0.25 mm 0.50 mm 0.75 mm	±45°	X-Flat/Edge Z-Edge
D790 [39]	0.00 mm	0° 90° ±45°	X-Flat/Edge Z-Edge	0.25 mm 0.50 mm 0.75 mm	±45°	X-Flat/Edge Z-Edge
D5379 [40]	0.00 mm	0° 90° ±45°	X-Flat/Edge Y-Flat/Edge Z-Flat/Edge	0.25 mm 0.50 mm 0.75 mm	±45°	X-Flat/Edge Y-Flat/Edge Z-Flat/Edge

different interior raster angles were studied: 0°, 90°, and ±45°. It should be noted that not all the raster angle values may be convenient for the use of sparse for structural applications as some values may cause issues between intra-layer raster connections. Unidirectional sparse configurations dramatically reduce the consistency of these low-density parts in some particular testing directions. Therefore, only the raster angle of ±45° was considered suitable for manufacturing with any sparse configuration. Regarding the dimensions of the ASTM specimens, the considered air gap values were 0.25 mm, 0.50 mm, and 0.75 mm.

Each solid and sparse configuration was characterized in all three cartesian orientations (X, Y, and Z), as shown in Fig. 2. Due to the shape of the ASTM specimens, infill toolpaths depend on the arrangement of the part on the building bed (Flat or Edge). Thus, the possible anisotropic properties of the material have to be evaluated for every raster angle, particularly when a unidirectional configuration is used (0° or 90°).

Tensile tests were carried along the X, Y, and Z axes to verify any possible degree of isotropy in every solid configuration, and particularly the expected orthotropy in the ±45° ones. Preliminary results demonstrated that equivalent specimens were obtained if samples are rotated 90° around the Z-axis of the printing bed. Therefore, the orientations X-Flat, X-Edge, and Z-Edge were considered enough for the complete evaluation of the tensile mechanical performance of the sparse samples.

Flexural tests were conducted in all configurations to study the differences between intra-layer and inter-layer bending properties. To this end, and considering the stated equivalence of samples, specimens were manufactured and evaluated just in X-Flat, X-Edge, and Z-Edge directions for both solid and sparse configurations.

Additionally, a full factorial design of experiments was performed for the shear tests. On this account, identical part orientations were tested in both solid and sparse configurations.

To test the repeatability of all experiments, a minimum of three specimens per infill configuration were tested for each orientation, as detailed in Fig. 2. This led to a total amount of 277 tested specimens.[1]

2.2. Manufacturing of samples

A Coordinate Machine Binary file (CMB) was generated for each sample using the Insight software from Stratasys. These files include all the necessary information for manufacturing the samples according to the proposed design of experiments. The slice height value was set to 0.254 mm. All the samples were built with one external contour to accentuate the impact of the infill configuration on the mechanical performance. The seam control options were modified in order to remove the joint of the contour from the gauge section and the transition radius region. Both contour and part raster widths were established at 0.508 mm. In all cases, the minimization of the transition moves was activated, and appropriate infill trajectories were achieved by adjusting the raster angle parameter. The parallel offset part rasters feature was applied for the preparation of the solid samples that needed an infill of 0° or 90°. This avoids having a continuous defect along the height of the part when a unidirectional raster angle is selected. Different sparse configurations were generated by adding distance between filaments with the raster-to-raster air gap value.

Samples were fabricated using a Stratasys Fortus 400mc FDM equipment. This printer is equipped with a temperature chamber that ensures a controlled temperature during the entire manufacturing process. This controlled environment is crucial as it significantly enhances the inter-layer cohesion between adjacent building layers. Regarding the supplier indications, the optimum working conditions for postprocessing PEI Ultem require an oven temperature of 195°C. The extrusion temperature for the model material (PEI Ultem) is 380°C, and for the support material (PSF polysulfone) is 421°C. Once the samples were printed, support structures were removed, and the mass and the dimensions of each sample were measured before testing.

2.3. Mechanical testing

Differences in the real effective cross-sectional area and in the front surface of the tensile samples are shown in Fig. 3. The schematic 3D representations depicted in Fig. 4 show the impact that the infill configuration has on both the size and the location of the internal gaps. However, for the sake of simplicity, the nominal section measurements were used for the stress calculations.

2.3.1. Experimental setup

Tensile, flexural, and shear tests were performed using ZwickRoell Z030 equipment. A 3D Digital Image Correlation (DIC) setup was integrated for the investigation of full-field deformation in tensile and shear tests. Two Allied Vision GigE MAKO G-507B cameras with APO-Xenoplan 1.4/23–0903 lens were used for recording the displacements on the surface of the samples. Specimens were previously sprayed with a black and white stochastic pattern. The system was calibrated with a GOM Correlate CP20/MV55x44 panel. The video sequences were treated with GOM Correlate Professional software to analyze the full-field deformation of the samples.

2.3.2. Tensile testing

Tensile tests were conducted following the ASTM D638 standard [38] (see Fig. 2). Specimen type IV was chosen with a thickness of 4 mm. The yield point was determined with an offset method of 0.1% strain. Two perpendicular DIC extensometers placed in the center of the gauge section of each specimen were used for the calculation of the Poisson's coefficients within the elastic region. Results of tensile modulus, yield stress, yield strain, tensile strength, and strain at tensile strength were reported.

2.3.3. Flexural testing

Three-point bending tests were conducted following the ASTM D790 standard [39] (see Fig. 2). The thickness of the specimens was set to 4 mm. The geometry of samples was defined with 64 mm support span, 10 mm width, and 127 mm length, in agreement with the test

[1] Tensile testing: 115 samples (70 solid and 45 sparse). Flexural testing: 54 samples (27 solid and 27 sparse). Shear testing: 108 samples (54 solid and 54 sparse).

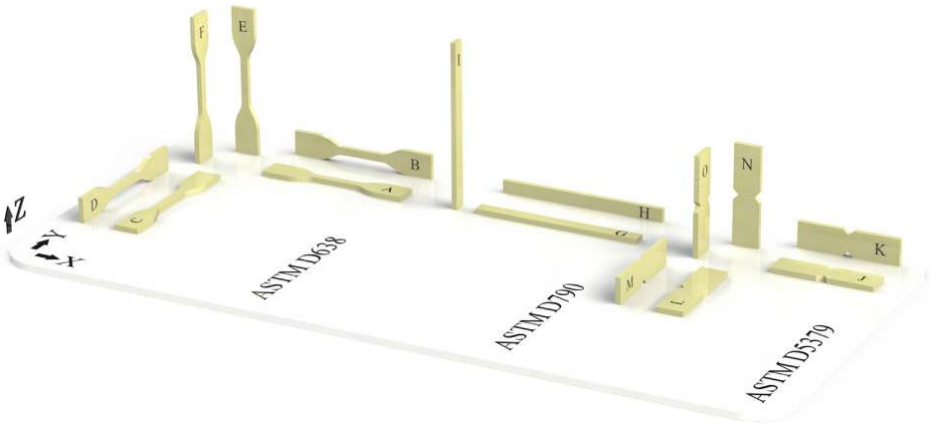

Fig. 2. Building orientations of all the manufactured test samples. ASTM D638 [38]: X-Flat (A), X-Edge (B), Y-Flat (C), Y-Edge (D), Z-Flat (E), Z-Edge (F); ASTM D790 [39]: X-Flat (G), X-Edge (H), Z-Edge (I); ASTM D5379 [40]: X-Flat (J), X-Edge (K), Y-Flat (L), Y-Edge (M), Z-Flat (N), Z-Edge (O).

standard. Under these conditions, the rate of crosshead displacement resulted in 1.71 mm/min. The yield point was determined with an offset method of 0.1% strain. Although ASTM D790 suggests ending the test when a 5% of strain is reached, all the samples were tested until failure occurred. Flexural modulus, yield stress, yield strain, flexural strength, and strain at flexural strength results were reported.

2.3.4. Shear testing

ASTM D5379 test standard [40] (see Figs. 2 and 5) was followed for shear testing. The thickness of the specimens was set to 4 mm. With the used samples, no twisting effect was observed during the test. Therefore, the use of additional tabs was unnecessary. DIC equipment allowed the measurement of the shear strain at the center of the specimen. Although the test standard recommends stopping the test when a 5% of strain is reached, the shear tests were conducted until failure occurred. The yield point was estimated using the offset method with a strain of 0.2%. Shear modulus, yield point data, shear strength, and strain at shear strength values were reported.

3. Results and discussion

3.1. Tensile testing

Fig. 6 shows representative data from the tensile tests conducted with the configurations previously described (see Fig. 2). Apparent differences in stress and strain values can be observed between samples. However, some samples present brittle fracture while others show a larger plastic region. It should be noted that, in the case of sparse configurations, the stress axis has been scaled for the reader's convenience.

Fig. 7 shows the results of tensile testing. The charts in the left column collect the results of the following tensile properties: tensile modulus, yield stress, strain at yield stress, and maximum stress and its corresponding strain. On the one hand, it was observed that the toolpaths in the gauge region have minor differences if the arrangement is Flat (6 × 4 mm) or Edge (4 × 6 mm). Thus, the mean value and the corresponding standard deviation of the results were calculated for every test orientation (X, Y, and Z) regardless of the fabrication arrangement (Flat or Edge). On the other hand, the charts in the right side of the figure show mass-normalized values of the properties mentioned above. These average values have been calculated by dividing the obtained test results of each specimen over its corresponding mass.

Focusing on the left column graphs, all solid configurations achieve similar results regardless of the orientation of the rasters, especially in the elastic region (charts *a*, *c*, and *e*). These results indicate the existence of an orthotropic behavior that does not become as outstanding as it was initially expected. This fact can be attributed to the strength of the existent joints between coplanar filaments (intra-layer unions) and between adjacent layers (inter-layer unions). The used 3D printer ensures that the temperature in the building chamber is tightly controlled during the entire manufacturing process to enhance this phenomenon. This reduces the thermal shock that takes place when the extruded filament is deposited and enters in contact with the last built layer to improve the quality of the final parts.

Nonetheless, the maximum strength of the specimens in the Z test orientation is markedly inferior to that achieved in the X and Y directions (51.2, 44.3% of reduction for 0°; 39.0, 44.7% for 90°; and 36.8, 39.1% for ±45° in X, Y directions, respectively). Furthermore, specimens oriented along the X or Y axes show a plastic fracture caused by the elongation of the deposited filaments. The fracture in the Z direction tests leads to the separation of two contiguous layers in manufacturing, which happens abruptly, resulting in a brittle type of failure. Thus, obtained results state the lower resistance of the joints between layers in comparison to that of the filament itself. This fact confirms a remarkable degree of orthotropy when the strength of the processed material is evaluated.

The results also verify that a 90° rotation of the parts around the Z-axis when manufacturing has insignificant effects on the mechanical properties. This equivalence of samples could initially be expected by analyzing the toolpaths generated in the CMB file. Furthermore, the noticeable similarities while comparing the experimental results obtained in the X_0-Y_{90}, X_{90}-Y_0, and $X_{\pm45}$-$Y_{\pm45}$ configurations evidence this hypothesis. These results confirm the reproducibility of the professional printer for manufacturing parts with the same toolpaths regardless of their rotation around the Z-axis on the building bed. The application of this assumption of equivalence of samples made it possible to remove the Y orientations from the design of experiments of the tests to perform with the sparse configurations.

Tests on sparse samples conclude that similar results are seen in the X orientation regardless of the degree of densification used. However, this air gap parameter appears to have a more evident impact when the material is evaluated in the Z orientation. This

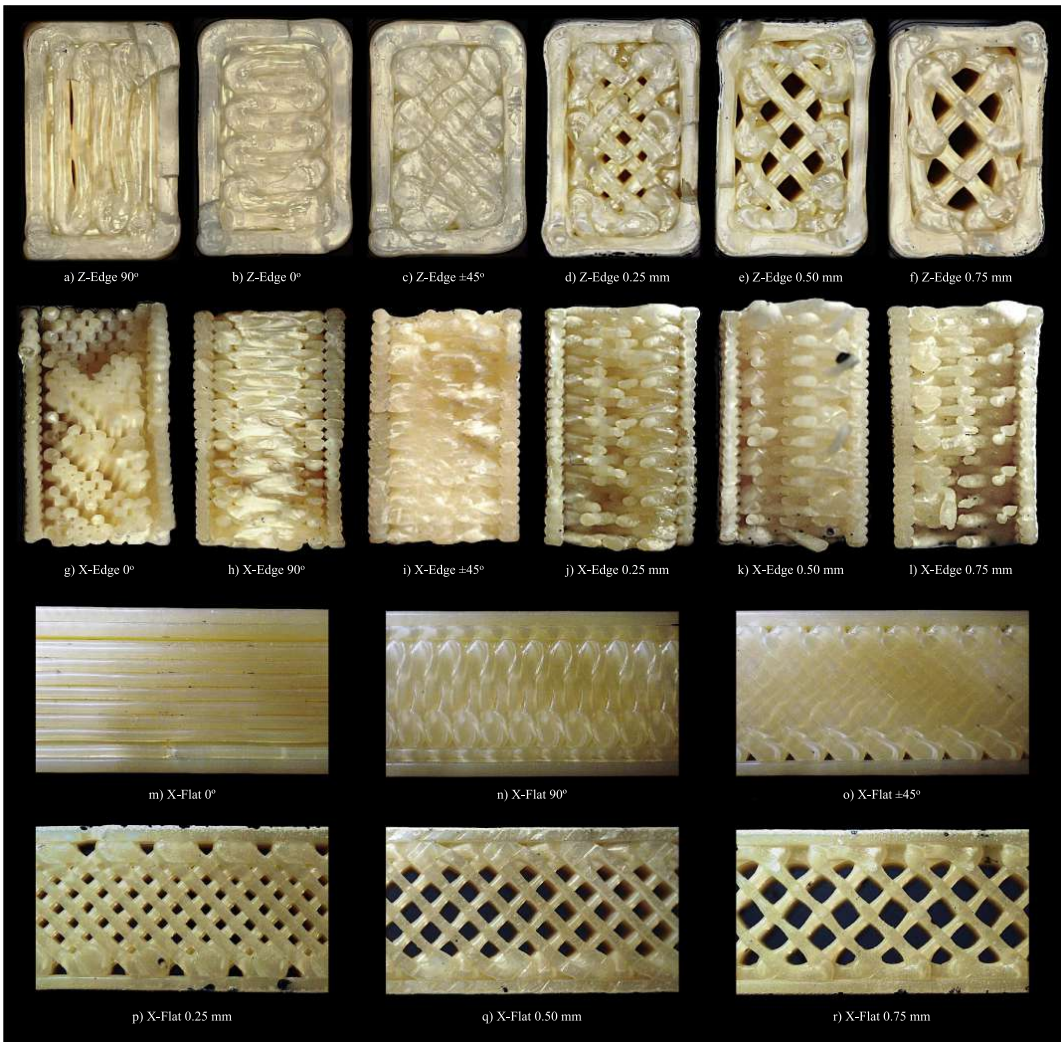

Fig. 3. Effective cross-sectional area (6 mm × 4 mm) (sub-figures a-l) and front surface (sub-figures m-r) of tensile samples in solid and sparse configurations (see Table 1).

observation can be explained by the significant reduction in the resistant cross-section with the modification of the air gap design parameter, which directly affects the mechanical performance of the specimens. The effect is minor in Flat samples because the effective cross-section is perpendicular to the building direction of the sparse structure (see Figs. 3 and 4).

Nevertheless, the results of the specific mechanical properties (charts in the right column) demonstrate a much more evident effect of the use of the sparse configurations. When the mass of the specimens is taken into account, the reduction of material in the effective cross-section of the sample is somehow quantified. On some occasions, sparse configurations show similar or even better specific mechanical properties to those of the equivalent $\pm 45^{\circ}$ solid family (commonly predefined for manufacturing). This fact can be seen in the specific deformation values achieved in the elastic and plastic zones.

3.2. Flexural testing

Fig. 8 depicts representative curves of solid (top) and sparse (bottom) configurations from the flexural tests. As before, the stress-strain curves differ in stiffness, maximum load, and material failure depending on the internal construction of the samples and the direction of testing. The shaded area of the graphs corresponds to the 5% strain threshold indicated in the ASTM D790 standard [39]. The nomenclature used on the labels refers to the manufacturing orientations detailed in Fig. 2.

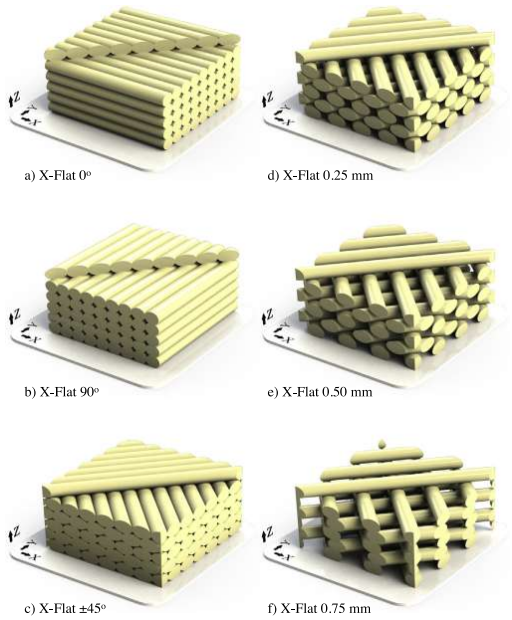

Fig. 4. Representation of the cross-sectional area of samples in X-Flat 0° (a), X-Flat 90° (b), and X-Flat ±45° (c) solid configurations, and X-Flat 0.25 mm (d), X-Flat 0.50 mm (e), and X-Flat 0.75 mm (f) sparse configurations (see Table 1).

Fig. 9 shows the results of the following flexural properties (charts in the left column): flexural modulus, yield stress, strain at yield stress, and maximum stress and its corresponding strain. In graphs *e* and *i*, the 5% of strain threshold is indicated. Applying again the assumption of equivalence of samples stated in tensile tests, the results from flexural tests were determined for X-Flat, X-Edge, and Z-Edge orientations exclusively. The charts shown in the right column of the figure correspond to the equivalent specific values of each of the properties to ease data interpretation. These values were calculated by normalizing according to the mass of each sample.

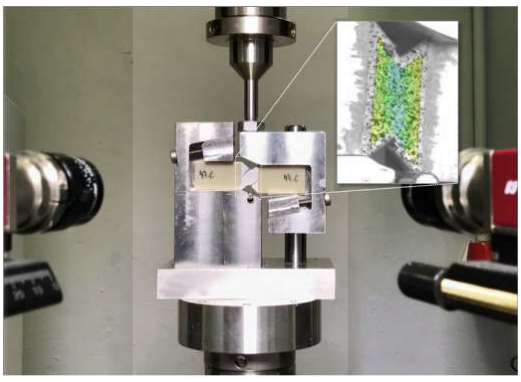

Fig. 5. Experimental setup for ASTM D5379 shear test standard with Digital Image Correlation equipment.

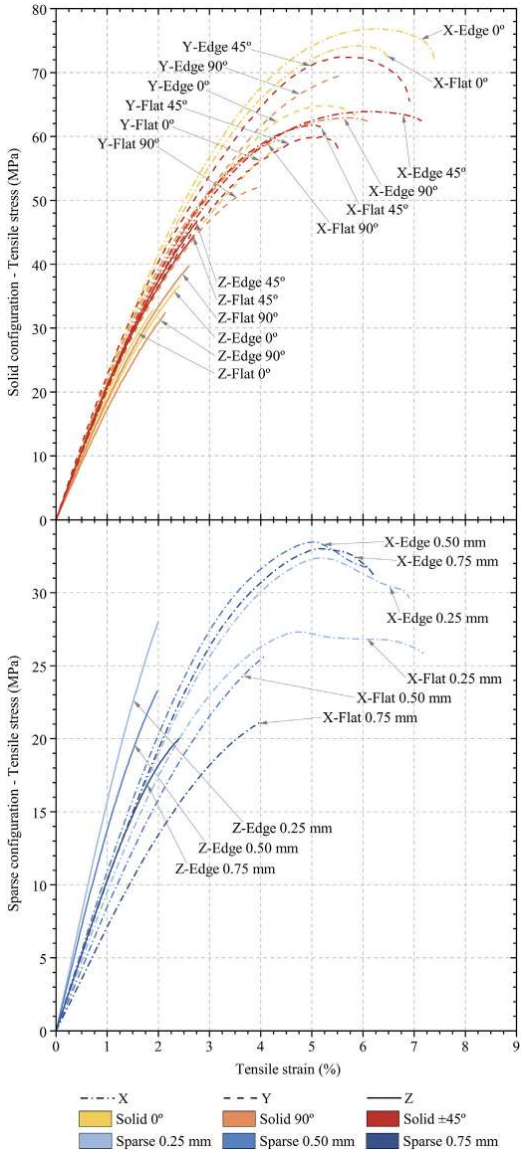

Fig. 6. Representative stress-strain data from the tensile test results of solid (top) and sparse (bottom) configurations with the different orientations of rasters and infill densities (see Fig. 2).

When flexural test results are compared with the data from the tensile tests, an inferior degree of isotropy is observed when the load is below the elastic limit. Minor differences are observed on the flexural moduli (X-Flat, X-Edge, and Z-Edge) of all solid samples (2260, 2360, 1950 MPa for 0°; 1847, 2112, 2073 MPa for 90°; and 1942, 2299, 1979 MPa for ±45°). However, noticeable deviations appear between

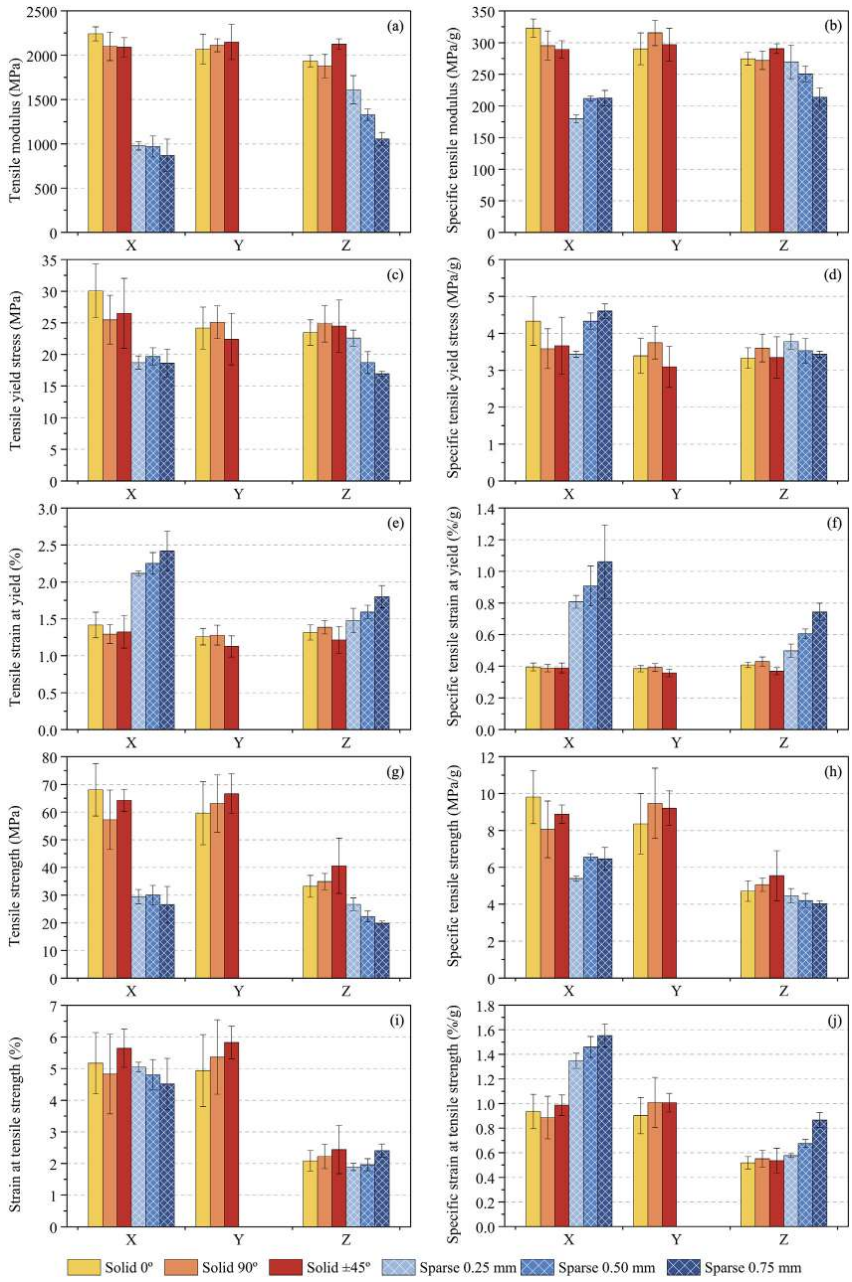

Fig. 7. Tensile test results comparision between solid and sparse configurations: tensile modulus (a), specific tensile modulus (b), tensile yield stress (c), specific tensile yield stress (d), tensile strain at yield (e), specific tensile strain at yield (f), tensile strength (g), specific tensile strength (h), strain at tensile strength (i), and specific strain at tensile strength (j).

the X-Flat and X-Edge test orientations when the yield point (charts *c* and *e*) and the maximum load (charts *g* and *i*) are analyzed. The highest and lowest values for stress and strain can be observed for 0° and 90° configurations, respectively. This occurs because the 90° configuration samples have intra-layer filaments parallel to the stress plane. In contrast, the 0° configuration specimens have the infill rasters perpendicular to the

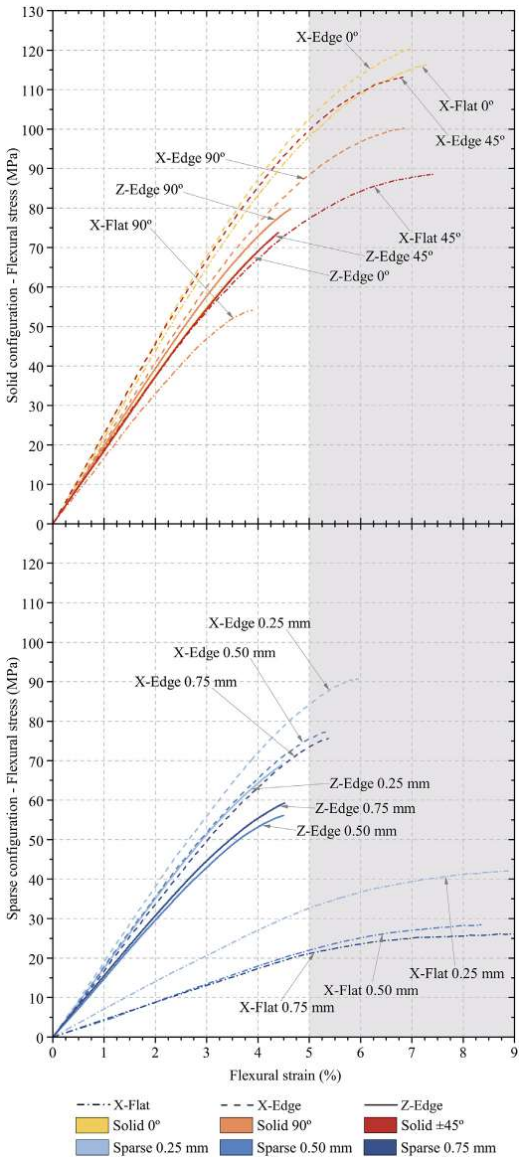

Fig. 8. Representative stress-strain data from the flexural test results of solid (top) and sparse (bottom) configurations with the different orientations of rasters and infill densities stated in Fig. 2. The beginning of the shaded area, where the major part of breaks occurs, refers to the calculation threshold established in the ASTM D790 [39] standard.

stress plane. Hence, the results indicate that both the resilience and the bending tenacity of solid samples are lower when the intra-layer unions support the stress. As an example, charts *c* and *e* in Fig. 9 show that the resilience of the samples is lower when the raster angle is set to 90°, and it increases when this parameter is set to ±45°. The maximum resilience is achieved when the orientation of the filaments coincides with the direction of the tensioned fiber (raster angle of 0°).

The sparse infill configuration shows a markedly different behavior between the X-Flat samples, and the X-Edge and Z-Edge specimens. Although the nominal second moment of inertia ($I = \frac{b \times h^3}{12}$) of all sections is equivalent,[2] the effective cross-sections are significantly different (see Figs. 3 and 4) depending on the testing orientation. Moreover, the layer contours in the outside of the specimen act as a reinforcement skin in the direction of the outer fiber in both X-Edge and Z-Edge orientations. Nevertheless, the X-Flat samples do not have any skin on the outer tensioned layer, so their stiffness is directly equivalent to that of the sparse core. This observation explains the noticeable differences between the values presented in chart *a* of Fig. 9.

When comparing mass-normalized values, the sparse configurations X-Edge and Z-Edge directions resemble average values achieved by the solid typologies. But the main variations occur in the X-Flat orientation. In this case, the specific mechanical performance of the sparse samples is notably close to the results stated by the solid ones, particularly for the yield point and peak strength values. Additionally, their specific deformation values at these points are above those of the solid families, and there is a three-fold increase in the X-Flat direction samples in particular.

These results prove that sparse configurations can be a suitable substitute for solid parts. However, the advantages become more apparent when they are used in geometries with large surfaces parallel to the printing bed. In those situations, the introduction of an air gap between the rasters decreases the mass and the cost of the parts significantly while maintaining similar mechanical properties overall.

3.3. Shear testing

Fig. 10 depicts the selected data from the results of the shear tests performed in solid (top) and sparse (bottom) configurations. The stress-strain curves differ in stiffness, maximum load, and material failure depending on the infill configuration and the direction of testing. In the case of sparse configurations, as before, the stress axis has been scaled for the reader's convenience. The shaded area of the graphs resembles the 5% strain threshold indicated in the ASTM D5379 standard [40], corresponding to 50 mε. The nomenclature used on the labels refers to the manufacturing orientation displayed in Fig. 2.

Fig. 11 displays the following shear properties (charts in the left column): shear modulus, yield stress, strain at yield stress, and maximum stress, as well as its corresponding strain. In charts *e* and *i*, the 50 mε of strain threshold is indicated. The charts on the right side of the figure show the mass-normalized values of the properties mentioned above, considering the mass of each tested sample.

Depicted results are average values obtained by testing the two possible arrangements of samples belonging to the same plane. As displayed in Fig. 2, the X-Flat (J) and Y-Flat (L) samples are contained in the same XY plane, but they have their infill filaments arranged in different alignments. The same applies to the X-Edge (K) and Z-Flat (N) samples in the XZ plane, and the Y-Edge (M) and Z-Edge (O) in the YZ plane. The obtained data shows that there is a distinct behavior between the samples contained in the same plane (Fig. 11). These differences are attributed to the modification of the effective cross-section of samples, due to the arrangement of filaments and layers. Accordingly, an average value was determined for each orthogonal plane (XY, XZ, and YZ) to calculate the constitutive matrix.

As shown in Fig. 11, the results for X-Flat and Y-Flat (XY and YX arrangements) with an air gap of 0.75 mm could not be determined. Due to the limited amount of rasters in this particular infill configuration, no recognizable stochastic pattern could be obtained for an accurate enough DIC post-process. Therefore, the mechanical properties results are only presented for the rest of the arrangements of this sparse

[2] 0.25 mm air gap samples averaged an inertia of 64.11 mm^4, while 64.51 mm^4 was registered by the 0.50 mm specimens, and 64.32 mm^4 by the 0.75 mm ones.

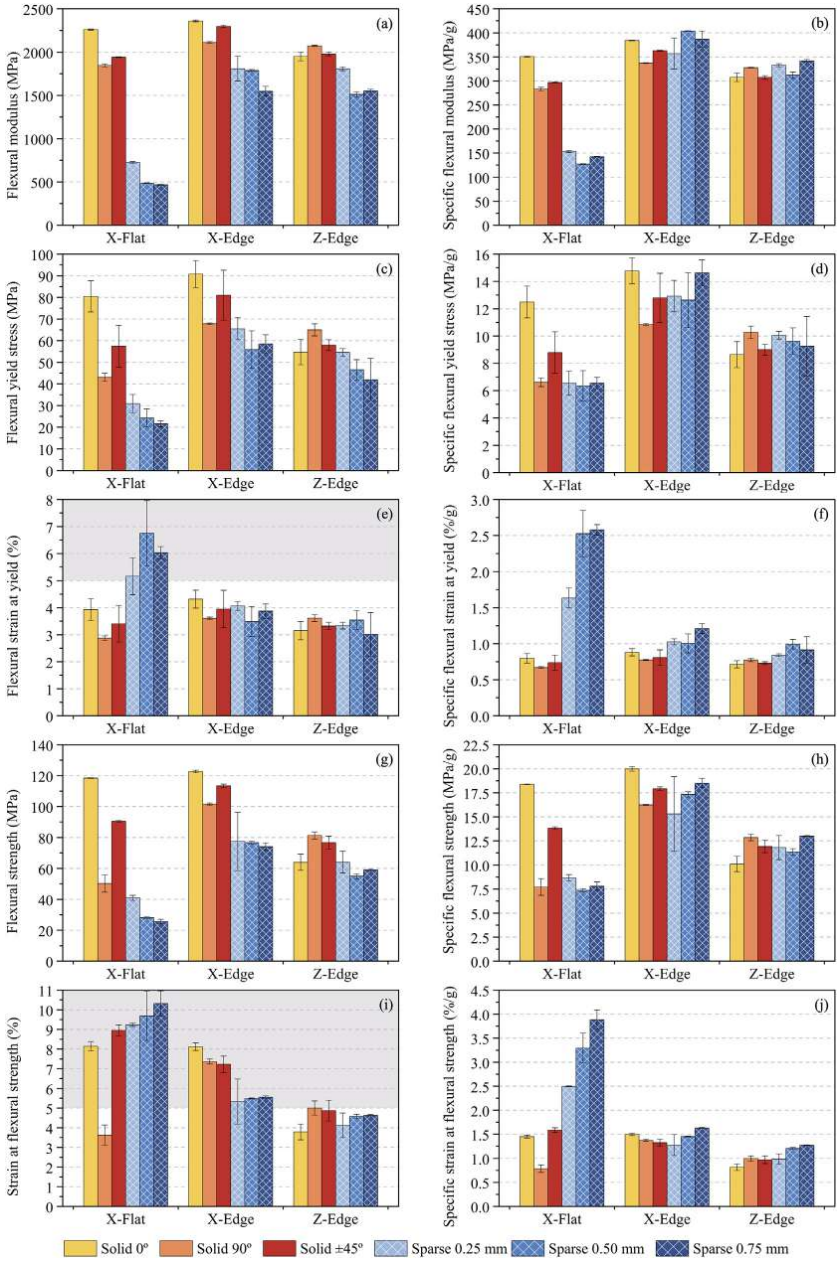

Fig. 9. Flexural test results comparision between solid and sparse configurations: flexural modulus (a), specific flexural modulus (b), flexural yield stress (c), specific flexural yield stress (d), flexural strain at yield (e), specific flexural strain at yield (f), flexural strength (g), specific flexural strength (h), strain at flexural strength (i), and specific strain at flexural strength (j).

typology. Additionally, the yield point of the X-Flat (XY) orientation with a 0.50 mm air gap could not be determined using the offset method indicated above.

Focusing on the charts in the left column of Fig. 11, solid and sparse configurations have different trends in the six evaluated arrangements. The equivalency of samples assumed from solid tensile test results is

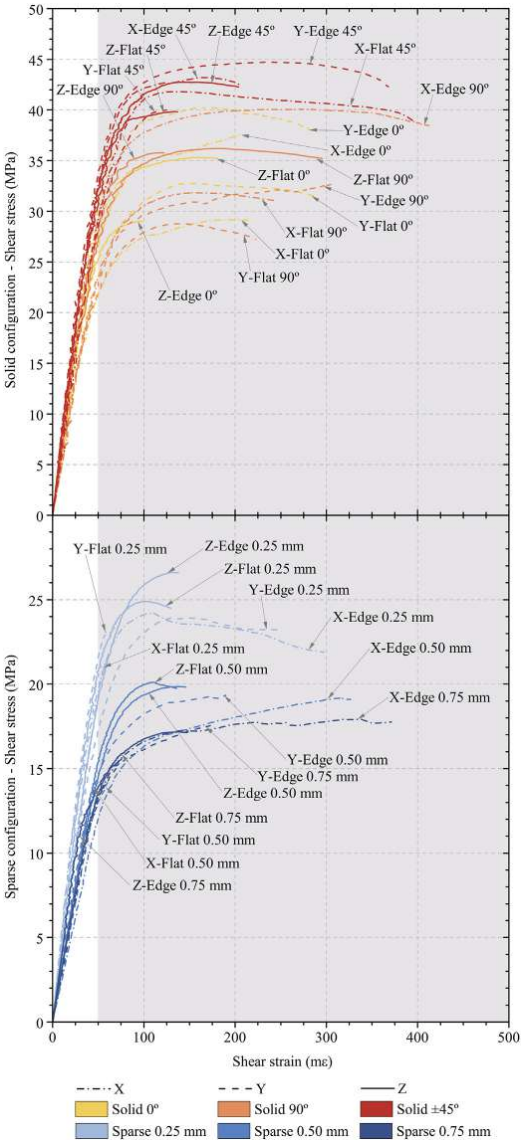

Fig. 10. Representative stress-strain data from the shear test results of solid (top) and sparse (bottom) configurations with the different orientations of rasters and infill densities stated in Fig. 2. The beginning of the shaded area, where the major part of breaks occurs, refers to the calculation threshold established in the ASTM D5379 [40] standard.

still noticeable. Actually, XY and YX results should be treated together, as well as the XZ and YZ, and the ZX and ZY. Furthermore, the raster orientation in the solid unidirectional configurations (0° and 90°) must be taken into account. Thus, the XY results of the 0° solid family are equivalent to the 90° results of the YX arrangement and vice versa. Similarly, the same deduction can be applied to the results of XZ and YZ dispositions, and those of ZX and ZY.

The analysis of the results of shear modulus from the solid samples concludes that very close values of stiffness are obtained with the 0° and 90° configurations. In all tests, the ±45° infill configuration presents superior rigidity. Regarding the sparse typologies, all samples display slightly higher values in the XY and YX arrangements (427, 477 MPa for 0.25 mm; and 328, 293 MPa for 0.50 mm in XY and YX arrangements, respectively). Moreover, the results prove the hypothesis that an increment of the air gap value leads to a decrease in stiffness, as expected.

As can be seen, yield stress values for the solid configurations are similar, being the ±45° samples the ones that offer higher results as compared to the 0° and 90° configurations. In the case of the sparse samples, the stress values obtained in the vertical arrangements (ZX and ZY) reduce significantly as the air gap value increases. Particularly, the obtained mean stresses at yield for solid ±45° samples were 29.3 MPa in ZX and 27.1 MPa in ZY. When a positive air gap is used, these values decrease to 18.9 MPa and 18.6 MPa for 0.25 mm, 15.6 MPa, and 16.1 MPa for 0.50 mm, and 13.7 MPa and 13.7 MPa for 0.75 mm, respectively. In samples manufactured in XZ and YZ, the increase in the air gap appears not to compromise this property.

At this point, it should be noted that the DIC post-process of shear test requires that a larger area of the pattern must be recognized during all the tests as a GOM Surface Component needs to be created. This fact results in a reduction of the DIC post-process accuracy in the shear tests in comparison with the tensile ones, which demand a 2-point extensometer. Thus, the wider dispersion of the results from shear tests makes it more challenging to find notable changes in this property. Nevertheless, as stated above, some trends can be observed that fit the hypothesis of this paper.

In contrast, the maximum strength values of the solid specimens show some clear tendencies. The sample equivalence already observed with the results from the tensile tests becomes even more evident. Specimens from 0° solid configuration exhibit lower strength in the XY and XZ directions. As the infill filaments are deposited perpendicularly to the resistant cross-section, they shear and slide during the test until the intra-layer unions (XY) or the inter-layer ones (XZ) fail. In vertical samples, the superior strength of this solid configuration is reached when the number of intra-layer filament unions in the effective cross-section is higher (ZY direction). In 90° solid configuration, the same phenomenon is observed in the YX, YZ directions, and, to a minor extent, in the ZX. This effect is not seen in the ±45° solid configuration, which has similar strength values in all arrangements. Also, this phenomenon is not appreciated in the sparse typologies. In these cases, the maximum strength decreases as the air gap increases.

Finally, the trends are slightly different when considering the normalized value of every property (charts in the right column). The specific stiffness results from XY and YX sparse samples are comparable to the ones from their solid counterparts. Moreover, the values from the sparse XZ, YZ, ZX, and ZY arrangements are also analogous to those of the solid ones. The same result can be found between sparse and solid configurations regarding yield stress properties. However, considering the deviations of the obtained results, their specific strains at this point are significantly higher as compared to those when no air gap is used. Furthermore, the mass contribution also sets the specific strength values of the sparse configurations slightly below those obtained by the solid families.

3.4. Compliance matrices

Table 2 (solid) and Table 3 (sparse) collect the average values and their corresponding standard deviation of the measured engineering constants. Analogous data already published from equivalent infill configurations is presented for comparison. As stated before, in some tests the thickness of the samples or the limited amount of rasters of some infill configurations compromised the accuracy of the DIC post-process. Accordingly, no data is presented for those cases when the stochastic pattern was not correctly recognized.

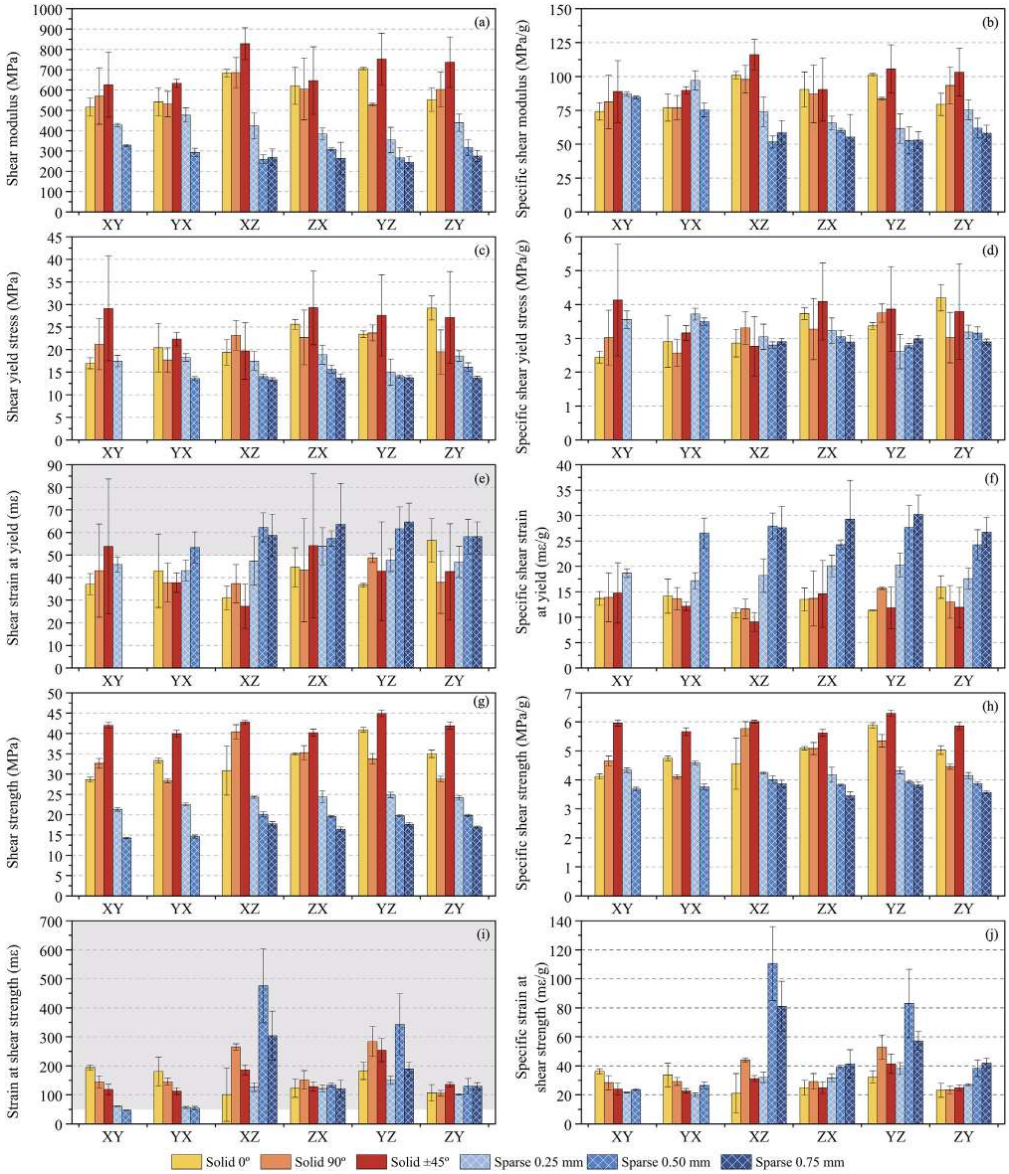

Fig. 11. Shear test results comparision between solid and sparse configurations: shear modulus (a), specific shear modulus (b), shear yield stress (c), specific shear yield stress (d), shear strain at yield (e), specific shear strain at yield (f), shear strength (g), specific shear strength (h), strain at shear strength (i), and specific strain at shear strength (j).

Based on the experimental results, the compliance matrix S for each studied configuration was calculated. Fig. 12 depicts the obtained compliance matrices describing the orthotropic elastic behavior of PEI Ultem parts processed by FFF in every one of the solid and sparse configurations investigated. The components of the diagonal correspond to: $S_{11} = \frac{1}{E_X}$, $S_{22} = \frac{1}{E_Y}$, $S_{33} = \frac{1}{E_Z}$, $S_{44} = \frac{1}{G_{YZ}}$, $S_{55} = \frac{1}{G_{XZ}}$, and $S_{66} = \frac{1}{G_{XY}}$; while the extension-extension coupling elements were calculated as: $S_{12} = mean(-\frac{\nu_{YX}}{E_Y}, -\frac{\nu_{XY}}{E_X})$, $S_{13} = mean(-\frac{\nu_{ZX}}{E_Z}, -\frac{\nu_{XZ}}{E_X})$, and $S_{23} = mean(-\frac{\nu_{ZY}}{E_Z}, -\frac{\nu_{YZ}}{E_Y})$. The extension-shear and shear-shear coupling elements are zero due to the orthotropic assumption.

Table 2
Comparison of the obtained engineering constants of the PEI Ultem with those published in the literature for solid configurations.

Raster angle	Tensile moduli (MPa)			Flexural moduli (MPa)			Shear moduli (MPa)			Poisson's ratio					
	E_X	E_Y	E_Z	E_{X-Flat}	E_{X-Edge}	E_{Z-Edge}	G_{XY}	G_{XZ}	G_{YZ}	ν_{XY}	ν_{YX}	ν_{XZ}	ν_{ZX}	ν_{YZ}	ν_{ZY}
0°	2242 ±79	2069 ±168	1935 ±67	2260 ±7	2360 ±10	1950 ±49	529 ±41	652 ±47	629 ±29	0.351 ±0.037	N/A	0.367 ±0.042	0.297 ±0.008	N/A	N/A
90°	2100 ±160	2113 ±74	1879 ±133	1847 ±16	2112 ±10	2073 ±7	551 ±76	646 ±84	566 ±44	0.328 ±0.047	N/A	0.387 ±0.053	0.389 ±0.083	0.352 ±0.029	N/A
±45°	2092 ±108	2150 ±198	2126 ±61	1942 ±3	2299 ±13	1979 ±22	630 ±81	737 ±92	745 ±89	0.344 ±0.007	N/A	0.392 ±0.002	0.348 ±0.029	N/A	N/A
±45° [a]	–	2510 ±60	2410 ±15	–	2400 ±30	2120 ±80	–	–	–	–	–	–	–	–	–
±45° [b]	2245 ±124	2280 ±385	2030 ±199	–	–	–	–	–	–	0.370	0.370	0.390	0.330	–	–
±45° [c]	1747 ±102	–	2092 ±130	–	–	–	–	–	–	–	–	–	–	–	–
±45° [d]	–	–	–	- 1875 ±12	2384 ±16	–	–	–	–	–	–	–	–	–	–
0° [e]	–	–	–	2233	–	–	–	–	–	–	–	–	–	–	–
90° [f]	–	–	–	2109	–	–	–	–	–	–	–	–	–	–	–
0° [g]	–	–	–	2351	–	–	–	–	–	–	–	–	–	–	–
90° [h]	–	–	–	1992	–	–	–	–	–	–	–	–	–	–	–
±45° [i]	1930 ±20	2090 ±30	–	–	–	–	–	–	–	–	–	–	–	–	–

[a] [22,23] Air gap 0.00 mm; Number of contours: 1; Contour width: N/A; Raster width: N/A.
[b] [27] Air gap 0.00 mm; Number of contours: N/A; Contour width: N/A; Raster width: N/A.
[c] [29] Air gap 0.00 mm; Number of contours: 1; Contour width: 0.508 mm; Raster width: 0.508 mm.
[d] [31] Air gap 0.00 mm; Number of contours: 1; Contour width: 0.508 mm; Raster width: 0.508 mm.
[e] [33] Air gap −0.0254 mm; Number of contours: 1; Contour width: 0.4064 mm; Raster width: 0.4064 mm.
[f] [33] Air gap −0.0254 mm; Number of contours: 1; Contour width: 0.4064 mm; Raster width: 0.4064 mm.
[g] [33] Air gap 0.00 mm; Number of contours: 1; Contour width: 0.4064 mm; Raster width: 0.4064 mm.
[h] [33] Air gap 0.00 mm; Number of contours: 1; Contour width: 0.4064 mm; Raster width: 0.4064 mm.
[i] [35] Air gap 0.00 mm; Number of contours: N/A; Contour width: N/A mm; Raster width: N/A mm.

Table 3
Comparison of the obtained engineering constants of the PEI Ultem with those published in the literature for sparse configurations.

Air gap (mm)	Tensile moduli (MPa)			Flexural moduli (MPa)			Shear moduli (MPa)			Poisson's ratio				
	E_X	E_Y	E_Z	E_{X-Flat}	E_{X-Edge}	E_{Z-Edge}	G_{XY}	G_{XZ}	G_{YZ}	ν_{XY}	ν_{YX}	ν_{XZ}	ν_{ZX}	ν_{YZ}	ν_{ZY}
0.25	978 ±48	N/A	1612 ±159	726 ±11	1809 ±143	1809 ±22	452 ± 18	403 ±35	397 ±38	0.436 ±0.024	N/A	0.289 ± 0.044	N/A	N/A	0.281 ±0.056
0.50	969 ±119	N/A	1329 ±65	487 ±4	1788 ±12	1512 ±30	310 ± 10	284 ±12	291 ±31	0.546 ±0.085	N/A	0.388 ±0.087	N/A	N/A	0.276 ±0.023
0.75	870 ±183	N/A	1056 ±73	468 ±4	1548 ±57	1554 ±16	N/A	266 ±45	260 ±20	0.505 ±0.071	N/A	0.363 ±0.017	N/A	N/A	0.241 ±0.076
2.54[a]	–	–	–	- 1786 ±26	1847 ±43	–	–	–	–	–	–	–	–	–	–

[a] [31] Raster angle ±45°; Number of contours: 1; Contour width: 0.508 mm; Raster width: 0.508 mm.

The extension coefficients[3] of the matrices of solid configurations confirm a similarity between the X and the Y axes (i.e., $S_{11} = S_{22}$) regardless of the orientation of the infill rasters. Slightly higher flexibility is observed in Z-direction in 0° and 90° samples (i.e., $S_{33} > S_{11}$), as expected. The ±45° configuration holds an equivalent Z-performance to X and Y results (i.e., $S_{33} \approx S_{11} \approx S_{22}$). This experimental observation may be considered to be related to the intra-layer and inter-layer cohesion. During the deposition of the material, the difference in temperature between contiguous filaments (intra-layer) is significantly lower than the thermal gradient between adjacent layers (inter-layer). As a result, the bond between parallel filaments is more rigid and resistant than the one between layers. Specifically, the oven temperature was set at 195°C, while the PEI Ultem extrusion temperature was 380°C. This evidence may explain why the stiffness in the filament direction is higher than between filaments.

Regarding the shear components, in all three solid configurations, higher flexibility is identified in the XY-plane (i.e., S_{66}). In contrast, despite some unavailable Poisson's ratio results, the impact of the direction of the infill rasters on the extension-extension coupling coefficients[4] appears to be negligible (i.e., $S_{12} \approx S_{13} \approx S_{23}$). Furthermore, if the flexibility of these configurations is analyzed, the ±45° raster angle provides a stiffer intra-layer and inter-layer cohesion than any unidirectional configuration.

Some authors [41,42] have recently assumed that, under a plane stress state, the printed parts present a transversely isotropic behavior of the plane parallel to the building bed. This hypothesis can be examined here from matrices presented in Fig. 12. Thus, an isotropic transverse behavior of the XY plane on a general stress state would be reflected as $S_{11} = S_{22}$, $S_{13} = S_{23}$, $S_{44} = S_{55}$, and the component $S_{66}^{Iso} = \frac{1}{G_{XY}} = \frac{2(1+\nu_{XY})}{E_X} = 2(S_{11} - S_{12})$. However, not all these component conditions are satisfied in this general stress state. Major differences are found on components S_{66}. For example, in the 0° solid configuration $S_{66}^{Iso} = 1.205\ GPa^{-1} < S_{66}^{Exp} = 1.891\ GPa^{-1}$. Analogous analyses could be done for the 90°[5] and ±45°[6] configurations considering the same plane. Another approach would be to assume a transversely isotropic behavior of the plane perpendicular to the filaments. Accordingly, in the 0° solid configuration, an isotropic transverse behavior of the YZ plane would be reflected as $S_{22} = S_{33}$, $S_{12} = S_{13}$, $S_{55} = S_{66}$ and the component $S_{44}^{Iso} = \frac{1}{G_{YZ}} = \frac{2(1+\nu_{YZ})}{E_Y} \approx 1.294\ GPa^{-1}$. Analogous analyses could be done for the 90° configuration regarding the XZ plane, and for the ±45° configuration considering both YZ and XZ planes. As before, the component conditions are not satisfied.

Overall, the experimental results show a more flexible behavior in the shearing plane than the transverse isotropy hypotheses. Consequently, the results of this investigation do not recognize transversely isotropic behavior neither on the plane XY, nor on the plane perpendicular to the filaments.

In the right column of Fig. 12, the results of the matrices of the sparse configurations are given. It should be noted that S_{22} components have taken the value of S_{11} since the corresponding tests were not conducted, following the conclusions drawn from the tensile tests with solid samples. As can be seen, the sparse compliance matrices display higher values than the solid ones, as expected. This fact agrees with the increased flexibility of the printed parts due to the addition of the air gap between filaments. Besides that, stiffness is less compromised in sparse configurations on Z-direction, as demonstrated by the fact that

[3] Extension coefficients were determined considering the tensile moduli results.
[4] Extension-extension coupling coefficients were determined considering the tensile moduli results.
[5] $S_{66}^{Iso} = 1.265\ GPa^{-1} < S_{66}^{Exp} = 1.816\ GPa^{-1}$.
[6] $S_{66}^{Iso} = 1.285\ GPa^{-1} < S_{66}^{Exp} = 1.587\ GPa^{-1}$.

Compliance matrix S in GPa^{-1} for solid 0º configuration

0.446 ±0.016	−0.156 ±0.018	−0.158 ±0.020	0	0	0
	0.483 ±0.039	N/A	0	0	0
		0.517 ±0.018	0	0	0
			1.589 ±0.073	0	0
	Sym.			1.534 ±0.109	0
					1.891 ±0.148

Compliance matrix S in GPa^{-1} for sparse 0.25 mm configuration

1.023 ±0.050	−0.446 ±0.033	−0.305 ±0.048	0	0	0
	1.023 ±0.050	−0.174 ±0.039	0	0	0
		0.621 ±0.061	0	0	0
			2.521 ±0.240	0	0
	Sym.			2.479 ±0.214	0
					2.212 ±0.089

Compliance matrix S in GPa^{-1} for solid 90º configuration

0.476 ±0.036	−0.156 ±0.025	−0.196 ±0.043	0	0	0
	0.473 ±0.017	−0.167 ±0.015	0	0	0
		0.532 ±0.038	0	0	0
			1.768 ±0.136	0	0
	Sym.			1.549 ±0.203	0
					1.816 ±0.251

Compliance matrix S in GPa^{-1} for sparse 0.50 mm configuration

1.032 ±0.127	−0.582 ±0.113	−0.401 ±0.102	0	0	0
	1.032 ±0.127	−0.208 ±0.020	0	0	0
		0.753 ±0.037	0	0	0
			3.432 ±0.369	0	0
	Sym.			3.522 ±0.147	0
					3.224 ±0.108

Compliance matrix S in GPa^{-1} for solid ±45º configuration

0.478 ±0.025	−0.164 ±0.009	−0.175 ±0.017	0	0	0
	0.465 ±0.043	N/A	0	0	0
		0.470 ±0.013	0	0	0
			1.342 ±0.160	0	0
	Sym.			1.356 ±0.169	0
					1.587 ±0.203

Compliance matrix S in GPa^{-1} for sparse 0.75 mm configuration

1.149 ±0.242	−0.581 ±0.147	−0.418 ±0.090	0	0	0
	1.149 ±0.242	−0.228 ±0.074	0	0	0
		0.947 ±0.065	0	0	0
			3.845 ±0.299	0	0
	Sym.			3.764 ±0.636	0
					N/A

Fig. 12. Compliance matrices describing the orthotropic elastic behavior of PEI Ultem processed by FFF in solid 0°, 90°, and ±45° and sparse 0.25 mm, 0.50 mm, and 0.75 mm configurations.

$S_{33} < S_{11}$ in all settings. This effect is because the air gap separation involves eliminating the intra-layer filament unions, but not the inter-layer cohesion. A similar effect is found in component S_{66}. In the solid ±45° samples, the intra-layer unions are stiffer than inter-layer ones, so $S_{66} > S_{55} \approx S_{44}$. In contrast, in all sparse configurations $S_{66} < S_{55} \approx S_{44}$ as the intra-layer filament unions are removed. Finally, a different trend from the solid ±45° configuration is observed when analyzing extension-extension coupling coefficients, as $S_{12} < S_{13} < S_{23}$ in all sparse cases.

4. Conclusions

The reported results are conclusive experimental evidence of the role that the infill parameters have on the mechanical performance and weight reduction of PEI Ultem processed by FFF under multiple load conditions.

Overall, the mechanical behavior of the printed parts depends on the material, and particularly on the FFF manufacturing parameters. The above analysis shows that the orientation and the infill settings have a

direct impact on the stiffness, the resilience, the maximum stress, and the type of failure of the processed parts. Consequently, the appropriate control of these design parameters would allow manufacturing final parts with optimal performance.

The obtained results indicate that both the intra-layer and the inter-layer bonds play a significant role in the behavior of the FFF samples. In this sense, the use of the thermal chamber reduces the temperature gradient between the deposited filament and the last layer built. This fact strengthens the unions, improves mechanical performance, and decreases the degree of orthotropy. Furthermore, the results obtained confirm that the stiffness on the direction of the extruded filament is higher than the one of the intra-layer unions between contiguous filaments. However, the rigidity of the inter-layer cohesion of adjacent layers is the lowest.

The use of the air gap in the design of the infill leads to a meaningful reduction of the manufacturing costs associated with the material and production time. The results of the mechanical tests that were conducted prove that the sparse infill has a quantifiable impact on the specific mechanical properties. The specific values obtained by normalizing the test results by the mass of every sample are comparable to those achieved with the solid configurations or even superiors, particularly in the strain range.

The calculated compliance matrices verify the inherent orthotropy of FFF technology. Results also ascertain the effect of the manufacturing parameters on the elastic behavior of the PEI Ultem printed parts. These matrices will be valuable for the validation of forthcoming numerical models addressing different infill configurations. The matrices analysis also enabled to determine a correlation between the FFF settings and the mechanical performance of the intra-layer and inter-layer unions.

Nevertheless, the development of FFF technology still has some open fronts. The behavior of the intra-layer unions depends to a large extent on the fact that the infill filaments are deposited as parallel as possible. Furthermore, special attention must be paid on the placement of the contour seam, as it can behave as a dramatic stress concentrator. All these facts can have a detrimental effect on the mechanical performance of the manufactured parts, thus being a challenge for FFF technology that should be further addressed.

Finally, this investigation contributes to the development of novel design-for-manufacturing strategies to obtain functional structural elements. This fact provides FFF with an outstanding competitive advantage in comparison to other AM technologies.

CRediT authorship contribution statement

Albert Forés-Garriga: Methodology, Validation, Investigation, Writing - original draft. **Marco A. Pérez:** Methodology, Conceptualization, Investigation, Writing - review & editing, Formal analysis, Funding acquisition. **Giovanni Gómez-Gras:** Methodology, Conceptualization, Investigation, Formal analysis. **Guillermo Reyes-Pozo:** Conceptualization, Formal analysis, Funding acquisition.

Declaration of competing interest

The authors declare that they have no known competing financial interests or personal relationships that could have appeared to influence the work reported in this paper.

Acknowledgments

This work has been supported by the Ministry of Science, Innovation and Universities through the project New Developments in Lightweight Composite Sandwich Panels with 3D Printed Cores (3DPC) - RTI2018-099754-A-I00; and by the RIS3CAT Llavor 3D Community co-financed by the Generalitat de Catalunya (ACCIÓ) through the project TRANSPORT COMRDI16-1-0010 - (2017-2020). The authors are very grateful to Ariadna Chueca de Bruijn for the constructive suggestions and for the assistance in conducting the experiments.

Data availability

The raw data required to reproduce these findings are available to download from Mendeley Data Repository: https://data.mendeley.com/datasets/xw37dn4549/draft?a=a54c51f6-d32f-4e4e-a3fb-1067f98a68d0.

References

[1] U.M. Dilberoglu, B. Gharehpapagh, U. Yaman, M. Dolen, The role of additive manufacturing in the era of Industry 4.0, Procedia Manuf 11 (2017) 545–554.
[2] K.S. Prakash, T. Nancharaih, V.V.S. Rao, Additive manufacturing techniques in manufacturing - an overview, Mater. Today 5 (2018) 3873–3882.
[3] A.J.J. Sheoran, H. Kumar, Fused deposition modeling process parameters optimization and effect on mechanical properties and part quality: review and reflection on present research, Mater. Today 21 (Part 3) (2020) 1659–1672, https://doi.org/10.1016/j.matpr.2019.11.296.
[4] B.A. Aloyaydi, S. Sivasankaran, H.R. Ammar, Influence of infill density on microstructure and flexural behavior of 3D printed PLA thermoplastic parts processed by fusion deposition modeling, AIMS Mater. Sci. 6 (2019) 1033–1048.
[5] J.R.C. Dizon, A.H. Espera Jr., Q. Chen, R.C. Advincula, Mechanical characterization of 3D-printed polymers, Addit. Manuf. 20 (2018) 44–67.
[6] D. Popescu, A. Zapciu, C. Amza, F. Baciu, R. Marinescu, FDM process parameters influence over the mechanical properties of polymer specimens: a review, Polym. Test. 69 (2018) 157–166.
[7] C. Gabor, M.A. Alin, D. Magli, T. Bedo, S.I. Munteanu, D. Munteanu, The optimization of the production procedure in relation to the mechanical properties of additively manufactured parts, Mater. Today 19 (2019) 1008–1013.
[8] T.D. McLouth, J.V. Severino, P.M. Adams, D.N. Patel, R.J. Zaldivar, The impact of print orientation and raster pattern on fracture toughness in additively manufactured ABS, Addit. Manuf. 18 (2017) 103–109.
[9] A.K. Sood, R.K. Ohdar, S.S. Mahapatra, Parametric appraisal of mechanical property of fused deposition modelling processed parts, Mater. Design 31 (2010) 287–295.
[10] C.W. Ziemian, R.D. Ziemian, Residual strength of additive manufactured ABS parts subjected to fatigue loading, Int. J. Fatigue 134 (2020) 105455, https://doi.org/10.1016/j.ijfatigue.2019.105455.
[11] S.-H. Ahn, M. Montero, D. Odell, S. Roundy, P.K. Wright, Anisotropic material properties of fused deposition modeling ABS, Rapid Prototyp. J. 8 (2002) 248–257.
[12] B. Wittbrodt, J.M. Pearce, The effects of PLA color on material properties of 3-D printed components, Addit. Manuf. 8 (2015) 110–116.
[13] C.-Y. Lee, C.-Y. Liu, The influence of forced-air cooling on a 3D printed part manufactured by fused filament fabrication, Addit. Manuf. 25 (2019) 196–203.
[14] J.M. Chacón, M.A. Caminero, E. García-Plaza, P.J. Núñez, Additive manufacturing of PLA structures using fused deposition modelling: effect of process parameters on mechanical properties and their optimal selection, Mater. Design 124 (2017) 143–157.
[15] G. Gómez-Gras, R. Jerez-Mesa, J.A. Travieso-Rodriguez, J. Lluma-Fuentes, Fatigue performance of fused filament fabrication PLA specimens, Mater. Design 140 (2018) 278–285.
[16] W.C. Smith, R.W. Dean, Structural characteristics of fused deposition modeling polycarbonate material, Polym. Test. 32 (2013) 1306–1312.
[17] M. Domingo-Espin, J.M. Puigoriol-Forcada, A.-A. Garcia-Granada, J. Llumà, S. Borros, G. Reyes, Mechanical property characterization and simulation of fused deposition modeling polycarbonate parts, Mater. Design 83 (2015) 670–677.
[18] I. Sedighi, M.R. Ayatollahi, B. Bahrami, M.A. Pérez, A.-A. Garcia-Granada, Mechanical behavior of an additively manufactured polycarbonate specimen: tensile, flexural and mode I fracture properties, Rapid Prototyp. J. 26 (2) (2019) 267–277, https://doi.org/10.1108/RPJ-03-2019-0055.
[19] B. Bahrami, M.R. Ayatollahi, I. Sedighi, M.A. Pérez, A.A. Garcia-Granada, The effect of in-plane layer orientation on mixed-mode I-II fracture behavior of 3D-printed polycarbonate specimens, Eng. Fract. Mech. 231 (2020) 107018.
[20] A.G. Salazar-Martín, M.A. Pérez, A.-A. García-Granada, G. Reyes, J.M. Puigoriol-Forcada, A study of creep in polycarbonate fused deposition Modelling parts, Mater. Design 141 (2018) 414–425.
[21] J.M. Puigoriol-Forcada, A. Alsina, A.G. Salazar-Martín, G. Gómez-Gras, M.A. Pérez, Flexural fatigue properties of polycarbonate fused-deposition modelling specimens, Mater. Design 155 (2018) 414–421.
[22] Stratasys, ULTEM™ 9085 Resin FDM: Thermoplastic Filament. Fit for High-Performance Applications, Technical Report 2019.
[23] Stratasys, Stratasys Materials Testing Procedure, Technical Report 2019.
[24] Stratasys, SDS ULTEM 9085 Natural Model Material, Technical Report 2017.
[25] L. Gasman, Additive aerospace considered as a business, in: F. Froes, R. Boyer (Eds.), Additive Manufacturing for the Aerospace Industry 2019, pp. 327–340.
[26] A. Ceruti, P. Marzocca, A. Liverani, C. Bil, Maintenance in aeronautics in an Industry 4.0 context: the role of augmented reality and additive manufacturing, J. Comput. Des. Eng. 6 (2019) 516–526.
[27] R.J. Zaldivar, D.B. Witkin, T. McLouth, D.N. Patel, K. Schmitt, J.P. Nokes, Influence of processing and orientation print effects on the mechanical and thermal behavior of 3D-printed ULTEM 9085 material, Addit. Manuf. 13 (2017) 71–80.

[28] A. Bagsik, V. Schöppner, Mechanical properties of fused deposition modeling Pards with Ultem* 9085, in: ANTEC 2011 Plastics, Boston.
[29] A. Bagsik, V. Schöppner, E. Klemp, FDM part quality manufactured with Ultem*9085, International Conference Polymeric Materials, 2010 , (Halle, Saale).
[30] A.W. Gebisa, H.G. Lemu, Influence of 3D printing FDM process parameters on tensile property of ULTEM 9085, Procedia Manuf 30 (2019) 331–338.
[31] K.P. Motaparti, Effect of Build Parameters on Mechanical Properties of Ultem 9085 Parts by Fused Deposition Modeling, Ph.D. thesis Missouri University of Science and Technology, 2016.
[32] K.I. Byberg, A.W. Gebisa, H.G. Lemu, Mechanical properties of ULTEM 9085 material processed by fused geposition modeling, Polym. Test. 72 (2018) 335–347.
[33] A.W. Gebisa, H.G. Lemu, Investigating effects of fused-deposition modeling (FDM) processing parameters on flexural properties of ULTEM 9085 using designed experiment, Materials 11 (2018) 1–23.
[34] S.H. Fard, S.M. Hashemi, On the strain-life fatigue parameters of additive manufactured plastic materials through used filament fabrication process, Addit. Manuf. 32 (2020).
[35] R.J. Zaldivar, T.D. Mclouth, G.L. Ferrelli, D.N. Patel, A.R. Hopkins, D. Witkin, Effect of initial filament moisture content on the microstructure and mechanical performance of ULTEM 9085 3D printed parts, Addit. Manuf. 24 (2018) 457–466.
[36] D.A. Roberson, A.R. Torrado Perez, C.M. Shemelya, A. Rivera, E. MacDonald, R.B. Wicker, Comparison of stress concentrator fabrication for 3D printed polymeric Izod impact test specimens, Addit. Manuf. 7 (2015) 1–11.
[37] A. Chueca de Bruijn, G. Gómez-Gras, M.A. Pérez, Mechanical study on the impact of an effective solvent support-removal methodology for FDM Ultem 9085 parts, Polym. Test. 85 (2020) 106433.
[38] ASTM D638-14, Standard Test Method for Tensile Properties of Plastics, ASTM International, West Conshohocken, PA, 2014.
[39] ASTM D790-17, Standard Test Methods for Flexural Properties of Unreinforced and Reinforced Plastics and Electrical Insulating Materials, ASTM International, West Conshohocken, PA, 2017.
[40] ASTM D5379 / D5379M-19, Standard Test Method for Shear Properties of Composite Materials by the V-Notched Beam Method, ASTM International, West Conshohocken, PA, 2019.
[41] T. Yao, J. Ye, Z. Deng, K. Zhang, Y. Ma, H. Ouyang, Tensile failure strength and separation angle of FDM 3D printing PLA material: experimental and theoretical analyses, Compos. B. Eng. 188 (2020).
[42] Y. Zhao, Y. Chen, Y. Zhou, Novel mechanical models of tensile strength and elastic property of FDM AM PLA materials: experimental and theoretical analyses, Mater. Design 181 (2019) 108089.

Publication II:

Mechanical performance of additively manufactured lightweight cellular solids: Influence of cell pattern and relative density on the printing time and compression behavior

10.1016/j.matdes.2022.110474

Materials & Design 215 (2022) 110474

Contents lists available at ScienceDirect

Materials & Design

journal homepage: www.elsevier.com/locate/matdes

Mechanical performance of additively manufactured lightweight cellular solids: Influence of cell pattern and relative density on the printing time and compression behavior

Albert Forés-Garriga, Giovanni Gómez-Gras, Marco A. Pérez *

IQS School of Engineering, Universitat Ramon Llull, Via Augusta 390, 08017 Barcelona, Spain

HIGHLIGHTS

- A broad spectrum of specific stiffness and strength is achieved from the infill pattern and density.
- Validated equations are given to estimate the relative density, stiffnesses and strengths.
- Manufacturing defects reveal the need to implement strategies to optimize printing trajectories.
- Sparse infill provides comparable performance with a considerably shorter manufacturing time.

GRAPHICAL ABSTRACT

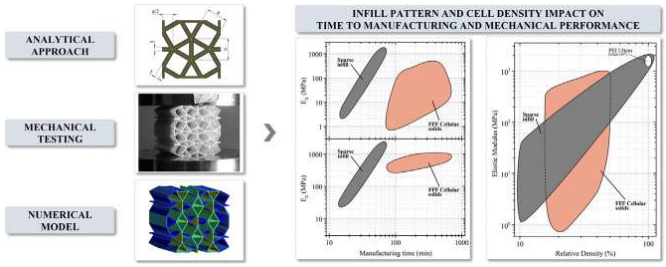

ARTICLE INFO

Article history:
Received 4 November 2021
Revised 24 January 2022
Accepted 16 February 2022
Available online 18 February 2022

Keywords:
Cellular structures
Additive manufacturing
Fused filament fabrication
Cell pattern
Relative density
Mechanical performance

ABSTRACT

A comprehensive investigation is presented on the Fused Filament Fabrication (FFF) technology's possibilities to create cellular solids with a broad spectrum of specific stiffness and strength, modifying cell geometry and size, while addressing manufacturing matters such as inherent defects and built time. Thirteen typologies of two-dimensional cellular patterns with different relative densities are examined. Results have allowed conclusions to be drawn regarding the influence of cell type and infill density on mechanical performance. Intra-layer and inter-layer inherent defects identified after manufacturing highlight the importance of optimizing filament trajectories. A reliable comparison of the elastic properties of the cellular patterns as a function of their density is presented. An experimentally validated numerical model is provided for predicting the compression stiffness of the different cell patterns with an average deviation below 5%. The model can reproduce the behavior in the elastic range based on tensile specimen properties and a Normal Stiffness Factor to account for the phenomenon of elastic asymmetry of the FFF printed samples. The wide range of results achieved is experimental confirmation of the potential of FFF cellular solids. Lastly, this investigation provides analytical, numerical, and empirical validated evidence to further design-for-additive manufacturing strategies with cellular solids for designing advanced lightweight structures.

1. Introduction

Cellular solids are defined as those made up of an interconnected network of solid struts or plates that form the edges and faces of cells, packed together to fill space [1]. Basically, there are

* Corresponding author.
E-mail address: marcoantonio.perez@iqs.url.edu (M.A. Pérez).

https://doi.org/10.1016/j.matdes.2022.110474
0264-1275/

two broad classes of cellular solids: one consists of a stochastic structure such as foams, whereas the other is composed of a periodic structure such as lattice truss and prismatic structures. Its properties depend directly on cells' shape and connectivity and the specific solid material they are made. The single most important feature of a cellular solid is its relative density, which is the quotient between the density of the cellular solid and the one of the solid material of which it is made.

Cellular solids appear in many natural materials and structures, such as cancellous bone, wood, cork, or sponges [2–4]. Man has used natural cellular materials for centuries since they have physical, mechanical, and thermal outstanding properties compared to fully dense solids. The human-made cellular solids exploit the unique combination of properties for a wide range of engineering applications, such as the low density, which allows the design of light and stiff components such as sandwich panels; the low thermal conductivity for manufacturing effective thermal insulation; or the low strength and large compressive strains which make them attractive for energy-absorbing applications [5–10].

Recent advances in additive manufacturing (AM) technologies have widened the horizons of the fabrication possibilities and application of cellular solids [11–18]. A major advantage of the AM technologies is its feasibility to fabricate lighter structures with a wide range of materials, printing the parts with solid shells filled with low-density infill. Accordingly, the infill stands as a manufacturing parameter that plays a significant role in the strategy to reduce weight, time to print, and print cost but also to design structures with tailored properties [19,20]. This provides AM an outstanding competitive advantage as compared to other conventional manufacturing technologies.

An additively manufactured part's infill density is an important design factor directly related to the cell size. The parameter can be adjusted as a percentage of filling or by controlling the internal raster-to-raster air gap. It has been shown that infill density has a noticeable effect on weight reduction, manufacturing time, and cost, but also on stiffness and strength of the printed part. Nevertheless, infill geometry defined by cell shape can play even a more significant role in the printed part's mechanical performance since it could allow producing components with tailored functional characteristics [21–27]. For example, when the cells are equiaxed, the properties are isotropic, but when the cells are even slightly elongated or flattened, the properties depend on the direction, presenting an orthotropic or even an auxetic behavior. Hence, if such parts are to be used in load-bearing components, understanding their mechanics is of utmost importance for an optimal design.

Several studies on the mechanical behavior of cellular solids manufactured by AM and, in particular, by Fused Filament Fabrication (FFF) can be found in the literature. Overall, the different works mainly investigate their mechanical behavior through numerical approaches, with some experimental validation examples [28–33]. These studies analyze the effect of infill density on mechanical performance by modifying the cell size, or the effect of infill geometry by changing the cell typology. In general, the studies focus on compression behavior and mostly on analyzing the auxetic behavior induced by cell geometry [34–51]. Other researchers have investigated the combination of different infill cells, creating the so-called hierarchical cell geometries with promising results [52–55]. However, most studies are bounded to analyzing some particular cell geometry or numerical modeling of various cell typologies, establishing comparisons based on their performance. Hence, in the authors' opinion, there is a need for more comprehensive research. Firstly, to explore FFF technology's possibilities to create multiple cellular solids able to broaden the spectrum of specific stiffness and strength from one single material. Secondly, to study the primary cell geometries together with the effect of cell size from a mechanical performance point of view, but also considering manufacturing issues, thus aimed to contribute to strengthen AM cellular solids designs' feasibility.

Accordingly, the purpose of this work is to investigate the role of the infill density together with the pattern geometry on the mechanical performance and weight reduction of cellular solids manufactured by FFF. The work is focused on two-dimensional geometries, thus avoiding the use of support material. This study aims to provide analytical, numerical, and experimental validated evidence to further contribute to design-for-additive manufacturing strategies with cellular solids, with an in-deep analysis of the infill's mechanical performance and addressing manufacturing matters, such as inherent defects and built time.

2. Cell designs

Since the cell pattern plays an essential role in the cellular solid's physical and mechanical properties [1], a broad and a representative number of the principal two-dimensional cell shapes found in the literature are examined in this work. In particular, the analysis encompasses the two-dimensional cell shapes Antitetrachiral, Circular, Hexachiral, Hexagon, Re-Entrant Hexagon type I and II, Lozenge Grids, Rotachiral, Sinusoidal Ligaments, Square Grids, SrCuBO, and Tetrachiral. The infill so-called Sparse, widely used in FFF printing strategies, has also been included for comparison. Fig. 1 depicts the unit cell shapes and a representative manufactured sample of each infill pattern assessed. Sub-figure *s* corresponds to a solid cube sample made by the same material as the cell walls, the results of which will be used for comparison.

As stated before, the single most important feature of a cellular solid is its relative density, which is the quotient between the density of the cellular solid (ρ^*) and the one of the solid material (ρ^s) of which it is made. Furthermore, the relative density is equivalent to the ratio between the elastic modulus along *z*-direction of the cellular solid and the one of the corresponding solid material [1], i.e.:

$$\frac{E_z^*}{E_z^s} = \frac{\rho^*}{\rho^s} \tag{1}$$

Generally speaking, natural cellular solids have relative densities which are less than about 30%.

The effective in-plane Young modulus (E_x^* and E_y^*) and strength (σ_x^* and σ_y^*) of two-dimensional lattice structures can be also estimated from the relative density and the Young modulus of the solid E^s. In particular, the scaling laws can be adequately represented by the power-law expressions [56]:

$$\frac{E_x^*}{E_x^s} = B_x\left(\frac{\rho^*}{\rho^s}\right)^b \qquad \frac{E_y^*}{E_y^s} = B_y\left(\frac{\rho^*}{\rho^s}\right)^b \tag{2}$$

$$\frac{\sigma_x^*}{E_x^s} = C_x\left(\frac{\rho^*}{\rho^s}\right)^c \qquad \frac{\sigma_y^*}{E_y^s} = C_y\left(\frac{\rho^*}{\rho^s}\right)^c \tag{3}$$

where $b = 1$ and $c = 1$ for stretch-dominated structures; $b = 3$ and $c = 2$ for bending-dominated structures; and B_x, B_y, C_x, and C_y are experimental coefficients that depend on the pattern cell geometry. This classification does not consider the overall effect of shear, hinging, and flexural stiffness; however, the predictions are reasonably acceptable. Although there are some works in the literature that provide some of these experimental factors, very few cell patterns are reported [1,23,56,57].

Given the relevance of relative density, in this work each cell shape's geometrical design has been parameterized with the variables indicated in Fig. 1. In this way, modifying the design parameters allows the building of cellular solids with different infill densities while keeping the cell pattern. Considering these design

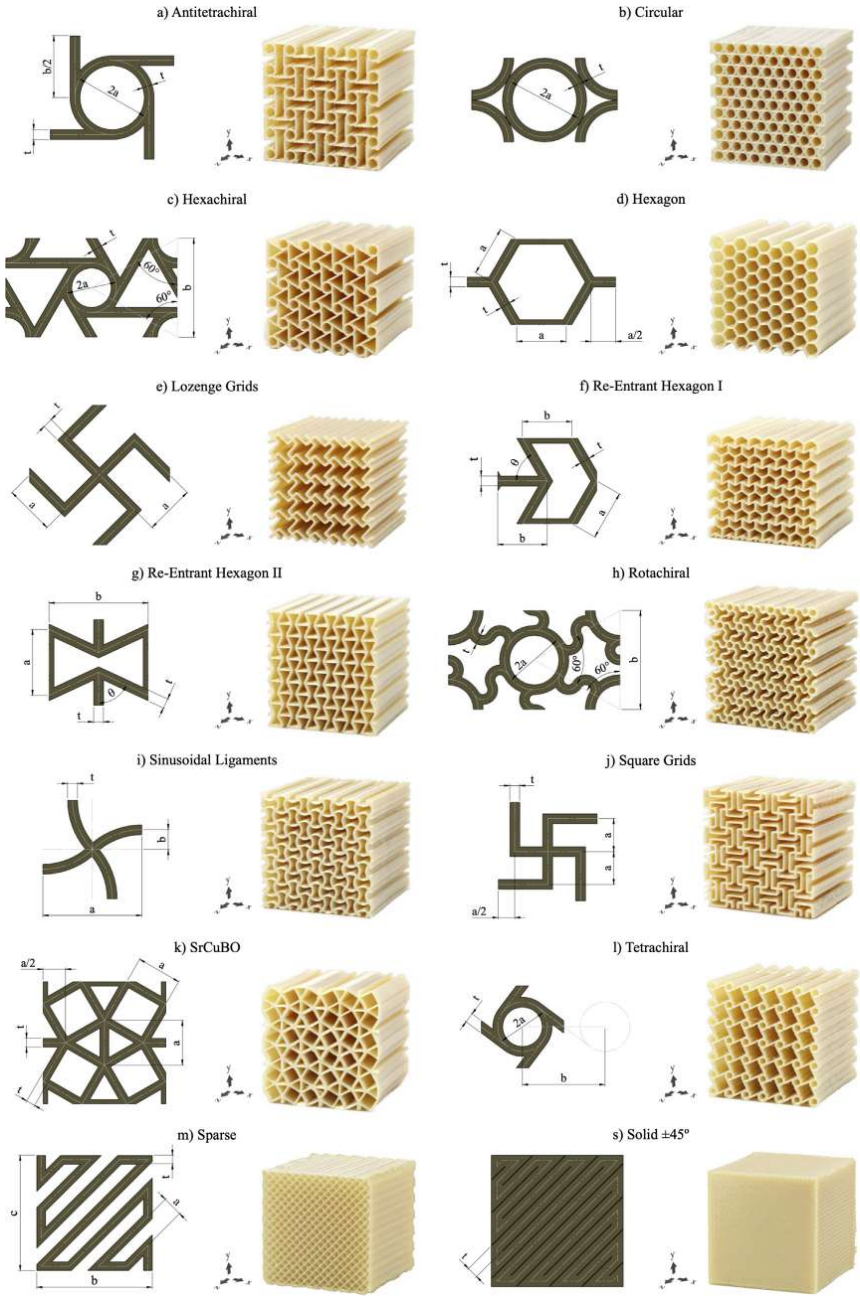

Fig. 1. Unit cell shapes design and corresponding FFF manufactured sample of each infill pattern assessed.

parameters, the analytical equations for the relative density of all the infill patterns have been determined, as shown below:

(a) Antitetrachiral

$$\frac{\rho^*}{\rho^s}=\frac{2}{b^2}\left[t(a\pi+b)+\frac{\sqrt{2}}{2}(2a-t)\sqrt{at}-\left(a+\frac{t}{2}\right)^2\arccos\left(\frac{2a-t}{2a+t}\right)\right] \tag{4}$$

(b) Circular

$$\frac{\rho^*}{\rho^s}=\frac{4}{\sqrt{3}}\frac{at\pi}{(2a+t)^2} \tag{5}$$

(c) Hexachiral

$$\frac{\rho^*}{\rho^s}=1-\frac{1}{b^2}\left[\frac{2\pi}{\sqrt{3}}\left(a-\frac{t}{2}\right)^2+\left(\sqrt{b^2-4a^2}-t\sqrt{3}\right)^2\right] \tag{6}$$

(d) Hexagon

$$\frac{\rho^*}{\rho^s}=\frac{t\sqrt{3}}{9a^2}\left(6a-t\sqrt{3}\right) \tag{7}$$

(e) Lozenge Grids

$$\frac{\rho^*}{\rho^s}=\frac{8a-t}{8a^2}t \tag{8}$$

(f) Re-Entrant Hexagon I

$$\frac{\rho^*}{\rho^s}=1-\frac{\left(a\sin\theta-\frac{t}{2}\right)\left(b-\frac{t}{\sin\theta}\right)}{ab\sin\theta} \tag{9}$$

(g) Re-Entrant Hexagon II

$$\frac{\rho^*}{\rho^s}=\frac{2t\left[a+\frac{1}{\sin\theta}(b-t)-\frac{t^2}{2\tan\theta}\right]}{b\left(2a-\frac{b}{\tan\theta}\right)} \tag{10}$$

(h) Rotachiral

$$\frac{\rho^*}{\rho^s}=\frac{\pi t(3b-2a)}{\sqrt{3}b^2}+\frac{\sqrt{3at(b-2a)(2a+b+2t)}}{\sqrt{2}b^2}-\\-\frac{2\sqrt{3}}{b^2}\left(\frac{b}{4}-\frac{a}{2}+\frac{t}{2}\right)^2\arccos\left(\frac{b^2+2bt-4a^2-12at}{[b+2(t-a)](2a+b)}\right)-\\-\frac{2\sqrt{3}}{b^2}\left(a+\frac{t}{2}\right)^2\arccos\left(\frac{6at+2ab+4a^2-bt}{(2a+t)(2a+b)}\right) \tag{11}$$

(i) Sinusoidal Ligaments

$$\frac{\rho^*}{\rho^s}=\frac{4}{a^2}\left[\left(b-\frac{t}{2}\right)^2+\left(b-\frac{t}{2}+\Psi\right)\left(\frac{a}{2}-b+\frac{t}{2}\right)+\left(\frac{a}{2}-\Psi\right)\left(\Omega-b+\frac{t}{2}\right)\right]+\\+\frac{2}{a^2}\left[\left(\frac{a^2}{8b}+\frac{b}{2}+\frac{t}{2}\right)^2(2\gamma-\sin(2\gamma))-\left(\frac{a^2}{8b}+\frac{b}{2}-\frac{t}{2}\right)^2(2\delta-\sin(2\delta))\right] \tag{12}$$

where:

$$\alpha=\arcsin\left(\frac{\sqrt{2}\left(a^2-4b^2-4ab\right)}{2\left(4b^2+a^2\right)}\right)$$

$$\beta=\arccos\left(-\frac{\sqrt{2}\left(-16b^4-32tb^3-8a^2b^2-8bta^2-a^4\right)}{2\left(4b(b+t)+a^2\right)\left(4b^2+a^2\right)}\right)$$

$$\gamma=\arcsin\left(\frac{\frac{a}{2}-\Psi}{\frac{a^2}{8b}+\frac{b}{2}+\frac{t}{2}}\right)$$

$$\delta=\arcsin\left(\frac{\frac{a}{2}-\Omega}{\frac{a^2}{8b}+\frac{b}{2}-\frac{t}{2}}\right)$$

$$\Psi=\frac{a}{2}-\left(\frac{a^2}{8b}+\frac{b+t}{2}\right)\cos\left(\frac{\pi}{2}+\alpha-\beta\right)$$

$$\Omega=-\frac{a^2}{8b}+\frac{b}{2}+\left(\frac{a^2}{8b}+\frac{b+t}{2}\right)\sin\left(\frac{\pi}{2}+\alpha-\beta\right)$$

(j) Square Grids

$$\frac{\rho^*}{\rho^s}=\frac{10a-t}{9a^2}t \tag{13}$$

(k) SrCuBO

$$\frac{\rho^*}{\rho^s}=\frac{20at-t^2\left(4+6\sqrt{3}\right)}{a^2\left(4+2\sqrt{3}\right)} \tag{14}$$

(l) Tetrachiral

$$\frac{\rho^*}{\rho^s}=\frac{2}{b^2}\left[t\left(a\pi+2\sqrt{\left(\frac{b}{2}\right)^2-a^2}\right)-\left(a+\frac{t}{2}\right)^2\arccos\left(\frac{2a-t}{2a+t}\right)\right]+\\+\frac{\sqrt{2}}{b^2}(2a-t)\sqrt{at} \tag{15}$$

(m) Sparse

$$\frac{\rho^*}{\rho^s}=\frac{bc+a(b+c-t)}{bc(t+a)}t$$

3. Methodology

3.1. Manufacturing of samples

To investigate the infill density's role together with the infill geometry on the mechanical performance and weight reduction of cellular solids, the thirteen above designs were evaluated with three different density levels, except for the Sparse type, for which six air gap values were considered, thus providing a total of 42 different filling configurations. Table 1 collects the design parameters selected for each configuration. Cell wall-thickness t was set to 0.508 mm for all configurations. An integer number of complete unit cells was settled to get a cubic specimen whose dimensions were as close as possible to $40 \times 40 \times 40$ mm.

Specimens were manufactured in a Stratasys Fortus 400mc FDM equipment using PEI Ultem 9085 material. This printer has a chamber that controls the temperature during the whole manufacturing process, improving the inter-layer adherence between adjacent building layers [19]. The optimum operating conditions for processing PEI Ultem require an oven temperature of 195 °C, while the extrusion temperature for the model material was set to 380°C. Insight 3D Printing Software (Stratasys) was used for the G-code generation. Samples were manufactured with a slice height of 0.254 mm and a nominal wall-thickness t of just one contour of 0.508 mm. This fact reduces the required material for building each cell pattern and its manufacturing time. Sparse patterns were created by including a separation between intra-layer filaments with the raster-to-raster air gap parameter. Due to the two-dimensional design of the unit cells and the upright orientation, no support material was necessary as geometries can stand by itself while building, which directly benefits the manufacturing time and material consumption. The estimated manufacturing time for each configuration is provided in Table 1.

Two samples were printed for each configuration and testing orientation, leading to a total of 198 samples. Once printed, samples were examined using a high-resolution Olympus DSX1000 digital microscope to assess the manufacturing process and identify possible defects. In addition, the mass and the nominal external dimensions of each manufactured sample were measured, and their density was determined. The experimental relative density was then calculated by dividing the average result of every considered infill pattern over the solid configuration value. These results are summarized in Table 1, where minor differences are noticed between the experimental relative density results and the corresponding analytical ones calculated with the equations Eq. (4)–(16).

Table 1
Design parameters, manufacturing time, and analytical and experimental relative densities.

Pattern	Density Level	Design dimensions			Manufacturing time (min)	Relative density (%)	
		a (mm)	*b* (mm)	*θ* (°)		*Anal.*	*Exp.*
(a) Antitetrachiral	I	1.30	4.00	-	608	46.07	44.58
	II	2.00	7.00	–	258	26.41	25.32
	III	2.75	10.00	–	111	18.73	16.60
(b) Circular	I	1.70	–	–	381	45.04	47.64
	II	2.20	–	–	206	37.22	40.18
	III	3.20	–	–	212	27.55	34.21
(c) Hexachiral	I	1.30	5.20	–	522	40.91	38.61
	II	1.90	7.50	–	265	30.16	27.18
	III	2.50	10.00	–	172	23.59	21.81
(d) Hexagon	I	2.35	–	–	265	26.37	25.25
	II	2.85	–	–	157	22.04	21.50
	III	3.85	–	–	98	16.58	16.44
(e) Lozenge Grids	I	1.70	–	–	205	32.54	32.60
	II	2.20	–	–	127	25.40	24.76
	III	2.70	–	–	101	20.83	20.90
(f) Re-Entrant Hexagon I	I	2.35	2.69	60	291	35.47	35.59
	II	2.85	3.19	60	217	30.17	30.02
	III	4.35	4.69	60	95	20.80	20.81
(g) Re-Entrant Hexagon II	I	3.80	5.80	65	198	38.36	37.17
	II	4.80	7.30	65	152	30.87	29.76
	III	5.80	8.30	65	100	25.55	25.33
(h) Rotachiral	I	1.25	6.00	–	488	38.86	37.22
	II	1.55	7.50	–	341	31.74	29.26
	III	2.05	10.00	–	203	24.33	23.06
(i) Sinusoidal Ligaments	I	3.00	1.00	–	434	45.35	46.15
	II	4.00	1.00	–	271	31.39	33.92
	III	6.00	1.00	–	140	19.73	20.05
(j) Square Grids	I	1.80	–	–	238	34.52	36.73
	II	2.30	–	–	157	27.21	28.72
	III	3.10	–	–	85	20.32	20.42
(k) SrCuBO	I	3.50	–	–	498	38.98	39.83
	II	5.00	–	–	249	28.39	31.38
	III	7.00	–	–	113	20.80	23.68
(l) Tetrachiral	I	1.30	5.00	–	341	30.74	28.23
	II	1.50	6.00	–	285	25.96	23.34
	III	2.00	8.00	–	148	20.09	17.15
(m) Sparse	I	0.25	–	–	45	70.66	69.13
	II	0.50	–	–	37	54.94	53.02
	III	0.75	–	–	36	45.13	42.76
	IV	1.50	–	–	27	29.88	27.71
	V	3.00	–	–	20	18.55	16.93
	VI	6.00	–	–	16	11.40	10.46
(s) Solid ±45°	S	–	–	–	66	100.00	100.00[a]

Stratasys PEI Ultem filament's density: 1.27 g/cm^3 [58].
Experimental measured wall-thickness $t = 0.5777$ mm. See Section 4.1 for more details.
[a] Experimental measured density of Solid ±45° pattern: 1.1457 g/cm^3.

3.2. Compression testing

The specimens were tested in compression in the in-plane *x* and *y*-directions, and the out-of-plane *z*-direction. For those symmetrical cells, such as Antitetrachiral, Lozenge Grids, Rotachiral, Sinusoidal Ligaments, Square Grids, SrCuBO, Tetrachiral, and Sparse patterns, only tests in *x* and *z*-directions were performed considering the equivalence of *x* and *y*-directions. Tests were conducted using ZwickRoell Z030 equipment (30 kN). A 3D Digital Image Correlation (DIC) was used to analyze full-field deformation. To create the speckled pattern, samples were painted with an airbrush spray gun with different tips. Microscopic analysis showed a highly contrasted, stochastic, and isotropic pattern, with an average black mark ratio of 41.7% (see Fig. 3 *r*). Two Allied Vision GigE MAKO G-507B cameras with APO-Xenoplan 1.4/23-0903 lenses were employed to record the samples' surface displacements. The set-up's calibration was performed with a GOM CP20/MV55x44 panel, reporting a deviation of 0.024 pixels. The sequences were finally post-processed with GOM Correlate Professional software using a facet size of 19x19 pixels.

For the compression test, the ASTM C365 standard [59] was followed with a crosshead rate of 3 mm/min, so that specimen failure occurred during 3 and 6 min of testing, according to the standard specification. The results of elastic modulus, first peak stress, and energy absorption up to first peak load were reported for each test direction. For stress calculations, the specimen's nominal external dimensions were considered. The Poisson's ratios were determined as the ratio between the two in-plane displacement components using DIC extensometers placed at a quarter (10 mm) and three-quarters (30 mm) of the specimen's height.

3.3. Finite element model

An Ansys FE implicit model was created to evaluate the elastic performance of each cellular geometry numerically. The pattern was directly imported in STEP format. Two rigid bodies were created on the top and bottom faces to represent compression test plates. Cellular geometries were meshed with 30 divisions in the *z*-direction (building direction) and with an element's size of 0.15 mm in the manufacturing plane. Higher-order 3D 20-node solid element SOLID186 was used. As a model example, Fig. 2 depicts the mesh for the Antitetrachiral pattern with density level II.

Displacements and rotations were restricted to fix the bottom plate, while a 0.1 mm displacement was imposed on the upper plate along the loading testing direction. Frictional contacts with asymmetric behavior were defined between the cellular pattern and the plates. According to PEI Ultem 1010 available datasheets [60], the friction coefficient was set to 0.42. The Augmented Lagrange formulation with a penetration tolerance of 0.1 mm was activated, and ramped effects were permitted. The reaction force was finally measured on the bottom surface to evaluate the stiffness of the cellular pattern.

The properties of the cell walls' material were adopted from a previous comprehensive study [19] on the material PEI Ultem 9085, where tensile, flexural, and shear behaviors were determined for different Solid and Sparse infill configurations. Main results of the Solid ±45° infill configuration are depicted in Table 2. In this case, three scenarios were examined on the simulations: orthotropic, quasi-isotropic and isotropic material. Since several authors have demonstrated the elastic asymmetry of FFF printed parts [61,62] due to the contribution of the filament bonds, the given properties needed to be adapted to the compression behavior. Hence, to reproduce the phenomenon of elastic asymmetry, the Normal Stiffness Factor (FKN) was included in the contacts' definition. FKN factors were calibrated from the Solid ±45° cube (Fig. 1 *s*) experimental results for the in-plane and the out-of-plane test, obtaining values of 0.215 and 0.050, respectively. With these FKN factor settings and defining the material with tensile and shear properties, the FE model described the FFF asymmetric compression elastic behavior with an accuracy of 99% when compared to the experimental results. The adjusted model was then used to simulate all the cellular patterns studied in each of the test directions.

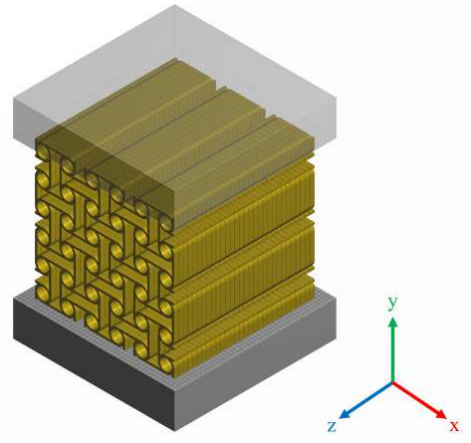

Fig. 2. Boundary conditions and generated mesh example of the FE model developed for the numerical simulation of the compression behavior of the cellular solid patterns.

The Sparse pattern was automatically created from a solid CAD part in Insight software,. In other words, the detailed pattern geometry was not available as in the other cells thus requiring a different model approach. Accordingly, the Representative Volume Element (RVE) method was adopted with homogeneous material properties recalculated using the obtained analytical model, as follows:

$$E_x^{sp} = \eta_2 E_x^s \quad E_y^{sp} = \eta_2 E_y^s \quad E_z^{sp} = \eta_3 E_z^s \tag{17}$$

$$\nu_{xy}^{sp} = \eta_1 \nu_{xy}^s \quad \nu_{yz}^{sp} = \eta_1 \nu_{yz}^s \quad \nu_{xz}^{sp} = \eta_1 \nu_{xz}^s \tag{18}$$

$$G_{xy}^{sp} = \eta_2 G_{xy}^s \quad G_{yz}^{sp} = \eta_3 G_{yz}^s \quad G_{xz}^{sp} = \eta_3 G_{xz}^s \tag{19}$$

$$\sigma_{T,x}^{sp} = \eta_1 \sigma_{T,x}^s \quad \sigma_{T,y}^{sp} = \eta_1 \sigma_{T,y}^s \quad \sigma_{T,z}^{sp} = \eta_1 \sigma_{T,z}^s \tag{20}$$

$$\sigma_{C,x}^{sp} = \eta_1 \sigma_{C,x}^s \quad \sigma_{C,y}^{sp} = \eta_1 \sigma_{C,y}^s \quad \sigma_{C,z}^{sp} = \eta_1 \sigma_{C,z}^s \tag{21}$$

$$\tau_{xy}^{sp} = \eta_1 \tau_{xy}^s \quad \tau_{yz}^{sp} = \eta_1 \tau_{yz}^s \quad \tau_{xz}^{sp} = \eta_1 \tau_{xz}^s \tag{22}$$

where the minoring factor $\eta_1 = \frac{\rho^*}{\rho^s}$ is taken from Eq. 16, $\eta_2 = \frac{E_x^*}{E_x^s} = \frac{E_y^*}{E_y^s}$ from Eq. 23, and $\eta_3 = \frac{E_z^*}{E_z^s}$ from Eq. 24. Superscript ^{sp} states Sparse properties, and superscript ^{s} refers to the properties of the solid material in ±45° printing configuration evaluated with tensile and shear tests (extracted from [19]).

4. Results and discussion

4.1. Microscopy analysis

4.1.1. Cell wall-thickness

The panel in Fig. 3 shows microscopic details of the intra-layer joints of each manufactured cellular pattern, inter-layer defects, and measurements of the thickness of the deposited filament.

Table 2
PEI Ultem elastic properties and stress limits used on the FE model.

Orthotropic Elasticity					Orthotropic Stress Limits				
Property	Symbol	Iso.	Q-Iso.	Ortho.	Property	Symbol	Iso.	Q-Iso.	Ortho.
Young's Modulus *x*-direction (MPa)	E_x^s	2123	2121	2092	Tensile *x*-direction (MPa)	$\sigma_{T,x}^s$	24.46	24.45	26.50
Young's Modulus *y*-direction (MPa)	E_y^s	2123	2121	2150	Tensile *y*-direction (MPa)	$\sigma_{T,y}^s$	24.46	24.45	22.40
Young's Modulus *z*-direction (MPa)	E_z^s	2123	2126	2126	Tensile *z*-direction (MPa)	$\sigma_{T,z}^s$	24.46	24.48	24.48
Poisson's Ratio *xy*	ν_{xy}^s	0.368	0.344	0.344	Compressive *x*-direction (MPa)	$\sigma_{C,x}^s$	−24.46	−24.45	−26.50
Poisson's Ratio *yz*	ν_{yz}^s	0.368	0.392	0.392	Compressive *y*-direction (MPa)	$\sigma_{C,y}^s$	−24.46	−24.45	−22.40
Poisson's Ratio *xz*	ν_{xz}^s	0.368	0.392	0.392	Compressive *z*-direction (MPa)	$\sigma_{C,z}^s$	−24.46	−24.48	−24.48
Shear Modulus *xy* (MPa)	G_{xy}^s	704	630	630	Shear *xy* (MPa)	τ_{xy}^s	25.86	25.72	25.72
Shear Modulus *yz* (MPa)	G_{yz}^s	704	741	745	Shear *yz* (MPa)	τ_{yz}^s	25.86	25.93	27.37
Shear Modulus *xz* (MPa)	G_{xz}^s	704	741	737	Shear *xz* (MPa)	τ_{xz}^s	25.86	25.93	24.48

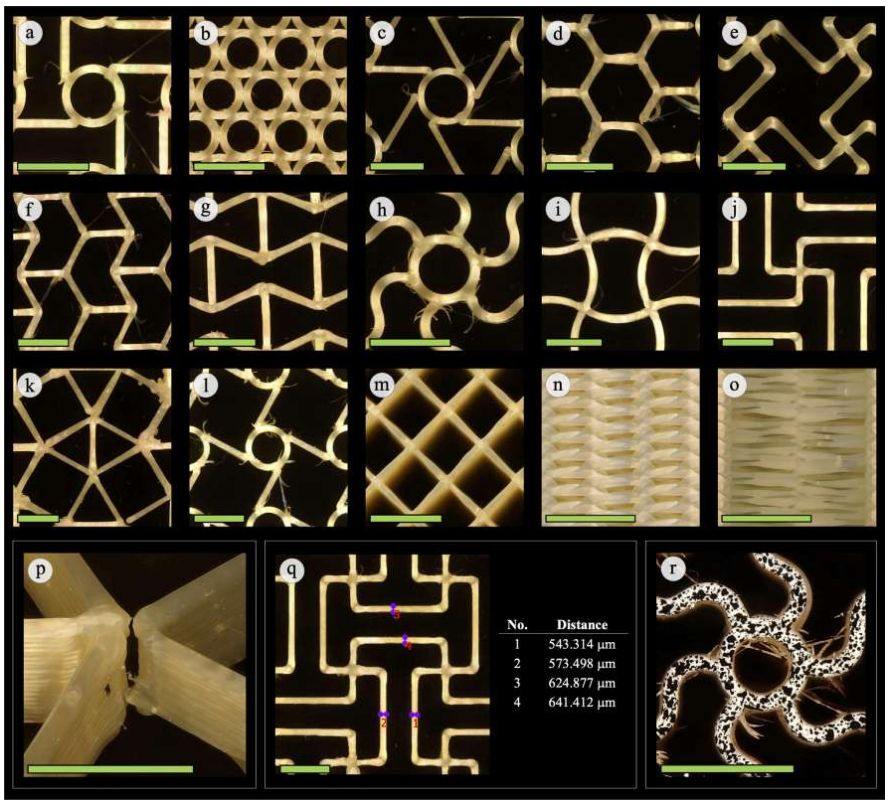

Fig. 3. Microscopic detail of the intra-layer joints - Antitetrachiral (*a*), Circular (*b*), Hexachiral (*c*), Hexagon (*d*), Lozenge Grids (*e*), Re-Entrant Hexagon I (*f*), Re-Entrant Hexagon II (*g*), Rotachiral (*h*), Sinusoidal Ligaments (*i*), Square Grids (*j*), SrCuBO (*k*), Tetrachiral (*l*), Sparse in-plane (*m*) and out-of-plane (*n-o*), inter-layer defects (*p*), measurements of the thickness of the filament (*q*), and DIC speckle pattern (*r*). Scale bar is 5 mm.

In Section 3.1, it is defined that the nominal cell wall-thickness t was set to 0.508 mm for all configurations. This value is commanded by the FFF tip used (here T16 with a nozzle diameter of 0.016 in or 0.4064 mm), whose size conditions the slice height (0.010 in or 0.254 mm) and the width of the extruded filament (approximately twice the height, i.e., 0.020 in or 0.508 mm). Nevertheless, as specified in Table 1, the value used for calculating the relative density from the analytical Eq. 4–16 was $t = 0.5777$ mm (± 0.0110 mm). This value corresponds to the average result measured on the microscopic analysis of the cell walls of printed samples (see image *q* in Fig. 3).

4.1.2. Manufacturing defects

Apart from the irregular filaments' thickness, the images in Fig. 3 also show some discontinuities in the trajectories in both the in-plane (intra-layer) and the out-of-plane (inter-layer) filament joints. Intra-layer joints are detailed in sub-figures *a-m*. As can be noted, deposited rasters' quality depends on the trajectories required to create the patterns. In those cases where circumferences appear in the pattern's cellular unit, the extruder head first creates the circles and later connects them with the bars (see Fig. 3 *a*, c, *h*, and *l*). As a result, the raster's joint that closes each circumference is almost unnoticeable, while the finish of the connections between these circles and the toolpaths that link the different cells is notably lower.

Defects in connections are more evident in some patterns formed by rectilinear trajectories. In such cases, the requirements to repeatedly pass over the same point to build the whole pattern led to several material blobs (see Fig. 3 *k*). Besides, the abrupt changes of direction of the nozzle or the end of the trajectory create deficiencies in cell-cell bonding (see Fig. 3 *d*), which could affect the mechanical performance. In contrast, the pattern's quality is highly improved in those cases that take advantage of the optimized toolpaths by reducing the amount of intra-layer unions such as the Sparse (see Fig. 3 *m*).

When successive in-plane imperfections occur in the same location for adjacent layers, an inter-layer defect appears, as shown in Fig. 3 *p*. This discontinuity has proved to dramatically impact the pattern's mechanical behavior when tested in the in-plane directions.

To prevent these inter-layer defects, it would be necessary to have a different start of each layer's path to avoid overlapping seams and force each layer's paths to be different. The last was not an option available in the Insight 3D Printing Software, so defects were not avoidable for these particular cell geometries. A compromise solution would be to increase the wall-thickness or

geometrically reinforce the joint, both of which would result in an undesirable increase in relative density of the cellular solid.

4.1.3. Sparse infill

The case of the Sparse infill deserves special consideration. Unlike the rest of the geometries in which the extruded filament is deposited over the preceding layer's filament, there is a 90° rotation of the toolpaths between two adjacent layers in the Sparse pattern when a raster angle of ±45° is employed. This fact causes inter-layer voids, as shown in Fig. 3 (*n-o*), whose magnitude increases as the air gap grows. This phenomenon causes a weakening of the stiffness in the out-of-plane direction (*z*-direction), as proved later, but essentially reduces the manufacturing time and material consumption, as shown in the next section, thus becoming an efficient solution for low-density infill.

4.2. Experimental analysis

4.2.1. Compressive behavior

Fig. 4 shows a representative example of load-displacement curves for the three levels of density of the Hexachiral and Re-Entrant Hexagon I patterns. The results presented were obtained from compression testing along *x*-direction (see Fig. 1). The results state a clear impact of both the pattern and the cell's dimensions on the mechanical behavior, as expected. In particular, the stiffness and the first detected peak load results vary significantly between the examined configurations.

Results obtained from the experimental compressive evaluation of the manufactured cellular patterns are summarized in Table 3. Elastic modulus values are given for the three orthogonal directions, and Poisson's Ratios (ν_{xy} and ν_{yx}), first peak stress and energy absorption efficiency data acquired in the in-plane tests are provided. Poisson's ratios are reported in the same strain range used to calculate the elastic moduli ($\varepsilon = 0.1\% - 0.3\%$). Nominal external

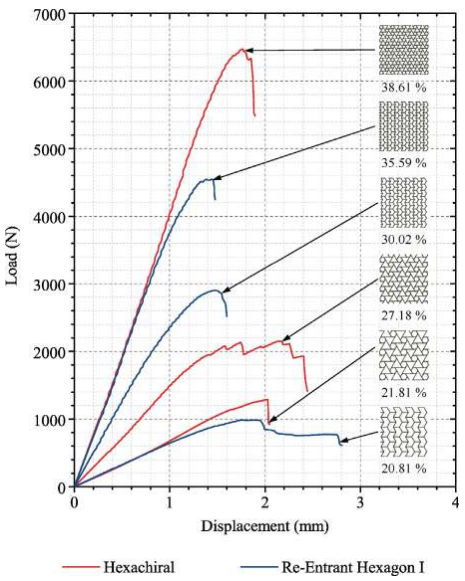

Fig. 4. Load-displacement curves for the three levels of density of the Hexachiral and Re-Entrant Hexagon I patterns. Experimental results of relative density are included.

dimensions were used for the calculation of the engineering properties, and energy absorption efficiency was calculated by relating the total amount of energy absorbed up to the first peak of load with the material volume estimated in the Insight 3D Printing Software. Finally, the adjusted coefficients *B* and *C* for the power-law expressions (see Eq. 2–3) are included together with the corresponding Coefficient of determination (R^2) in Table 3.

On the one hand, compression testing results show a clear difference between the in-plane and the out-of-plane behavior. In particular, the *z*-direction's elastic moduli results exceed those in the *x* and *y* orientations by one order of magnitude in most cases. Moreover, the DIC post-process allowed detecting that the in-plane tests' failure of the patterns was initiated at the intra-layer joints that arise from the FFF manufacturing toolpaths. Hence, as proved in a previous work [19], the intra-layer unions are weakened points that can limit the maximum reachable load.

On the other hand, the different density levels' trends confirm the effect of mass decrease on the mechanical properties of the cellular solids. As can be gathered from the values in Table 3, both the elastic modulus and the maximum load decrease with the density of the pattern, as expected. However, the energy absorption efficiency does not always follow the same trend. A clear example of this is shown by the Sparse infill, where density level IV (air gap 1.50 mm) has delivered 2.28 times the energy efficiency of level I (air gap 0.25 mm).

4.2.2. Mechanical performance versus manufacturing time

Results trends differ even more if the mechanical properties are related to each sample's printing time. It is considered a relevant issue when contemplating manufacturing lightweight components with cellular solid designs while preserving their feasibility from the fabrication perspective. Fig. 5 and Fig. 6 depict the obtained elastic modulus and energy absorption efficiency results versus the manufacturing time of each pattern, respectively.

Data presented in Fig. 5 and Fig. 6 confirm a manufacturing advantage of the Sparse over the rest of the infill patterns. As shown, the optimization of the printing toolpaths of the Sparse pattern reduces the time needed for their construction by at least one order of magnitude. In addition, the results of elastic moduli show a clear trend towards the solid cube result as the air gap parameter decreases (see Table 1). It should be seen that the main differences in the elastic modulus correspond to the E_z. This is due to the filaments' arrangement between two adjacent layers, which produces an inter-layer weakness, as observed in Fig. 3 (*n-o*).

It should be noted that the Sparse design simplifies the manufacturing trajectories compared to the other analyzed patterns. The cellular pattern designs located on the right side of the graphs required longer fabrication time since their cells were printed one by one instead of using optimized toolpaths. Accordingly, including these pattern designs with improved trajectories into the slicing software would reduce the number of abrupt transitions of the head direction as well as filament discontinuities. This fact would also reduce the required time to manufacture most of the examined patterns and aid to the applicability of FFF cellular solids.

4.3. Finite element analysis

The Finite Element Analysis aimed to evaluate each cellular geometry's elastic performance, addressing the effect of the material model definition (orthotropic, quasi-isotropic, or isotropic) and the cell wall-thickness.

4.3.1. Cell wall-thickness

Although the deposited filament's thickness should be $t = 0.508$ mm according to the Insight 3D Printing Software preferences,

Table 3
Compressive experimental results of elastic modulus, first peak stress, energy absorption efficiency, and Poisson's Ratio, of each cell pattern and density level tested. The results shown are average values with corresponding standard deviations. *B* and *C* are the adjusted coefficients for power-law expressions.

Pattern	Relative density (%)	Elastic Modulus (MPa)			1*st* Peak Stress (MPa)		Energy Abs. Efficiency (J/cm^3)		Poisson's Ratio		Power-Law Adjusted Coefficients			
		E_x	E_y	E_z	σ_x^{1st}	σ_y^{1st}	W_x	W_y	ν_{xy}	ν_{yx}				
(a) Antitetrachiral†§	44.58	24 ± 0	Sym.	888 ± 5	8.99 ± 2.44	Sym.	1011 ± 394	Sym.	−1.081 ± 0.001	Sym.	0.210	Sym.	0.226	Sym.
	25.32	4 ± 0		484 ± 5	0.42 ± 0.00		129 ± 2		−0.431 ± 0.026		R^2=99.8%		R^2=87.2%	
	16.60	2 ± 0		350 ± 2	0.18 ± 0.02		78 ± 19		−0.785 ± 0.009					
(b) Circular§	47.64	348 ± 19	274 ± 38	882 ± 63	18.02 ± 1.07	15.58 ± 0.38	1011 ± 299	782 ± 29	0.324 ± 0.007	0.298 ± 0.010	2.696	2.099	0.370	0.332
	40.18	262 ± 23	209 ± 55	842 ± 42	6.90 ± 1.85	6.86 ± 0.64	314 ± 240	356 ± 183	0.362 ± 0.009	0.198 ± 0.002	R^2=88.5%	R^2=90.1%	R^2=69.5%	R^2=75.6%
	34.21	151 ± 3	101 ± 16	624 ± 2	7.79 ± 0.68	7.19 ± 0.61	697 ± 48	501 ± 75	0.465 ± 0.006	0.350 ± 0.011				
(c) Hexachiral†§	38.61	101 ± 3	96 ± 9	716 ± 64	3.86 ± 0.31	3.42 ± 0.25	234 ± 35	204 ± 56	−0.068 ± 0.002	−0.188 ± 0.001	1.370	1.284	0.134	0.123
	27.18	36 ± 1	32 ± 0	532 ± 17	1.49 ± 0.07	1.63 ± 0.05	131 ± 5	222 ± 41	−0.130 ± 0.003	−0.219 ± 0.005	R^2=100.0%	R^2=99.7%	R^2=95.0%	R^2=97.3%
	21.81	19 ± 2	14 ± 0	457 ± 34	0.84 ± 0.06	0.76 ± 0.13	101 ± 18	104 ± 33	−0.531 ± 0.001	−0.320 ± 0.003				
(d) Hexagon§	25.25	36 ± 2	Sym.	434 ± 3	1.25 ± 0.30	Sym.	138 ± 100	Sym.	0.823 ± 0.015	Sym.	1.746	Sym.	0.110	Sym.
	21.50	23 ± 1		390 ± 7	1.06 ± 0.10		170 ± 28		0.672 ± 0.002		R^2=99.6%		R^2=87.6%	
	16.44	9 ± 1		320 ± 3	0.35 ± 0.02		45 ± 8		0.757 ± 0.006					
(e) LozengeGrids†§	32.60	17 ± 2	Sym.	593 ± 10	1.35 ± 0.00	Sym.	258 ± 28	Sym.	−0.007 ± 0.002	Sym.	0.396	Sym.	0.063	Sym.
	24.76	9 ± 1		480 ± 12	0.56 ± 0.02		168 ± 21		−0.035 ± 0.003		R^2=97.1%		R^2=90.1%	
	20.90	5 ± 0		394 ± 0	0.37 ± 0.00		145 ± 15		−0.021 ± 0.007					
(f) Re − EntrantHexagonI†§	35.59	107 ± 7	83 ± 6	640 ± 21	3.06 ± 0.03	2.38 ± 0.18	194 ± 19	108 ± 25	−0.147 ± 0.013	−0.110 ± 0.003	1.871	1.469	0.125	0.101
	30.02	69 ± 0	56 ± 3	597 ± 23	1.92 ± 0.05	1.66 ± 0.09	144 ± 8	105 ± 2	−0.139 ± 0.004	−0.251 ± 0.010	R^2=99.0%	R^2=98.2%	R^2=94.3%	R^2=96.8%
	20.81	17 ± 1	13 ± 1	423 ± 24	0.64 ± 0.07	0.57 ± 0.02	76 ± 21	76 ± 3	−0.132 ± 0.016	−0.306 ± 0.006				
(g) Re − EntrantHexagonII†§	37.17	14 ± 1	81 ± 1	705 ± 0	0.96 ± 0.01	2.26 ± 0.00	108 ± 5	144 ± 1	−0.334 ± 0.001	−2.076 ± 0.010	0.213	1.320	0.040	0.092
	29.76	7 ± 0	48 ± 4	559 ± 7	0.70 ± 0.03	1.47 ± 0.04	142 ± 15	140 ± 8	−0.264 ± 0.006	−2.511 ± 0.008	R^2=99.2%	R^2=70.9%	R^2=96.1%	R^2=97.2%
	25.33	5 ± 0	42 ± 1	430 ± 78	0.47 ± 0.06	1.19 ± 0.05	102 ± 29	126 ± 10	−0.147 ± 0.043	−2.483 ± 0.014				
(h) Rotachiral†§	37.22	33 ± 4	Sym.	672 ± 25	2.02 ± 0.20	Sym.	250 ± 71	Sym.	−0.080 ± 0.002	Sym.	0.489	Sym.	0.076	Sym.
	29.26	14 ± 1		547 ± 8	1.12 ± 0.07		156 ± 22		−0.020 ± 0.007		R^2=98.4%		R^2=95.5%	
	23.06	9 ± 1		415 ± 24	0.55 ± 0.04		98 ± 14		−0.024 ± 0.003					
(i) SinusoidalLigaments†‡	46.15	32 ± 6	Sym.	793 ± 11	10.87 ± 0.28	Sym.	3060 ± 32	Sym.	−0.029 ± 0.019	Sym.	0.060	Sym.	0.094	Sym.
	33.92	29 ± 9		589 ± 7	3.10 ± 0.31		446 ± 77		−0.116 ± 0.040		R^2=63.9%		R^2=59.5%	
	20.05	19 ± 0		416 ± 10	1.13 ± 0.04		201 ± 5		−0.118 ± 0.028					
(j) SquareGrids†§	36.73	5 ± 1	Sym.	665 ± 9	2.71 ± 0.43	Sym.	642 ± 186	Sym.	−0.105 ± 0.031	Sym.	0.076	Sym.	0.108	Sym.
	28.72	2 ± 0		515 ± 31	1.49 ± 0.22		431 ± 75		−0.056 ± 0.019		R^2=98.3%		R^2=98.7%	
	20.42	1 ± 0		443 ± 4	0.87 ± 0.08		312 ± 3		−0.028 ± 0.008					
(k) SrCuBO†	39.83	203 ± 13	Sym.	733 ± 37	6.72 ± 1.30	Sym.	281 ± 117	Sym.	0.223 ± 0.004	Sym.	0.363	Sym.	0.083	Sym.
	31.38	145 ± 20		507 ± 5	4.90 ± 0.80		369 ± 26		0.200 ± 0.002		R^2=85.4%		R^2=74.5%	
	23.68	83 ± 4		437 ± 6	2.06 ± 0.20		172 ± 2		0.194 ± 0.002					
(l) Tetrachiral§	28.23	38 ± 6	Sym.	577 ± 6	1.80 ± 0.07	Sym.	294 ± 3	Sym.	0.102 ± 0.002	Sym.	1.352	Sym.	0.117	Sym.
	23.34	24 ± 0		458 ± 7	1.06 ± 0.08		194 ± 10		0.056 ± 0.003		R^2=98.9%		R^2=94.9%	
	17.15	9 ± 0		338 ± 8	0.47 ± 0.02		147 ± 1		0.039 ± 0.001					
(m) Sparse§	69.13	418 ± 3	Sym.	871 ± 23	17.22 ± 0.00	Sym.	727 ± 18	Sym.	0.614 ± 0.067	Sym.	1.044	Sym.	0.210	Sym.
	53.02	228 ± 18		548 ± 13	11.68 ± 0.02		1425 ± 57		0.151 ± 0.042		R^2=96.7%		R^2=97.6%	
	42.76	155 ± 2		385 ± 3	7.89 ± 0.09		1270 ± 8		0.268 ± 0.030					
	27.71	46 ± 0		178 ± 1	2.89 ± 0.03		1663 ± 50		1.031 ± 0.113					
	16.93	10 ± 1		43 ± 0	0.79 ± 0.02		937 ± 77		0.814 ± 0.077					
	10.46	3 ± 0		34 ± 1	0.13 ± 0.01		75 ± 10		1.327 ± 0.101					
(s) Solid	100.00	1286 ± 0	Sym.	1905 ± 0	181[a]	Sym.	–	Sym.	0.554 ± 0.040	Sym.	–	–	–	–

† Auxetic cell pattern.
‡ Stretching-dominated pattern.
§ Bending-dominated pattern.
[a] ASTM D695 Compressive Strength, Ultimate (Method 1, 0.05″/min) [63].

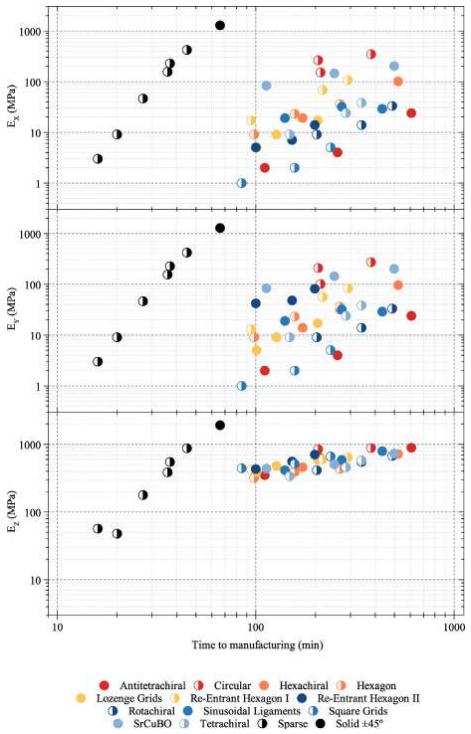

Fig. 5. Relation between the elastic modulus experimental results versus the manufacturing time for each pattern. See Fig. 1 and Tables 1 and 3 for more detail.

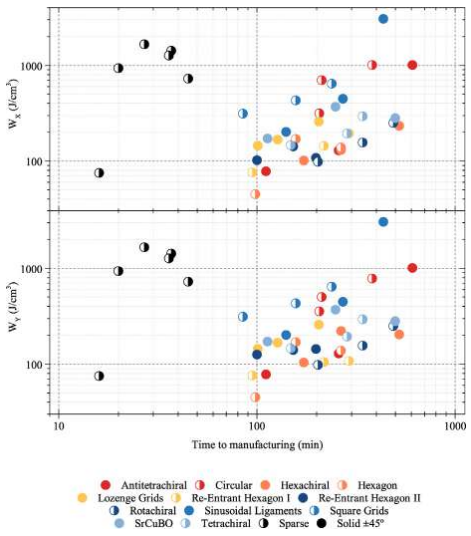

Fig. 6. Relation between the energy absorption efficiency experimental results versus the manufacturing time for each pattern. See Fig. 1 and Tables 1 and 3 for more detail.

walls in the patterns' CAD design must be widened to $t = 0.60$ mm to generate the fabrication toolpaths correctly. Nevertheless, the thickness measured on the microscopic analysis was $t = 0.5777$ mm. Hence, the three wall-thicknesses were assessed together with the three material models to conclude their effect on the mechanical behavior.

A total of 864 different models were simulated. Fig. 7 shows the boxplot diagram depicting the deviation between the numerical and experimental elastic modulus for each wall-thickness and material model considered. As can be seen, the boxplot diagram displays more widespread whiskers or a higher number of outliers when the Isotropic model is used, regardless of the wall-thickness. Besides, minor differences are observed when Quasi-Isotropic and Orthotropic models are compared. Therefore, using the Quasi-Isotropic model material allows simplifying the FFF material's model complexity without meaning noticeable variances regarding the Orthotropic model results. The results also show that wall-thickness plays a significant role in cellular solids' stiffness, as expected. Experimentally measured thickness $\{t = 0.5777\}$ mm has achieved the highest accuracy in both the Quasi-Isotropic and Orthotropic models. In particular, more than half of the Quasi-Isotropic simulations exhibited less than 10% of deviation when using the experimental t.

4.3.2. Compressive behavior

Table 4 compares the numerical, experimental, and analytical results of the cellular solids' stiffnesses in each of the three test directions, as well as the in-plane first peak stress experimental data. Numerical results were obtained considering the Quasi-Isotropic model and a wall-thickness t = 0.5777 mm. The analytical results in z-direction were calculated using Eq. 1 for each pattern and density level, except for the Sparse infill, as explained in Section 4.4. Power-law (Eq. 2 and Eq. 23) results are also included. The agreement of the results enables the validation of the developed FE model and the analytical equations. The differences observed between the experimental data and the estimated results from the power-law expressions are attributed to the identified manufacturing defects.

Fig. 8 (*left*) depicts a comparison between the simulated deformed shape and the recorded images using DIC of Antitetrachi-

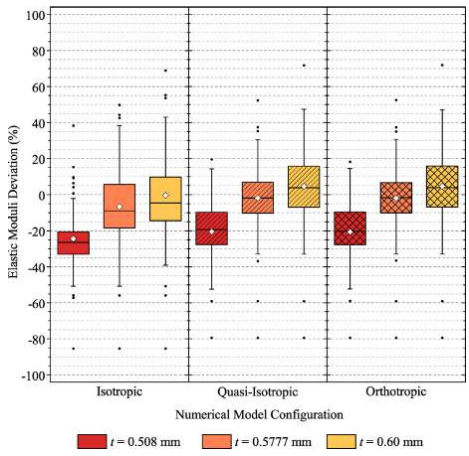

Fig. 7. Boxplot diagrams depicting the deviation of the elastic moduli between the FE model results and the experimental data for different material models and cell wall-thickness.

Table 4
Comparison of analytical, experimental and numerical results.

Pattern	Relative density (%)	E_x (MPa)			E_y (MPa)			E_z (MPa)			σ_x (MPa)		σ_y (MPa)	
		Power-Law	Num.	Exp.	Power-Law	Num.	Exp.	Analytical	Num.	Exp.	Power-Law	Exp.	Power-Law	Exp.
(a) Antitetrachiral†§	44.58	24	24	24 ± 0		Sym.		877	801	888 ± 5	8.14	8.99	Sym.	
	25.32	4	6	4 ± 0				503	483	484 ± 5	2.63	0.42		
	16.60	1	3	2 ± 0				357	363	350 ± 2	1.13	0.18		
(b) Circular§	47.64	375	328	348 ± 19	292	284	274 ± 38	858	815	882 ± 63	15.20	18.02	13.64	15.58
	40.18	225	233	262 ± 23	175	204	209 ± 55	709	679	842 ± 42	10.82	6.90	9.70	6.86
	34.21	139	119	151 ± 3	108	102	101 ± 16	525	514	624 ± 2	7.84	7.79	7.03	7.19
(c) Hexachiral†§	38.61	101	132	101 ± 3	95	100	96 ± 9	779	711	716 ± 64	3.61	3.86	3.32	3.42
	27.18	35	34	36 ± 1	33	35	32 ± 0	574	526	532 ± 17	1.79	1.49	1.65	1.63
	21.81	18	21	19 ± 2	17	15	14 ± 0	449	411	457 ± 34	1.15	0.84	1.06	0.76
(d) Hexagon§	25.25	36	47	36 ± 2		Sym.		502	471	434 ± 3	1.27	1.25	Sym.	
	21.50	22	30	23 ± 1				420	397	390 ± 7	0.92	1.06		
	16.44	10	13	9 ± 1				316	303	320 ± 3	0.54	0.35		
(e) LozengeGrids†§	32.60	18	13	17 ± 2		Sym.		620	527	593 ± 10	1.22	1.35	Sym.	
	24.76	8	6	9 ± 1				484	430	480 ± 12	0.70	0.56		
	20.90	5	4	5 ± 0				397	362	390 ± 0	0.50	0.37		
(f) Re – EntrantHexagonI†§	35.59	108	116	107 ± 7	85	83	83 ± 6	676	624	640 ± 21	2.86	3.06	2.31	2.38
	30.02	65	67	69 ± 0	51	56	56 ± 3	575	533	597 ± 23	2.03	1.92	1.65	1.66
	20.81	22	19	17 ± 1	17	15	13 ± 1	396	375	423 ± 24	0.98	0.64	0.79	0.57
(g) Re – EntrantHexagonII†§	37.17	14	13	14 ± 1	87	105	81 ± 1	731	658	705 ± 0	1.00	0.96	2.31	2.26
	29.76	7	7	7 ± 0	45	56	48 ± 4	588	537	559 ± 7	0.64	0.70	1.48	1.47
	25.33	4	5	5 ± 0	28	36	42 ± 1	487	453	430 ± 78	0.47	0.47	1.07	1.19
(h) Rotachiral†§	37.22	32	29	33 ± 4		Sym.		740	663	672 ± 25	1.91	2.02	Sym.	
	29.26	16	15	14 ± 1				605	544	547 ± 8	1.18	1.12		
	23.06	8	8	9 ± 1				463	417	415 ± 24	0.73	0.55		
(i) SinusoidalLigaments†‡	46.15	36	28	32 ± 6		Sym.		864	762	793 ± 11	7.89	10.87	Sym.	
	33.92	26	25	29 ± 9				598	552	589 ± 7	5.80	3.10		
	20.05	15	19	19 ± 0				376	365	416 ± 10	3.43	1.13		
(j) SquareGrids†§	36.73	5	4	5 ± 1		Sym.		657	603	665 ± 9	2.65	2.71	Sym.	
	28.72	2	2	2 ± 0				518	482	515 ± 31	1.62	1.49		
	20.42	1	1	1 ± 0				387	371	443 ± 4	0.82	0.87		
(k) SrCuBO†	39.83	186	218	203 ± 13		Sym.		742	681	733 ± 37	5.98	6.72	Sym.	
	31.38	146	138	145 ± 20				541	492	507 ± 5	4.71	4.90		
	23.68	110	92	83 ± 4				396	360	437 ± 6	3.56	2.06		
(l) Tetrachiral§	28.23	39	39	38 ± 6		Sym.		585	548	577 ± 6	1.68	1.80	Sym.	
	23.34	22	25	24 ± 0				494	468	458 ± 7	1.15	1.06		
	17.15	9	11	9 ± 0				383	372	338 ± 8	0.62	0.47		
(m) Sparse§	69.13	444	503	418 ± 3		Sym.		928	763	871 ± 23	18.16	17.22	Sym.	
	53.02	200	251	228 ± 18				547	434	548 ± 13	10.68	11.68		
	42.76	105	143	155 ± 2				361	282	385 ± 3	6.95	7.89		
	27.71	29	40	46 ± 0				147	113	178 ± 1	2.92	2.89		
	16.93	7	8	10 ± 1				50	37	43 ± 0	1.09	0.79		
	10.46	2	1	3 ± 0				15	11	34 ± 1	0.42	0.13		
(s) Solid ± 45°	100.00	–	1300	1286 ± 0		Sym.		–	1776	1905 ± 0	–	181[a]	Sym.	

† Auxetic cell pattern.
‡ Stretching-dominated pattern.
§ Bending-dominated pattern.
[a] ASTM D695 Compressive Strength, Ultimate (Method 1, 0.05"/min) [63].

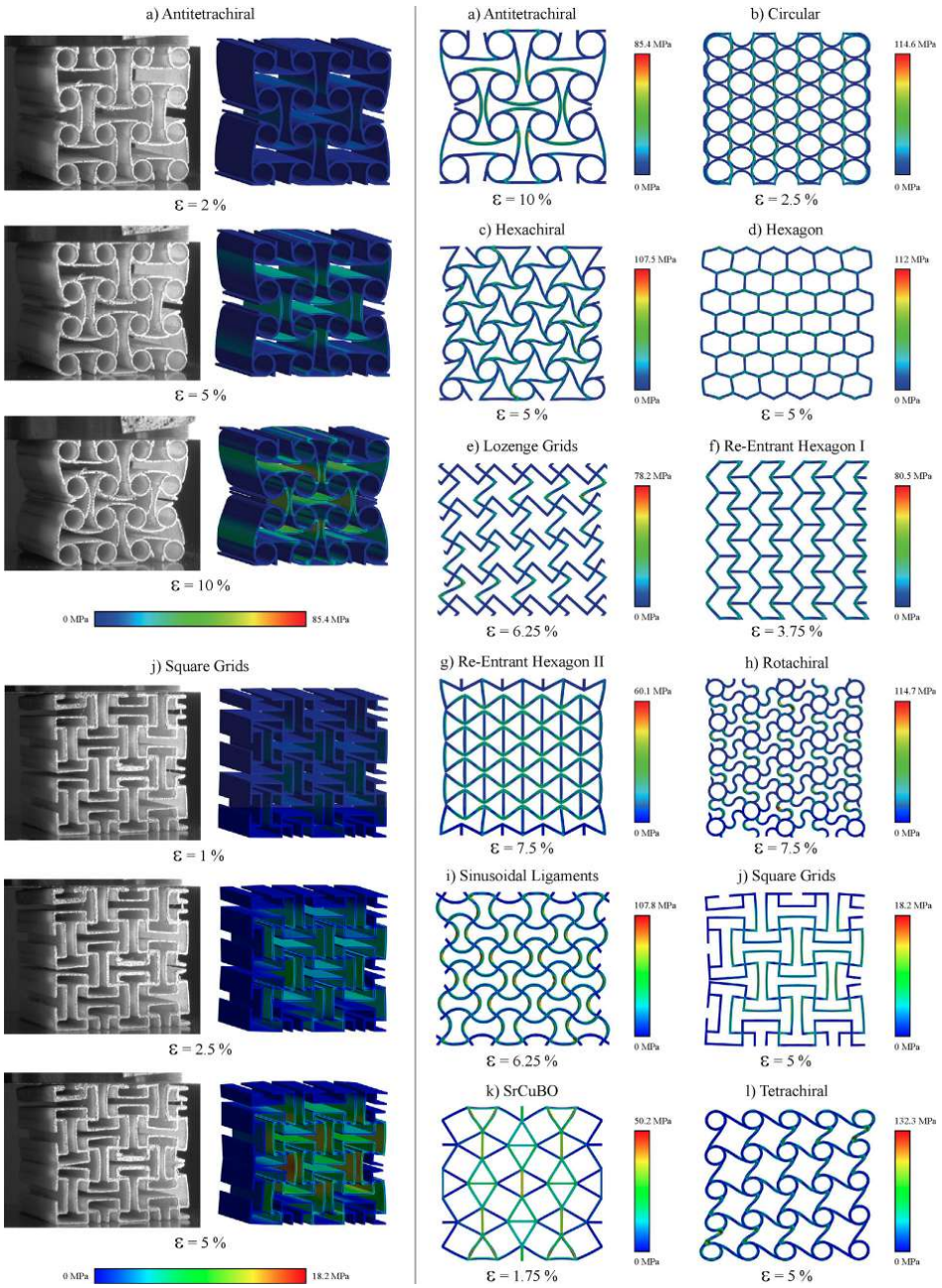

Fig. 8. Comparison of the experimental and numerical deformed shape sequences of the Antitetrachiral and Square Grids patterns (*left*). Deformed shape of each patterns before the first load peak or any internal contact was detected (*right*). Colormap stands for Von Mises stress.

ral and Square Grids as representative patterns at different strain stages. The sequences correspond to the *x*-direction tests with density level III. The colormap corresponds to the Von Mises stress results. This qualitative comparison shows a kinematic correspondence between the numerical and experimental results, with a marked auxetic behavior of both patterns. The numerical results allow identifying the most stressed zones and the contact points between the cell walls. Cross-sections of each analyzed pattern are shown on the right side of Fig. 8. Results correspond to the Von Misses stress before the first load peak, or any internal contact was detected. As can be seen, the patterns' deformed shapes are mostly bending-dominated. It can also be seen that some geometries display the maximum stress values at the joints of the unit cells. The localized stress values should indicate the failure zone of the material. However, experimental evidence has revealed that failure occurs mainly at the cell joints due to weaknesses and the reported manufacturing defects. In the experimental results of maximum stress shown in Table 3, the highest values of specific strength correspond to geometries as for example Circular, in whose microscopic analysis no discontinuity is observed in the trajectory of the filaments. This evidence highlights the importance of reducing defects of intra-layer joints to prevent premature pattern failure. So, once again, the importance of optimizing the printing toolpaths is justified, as it would reduce the amount of intra-layer manufacturing defects.

4.4. Verification of the numerical and analytical sparse infill model

The simple arrangement of the cell walls on the Sparse infill allows the derivation of an analytical expression to determine the relative elastic moduli in each of the test directions. Fig. 9 (*left*) illustrates the unit cell of the Sparse infill with boundary conditions corresponding to an in-plane compression test. Using an approach based on standard beam bending theory, Eq. 23 was derived to calculate the relative in-plane elastic moduli. E^s refers to the elastic modulus of the solid material.

$$\frac{E_x^*}{E_x^s} = \frac{E_y^*}{E_y^s} = \frac{2t^3}{a^3 + 3ta^2 + 4at^2 + 2t^3} \tag{23}$$

The elastic modulus along *z*-direction deserved a different approach. Inter-layer voids were identified in Fig. 3 (*n-o*), which weaken the stiffness in the out-of-plane direction. Accordingly, the relative elastic modulus has been determined from the effective load-bearing areas in the *z*-direction as depicted in Fig. 9 (*right*), obtaining the following expression:

$$\frac{E_z^*}{E_z^s} = \frac{t^2}{(a+t)^2} \tag{24}$$

The numerical and experimental results of the relative moduli for each Sparse infill as a function of the air gap and the analytical curves (Eq. 23 and 24) are plotted in Fig. 10 to assess the accuracy of the analytical expressions' prediction. The curve corresponding to the analytical adjustment of the relative density (Eq. 16) and its

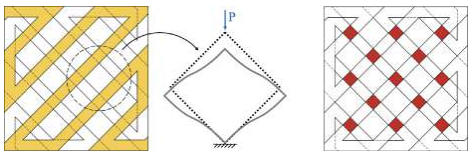

Fig. 9. Sparse pattern's cellular unit with boundary conditions corresponding to an in-plane compression test (*left*). Overlapping of two layers in the Sparse infill. The red shaded area corresponds to the contact points between layers (*right*).

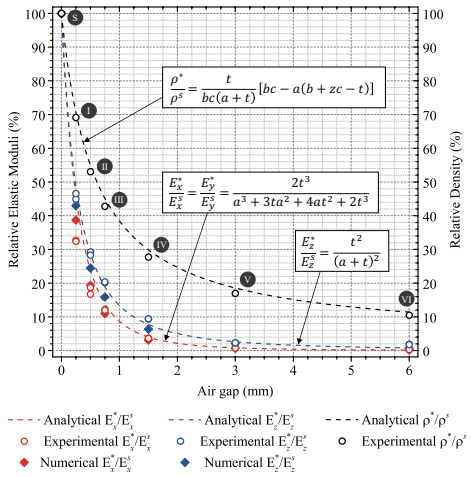

Fig. 10. Numerical, experimental, and analytical results of the relative elastic moduli and relative density of each Sparse pattern assessed in terms of the air gap.

experimental measurements are overlapped and represented on the right-hand axis.

As can be seen, the results calculated using the provided analytical equation are in good agreement with the experimental values obtained in both test directions. Furthermore, it should be noted that the analytical expression (Eq. 24) diverges from the calculation of the out-of-plane relative elastic moduli of the other cellular patterns presented in Section 2, which were obtained from a ratio of its relative density (see Eq. 1).

4.5. Comparative overall performance of FFF cellular solids

The elastic moduli results given in Table 4 are now depicted in the upper plot of Fig. 11 as a function of the relative density. The experimental densities are used for data representation. Values with diamonds correspond to numerical results, while circulars are the experimental ones. The dark shaded area states the Sparse samples' spectrum, and the red-orange area corresponds to the rest of the cellular solids. The black dots on the upper right-hand side of the graph indicate the PEI Ultem material performance, corresponding to the solid cell wall material properties.

Regarding the non-Sparse patterns, the results grouped at the top of the graph are the stiffnesses of the cellular solids in the *z*-direction, while the bottom data correspond to the *x-y* in-plane elastic moduli. The duplicity of results for the same geometry and relative density is due to the orthotropic behavior of some cell patterns. Specifically, the values at the bottom correspond to the cell's patterns with auxetic behavior. For a detailed identification of the auxetic patterns, see Table 4.

Overall, the divergence of the results for equivalent relative densities is evidence of the influence of the cellular pattern design. The results clustered at the top are related to the relative density, but the elastic *z*-modulus proves to be independent of the cell pattern. These data particularly show a good adjustment with the line plotted from the analytical Eq. 1.

Regarding the Sparse infill samples, results show a lower scatter between in-plane and out-of-plane stiffnesses. As shown, the elastic *z*-modulus of the Sparse infill is below the z-modulus of the other cellular geometries, as expected, and its data fit

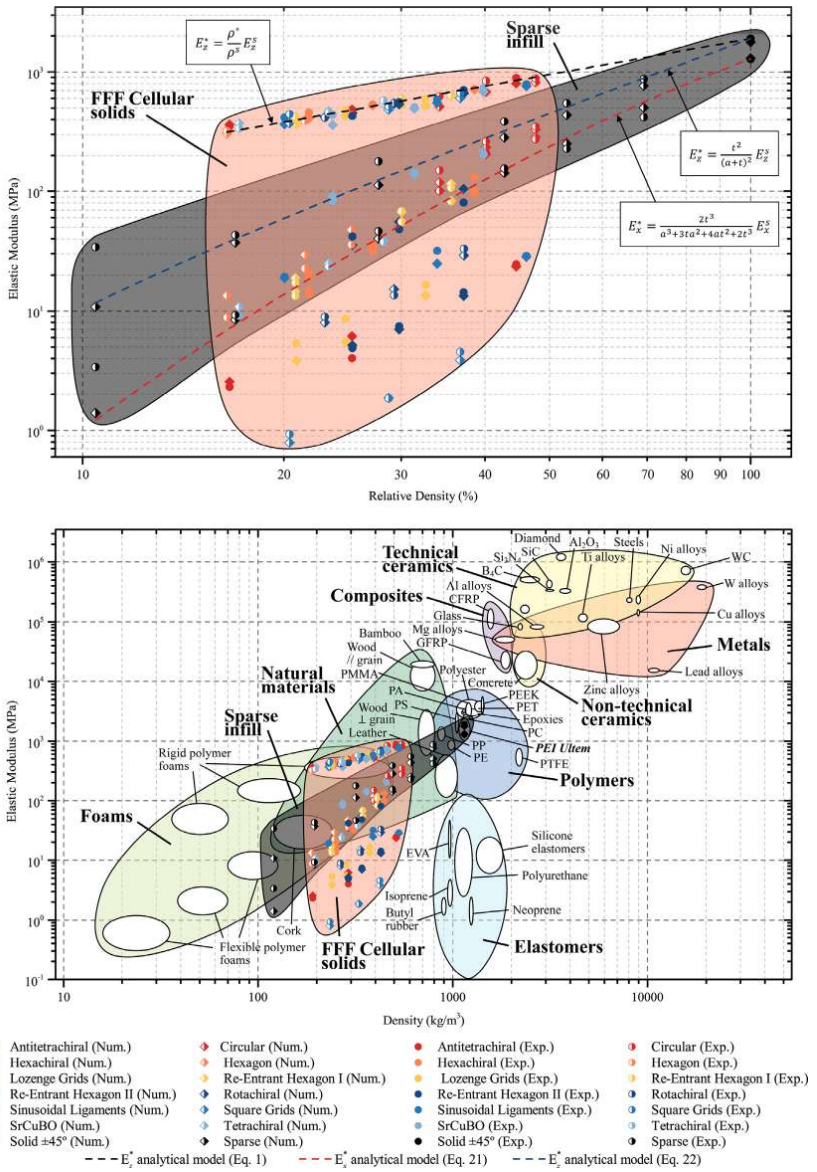

Fig. 11. Material property chart including analytical, experimental and numerical results (*top*) and materials database diagram (*bottom*). Adapted from CES EduPack 2019, ANSYS Granta © 2020 Granta Design, with permission.

accurately to the curve of the proposed Eq. 24 for the relative stiffness calculation. In addition, the results achieved in experiments along *x* and *y*-directions are also in agreement with the Eq. 23 adjustment.

Lastly, to conclude the study, the stiffnesses obtained for each cellular pattern are compared to other materials as a function of its density in the bottom graph of Fig. 11. Ansys GRANTA EduPack materials database is included for comparison. As can be seen, the specific stiffness properties of the analyzed FFF cellular solids cover a wide area that is comprised between foams, natural materials, polymers, and elastomers. The stiffnesses of the cellular solids are lower than those of the solid material, but both the geometry

and the cell size prove to play a significant role, as was intended to be demonstrated. The wide range of specific stiffnesses achieved is thus evidence of the potentials of FFF lightweight cellular solids.

5. Conclusions

This paper presents comprehensive research of the FFF technology's possibilities to create cellular solids with a broad spectrum of specific stiffness and strength, from the cell geometry and cell size, while addressing manufacturing matters such as inherent defects and manufacturing time. Thirteen typologies of two-dimensional cellular patterns with different relative densities were investigated and tested in compression in different directions, resulting in 42 different filling configurations.

The analytical approach has led to parametric equations to predict the relative density of each pattern, which have been successfully verified with experimental results. These expressions also allow the calculation of the elastic modulus in the three mutually perpendicular directions of the cells from the solid material properties.

Microscopic analysis revealed different manufacturing defects and highlighted the importance of optimizing filament trajectories. Intra-layer defects occur in certain types of cell patterns depending on their design, either due to defects in the connection of the cells or due to excessive deposition of material at filament's intersection points. Inter-layer defects are due to weak cell wall connectivity and dramatically impact the pattern's mechanical behavior when tested in the in-plane directions. To overcome these defects, it would be necessary to customize layer by layer the configuration of the filament trajectories and address its optimization.

The microscopic study also revealed the optimized arrangement of the filaments in the Sparse infill pattern, creating intentional inter-layer voids that essentially allow for a reduction in manufacturing time while maintaining satisfying mechanical properties, thus becoming an efficient solution for achieving a low-density infill.

Compression test results have allowed conclusions to be drawn regarding the influence of cell type and infill density on the mechanical performance. As expected, stiffness and stress decrease with the density of the pattern, but energy absorption efficiency does not always follow the same trend, such as in the case of the Sparse infill. Printing defects have also shown to have a critical effect on the strength of the cell patterns. Moreover, the time-to-print analysis has shown the competitive advantage of the Sparse infill over the rest of the patterns, as it provides comparable stiffness and strength properties with considerably shorter manufacturing times. This again highlights the relevance of optimizing filament trajectories in the slicing software to contribute in the application of FFF cellular solids.

The numerical study has provided a model for predicting the compressive stiffness of the different patterns, which has been validated with experimental results. The model can reproduce the behavior in the elastic range, based on tensile specimen properties and a Normal Stiffness Factor to account for the phenomenon of elastic asymmetry of the FFF printed samples. The study has evaluated the influence of the wall thickness and the material model used. The results demonstrate the validity of the hypothesis assuming a quasi-isotropic behavior of the cell wall material.

Given the outstanding behavior of the Sparse infill, its elastic performance has been deeply analyzed, obtaining analytical expressions for the calculation of the elastic moduli in the three perpendicular directions. The equations have been compared and successfully validated with numerical and experimental results. Regarding the stiffness in the out-of-plane direction, the prediction model proposed departs from approaches based on relative stiffness but shows a better correlation with experimental data.

Finally, the extensive study has allowed a reliable comparison of the elastic properties of the cellular patterns as a function of their density. The wide range of results achieved is experimental evidence of the potential of FFF lightweight cellular solids.

Data availability

The raw data required to reproduce these findings are available to download from Mendeley Data, doi: 10.17632/kf858mny8b.1. Kindly cite this article and the dataset if utilizing or modifying the data in your work.

Declaration of Competing Interest

The authors declare that they have no known competing financial interests or personal relationships that could have appeared to influence the work reported in this paper.

Acknowledgements

This work has been supported by the Ministry of Science, Innovation and Universities through the project New Developments in Lightweight Composite Sandwich Panels with 3D Printed Cores (3DPC) - RTI2018-099754-A-I00; and by the RIS3CAT Llavor 3D Community co-financed by the Generalitat de Catalunya (ACCIÓ) through the project TRANSPORT COMRDI16-1-0010 - (2017–2020). The authors would like to acknowledge their gratitude to J. Portero and F. Núñez from Olympus Iberia, A. Chueca, A. Watel, and T. Ceyrat for the assistance in conducting test experiments and finite element model respectively.

References

[1] L.J. Gibson, M.F. Ashby, Cellular solids - Structure and properties, second ed., Cambridge University Press, 1997.
[2] U.G. Wegst, H. Bai, E. Saiz, A.P. Tomsia, R.O. Ritchie, Bioinspired structural materials, Nat. Mater. 14 (2015) 23–36.
[3] H.N.G. Wadley, N.A. Fleck, A.G. Evans, Fabrication and structural performance of periodic cellular metal sandwich structures, Compos. Sci. Technol. 63 (2003) 2331–2343.
[4] M. Vijay Kumar, B. Soragaon, Fabrication and evaluation of multilayered polyurethane foam core sandwich panels for static flexural stiffness, Procedia Eng. 97 (2014) 1227–1236.
[5] D. Zhu, H. Shi, H. Fang, W. Liu, Y. Qi, Y. Bai, Fiber reinforced composites sandwich panels with web reinforced wood core for building floor applications, Compos. B. Eng. 150 (2018) 196–211.
[6] B. Castanie, C. Bouvet, M. Ginot, Review of composite sandwich structure in aeronautic applications, Compos. Part C. 1 (2020) 100004.
[7] J. Sargianis, H.I. Kim, J. Suhr, Natural cork agglomerate employed as an environmentally friendly solution for quiet sandwich composites, Sci. Rep. 2 (2012) 1–6.
[8] J. Banhart, H.W. Seeliger, Aluminium Foam Sandwich Panels: Metallurgy, Manufacture and Applications, Adv. Eng. Mater. 10 (2008) 3–6.
[9] R. Roy, S.J. Park, J.H. Kweon, J.H. Choi, Characterization of Nomex honeycomb core constituent material mechanical properties, Compos. Struct. 117 (2014) 255–266.
[10] X. Li, F. Lu, Y. Zhang, Y. Lin, Y. Meng, Experimental study on out-of-plane mechanical and energy absorption properties of combined hexagonal aluminum honeycombs under dynamic impact, Mater. Des. 194 (2020) 108900.
[11] Y.L. Tee, T. Maconachie, P. Pille, M. Leary, T. Do, P. Tran, From nature to additive manufacturing: Biomimicry of porcupine quill, Mater. Des. 210 (2021) 110041.
[12] Q. Liu, R. Xu, Y. Zhou, J. Ge, S. Yuan, Y. Long, T. Shi, Metamaterials mapped lightweight structures by principal stress lines and topology optimization: Methodology, additive manufacturing, ductile failure and tests, Mater. Des. 212 (2021) 110192.
[13] C.O. Ufodike, H. Wang, M.F. Ahmed, G. Dolzyk, S. Jung, Design and modeling of bamboo biomorphic structure for in-plane energy absorption improvement, Mater. Des. 205 (2021) 109736.
[14] D.J. McGregor, S. Tawfick, W.P. King, Mechanical properties of hexagonal lattice structures fabricated using continuous liquid interface production additive manufacturing, Addit. Manuf. 25 (2019) 10–18.
[15] C. Li, H. Lei, Z. Zhang, X. Zhang, H. Zhou, P. Wang, D. Fang, Architecture design of periodic truss-lattice cells for additive manufacturing, Addit. Manuf. 34 (2020) 101172.

[16] K.S. Prakash, T. Nancharaih, V.V.S. Rao, Additive Manufacturing Techniques in Manufacturing - An Overview, Mater. Today 5 (2018) 3873–3882.
[17] N. van de Werken, H. Tekinalp, P. Khanbolouki, S. Ozcan, A. Williams, M. Tehrani, Additively manufactured carbon fiber-reinforced composites: State of the art and perspective, Addit. Manuf. 31 (2020).
[18] D. Solari, I. Papallo, L. Ugga, L.M. Cavallo, I. Onofrio, R. Cuocolo, G. Improta, A. Brunetti, M. Martorelli, A. Gloria, P. Cappabianca, T. Russo, Novel concepts and strategies in skull base reconstruction after endoscopic endonasal surgery, Acta Imeko 9 (2020) 67–73.
[19] A. Forés-Garriga, M.A. Pérez, G. Gómez-Gras, G. Reyes-Pozo, Role of infill parameters on the mechanical performance and weight reduction of PEI Ultem processed by FFF, Mater. Des. 193 (2020) 108810.
[20] J.M. Chacón, M.A. Caminero, E. García-Plaza, P.J. Núez, Additive manufacturing of PLA structures using fused deposition modelling: effect of process parameters on mechanical properties and their optimal selection, Mater. Des. 124 (2017) 143–157.
[21] K. Wei, X. Xiao, J. Chen, Y. Wu, M. Li, Z. Wang, Additively manufactured bi-material metamaterial to program a wide range of thermal expansion, Mater. Des. 198 (2021) 109343.
[22] D. Downing, A. Jones, M. Brandt, M. Leary, Increased efficiency gyroid structures by tailored material distribution, Mater. Des. 197 (2021) 109096.
[23] C. Lubombo, M.A. Huneault, Effect of infill patterns on the mechanical performance of lightweight 3D-printed cellular PLA parts, Mater. Today Commun. 17 (2018) 214–228.
[24] Z.P. Sun, Y.B. Guo, V.P.W. Shim, Deformation and energy absorption characteristics of additively-manufactured polymeric lattice structures — Effects of cell topology and material anisotropy, Thin-Walled Struct. 169 (2021).
[25] S. Kumar, J. Ubaid, R. Abishera, A. Schiffer, V.S. Deshpande, Tunable Energy Absorption Characteristics of Architected Honeycombs Enabled via Additive Manufacturing, ACS Appl. Mater. Interfaces 11 (2019) 42549–42560.
[26] S.O. Obadimu, K.I. Kourousis, Compressive behaviour of additively manufactured lattice structures: A review, Aerospace 8 (2021).
[27] N. Kladovasilakis, K. Tsongas, D. Tzetzis, Mechanical and FEA-assisted characterization of fused filament fabricated triply periodic minimal surface structures, J. Compos. Sci. 5 (2021).
[28] Z. Alomar, F. Concli, Compressive behavior assessment of a newly developed circular cell-based lattice structure, Mater. Des. 205 (2021) 109716.
[29] K. Dong, H. Ke, M. Panahi-Sarmad, T. Yang, X. Huang, X. Xiao, Mechanical properties and shape memory effect of 4D printed cellular structure composite with a novel continuous fiber-reinforced printing path, Mater. Des. 198 (2021) 109303.
[30] Y. Xu, E. Schlangen, M. Luković, B. Šavija, Tunable mechanical behavior of auxetic cementitious cellular composites (CCCs): Experiments and simulations, Constr. Build. Mater. 266 (2021).
[31] Y. Jiang, B. Rudra, J. Shim, Y. Li, Limiting strain for auxeticity under large compressive Deformation: Chiral vs. re-entrant cellular solids, Int. J. Solids Struct. 162 (2019) 87–95.
[32] K.R. Olympio, F. Gandhi, Flexible skins for morphing aircraft using cellular honeycomb cores, J. Intell. Mater. Syst. Struct. 21 (2010) 1719–1735.
[33] D. Bornengo, F. Scarpa, C. Remillat, Evaluation of hexagonal chiral structure for morphing airfoil concept, Proc. Inst. Mech. Eng. G.J. Aerosp. Eng. 219 (2005) 185–192.
[34] J.J. Andrew, H. Alhashmi, A. Schiffer, S. Kumar, V.S. Deshpande, Energy absorption and self-sensing performance of 3D printed CF/PEEK cellular composites, Mater. Des. 208 (2021) 109863.
[35] S.R.G. Bates, I.R. Farrow, R.S. Trask, 3D printed polyurethane honeycombs for repeated tailored energy absorption, Mater. Des. 112 (2016) 172–183.
[36] S.R. Bates, I.R. Farrow, R.S. Trask, Compressive behaviour of 3D printed thermoplastic polyurethane honeycombs with graded densities, Mater. Des. 162 (2019) 130–142.
[37] V. Caccese, J.R. Ferguson, M.A. Edgecomb, Optimal design of honeycomb material used to mitigate head impact, Compos. Struct. 100 (2013) 404–412.
[38] Q. Ma, M.R. Rejab, A.P. Kumar, H. Fu, N.M. Kumar, J. Tang, Effect of infill pattern, density and material type of 3D printed cubic structure under quasi-static loading, Proc. Inst. Mech. Eng. C J. Mech. Eng. Sci. (2020).
[39] A. Alderson, K.L. Alderson, D. Attard, K.E. Evans, R. Gatt, J.N. Grima, W. Miller, N. Ravirala, C.W. Smith, K. Zied, Elastic constants of 3-, 4- and 6-connected chiral and anti-chiral honeycombs subject to uniaxial in-plane loading, Compos. Sci. Technol. 70 (2010) 1042–1048.
[40] F. Scarpa, S. Blain, T. Lew, D. Perrott, M. Ruzzene, J.R. Yates, Elastic buckling of hexagonal chiral cell honeycombs, Compos. Part A Appl. Sci. Manuf. 38 (2007) 280–289.
[41] L.L. Hu, M.Z. Zhou, H. Deng, Dynamic crushing response of auxetic honeycombs under large deformation: Theoretical analysis and numerical simulation, Thin-Walled Struct. 131 (2018) 373–384.
[42] S. Hou, T. Li, Z. Jia, L. Wang, Mechanical properties of sandwich composites with 3d-printed auxetic and non-auxetic lattice cores under low velocity impact, Mater. Des. 160 (2018) 1305–1321.
[43] M. Mir, M.N. Ali, J. Sami, U. Ansari, Review of mechanics and applications of auxetic structures, Adv. Mater. Sci. Eng. (2014).
[44] J.C. Álvarez Elipe, A. Díaz Lantada, Comparative study of auxetic geometries by means of computer-aided design and engineering, Smart. Mater. Struct. 21 (2012).
[45] Y. Prawoto, Seeing auxetic materials from the mechanics point of view: A structural review on the negative Poisson's ratio, Comput. Mater. Sci. 58 (2012) 140–153.
[46] Y. Liu, H. Hu, A review on auxetic structures and polymeric materials, Sci. Res. Essays 5 (2010) 1052–1063.
[47] J.N. Grima, R. Gatt, P.S. Farrugia, On the properties of auxetic meta-tetrachiral structures, Phys. Status Solidi B 245 (2008) 511–520.
[48] N. Gaspar, X.J. Ren, C.W. Smith, J.N. Grima, K.E. Evans, Novel honeycombs with auxetic behaviour, Acta Mater. 53 (2005) 2439–2445.
[49] J.P.M. Whitty, A. Alderson, P. Myler, B. Kandola, Towards the design of sandwich panel composites with enhanced mechanical and thermal properties by variation of the in-plane Poisson's ratios, Compos. Part A Appl. Sci. Manuf. 34 (2003) 525–534.
[50] F. Scarpa, P.J. Tomlin, On the transverse shear modulus of negative Poisson's ratio honeycomb structures, Fatigue Fract. Eng. Mater. Struct. 23 (2000) 717–720.
[51] N. Kladovasilakis, P. Charalampous, K. Tsongas, I. Kostavelis, D. Tzetzis, D. Tzovaras, Experimental and computational investigation of lattice sandwich structures constructed by additive manufacturing technologies, J. Manuf. Mater. Process. 5 (2021).
[52] A. Ajdari, B.H. Jahromi, J. Papadopoulos, H. Nayeb-Hashemi, A. Vaziri, Hierarchical honeycombs with tailorable properties, Int. J. Solids Struct. 49 (2012) 1413–1419.
[53] D. Mousanezhad, H. Ebrahimi, B. Haghpanah, R. Ghosh, A. Ajdari, A.M.S. Hamouda, A. Vaziri, Spiderweb honeycombs, Int. J. Solids Struct. 66 (2015) 218–227.
[54] D.M. Correa, T. Klatt, S. Cortes, M. Haberman, D. Kovar, C. Seepersad, Negative stiffness honeycombs for recoverable shock isolation, Rapid Prototyp. J. 21 (2015) 193–200.
[55] C. Lira, F. Scarpa, Y.H. Tai, J.R. Yates, Transverse shear modulus of SILICOMB cellular structures, Compos. Sci. Technol. 71 (2011) 1236–1241.
[56] N.A. Fleck, V.S. Deshpande, M.F. Ashby, Micro-architectured materials: Past, present and future, Proc. R. Soc. A 466 (2010) 2495–2516.
[57] A.J. Wang, D.L. McDowell, In-plane stiffness and yield strength of periodic metal honeycombs, J. Eng. Mater. Technol. 126 (2004) 137–156.
[58] Materialise, Ultem 9085 Datasheet, Technical Report, 2021.
[59] ASTM C365, Standard Test Method for Flatwise Compressive Properties of Sandwich Cores, ASTM International, West Conshohocken, PA (2003).
[60] P.-T.I. Inc, Ultem 1010 (Polyetherimide), Technical Report, 2011.
[61] M.M. Pastor-Artigues, F. Roure-Fernández, X. Ayneto-Gubert, J. Bonada-Bo, E. Pérez-Guindal, I. Buj-Corral, Elastic asymmetry of PLA material in FDM-printed parts: Considerations concerning experimental characterisation for use in numerical simulations, Materials 13 (2020) 1–24.
[62] C. Perkowski, Tensile-compressive asymmetry and anisotropy of fused deposition modeling PLA under monotonic conditions, Ph.D. thesis, 2017.
[63] Stratasys Inc, Ultem 9085 Production-Grade Thermoplastic for Fortus 3D Printers, Technical Report, 2017.

Publication III:

Additively manufactured three-dimensional lightweight cellular solids: Experimental and numerical analysis

10.1016/j.matdes.2023.111641

Materials & Design 226 (2023) 111641

Contents lists available at ScienceDirect

Materials & Design

journal homepage: www.elsevier.com/locate/matdes

Additively manufactured three-dimensional lightweight cellular solids: Experimental and numerical analysis

Albert Forés-Garriga, Giovanni Gómez-Gras, Marco A. Pérez *

IQS School of Engineering, Universitat Ramon Llull, Via Augusta 390, 08017 Barcelona, Spain

HIGHLIGHTS

- 3D cellular designs exhibit an improved and more isotropic mechanical performance than 2D patterns at similar levels of density.
- Although most of the 3D designs require support structures for their manufacturing, no increase in building time is noticed.
- The implementation of the sparse infill saves material, weight and printing time, while performance is slightly impacted.
- A novel and more consistent method for quantifying the isotropy of cellular solids fabricated with additive manufacturing technologies is provided.
- The homogenized numerical approach employing representative volume element properties saves important computation time with enough accuracy.

GRAPHICAL ABSTRACT

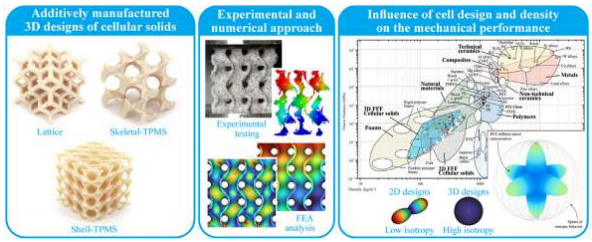

ARTICLE INFO

Article history:
Received 17 July 2022
Revised 16 January 2023
Accepted 17 January 2023
Available online 21 January 2023

Keywords:
Fused filament fabrication
Triply periodic minimal surfaces
Lattice
Material properties
Finite element analysis
Homogenization

ABSTRACT

The development of cellular solids is one of the research fields in which additive manufacturing has made relevant progress in producing lightweight components and enhancing their performance. This work presents comprehensive research on the mechanical performance of fused filament fabricated three-dimensional lightweight cellular solids, including open-cell and closed-cell lattice designs and triply periodic minimal surfaces (TPMS), with different cell sizes and infill densities. The aim of this work is to determine the range and limits of the achievable mechanical behavior by employing different cell designs made from a single material and manufacturing technique. Experimental results obtained with cell designs fabricated with a high-performance polymer (PEI Ultem) showed wide ranges of effective stiffnesses from 1 to 293 MPa, strengths from 0.1 to 18.1 MPa, and densities from 0.066 to 0.541 g/cm^3. Furthermore, two validated numerical approaches are provided to simulate their mechanical performance accurately. Moreover, a novel and robust index to quantify the isotropy of additively manufactured cellular solids based on the graphical representation of the homogenized stiffness tensor is proposed. Finally, experimental evidence states that the Shell-TPMS designs proved to be the most efficient cellular pattern, followed by the Skeletal-TPMS and the lattice configurations.

* Corresponding author.
E-mail address: marcoantonio.perez@iqs.url.edu (M.A. Pérez).

https://doi.org/10.1016/j.matdes.2023.111641
0264-1275/

1. Introduction

Additive manufacturing (AM) has attracted enormous attention from the scientific community and different industrial sectors in the last decade. It undoubtedly constitutes one of the strategic pillars of the global transformation towards Industry 4.0. Moreover, the rapid transition between research developments and industrial applications has been consolidated due to the ability to fabricate functional parts with complex geometries, which are unfeasible to obtain using conventional manufacturing techniques.

In particular, one of the research fields in which AM has made relevant progress is the development and manufacturing of cellular solids [1–4]. These bio-inspired structures are formed by a complex interconnected network of solid struts or shells that cover the space while considerably reducing the weight of the components [5–7]. Depending on the unit cells' typology and arrangement, cellular solids can be classified into two principal categories: closed-cell designs, such as foams, or open-cell ones, composed of reticular microstructures, such as lattices [8]. The properties of these cellular solids directly depend on the shape and connectivity of the unit cells and the solid material used for their manufacturing [9,10]. Thus, this advanced and optimized microarchitecture gives them properties of great interest and applicability, such as rigidity and specific resistance, thermal and acoustic insulation, or impact absorption capacity [11–21].

Some of these designs have already been incorporated into 3D printing equipment as an infill method for parts construction, with the aim to reduce manufacturing time and costs associated with material consumption [22]. However, an advanced design of cellular solids demands tight control of the kinematics of their deformation to achieve the desired microstructure properties to satisfy specific design requirements [23–31]. Therefore, a better understanding of the structure's behavior allows for finer control of mechanical properties [32,33]. Hence, architectural cellular materials are very versatile, as their performance can be tailored by simply modifying the geometrical or topological parameters of the design. Thus, according to the vast literature published in the last five years, it can be stated that there is an interest in the scientific community in deepening the knowledge, development, and fabrication of these bio-inspired microstructures for their application in advanced structural components.

Previous research has demonstrated that specific AM techniques are better suited for manufacturing certain typologies of cellular solids. In particular, the fabrication of lattice-type arrangements often requires intensive use of support structures. In this sense, employing powder bed technologies avoids the fabrication of supports, since the whole powder volume sustains the following constructed layer [34–41]. Therefore, powder bed fusion (PFB) is the most used technique for manufacturing truss-like cellular solids [42–48]. On the other hand, fused filament technologies deposit a thermoplastic material layer by layer according to the trajectories of a moving extruder head. Therefore, studies employing fused filament fabrication (FFF) generally deal with cell geometries composed of shell-like walls, as the vertical overlapping of the deposited rasters favors the construction of honeycomb-like designs [49–51]. Nevertheless, its implementation in manufacturing lightweight three-dimensional structures, such as lattice designs, requires removable auxiliary supports to hold inclined walls or struts during their construction.

In spite of this shortcomings, FFF stands as the most accessible, cost-effective, fastest, and user-friendly technique compared to the rest of the AM technologies. Moreover, its benefits for constructing two-dimensional cellular solids have been sufficiently consolidated [52,53]. However, the extrusion plane present in all of these designs significantly increases the degree of anisotropy of the structures, which exhibit a maximum in-plane stiffness while dramatically compromising the perpendicular one [54]. On the contrary, this phenomenon does not appear in three-dimensional designs, which leads to higher degrees of isotropy [55]. For this reason, many authors have recently focused on exploring the capabilities of this technology to manufacture three-dimensional structures using a much more economical and sustainable process [56–58].

One of the most promising developments in three-dimensional cellular solids for lightweight applications are the called triply periodic minimal surfaces (TPMS) [59,60]. These geometries are mathematically created to minimize the surface area for a given volume, having no self-intersecting or enveloping surfaces. Moreover, the lack of nodes and discontinuities in their curvature reduces stress concentration, thus improving their mechanical performance [61,62]. In addition, the average curvature at each point of the geometry is zero, hence making them self-supporting and able to be fabricated by FFF without requiring support structures [52,63–66].

Despite the high interest in cellular solids several uncertainties remain, especially for employing them in high-performance structural applications, such as composite material sandwich structures. Thus, and taking advantage of the most recent developments in AM technologies, these designs can become a turning point for obtaining novel lightweight cores with more isotropic and customized properties.

Accordingly, this work investigates the mechanical performance of FFF three-dimensional cellular solids to comprehend their benefits over two-dimensional designs in terms of stiffness and strength while attending manufacturing aspects such as printing time. The aim of this work is to explore the capabilities of cellular solids to achieve, from a single high-performance polymeric material, very different mechanical behaviours that allow broad applicability of this lightweight structures by customising only the cell design. In order to do so, the compressive behavior of twenty designs, including both open-cell and closed-cell patterns with different cell sizes and infill densities, is experimentally analyzed. In contrast to some previously published works, this study is conducted using professional FFF equipment, which incorporates a heating chamber to improve the cohesion between layers and increase the stiffness of the joints of the melted material. Furthermore, to inspect the structural capabilities of each design, a high-performance technical polymer with an outstanding strength-to-weight ratio is used. Additionally, the isotropy of the manufactured cell type is evaluated by employing a numerical homogenization strategy. Lastly, two validated numerical approaches are provided to efficiently simulate the compression and bending response of cellular designs, further contributing to novel design-for-manufacturing strategies of lightweight cores for sandwich structures.

2. Methodology

2.1. Manufacturing of the samples

A total of 20 different three-dimensional cellular solids were selected to analyse the impact that both the unit cell geometry and the relative density may have on the mechanical performance and manufacturing feasibility (see Fig. 1 and Table 1). For simplicity, from now on, pattern names and specimen identifications are referenced with the corresponding ID. Although FFF might be an unconventional choice for manufacturing certain geometries, this work comprises the study of all typologies of three-dimensional cellular solids, including lattice (*A* to *H*), Skeletal-TPMS (*I* to *O*), and Shell-TPMS (*P* to *T*).

Fig. 1. Unit-cells (Specimen ID_1) and eight-cells (Specimen ID_8) samples of the three-dimensional patterns manufactured with FFF (see Table 1).

Lattice geometries have been created using SolidWorks. On the other hand, the novel TPMSgen [67] open-source Python application was developed to parametrically generate the Skeletal-TPMS and Shell-TPMS designs employing the corresponding equations (see Appendix A). In each case, a cubic volume of 40 mm of side length was covered using two different unit cell sizes (I: $40 \times 40 \times 40$ mm; II: $20 \times 20 \times 20$ mm), thus resulting in structures made of a single cell (Specimen ID_1) and others of eight cells

Table 1
Pattern ID, manufacturing time, and relative density of the analyzed three-dimensional cellular solids.

Pattern (see Fig. 1)	Family ID	Typology	Specimen ID	Solid ± 45° Infill		Sparse 0.25 mm Infill		
				Manufacturing time (min)	Relative density (%)	Manufacturing time (min)	Relative density (%)	Rel. density reduction (%)
Reinforced body centered cube ‡	A	Lattice	A_1	311	27.11	305	24.23	2.88
			A_8	492	27.83	490	26.67	1.16
Dode medium ‡	B	Lattice	B_1	224	13.16	222	12.04	1.12
			B_8	416	13.44	416	13.33	0.11
Dode thick ‡	C	Lattice	C_1	221	25.51	212	21.41	4.10
			C_8	377	26.29	377	25.36	0.93
G-Structure 9 ‡	D	Lattice	D_1	178	23.35	171	19.55	3.80
			D_8	299	23.62	292	20.85	2.77
G-Structure 10 ‡	E	Lattice	E_1	180	30.33	182	26.87	3.47
			E_8	293	31.52	292	26.81	4.71
Octet truss ‡	F	Lattice	F_1	250	30.32	244	27.09	3.23
			F_8	435	30.16	432	28.03	2.13
Rhombic dodecahedron ‡	G	Lattice	G_1	237	30.65	227	25.87	4.79
			G_8	410	31.05	408	29.76	1.28
Truncated octa light ‡	H	Lattice	H_1	233	21.25	226	18.09	3.16
			H_8	373	20.94	373	20.86	0.08
Neovius surface ‡	I	Sk-TPMS	I_1	227	23.75	222	21.71	2.04
			I_8	339	23.63	336	22.23	1.40
Schoen gyroid ‡	J	Sk-TPMS	J_1	197	20.68	192	17.65	3.03
			J_8	289	23.69	280	18.77	4.92
Schwarz diamond ‡	K	Sk-TPMS	K_1	190	24.63	192	22.40	2.23
			K_8	300	24.57	296	23.51	1.06
Cylinder grid ‡	L	Sk-TPMS	L_1	174	26.77	168	21.79	4.98
			L_8	225	27.16	216	21.98	5.17
Schwarz primitive (pinched)‡	M	Sk-TPMS	M_1	185	29.81	179	23.84	5.97
			M_8	241	29.93	234	24.82	5.11
Schwarz primitive ‡	N	Sk-TPMS	N_1	173	18.38	170	14.57	3.80
			N_8	234	18.22	230	15.23	2.99
Body diagonals with nodes ‡	O	Sk-TPMS	O_1	193	46.13	182	37.79	8.34
			O_8	295	47.26	286	39.62	7.65
Gyroid †	P	Sh-TPMS	P_1	29	8.01	–	–	–
			P_8	49	15.99			
Diamond †	Q	Sh-TPMS	Q_1	34	9.75	–	–	–
			Q_8	61	19.45			
Lidinoid †	R	Sh-TPMS	R_1	56	16.29	–	–	–
			R_8	158	30.88			
Split-P †	S	Sh-TPMS	S_1	37	11.74	–	–	–
			S_8	101	21.66			
Schwarz †	T	Sh-TPMS	T_1	25	5.79	–		
			T_8	42	11.78			
Reference	REF	Solid ± 45°	So	66	100.00[a]	–		–

[a] Experimental measurement of Solid ± 45° pattern's density: 1.1457 g/cm^3. Sk-TPMS and Sh-TPMS stand for Skeletal and Shell triply periodic minimal surfaces, respectively.‡ Pattern manufactured with support structures.† Pattern manufactured without support structures.

(Specimen ID_8), respectively. It should be noted that, in some cell designs, the minimum wall thickness achievable by the additive manufacturing equipment limited the range of densities. Thus, the priority has been given to the printability of the samples, not the uniformity of the porosity of the designs.

Specimens were fabricated in a Stratasys Fortus 400mc FFF equipment employing PEI Ultem 9085 (PEI Ultem) material, a high-performance technical polymer with an outstanding strength-to-weight ratio [68]. This professional equipment has a thermal chamber controlled during the printing process. This fact significantly improves the inter-layer adherence between adjacent building layers, thus leading to a higher strength. The oven temperature was set at 195 °C and the model extrusion temperature at 380 °C. All the specimens were manufactured with a layer height of 0.254 mm.

Specimens *A* to *O* were evaluated with two different infill configurations: solid and sparse. Sparse patterns were generated by introducing a separation of 0.25 mm between intra-layer filaments using the raster-to-raster air gap parameter. On the other hand, the constant thickness of Shell-TPMS patterns (*P* to *T*) allows a higher accurate control over the density of the final structure. Thus, aiming to evaluate the potential of FFF technology to produce structures as light as possible, these patterns were printed with solid walls fabricated with a wall thickness of two contours (1.016 mm). Furthermore, a reference solid ± 45° configuration was included in this study. In all cases, two samples of each specimen were manufactured to validate the repeatability of the experimental tests, resulting in 142 manufactured patterns.

The geometric complexity of the studied three-dimensional patterns entailed multiple areas with overhangs, which required support material (polysulfone) for their construction (see Fig. 2). Hence, an optimized procedure employing a recently proposed solvent of 20% v/v aniline in toluene dissolution was used for removing support structures [69,70]. Fig. 1 depicts both unit and eight cells of every considered pattern once the support structures had been chemically removed.

Once all the samples were cleaned, the ratio between each specimen's mass and the Solid ± 45° cube configuration one was calculated (ρ^*/ρ^S) to obtain the relative density measurements. The average result of each pattern and infill configuration is given in Table 1. It should be noted that, since the unit cell in Specimens ID_8 *A* to *O* is equal to the corresponding Specimen ID_1 with a downscaling factor of 50%, the experimental measurement of the relative density leads to equivalent results in all cases. Meanwhile, as pat-

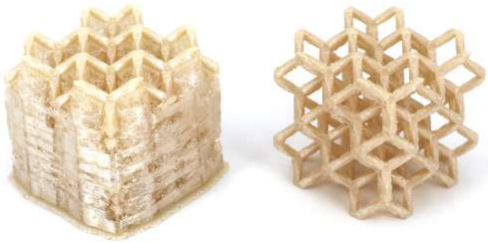

Fig. 2. Appearance of a three-dimensional FFF cellular solid (B_8) with the required support structures for its manufacturing (*left*) and after the cleaning treatment with the 20% v/v aniline in toluene solution (*right*).

terns *P* to *T* were all manufactured with two contours regardless of the unit cell size, the relative density of Specimen ID_8 is double the one corresponding to Specimen ID_1. However, different trends are observed when analyzing the estimated manufacturing time data since Specimens ID_8 required almost twice as much time to build as ID_1 in all cases.

The contribution of the sparse infill to weight reduction depends on the shape of the different building layers that constitute the manufactured part itself. In other words, if any portion of the cross-sectional area of the printed volume is too narrow for fitting both the contours and the infill region with separated rasters, the slicer software automatically sets it as solid. Therefore, weight reduction and printing time savings associated with the use of sparse infill are more evident in those designs where the unit cells are larger. As can be noticed from Table 1 data, sparse infill can suppose up to 8.34% of weight reduction (A_1), whereas just a 0.08% loss is noticeable in other cases (H_8), depending on the pattern's shape. Moreover, the scaling factor used in Specimen ID_8 narrows its cross-section compared to Specimen ID_1. Accordingly, the effectivity of the sparse infill might be limited when used in smaller FFF patterns.

2.2. Compression testing

Printed specimens were tested in compression along the perpendicular axis to the printing plane (see Fig. 3). Tests were conducted using ZwickRoell Z030 30 kN equipment following the ASTM C365 standard [71]. The crosshead rate was set to 3 mm/min. Results from the elastic modulus, the maximum stress prior to first failure (FF), and the corresponding absorbed energy were reported. The specimens' nominal external dimensions (40 × 40 × 40 mm) were employed for effective stress and strain calculations. The experimental elastic moduli were determined from test data between 0.1% and 0.3% of compressive strain using linear regression. Finally, the energy absorption efficiency was calculated as the ratio between the area under the load–displacement curve and the material's volume used for manufacturing each cell pattern.

Each specimen was previously sprayed with a black and white stochastic pattern to determine the full-field deformation of the samples with a 3D Digital Image Correlation (DIC) system. Two Allied Vision GigE MAKO G-507B cameras with APO-Xenoplan 1.4/23–0903 lenses were used to record the tests. A GOM CP20/MV55x44 panel was employed for the setup's calibration. The recorded sequences were post-processed with GOM Correlate Professional software to evaluate the deformation of the samples' surface until failure occurred.

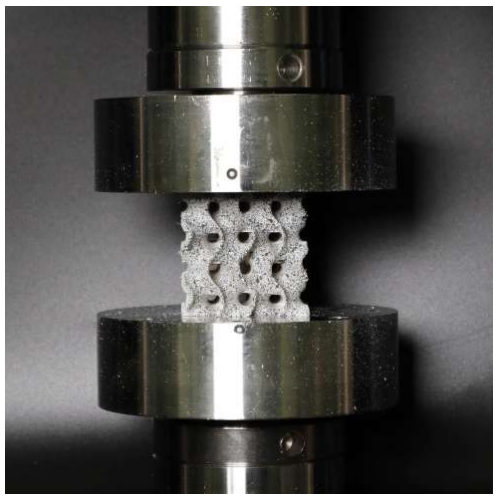

Fig. 3. Experimental setup for compression tests, corresponding to the Specimen P_8.

2.3. Numerical analysis

To assess the elastic performance of each cellular solid numerically, an Ansys FE implicit model was developed[1]. Two approaches were used for numerical analysis: the solid-element model (SE) and the homogenized representative volume element model (H-RVE). In both cases, two rigid bodies were first created on the top and bottom faces of the specimens to represent compression test plates. Displacements and rotations were restricted to fix the bottom plate, while a 0.1 mm displacement was imposed on the upper plate along the loading testing direction. A Normal Stiffness Factor (FKN) was included in the contacts' definition to reproduce the phenomenon of elastic asymmetry [72]. This factor was calibrated with the experimental data from Solid ± 45° infill samples, obtaining a FKN factor of 0.050. Next, frictional contacts with asymmetric behavior were defined between the cellular pattern and the plates, with a friction coefficient of 0.42. In addition, augmented Lagrange formulation with a penetration tolerance of 0.1 mm was activated, and ramped effects were permitted. The reaction force was finally calculated on the bottom surface to determine the stiffness of the cellular pattern. In every case, both displacement and load values were stored for every intermediate step of the simulation until the convergence of the model was reached. Finally, the numerical elastic moduli were again determined using linear regression and the nominal external dimensions of the sample.

For the SE approach, the CAD geometry of the cellular pattern was imported and discretized with a body mesh method, employing higher-order 20-node SOLID186 elements of 0.50 mm. The mechanical properties of the PEI Ultem 3D printed material were adopted from a previous comprehensive study [68], and are summarized in Table 2.

The second approach aimed to validate a more computationally efficient strategy for numerical analysis through a homogenized RVE model [73,74]. First, each three-dimensional pattern's unit cell was numerically homogenized using Ansys Material Designer with periodic boundary conditions, obtaining the performance compli-

[1] FE models were solved using the following hardware: AMD Ryzen Threadripper 2920X 12-Core Processor and RAM Memory 64 Gb DDR4 2133 MHz; License Solver: 4 Physical CPU Cores Used

Table 2
PEI Ultem 9085 Quasi-Isotropic elastic properties and stress limits used in the solid-element model (SE) [57].

Orthotropic Elasticity		
Young's Modulus *x*-direction (MPa)	E_x^s	2121
Young's Modulus *y*-direction (MPa)	E_y^s	2121
Young's Modulus *z*-direction (MPa)	E_z^s	2126
Poisson's Ratio *xy*	ν_{xy}^s	0.344
Poisson's Ratio *yz*	ν_{yz}^s	0.392
Poisson's Ratio *xz*	ν_{xz}^s	0.392
Shear Modulus *xy* (MPa)	Gs_{xy}	630
Shear Modulus *yz* (MPa)	G_{yz}^s	741
Shear Modulus *xz* (MPa)	G_{xz}^s	741
Orthotropic Stress Limits		
Tensile *x*-direction (MPa)	$\sigma_{T,x}^s$	24.45
Tensile *y*-direction (MPa)	$\sigma_{T,y}^s$	24.45
Tensile *z*-direction (MPa)	$\sigma_{T,z}^s$	24.45
Compressive *x*-direction (MPa)	$\sigma_{C,x}^s$	−24.45
Compressive *y*-direction (MPa)	$\sigma_{C,y}^s$	−24.45
Compressive *z*-direction (MPa)	$\sigma_{C,z}^s$	−24.45
Shear *xy* (MPa)	τ_{xy}^s	25.72
Shear *yz* (MPa)	τ_{yz}^s	25.93
Shear *xz* (MPa)	τ_{xz}^s	25.93

ance matrix of each cellular solid. Next, the cubic nominal volume was also modeled with a body mesh method, employing the previously mentioned element type and size. Finally, the homogenized performance tensors were introduced in the FE model, and the effective elastic properties were applied to the cubic RVE for the numerical analysis.

2.4. Degree of anisotropy

The degree of anisotropy quantifies the uniformity of the mechanical performance of a material in all the orientations. Three approaches have been adopted for comparative purposes to estimate the degree of anisotropy: the Zener index [75], the Universal anisotropy index [76], and the volume-based index proposed in this work.

The Zener anisotropy index *A*, which was initially introduced to measure the anisotropy of cubic crystals, can be directly computed from the coefficients of their stiffness tensor ($\boldsymbol{C}$) as:

$$A = \frac{2C_{44}}{C_{11} - C_{12}} \tag{1}$$

where:

$$\boldsymbol{C} = \begin{bmatrix} C_{11} & C_{12} & C_{13} & 0 & 0 & 0 \\ & C_{22} & C_{23} & 0 & 0 & 0 \\ & & C_{33} & 0 & 0 & 0 \\ & & & C_{44} & 0 & 0 \\ & Sym. & & & C_{55} & 0 \\ & & & & & C_{66} \end{bmatrix}$$

Physically, C_{44} represents the stiffness with respect to a shearing stress applied across the (1,0,0) plane in the [0,1,0] direction. Similarly, $(C_{11} - C_{12})/2$ represents the resistance to shear deformation by shear stress applied across the (1,1,0) plane in the [1,-1,0] direction (see Fig. 4). This calculation results in *A* values that range from 0 to ∞, depending on the coefficients of the stiffness tensor ($\boldsymbol{C}$), becoming $A = 1$ for a locally isotropic solid since the above shear resistances would be equal. Moreover, some authors prefer to quantify the anisotropy as A^{-1} instead of *A*. Thus, and despite the fact the Zener index has been recently applied in the field of

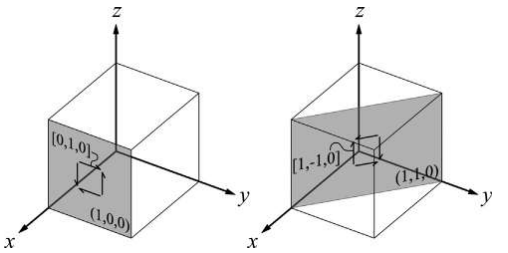

Fig. 4. Diagrams of the shear stresses corresponding to C_{44} (*left*) and $(C_{11} - C_{12})/2$ (*right*) that are evaluated for the calculation of the Zener anisotropy index (*A*).

FFF cellular solids [6,77], other authors previously concluded that *A* is restricted to cubic crystals and lacks universality [76], and the Universal anisotropy index A^U was proposed:

$$A^U = \frac{6}{5}\left(\sqrt{A} - \frac{1}{\sqrt{A}}\right)^2 \tag{2}$$

A^U is a single-valued measure whose null value stands for isotropic behavior. However, *A* and A^U assume that $C_{11} = C_{22} = C_{33}$, $C_{12} = C_{13} = C_{23}$, and $C_{44} = C_{55} = C_{66}$ in the stiffness tensor (*C*). Thus, although three-dimensional cellular solids usually display an apparent symmetry in the 3D space, these assumptions may be questioned regarding the inherent anisotropy of AM-fabricated patterns which has been widely reported, especially in extruded-like designs [78,79]. Therefore, a more general and robust method to quantify the anisotropy of additively manufactured cellular solids should contribute to the development of functional designs that can be implemented in fully end-parts.

Accordingly, a novel degree of anisotropy index A^V is proposed in this work based on the ratio between the volumes of the graphical representation of the whole stiffness tensor and the corresponding isotropy circumscribed sphere (see Fig. 5). This index can only handle values from 0 to 1, being $A^V = 1$ perfectly isotropic.

2.5. Flexural validation test

Finally, to validate and compare both numerical approaches, the performance of a two-dimensional pattern (Hexachiral), and a three-dimensional Shell-TPMS design (*Q*) were experimentally and numerically evaluated under a centered 3-point bending load case. Tests were conducted using ZwickRoell Z030 30 kN equipment, following the ASTM D790 standard [80]. The crosshead rate was set to 3 mm/min. The sample's nominal external dimensions (20 × 20 × 200 mm) were considered to calculate stress and strain data. In both cases, two repetitions were tested to validate the experimental results.

3. Results and discussion

3.1. Compressive performance

Fig. 6 depicts representative stress–strain curves obtained thought the experimental compression tests of the 3D printed specimens. The data presented corresponds to the unit (ID_1) and the eight-cell (ID_8) samples of lattice (*E*), Skeletal-TPMS (*I*), and Shell-TPMS (*Q*) patterns with both solid and sparse infill configurations.

As can be seen, depicted results are experimental evidence of the pattern design's influence on mechanical performance. Moreover, it should be noted that each cellular solid exhibits a similar

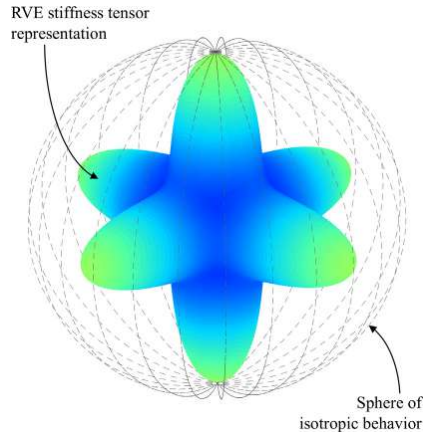

Fig. 5. Volumetric representation of the RVE stiffness tensor corresponding to the family M, and the isotropic circumscribed sphere. The ratio of these two volumes is the A^V anisotropy index.

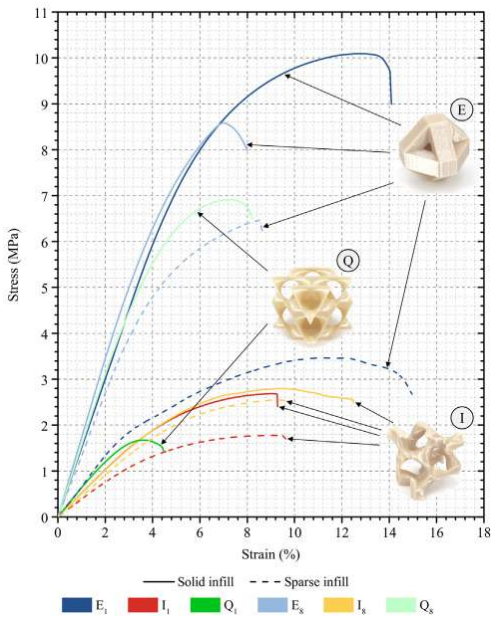

Fig. 6. Stress–strain representative curves obtained from the experimental compression tests performed on the cellular solids patterns.

stiffness regardless of the unit cell's dimensions when its geometry is perfectly scaled (see solid examples *E* and *I*). On the contrary, in those specimens where wall thickness was kept fixed at two contours (see example *Q*), the elastic modulus of Specimen ID_8 approximately doubles the corresponding unit-cell sample, as the first one is denser and exhibits a larger effective area. Furthermore, the stress–strain curves confirm that the bigger the unit cell is, the higher the yield and maximum stress the structure reaches. Hence, although scaling the cell size may not influence the stiffness property, the FFF toolpaths that constitute the resulting part must be considered. Thus, using tiny unit cells in this AM technology can lead to the appearance of multiple infill voids that might become stress concentrators as the 3D printing equipment resolution is still limited.

Major variations arise when comparing the performance of the solid and the sparse infill samples. In particular, when sparse infill is used in patterns formed by larger unit cells, the infill setting has a more significant impact on the structures' mechanical behavior, as expected. This point is related to the fact that having too narrow areas in the cross-section disables sparse infill in favor of solid infill in the affected areas. Accordingly, as pointed out when the relative density data was presented (see Section 2.1), many of the Specimen ID_8 samples are practically solid despite using the sparse infill setting in the slicer software. This fact is noticeable on stress–strain curves from samples *E* and *I*. As shown, sparse infill in Specimens ID_1, which have thicker unit cells than Specimens ID_8, leads to a more significant decrease in the elastic modulus, the maximum strength, and the total absorbed energy before the first failure (FF) occurs.

Fig. 7 depicts the results of the experimental compression performance of the three-dimensional cellular solids in terms of the relative density (*left*) and the time required for the fabrication (*right*). Experimental data of PEI Ultem two-dimensional patterns from a previous research [54], which were fabricated and tested employing the same methodology described in the present study, is overlapped for comparison.

The mechanical performance of families *E*, *M*, and *Q* is highlighted in each plot as representative patterns of lattice, Skeletal-TPMS, and Shell-TPMS typologies, respectively. Depicted results allow several conclusions to be drawn. On the one hand, cell geometry design leads to different dimensions and orientations of the resistant sections. This fact explains the differences in the results on the vertical axis within specimens of similar relative density in the charts in the left column. On the other hand, the elastic modulus, the compression strength at failure, and the energy absorption efficiency are significantly superior to that obtained by two-dimensional patterns in the in-plane cell's orientation for an equivalent relative density. This difference is mainly attributed to the material's distribution in their cross-section and the presence of manufacturing defects. That is, as the two-dimensional designs have mainly closed cells and were printed with the thinnest wall-thickness possible of one single contour, the filament paths create numerous discontinuities (intra-layer defects), resulting in manufacturing imperfections that compromise the load-bearing capacity and energy absorption efficiency. In contrast, the three-dimensional patterns show a wide range of wall thicknesses depending on the chosen cell design, which are manufactured with multiple filament contours. Hence, the material's deposition is concentrated in stronger sections while keeping the same relative density and employing continuous filament paths, which favors the reduction of defects between joints and significantly improves the load capacity and energy absorption efficiency. For these reasons, deposition imperfections become more critical for the mechanical performance of 2D patterns than in 3D designs since an inaccurate union of the cells (intra-layer defects) of the former results in an earlier breakage. Therefore, as the absorbed energy efficiency results have been reported up to the first failure of the specimens, thin-walled two-dimensional morphologies are less efficient in absorbing energy than three-dimensional alternatives, despite exhibiting equivalent relative densities. However, none of the three-dimensional specimens displayed a stiffness higher than the one achieved with two-dimensional patterns' in the out-of-plane arrangement (perpendicular to the printing plane). This fact is explained because 3D patterns mainly work under bending

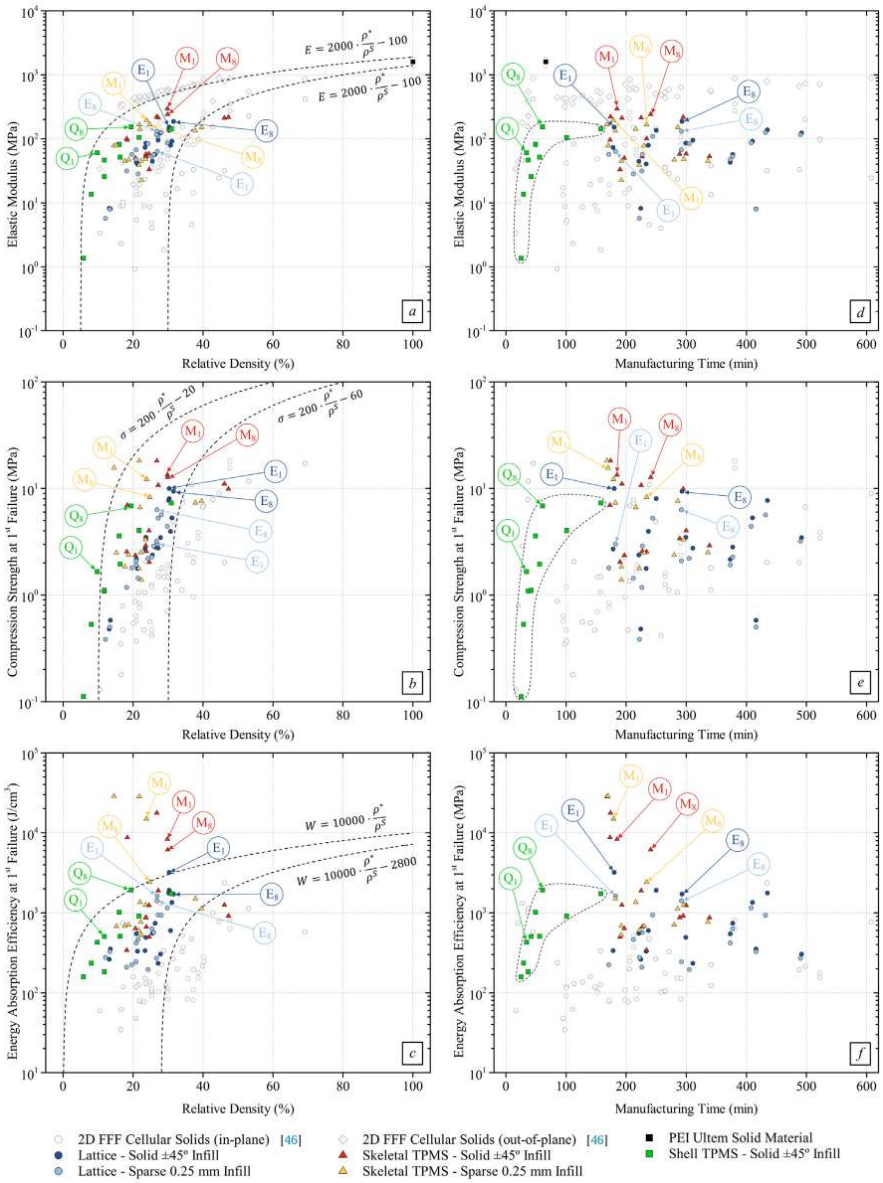

Fig. 7. Experimental results of the elastic modulus (*a, d*), compression strength (*b, e*) and energy absorption efficiency (*c, f*) in terms of relative density and manufacturing time for each cellular solids pattern.

stress, thus showing a more flexible performance, while compression stresses in 2D patterns produce the buckling of the cell walls.

Despite dispersion, scatter plots *a*, *b*, and *c* in Fig. 7 show a trend between mechanical performance and the relative density of the samples, as expected. Focusing on maximizing the mechanical properties (*y*-axis) and minimizing the weight of the structures (*x*-axis), an in-depth analysis of these charts provides relevant information to determine which cell typologies stand out. Accordingly, experimental evidence states that the Shell-TPMS designs proved to be the most efficient ones, followed by the Skeletal-TPMS and, finally, the lattice configurations. Furthermore, paying attention to the fabrication process, the scatter plots

d, *e*, and *f* show that the Shell-TPMS designs require less than half the fabrication time as the other cell patterns. This fact is explained by the need to use support structures to fabricate the other patterns, which involve a time-consuming material deposition sequence.

Accordingly, the Shell-TPMS designs allow the fabrication without support structures, which means that the FFF equipment does not need to perform the material change sequence, and a considerable amount of time is saved by avoiding purging steps. However, despite requiring purging steps, Skeletal-TPMS and lattice designs still can compete in manufacturing time against two-dimensional patterns. Fig. 7 highlights that three-dimensional designs offer better mechanical performance than two-dimensional patterns employing the same amount of time for construction.

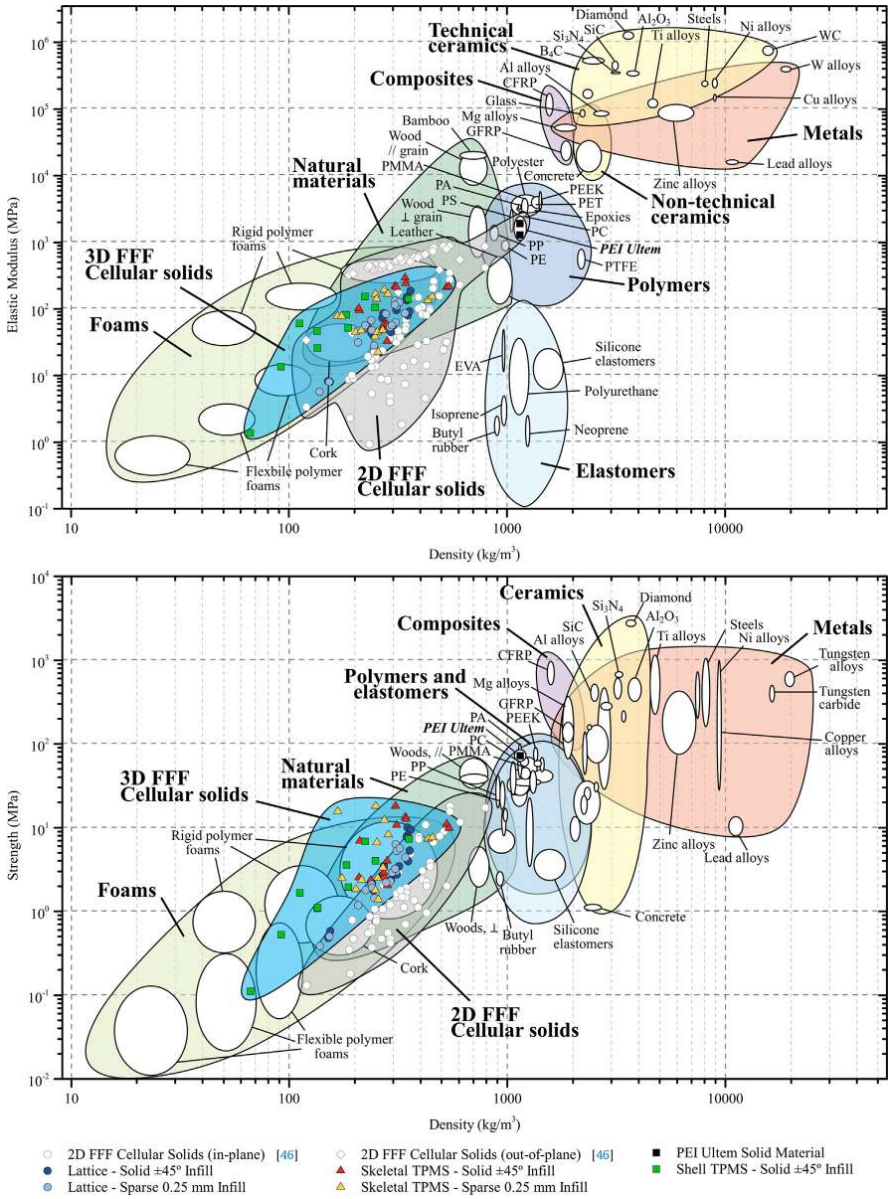

Fig. 8. Comparison of the experimental performance of the 2D [57] and 3D FFF cellular solids with materials database adapted from CES EduPack 2019, ANSYS Granta © 2020 Granta Design, with permission.

3.2. Comparative performance

Experimental results have been represented in Fig. 8 to compare the structural performance of the FFF cellular solids patterns in terms of stiffness, compression strength, and density. In addition, results from available PEI Ultem two-dimensional cellular solids are included in a gray shaded area, as well as the mechanical properties of other materials from the Ansys GRANTA EduPack database, for comparison. As shown, the performance of cellular solids is contained in the range of foams and natural materials. However, the three-dimensional designs cover a different region from the two-dimensional ones.

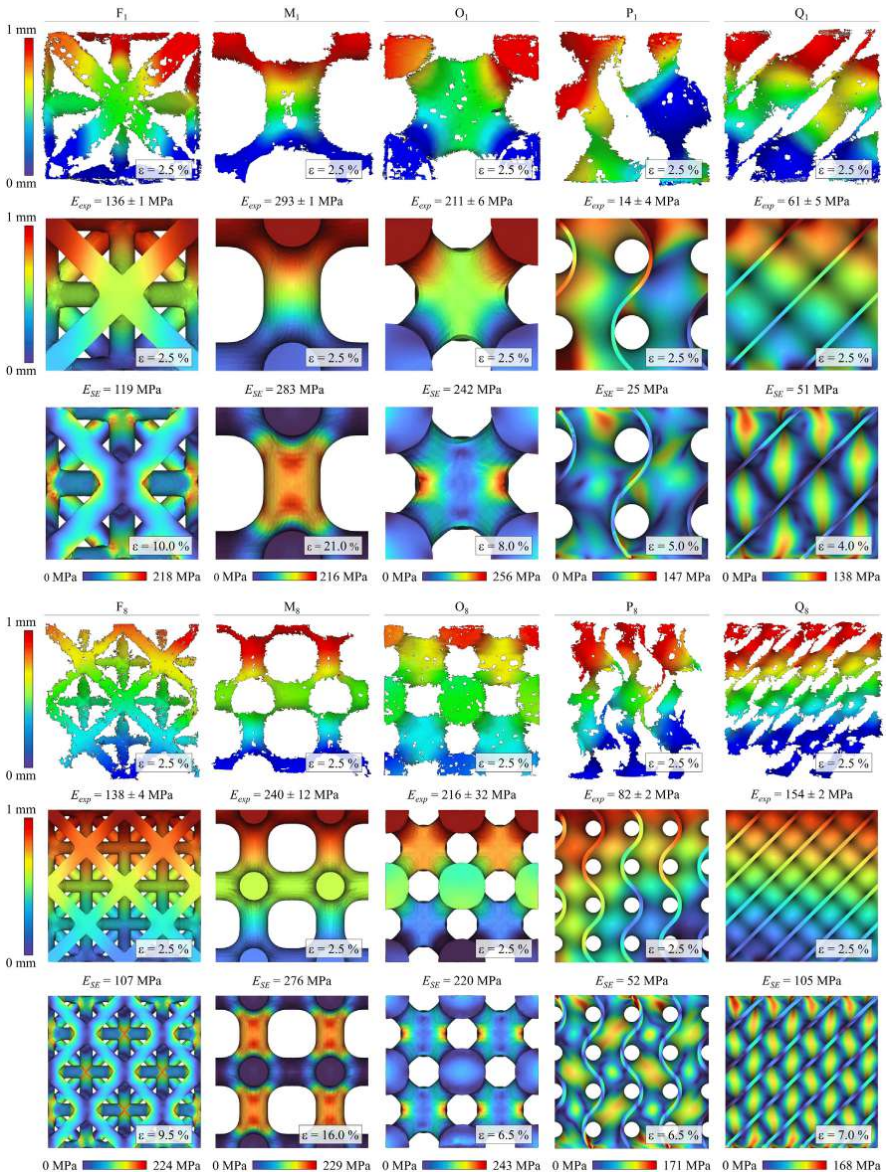

Fig. 9. Comparison results of the numerical solid-element model and experimental data of ten representative cellular solids tested under compression load. The first and fourth rows correspond to the experimental displacement field obtained via digital image correlation. The second and fifth rows are the analogous numerical displacement fields, while the third and sixth rows display the numerical Von Mises stress before the specimen's failure.

Both charts in Fig. 8 contain black square dots representing the reference PEI Ultem material properties processed in FFF (Solid ± 45° with 100% infill density). Focusing on the *top* chart, cellular patterns display lower elastic modulus than the solid reference, attending to the fact that less material is used. On the other hand, regarding the wide spectrum of the achieved results, the cell's design plays an important role on the mechanical properties and density of the pattern, as was intended to demonstrate. As previously noticed in Fig. 7, when samples of similar densities are compared, three-dimensional patterns exhibit intermediate stiffnesses between two-dimensional designs' in-plane and out-of-plane behaviors. In particular, while their elastic moduli are not too far from the results achieved with the optimum out-of-plane orientation of two-dimensional designs, the in-plane performance is improved by up to two orders of magnitude. Therefore, three-dimensional designs tend to reduce the orthotropy of the cellular solid, as will be further discussed in Section 3.4.

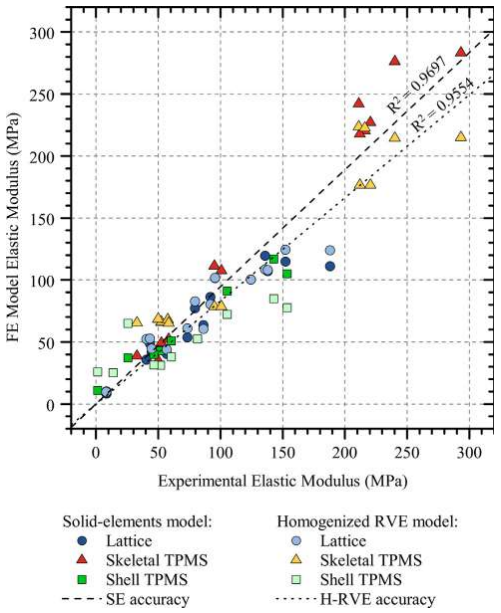

Fig. 10. Comparison of the accuracy of the solid-element and homogenized RVE numerical models in constrast to experimental data.

The *bottom* chart in Fig. 8 allows the comparison of the different materials in terms of compression strength and density. It should be noted that out-of-plane compression strength results from two-dimensional cellular solids are not reported in the literature, hence not included. Overall, when similar densities are examined, depicted results state that the compression strength of the three-dimensional designs is significantly higher than the in-plane strength of the two-dimensional cell designs. This experimental evidence is explained by the fact that 3D geometries behave stretch-dominated while 2D behave bending-dominated. Moreover, inherent manufacturing imperfections extensively reported in [54] create discontinuities in the cell-wall connections, which proved to have dramatic effects on the performance of two-dimensional cellular solids. In contrast, three-dimensional cell patterns proved to be less prone to manufacturing defects.

3.3. Numerical analysis

Firstly, the numerical results obtained with the SE approach are discussed. This model offers a shorter setup and accounts for geometric details from the cellular solids while considering edge

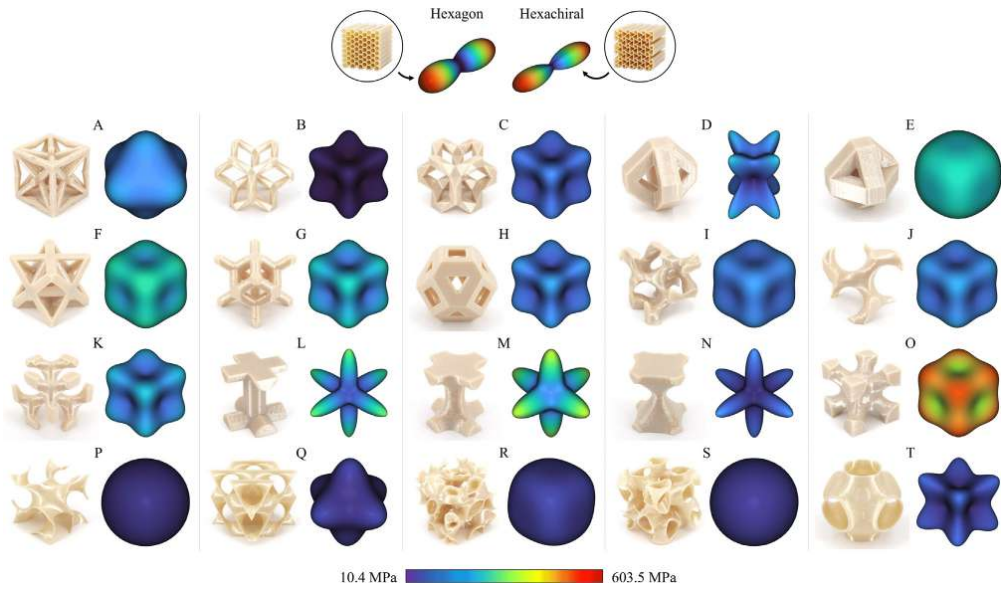

Fig. 11. Homogenized stiffness tensor representations for each of the studied patterns (see 6). Two-dimensional cellular designs (Hexagonal and Hexachiral) are included for comparison.

effects. Nevertheless, it presents a major drawback of being very computationally expensive. Fig. 9 compares the numerical and experimental data of ten representative cellular solids tested under compression load. The first and fourth rows correspond to the experimental displacement field obtained via digital image correlation (DIC) for a 1 mm (2.5% of strain) compression displacement along the perpendicular axis to the printing plane. Deficiencies observed in the displacement field are due to limitations in recognizing the stochastic pattern sprayed on the surface of the samples, particularly on regions not visible to one of the cameras (see specimens *P* and *Q*). The second and fifth rows are the analogous numerical displacement fields, while the third and sixth rows display the numerical Von Mises stress before the specimen's failure. In addition, the experimental and numerical stiffness moduli are indicated below each image, corresponding to the results obtained from compression tests and employing the SE model, respectively. In general, the numerical results agree with experimental values as well as with reference material data [81], thus validating the numerical model.

Von Mises stresses show different trends between cellular patterns, particularly on Shell-TPMS designs (see specimens *P* and *Q*). Overall, the identified areas of stress concentration match the experimental failure regions of the cellular solids. Note that walls in Shell-TPMS designs are not self-intersecting surfaces, hence avoiding joints and discontinuities in filament deposition. This fact favors the stress distribution and improves the mechanical performance of the cellular structure, thus confirming the experimental evidence.

Secondly, a much more computationally efficient alternative to simulate cellular structures is implementing the H-RVE model. Specifically, the effective and homogenized elastic properties of a RVE are used to define the behavior of the cellular structure which, in this case, is simplified into a completely solid model that covers the cubic envelope of the sample. Thus, it is a remarkably robust method to simulate cellular solids regardless of their geometrical complexity, density, and cell dimensions, reducing the meshing process complexity considerably.

However, implementing the H-RVE approach for simulating periodic structures has certain drawbacks that must also be considered. On the one hand, it is only suitable for uniform repetitive geometries, as the effective RVE properties are supposed to be constant throughout the volume. On the other hand, this approach requires computing more steps since a homogenization of the unit cell has to be performed before addressing the whole design. Moreover, this numerical analysis tends to be less accurate than the SE method because neither edge effects nor stress concentrations are considered due to the simplification of the model.

The accuracy of both numerical methods is presented in Fig. 10, where the values of the estimated elastic moduli of each cellular solid are compared with the experimentally determined ones. A regression line is fitted to each numerical approach, and the coefficient R^2 is given to quantify the degree of correlation. As can be

Table 3
Results of three indices to quantify the degree of anisotropy of each cell pattern.

Specimen ID	A^V	A[6,75,77]	A^U[79]	Relative density (%)	Elastic modulus (MPa)	Compression strength at FF (MPa)	Energy absoroption efficiency at FF (J/cm^3)
S_8	0.997	0.999	0.000	21.7	105 ± 0	4 ± 0.0	908 ± 8
S_1	0.966	1.030	0.001	11.7	47 ± 3	1.1 ± 0.0	184 ± 5
P_1	0.950	1.051	0.003	8.0	14 ± 4	0.5 ± 0.1	235 ± 15
P_8	0.911	1.087	0.008	16.0	82 ± 2	3.6 ± 0.1	1019 ± 60
R_8	0.876	1.141	0.021	30.9	143 ± 1	7.3 ± 0.1	1733 ± 28
E_8	0.829	1.204	0.041	31.5	188 ± 21	9.4 ± 1.2	1722 ± 598
E_1	0.827	1.207	0.042	30.3	152 ± 3	10 ± 0.1	3209 ± 55
R_1	0.820	1.220	0.047	16.3	52 ± 2	2 ± 0.1	511 ± 3
F_1	0.632	1.641	0.301	30.3	136 ± 1	8 ± 0.1	1924 ± 77
F_8	0.631	1.633	0.294	30.2	138 ± 4	7.7 ± 0.2	1775 ± 67
A_1	0.611	0.709	0.144	27.1	96 ± 12	2.8 ± 0.1	234 ± 34
A_8	0.610	0.709	0.143	27.8	124 ± 2	3.5 ± 0.2	305 ± 34
I_1	0.606	1.653	0.310	23.7	52 ± 1	2.6 ± 0.2	664 ± 103
I_8	0.605	1.639	0.299	23.6	53 ± 1	2.9 ± 0.2	863 ± 28
O_1	0.590	1.843	0.463	46.1	211 ± 6	11 ± 0.6	1252 ± 182
O_8	0.589	1.852	0.470	47.3	216 ± 32	9.9 ± 1.6	914 ± 163
J_1	0.585	1.812	0.437	20.7	50 ± 2	2.4 ± 0.1	635 ± 143
J_8	0.582	1.791	0.419	23.7	58 ± 0	3.4 ± 0.3	873 ± 95
Q_8	0.570	0.682	0.178	19.4	154 ± 2	6.9 ± 0.1	1927 ± 12
G_1	0.548	2.070	0.664	30.7	80 ± 4	4 ± 0.3	601 ± 134
G_8	0.547	2.101	0.693	31.0	92 ± 2	5.3 ± 0.2	1350 ± 26
H_8	0.524	2.419	0.998	25.5	43 ± 1	2.2 ± 0.0	545 ± 103
H_1	0.523	2.411	0.991	20.9	40 ± 1	1.8 ± 0.0	331 ± 5
C_1	0.523	2.294	0.876	21.3	45 ± 0	2.4 ± 0.1	554 ± 18
C_8	0.521	2.347	0.927	26.3	57 ± 0	2.8 ± 0.0	741 ± 31
K_8	0.520	2.313	0.894	24.6	58 ± 0	4 ± 0.0	1243 ± 34
K_1	0.519	2.327	0.908	24.6	33 ± 3	2 ± 0.4	496 ± 164
Q_1	0.508	0.590	0.342	9.8	61 ± 5	1.7 ± 0.0	429 ± 2
T_8	0.503	2.611	1.193	11.8	26 ± 0	1.1 ± 0.0	507 ± 28
B_1	0.494	2.656	1.239	13.2	8 ± 0	0.5 ± 0.0	263 ± 5
B_8	0.491	2.597	1.179	13.4	8 ± 0	0.6 ± 0.0	352 ± 5
T_1	0.473	3.271	1.892	5.8	1 ± 0	0.1 ± 0.0	158 ± 46
M_1	0.392	0.290	2.091	29.8	293 ± 1	13.3 ± 1.5	8302 ± 1451
M_8	0.391	0.289	2.103	29.9	240 ± 12	12.7 ± 0.4	6125 ± 257
D_8	0.385	0.126	7.285	18.2	86 ± 1	3.5 ± 0.2	493 ± 94
D_1	0.365	0.124	7.415	18.4	73 ± 4	2.7 ± 0.1	337 ± 13
N_1	0.365	0.184	4.351	26.8	95 ± 3	6.9 ± 0.3	8710 ± 1477
N_8	0.364	0.184	4.351	27.2	101 ± 3	2.5 ± 0.0	339 ± 17
L_1	0.360	0.181	4.443	23.4	221 ± 19	18.1 ± 0.0	17764 ± 690
L_8	0.360	0.182	4.413	23.6	212 ± 3	10.7 ± 0.1	1887 ± 51

seen, both models tend to underpredict the cellular stiffness, but the best fit corresponds to the SE model, even though the H-RVE model leads to huge computational time savings.

3.4. Degree of anisotropy

The geometric complexity of cell pattern designs, which strongly influences mechanical performance, is linked to the degree of anisotropy. To better illustrate the concept of degree of anisotropy, Fig. 11 depicts the stiffness tensor representations for each of the studied patterns. This graphical depiction allows visualization of the effective elastic modulus in each direction of the space. Thus, the more spherical this graphic is, the more isotropic the cellular pattern performs. These plots are obtained by rotating the homogenized stiffness tensor about the three global coordinate axes, as detailed in Appendix B. The tensor representations of two two-dimensional cellular designs (Hexagonal and Hexachiral) have also been included for comparison.

A first qualitative analysis of these results confirms the influence of the patterns' geometry on the degree of anisotropy. Firstly, there is a noticeable difference between the results of two and three-dimensional cellular solids. The extruded-like geometry of the firsts gives them a high out-of-plane stiffness, while the rigidity in the other planes is compromised. The three-dimensional designs provide balanced stiffness in orthogonal directions, making the graphical representation of the tensor less direction-dependent. Secondly, the arrangement and orientation of the cells, together with the density of the pattern, directly affect the dimensions and orientations of the resistant sections, thus conditioning the performance, as previously verified by experimental tests.

Three approaches were used for comparative purposes to quantify the degree of anisotropy: the Zener index A, the Universal anisotropy index A^U, and a novel proposed volume-based index A^V. Results of three indices are collected in Table 3. According to the A^V index, specimen IDs are sorted from the highest to the lowest degree of isotropy achieved. In addition, results of the mechanical behavior characterization have also been included. As observed, the cell patterns *S*, *P*, *R*, and *E* present the highest isotropic behavior, agreeing with the results depicted in Fig. 11. As can be seen, the reported values highlight the instability of the other indices, A^U and particularly A, to sort the different designs according to their anisotropy degree accurately. In detail, the three indices coincide in the first few patterns, but from the ninth row onwards, the degree of anisotropy obtained by the different indicators diverges significantly. It is explained by the fact that the A^V index is determined employing the whole stiffness tensor, considering the inherent anisotropy of the AM patterns, in contrast to the A^U and A indices.

Fig. 12 depicts the experimental results of the stiffness and specific strength against the degree of anisotropy index A^V. Note that axes are presented in logarithmic scale, and comparison lines are included based on the design criteria E/A^V, $E^{-1/2}/A^V$, and $E^{-1/3}/A^V$. As can be noticed, the three inspected typologies of solid cellular families occupy distinguishable regions in both graphs. The main differences are observed between skeletal and Shell-TPMS patterns. Overall, the former exhibits a superior mechanical performance, while the latter shows higher isotropy. Meanwhile, lattice designs are mainly located in the central area of both plots. In addition, the results also allow determining the effect of cell size. As shown, some geometries have the same anisotropy index, regardless of cell size. However, it does not happen in those specimens where wall thickness was kept fixed at two contours (patterns *P* to *T*), where the relative density of Specimen ID_8 is double the one corresponding to ID_1, and the elastic modulus of Specimen ID_8 has approximately doubled the corresponding unit cell sample

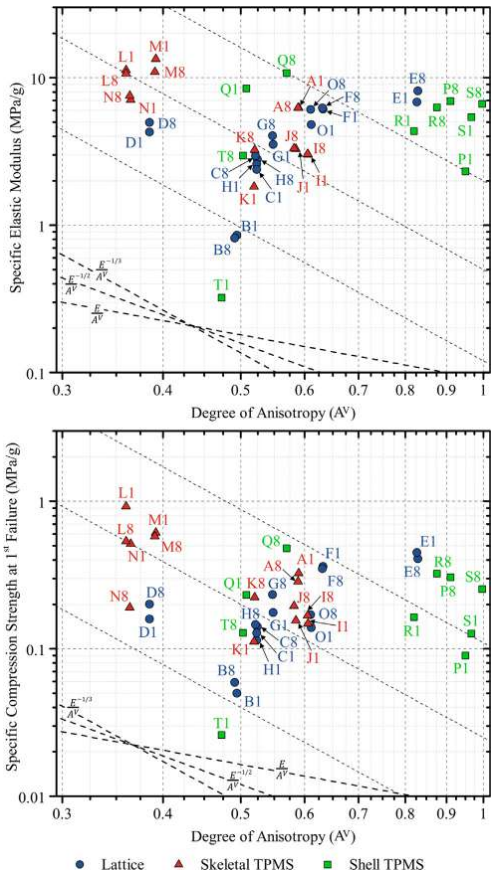

Fig. 12. Experimental results of the specific elastic modulus and compression strength against the degree of anisotropy index A^V of each cellular pattern (see Fig. 1 and Table 1).

(see example *Q*) due to the fact that the first one is denser, hence exhibiting a larger effective area. Finally, this comparison highlights the mechanical behavior of the Shell-TMPS type patterns, which is added to the advantages in manufacturing time presented above.

3.5. Validation test

Finally, to validate and compare both numerical approaches, the behaviors of a two-dimensional pattern (Hexachiral) and a three-dimensional Shell-TPMS design (Q) were experimentally and numerically evaluated under a centered 3-point bending load case.

The numerical and experimental results of both solid cellular patterns are represented in Fig. 13. The left-hand column corresponds to the two-dimensional Hexachiral pattern and the right-hand column to the three-dimensional Shell-TPMS pattern. The depicted results of each pattern were evaluated when failure occurred. The provided numerical plots show the total displacement and the Von Mises stress obtained results for both patterns employing the SE and the H-RVE approaches, respectively. In addi-

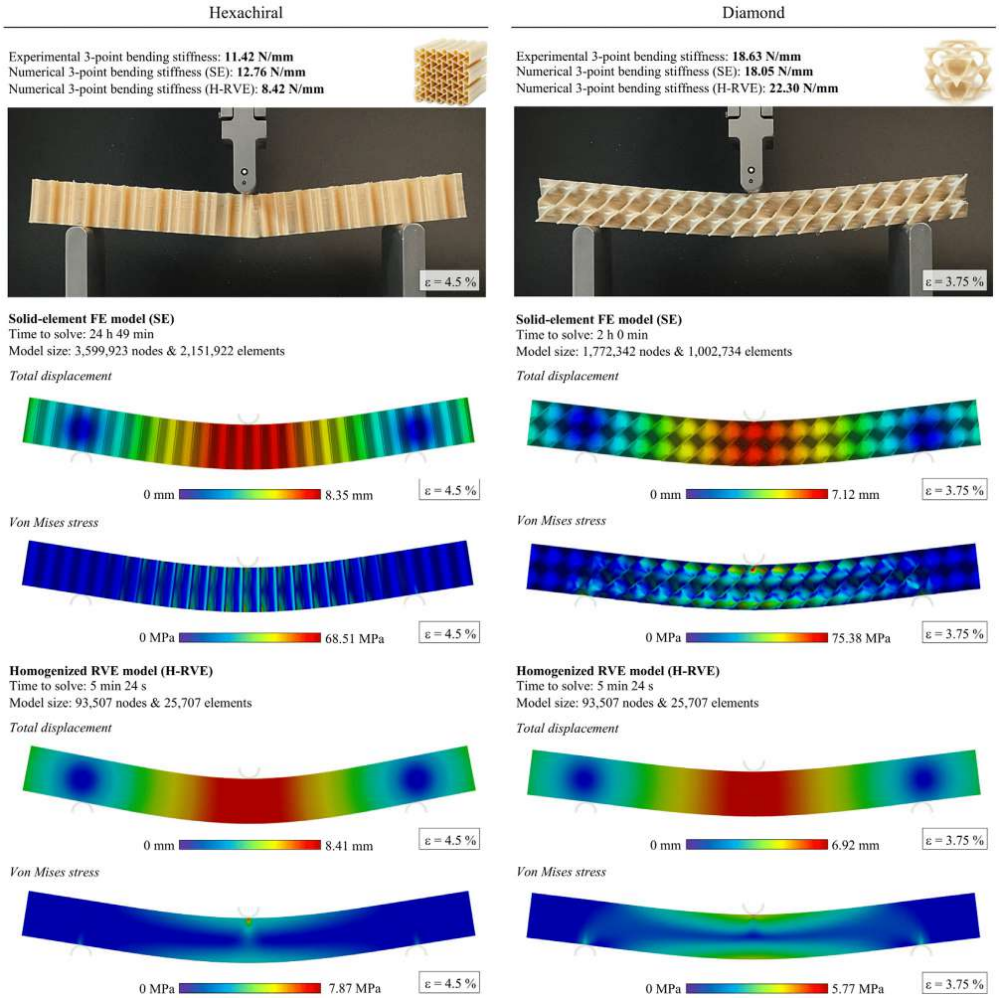

Fig. 13. Validation results of solid-element and homogenized RVE numerical models for Hexachical (*left*) and Diamond (*right*) cellular patterns.

tion, the experimental stiffness of each pattern is included together with the values calculated using both FE methods. Lastly, other model details including the computational time and size are provided.

The numerical stiffness values agree with the experimental result for both types of cellular solids. The higher divergence is observed in the H-RVE approach, which is attributed to the simplification of the homogenized model. Regarding this model, the displacement results from the Hexachiral pattern analysis are satisfactory. However, the bending-torsion coupling effect observed in the Diamond pattern is not identified. Note the slightly different stress field on the surrounding area of supports. Similarly, as displayed on the Von Mises stress plots, the stress concentrators are not captured in the homogenized model. Therefore, only effective stress values can be determined if this approach is implemented. Note the difference between the maximum Von Mises stresses results obtained with the H-RVE and SE methods. Nevertheless, despite these points, the accuracy of the numerical results confirms the capability of both approaches to reproduce the elastic behavior of cellular solids with adequate confidence.

4. Conclusions

This work presents comprehensive research on the mechanical performance of additively manufactured three-dimensional lightweight cellular solids, including open-cell and closed-cell patterns with different cell sizes and infill densities. The paper provides experimental evidence on the differences over two-dimensional designs in terms of stiffness and strength while attending to manufacturing aspects such as printing time, proving that the elastic modulus, the compression strength, and the energy absorption efficiency are significantly superior to that obtained by two-dimensional patterns in the in-plane cell's orientation for an equiv-

alent relative density. The control of the examined engineering parameters allows producing lightweight structures with an extensive spectrum of specific stiffness and strength, starting from the intrinsic properties of a single material. Experimental evidence states that the Shell-TPMS designs proved to be the most efficient cellular pattern, followed by the Skeletal-TPMS and, finally, the lattice configurations. Regarding the fabrication process, results showed that the Shell-TPMS designs require less than half the fabrication time of the other cell patterns.

Two validated strategies for simulating the elastic behavior of cellular solids have also been presented, comparing their accuracy and computational requirements. In short, the homogenized representative volume element approach (H-RVE) has computational advantages (90% less time) but does not allow the simulation of local effects on the cell walls. In contrast, the solid-element approach (SE) can simulate the elastic behavior satisfactorily, including local effects, but at a higher computational cost. In particular, this approach successfully identified the stress concentration regions of the lattice and Skeletal-TPMS patterns where experimental failure occured. In addition, the obtained results proved that the morphology of Shell-TPMS designs favors a more homogeneous stress distribution, which improves the mechanical performance of the cellular structure.

Moreover, the novel method for quantifying the isotropy of the additively manufactured cellular solids presented, based on the graphical representation of the homogenized stiffness tensor, allows comparing the degree of anisotropy of the complex structures in a more robust way, regarding important aspects such as the inherent anisotropy of additively manufactured components.

Lastly, the obtained results highlight how pattern design impacts the cellular solids' density and mechanical behavior. Thus, an accurate adjustment of the unit cell shape can lead to structures with equivalent densities but with very contrasting performances. This fact is illustrated by the significant differences that emerge between the performance that can be achieved with two-dimensional and three-dimensional cellular solids. In particular, the geometric homogeneity in the 3D space of many considered patterns results in a higher degree of isotropy in contrast to the one that is exhibited by the extruded-like designs. Overall, the gathered experimental and numerical data states the advances in mechanical performance and isotropy that implementing three-dimensional designs brings, compared to the more classical two-dimensional patterns.

Data availability

The raw data required to reproduce these findings are available to download from Mendeley Data, https://doi.org/10.17632/zhygf2vdsr.1, including the original STL files that were used to fabricate the samples for this research, mechanical testing raw data, and HD images. Kindly cite this article and the dataset if utilizing or modifying the data in your work.

Declaration of Competing Interest

The authors declare that they have no known competing financial interests or personal relationships that could have appeared to influence the work reported in this paper.

Acknowledgments

This work has been supported by the Ministry of Science, Innovation and Universities through the projects New Developments in Lightweight Composite Sandwich Panels with 3D Printed Cores (3DPC) - RTI2018-099754-A-I00 and Development of Gyroid-Type Cellular Metallic Microstructures by FFF to Optimize Structural Components with High Added-Value (GRIM) - PID2021-123876OB-I00. The authors would like to acknowledge their gratitude to A. Chueca, H. García, S. Oudas, and R. Estrada for the assistance during this research and constructive suggestions.

Appendix A. Generation methods of TPMS cellular solids

All Skeletal-TPMS and Shell-TPMS designs analyzed in this research were generated with TPMSgen [70] from the corresponding mathematical equation presented below:

$$J \rightarrow \sin(x)\cdot\cos(y)+\sin(y)\cdot\cos(z)+\sin(z)\cdot\cos(x)=1 \tag{A.1}$$

$$K \rightarrow \cos(x)\cdot\cos(y)\cdot\cos(z)+\sin(x)\cdot\sin(y)\cdot\sin(z)=\frac{1}{2} \tag{A.2}$$

$$M \rightarrow \cos(x)+\cos(y)+\cos(z)=\frac{1}{2.5} \tag{A.3}$$

$$N \rightarrow \cos(x)+\cos(y)+\cos(z)=\frac{1}{1.5} \tag{A.4}$$

$$O \rightarrow 2\cdot[\cos(x)\cdot\cos(y)+\cos(y)\cdot\cos(z)+\cos(z)\cdot\cos(x)] - [\cos(2x)+\cos(2y)+\cos(2z)]=1 \tag{A.5}$$

$$P \rightarrow \sin(x)\cdot\cos(y)+\sin(y)\cdot\cos(z)+\sin(z)\cdot\cos(x)=0 \tag{A.6}$$

$$Q \rightarrow \sin(x)\cdot\sin(y)\cdot\sin(z)+\sin(x)\cdot\cos(y)\cdot\cos(z) + \cos(x)\cdot\sin(y)\cdot\cos(z)+\cos(x)\cdot\cos(y)\cdot\sin(z)=0 \tag{A.7}$$

$$R \rightarrow \sin(2x)\cdot\cos(y)\cdot\sin(z)+\sin(x)\cdot\sin(2y)\cdot\cos(z) + \cos(x)\cdot\sin(y)\cdot\sin(2z)-\cos(2x)\cdot\cos(2y) - \cos(2y)\cdot\cos(2z)-\cos(2z)\cdot\cos(2x)+0.3=0 \tag{A.8}$$

$$S \rightarrow 1.1\cdot[\sin(2x)\cdot\cos(y)\cdot\sin(z)+\sin(x)\cdot\sin(2y)\cdot\cos(z) + \cos(x)\cdot\sin(y)\cdot\sin(2z)]-0.2\cdot[\cos(2x)\cdot\cos(2y) + \cos(2y)\cdot\cos(2z)+\cos(2z)\cdot\cos(2x)] - 0.4\cdot[\cos(2x)+\cos(2y)+\cos(2z)]=0 \tag{A.9}$$

$$T \rightarrow \cos(x)+\cos(y)+\cos(z)=0 \tag{A.10}$$

Appendix B. 3D representation of the stiffness tensor

The following steps allow obtaining the graphical representation of the homogenized stiffness tensor ($\boldsymbol{C^H}$) of the RVE of a cellular solid, expressed in Voigt notation and referenced to the global *XYZ* coordinate system.

First, the generalized Hooke's law for continuous media is expressed as:

$$\boldsymbol{\sigma} = \boldsymbol{C^H}\times\boldsymbol{\varepsilon} \tag{B.1}$$

where $\boldsymbol{\sigma}$ and $\boldsymbol{\varepsilon}$ are the stress and strain tensors referenced to the global *XYZ* coordinates, respectively.

A rotation around the *x*-axis (α), *y*-axis (β), and *z*-axis (γ) can be introduced to evaluate the stress and strain tensors $\boldsymbol{\sigma_{\alpha\beta\gamma}}$ and $\boldsymbol{\varepsilon_{\alpha\beta\gamma}}$ as:

$$\begin{aligned}\boldsymbol{\sigma}_{\alpha\beta\gamma} &= \mathbf{L}^{\sigma}_{\alpha\beta\gamma}\times\boldsymbol{\sigma}\\ \boldsymbol{\varepsilon}_{\alpha\beta\gamma} &= \mathbf{L}^{\varepsilon}_{\alpha\beta\gamma}\times\boldsymbol{\varepsilon}\end{aligned} \tag{B.2}$$

where $\boldsymbol{L^{\sigma}_{\alpha\beta\gamma}}$ and $\boldsymbol{L^{\varepsilon}_{\alpha\beta\gamma}}$ are the bond-stress and strains transformation matrices, which are determined from the rotation matrix $\boldsymbol{Q}$ and classical rotation matrices $\boldsymbol{R_x}$, $\boldsymbol{R_y}$, and $\boldsymbol{R_z}$ as detailed in B.3.where:

$$\boldsymbol{L}^{\sigma}_{\alpha\beta\gamma} = \begin{bmatrix} Q_{11}^2 & Q_{12}^2 & Q_{13}^2 & 2Q_{12}Q_{13} & 2Q_{11}Q_{13} & 2Q_{11}Q_{12} \\ Q_{21}^2 & Q_{22}^2 & Q_{yz}^2 & 2Q_{22}Q_{yz} & 2Q_{21}Q_{yz} & 2Q_{21}Q_{22} \\ Q_{31}^2 & Q_{31}^2 & Q_{33}^2 & 2Q_{31}Q_{33} & 2Q_{31}Q_{33} & 2Q_{31}Q_{31} \\ Q_{21}Q_{31} & Q_{22}Q_{31} & Q_{yz}Q_{33} & Q_{22}Q_{33}+Q_{yz}Q_{31} & Q_{21}Q_{33}+Q_{yz}Q_{31} & Q_{21}Q_{31}+Q_{22}Q_{31} \\ Q_{11}Q_{31} & Q_{12}Q_{31} & Q_{13}Q_{33} & Q_{12}Q_{33}+Q_{13}Q_{31} & Q_{11}Q_{33}+Q_{13}Q_{31} & Q_{11}Q_{31}+Q_{12}Q_{31} \\ Q_{11}Q_{21} & Q_{12}Q_{22} & Q_{13}Q_{yz} & Q_{12}Q_{yz}+Q_{13}Q_{22} & Q_{11}Q_{yz}+Q_{13}Q_{21} & Q_{11}Q_{22}+Q_{12}Q_{21} \end{bmatrix}$$

$$\boldsymbol{L}^{\varepsilon}_{\alpha\beta\gamma} = \begin{bmatrix} Q_{11}^2 & Q_{12}^2 & Q_{13}^2 & Q_{12}Q_{13} & Q_{11}Q_{13} & Q_{11}Q_{12} \\ Q_{21}^2 & Q_{22}^2 & Q_{yz}^2 & Q_{22}Q_{yz} & Q_{21}Q_{yz} & Q_{21}Q_{22} \\ Q_{31}^2 & Q_{31}^2 & Q_{33}^2 & Q_{31}Q_{33} & Q_{31}Q_{33} & Q_{31}Q_{31} \\ 2Q_{21}Q_{31} & 2Q_{22}Q_{31} & 2Q_{yz}Q_{33} & Q_{22}Q_{33}+Q_{yz}Q_{31} & Q_{21}Q_{33}+Q_{yz}Q_{31} & Q_{21}Q_{31}+Q_{22}Q_{31} \\ 2Q_{11}Q_{31} & 2Q_{12}Q_{31} & 2Q_{13}Q_{33} & Q_{12}Q_{33}+Q_{13}Q_{31} & Q_{11}Q_{33}+Q_{13}Q_{31} & Q_{11}Q_{31}+Q_{12}Q_{31} \\ 2Q_{11}Q_{21} & 2Q_{12}Q_{22} & 2Q_{13}Q_{yz} & Q_{12}Q_{yz}+Q_{13}Q_{22} & Q_{11}Q_{yz}+Q_{13}Q_{21} & Q_{11}Q_{22}+Q_{12}Q_{21} \end{bmatrix} \tag{B.3}$$

$\boldsymbol{Q_{ij}}$ corresponds to the element located in row i and column j in $\boldsymbol{Q}$.

$$\boldsymbol{Q} = \boldsymbol{R_x} \times \boldsymbol{R_y} \times \boldsymbol{R_z}$$

$$\boldsymbol{R_x}(\alpha) = \begin{bmatrix} 1 & 0 & 0 \\ 0 & \cos(\alpha) & -\sin(\alpha) \\ 0 & \sin(\alpha) & \cos(\alpha) \end{bmatrix}$$

$$\boldsymbol{R_y}(\beta) = \begin{bmatrix} \cos(\beta) & 0 & \sin(\beta) \\ 0 & 1 & 0 \\ -\sin(\beta) & 0 & \cos(\beta) \end{bmatrix} \quad \boldsymbol{R_z}(\gamma) = \begin{bmatrix} \cos(\gamma) & -\sin(\gamma) & 0 \\ \sin(\gamma) & \cos(\gamma) & 0 \\ 0 & 0 & 1 \end{bmatrix}$$

Substituting Eqs. (B.2) into Eq. (B.1), the following expression Eq. (B.4) is obtained:

$$\sigma_{\alpha\beta\gamma} = L^{\sigma}_{\alpha\beta\gamma} \times C^{H} \times L^{\varepsilon-1}_{\alpha\beta\gamma} \times \varepsilon_{\alpha\beta\gamma} \tag{B.4}$$

Then, the effective stiffness tensor in a specific orientation ($\boldsymbol{C^H_{\alpha\beta\gamma}}$) can be determined as:

$$C^{H}_{\alpha\beta\gamma} = L^{\sigma}_{\alpha\beta\gamma} \times C^{H} \times L^{\varepsilon-1}_{\alpha\beta\gamma} \tag{B.5}$$

At this point, the corresponding compliance tensor $\boldsymbol{S^H_{\alpha\beta\gamma}}$ can be directly calculated by inverting $\boldsymbol{C^H_{\alpha\beta\gamma}}$. Thus, for example, taking the global x-axis reference, the effective Young's modulus $E_{\alpha\beta\gamma}$ is:

$$E_{\alpha\beta\gamma} = \frac{1}{S^{H}_{\alpha\beta\gamma 11}} \tag{B.6}$$

where $S^{H}_{\alpha\beta\gamma 11}$ is the first term of the effective compliance tensor $\boldsymbol{S^H_{\alpha\beta\gamma}}$.

Finally, the graphical representation of the homogenized stiffness tensor can be plotted with the sequential computation of different rotation angles α, β, and γ. Each combination will rotate the tensor and evaluate the effective stiffness in a particular examined direction $d_{\alpha\beta\gamma}$:

$$\boldsymbol{d_{\alpha\beta\gamma}} = \boldsymbol{Q} \times \begin{bmatrix} 1 \\ 0 \\ 0 \end{bmatrix} \tag{B.7}$$

Accordingly, given an orientation $\boldsymbol{d_{\alpha\beta\gamma}}$ and the corresponding effective Young's modulus $E_{\alpha\beta\gamma}$, the coordinates x , y, and z, of a point in the graphical representation of the stiffness tensor are obtained as:

$$\begin{cases} x = E_{\alpha\beta\gamma}.d_{\alpha\beta\gamma 1} \\ y = E_{\alpha\beta\gamma}.d_{\alpha\beta\gamma 2} \\ z = E_{\alpha\beta\gamma}.d_{\alpha\beta\gamma 3} \end{cases} \tag{B.8}$$

References

[1] L.J. Gibson, M.F. Ashby. Cellular solids - Structure and properties. Cambridge University Press, 2n edition edition, 1997. ISBN 0-521-49911-9. URL https://doi.org/10.1017/CBO9781139878326.

[2] Y. Liu and H. Hu. A review on auxetic structures and polymeric materials. *Sci. Res. Essays*, 5(10):1052–1063, 2010. ISSN 1992-2248. URL https://doi.org/10.5897/SRE.9000104.

[3] J.C. Álvarez-Elipe, A. Díaz-Lantada, Comparative study of auxetic geometries by means of computer-aided design and engineering, Smart Mater. Struct. 21 (2012) 0964–1726, https://doi.org/10.1088/0964-1726/21/10/105004.

[4] N. A. Fleck, V. S. Deshpande, and M. F. Ashby. Micro-architectured materials: past, present and future, Proc. R. Soc. A 466(2121):2495–2516, 2010. ISSN 1364-5021. URL https://doi.org/10.1098/rspa.2010.0215.

[5] K. Refai, M. Montemurro, C. Brugger, N. Saintier, Determination of the effective elastic properties of titanium lattice structures, Mech. Adv. Mater. Struct. 27 (2020) 1537–6494, https://doi.org/10.1080/15376494.2018.1536816.

[6] Q. Liu, R. Xu, Y. Zhou, J. Ge, S. Yuan, Y. Long, and T. Shi. Metamaterials mapped lightweight structures by principal stress lines and topology optimization: Methodology, additive manufacturing, ductile failure and tests. Mater. Des. 212:110192, 2021. ISSN 0264-1275. URL https://doi.org/10.1016/j.matdes.2021.110192.

[7] L. Cheng, J. Bai, A.C. To. Functionally graded lattice structure topology optimization for the design of additive manufactured components with stress constraints. Comput. Methods Appl. Mech. Eng., 344:334–359, 2019. ISSN 0045-7825. URL https://doi.org/10.1016/j.cma.2018.10.010.

[8] J. Aquino, I. Duarte, J. Dias-de Oliveira, Modelling and effective properties prediction of metal foams, Sci. Tech. Mater., 30(1), 43–49, 2018. ISSN 2603-6363. URL https://doi.org/10.1016/j.stmat.2018.01.004.

[9] Y. Feng, T. Huang, Y. Gong, P. Jia. Stiffness optimization design for TPMS architected cellular materials, Mater. Des. 222: 111078, 2022. ISSN 1873-4197. URL https://doi.org/10.1016/j.matdes.2022.111078.

[10] N. Yang, H. Wei, and Z. Mao. Tuning surface curvatures and young's moduli of TPMS-based lattices independent of volume fraction. *Mater. Design*, 216:110542, 2022. ISSN 1873-4197. URL https://doi.org/10.1016/j.matdes.2022.110542.

[11] C. Lin, G. Wen, H. Yin, Z.-P. Wang, J. Liu, Y.M. Xie, Revealing the sound insulation capacities of TPMS sandwich panels, J. Sound Vib. 540 (2022) 117303.

[12] C. Zeng, W. Wang, Modeling method for variable and isotropic permeability design of porous material based on TPMS lattices, Tribol. Int. 176 (2022) 107913.

[13] S. Pramanik, D. Milaege, K.-P. Hoyer, M. Schaper, Additively manufactured novel Ti6Al7Nb circular honeycomb cellular solid for energy absorbing applications, Mater. Sci. Eng. A 854 (2022), https://doi.org/10.1016/j.msea.2022.143887 143887.

[14] J. W. Lee, S. H. Oh, E. Jeon, J. Kim, and K. Park. Functional gradation of the morphological properties of TPMS channel for enhanced flow performance, Mater. Des. 224:111413, 2022. ISSN 1873-4197. URL https://doi.org/10.1016/j.matdes.2022.111413.

[15] N. Novak, D. Kytyr, V. Rada, T. Doktor, O. Al-Ketan, R. Rowshan, M. Vesenjak, Z. Ren, Compression behaviour of TPMS-filled stainless steel tubes, Mater. Sci. Eng. A, 852:143680, 2022. ISSN 0921-5093. URL https://doi.org/10.1016/j.msea.2022.143680.

[16] K. Wei, X. Xiao, J. Chen, Y. Wu, M. Li, and Z. Wang. Additively manufactured bi-material metamaterial to program a wide range of thermal expansion, Mater. Des. 198:109343, 2021. ISSN 0264-1275. URL https://doi.org/10.1016/j.matdes.2020.109343.

[17] Y. L. Tee, T. Maconachie, P. Pille, M. Leary, T. Do, P. Tran, From nature to additive manufacturing: biomimicry of porcupine quill, Mater. Des. 210:110041, 2021. ISSN 0264-1275. URL https://doi.org/10.1016/j.matdes.2021.110041.

[18] M. Ouda, O. Al-Ketan, N. Sreedhar, M.I. Hasan Ali, R.K. Abu Al-Rub, S. Hong, H.A. Arafat, Novel static mixers based on triply periodic minimal surface (TPMS) architectures, J. Environ Chem. Eng. 8 (2020) 2213–2929, https://doi.org/10.1016/j.jece.2020.104289.

[19] C. Yang, Q.M. Li. Advanced lattice material with high energy absorption based on topology optimisation, Mech. Mater. 148:103536, 2020. ISSN 0167-6636. URL https://doi.org/10.1016/j.mechmat.2020.103536.

[20] Y. Xu, D. Zhang, S. Hu, R. Chen, Y. Gu, X. Kong, J. Tao, Y. Jiang, Mechanical properties tailoring of topology optimized and selective laser melting fabricated Ti6Al4V lattice structure, J. Mech. Behav. Biomed. Mater. 99 (2019) 225–239. ISSN 1751-6161. URL https://doi.org/10.1016/j.jmbbm.2019.06.021.

[21] Z. Qin, G. S. Jung, M. J. Kang, M.J. Buehler, The mechanics and design of a lightweight three-dimensional graphene assembly, Sci. Adv, 3(1) (2017) 1–9. ISSN 2375-2548. URL https://doi.org/10.1126/sciadv.1601536.

[22] J.A. Gopsill, J. Shindler, B.J. Hicks, Using finite element analysis to influence the infill design of fused deposition modelled parts, Prog. Addit. Manuf., 3 (2018) 145–163. ISSN 2363-9520. URL https://doi.org/10.1007/s40964-017-0034-y.

[23] C.O. Ufodike, H. Wang, M.F. Ahmed, G. Dolzyk, S. Jung, Design and modeling of bamboo biomorphic structure for in-plane energy absorption improvement, Mater. Des. 205 (2021) 109736. ISSN 0264-1275. URL https://doi.org/10.1016/j.matdes.2021.109736.

[24] L. Bai, Y. Xu, X. Chen, L. Xin, J. Zhang, K. Li, Y. Sun. Improved mechanical properties and energy absorption of Ti6Al4V laser powder bed fusion lattice structures using curving lattice struts, Mater. Des. 211:110140, 2021. ISSN 0264-1275. URL https://doi.org/10.1016/j.matdes.2021.110140.

[25] G. Ye, H. Bi, Y. Hu, Compression behaviors of 3D printed pyramidal lattice truss composite structures, Compos. Struct. 233 (2020) 111706. ISSN 0263-8223. URL https://doi.org/10.1016/j.compstruct.2019.111706.

[26] A. Arjunan, M. Singh, A. Baroutaji, C. Wang. Additively manufactured AlSi10Mg inherently stable thin and thick-walled lattice with negative Poisson's ratio, Compos. Struct. 247 (2020) 112469. ISSN 0263-8223. URL https://doi.org/10.1016/j.compstruct.2020.112469.

[27] B. Bahrami Babamiri, H. Askari, K. Hazeli, Deformation mechanisms and post-yielding behavior of additively manufactured lattice structures, Mater. Des. 188 (2020) 108443. ISSN 0264-1275. URL https://doi.org/10.1016/j.matdes.2019.108443.

[28] L. Azzouz, Y. Chen, M. Zarrelli, J. M. Pearce, L. Mitchell, G. Ren, M. Grasso. Mechanical properties of 3-D printed truss-like lattice biopolymer non-stochastic structures for sandwich panels with natural fibre composite skins, Compos. Struct. 213 (2019) 220–230. ISSN 0263-8223. URL https://doi.org/10.1016/j.compstruct.2019.01.103.

[29] X. Y. Zhang, G. Fang, L. L. Xing, W. Liu, J. Zhou, Effect of porosity variation strategy on the performance of functionally graded Ti-6Al-4V scaffolds for bone tissue engineering, Mater. Des. 157, 523–538, 2018. ISSN 0264-1275. URL https://doi.org/10.1016/j.matdes.2018.07.064.

[30] S. R. G. Bates, I. R. Farrow, and R. S. Trask. 3D printed elastic honeycombs with graded density for tailorable energy absorption. In: SPIE Smart Structures and Materials + Nondestructive Evaluation and Health Monitoring, Las Vegas, NV, 2016. URL https://doi.org/10.1117/12.2219322.

[31] Y.L. Yap, W.Y. Yeong, Shape recovery effect of 3D printed polymeric honeycomb: this paper studies the elastic behaviour of different honeycomb structures produced by PolyJet technology, Virtual Phys. Prototyp. 10 (2015) 1745–2767, https://doi.org/10.1080/17452759.2015.1060350.

[32] X. Chen, M. Hu, Y. Sun, J. Yang, L. Bai, Y. Xiong. Wide-range tuning of the mechanical properties of TPMS lattice structures through frequency variation, Mater. Des. 224 (2022) 111370. ISSN 0264-1275. URL https://doi.org/10.1016/j.matdes.2022.111370.

[33] J. Fu, P. Sun, Y. Du, H. Li, X. Zhou, Q. Tian, Isotropic design and mechanical characterization of TPMS-based hollow cellular structures, Compos. Struct. 279 (2022), https://doi.org/10.1016/j.compstruct.2021.114818 114818.

[34] X. Yang, Q.Y.Y. Shi, L. Yang, S. Wu, C. Yan, Y. Shi, Effect of volume fraction and unit cell size on manufacturability and compressive behaviors of Ni-Ti triply periodic minimal surface lattices, Addit. Manuf. 54 (2022) 102737.

[35] A. Jones, M. Leary, S. Bateman, M. Easton, Parametric design and evaluation of TPMS-like cellular solids, Mater. Des. 221 (2022) 110908, 2022. ISSN 1873-4197. URL https://doi.org/10.1016/j.matdes.2022.110908.

[36] Z. Alomar, F. Concli, Compressive behavior assessment of a newly developed circular cell-based lattice structure, Mater. Des. 205 (2021) 109716, ISSN 0264-1275. URL https://doi.org/10.1016/j.matdes.2021.109716.

[37] R. Ding, J. Yao, B. Du, L. Zhao, Y. Guo, Mechanical properties and energy absorption capability of ARCH lattice structures manufactured by selective laser melting, Adv. Eng. Mater. 22 (2020) 1438–1656, https://doi.org/10.1002/adem.201901534.

[38] C. Li, H. Lei, Y. Liu, X. Zhang, J. Xiong, H. Zhou, D. Fang, Crushing behavior of multi-layer metal lattice panel fabricated by selective laser melting, Int. J. Mech. Sci. 145 (2018) 389–399. ISSN 00207403. URL https://doi.org/10.1016/j.ijmecsci.2018.07.029.

[39] Z. Xiao, Y. Yang, R. Xiao, Y. Bai, C. Song, D. Wang. Evaluation of topology-optimized lattice structures manufactured via selective laser melting, Mater. Des. 143 (2018) 27–37. ISSN 0264-1275. URL https://doi.org/10.1016/j.matdes.2018.01.023.

[40] X. Cao, S. Duan, J. Liang, W. Wen, D. Fang, Mechanical properties of an improved 3D-printed rhombic dodecahedron stainless steel lattice structure of variable cross section, Int. J. Mech. Sci. 145 (2018) 53–63, ISSN 0020-7403. URL https://doi.org/10.1016/j.ijmecsci.2018.07.006.

[41] R. Gümrük, R.A. Mines, S. Karadeniz, Static mechanical behaviours of stainless steel micro-lattice structures under different loading conditions, Mater. Sci. Eng. A 586 (2013) 392–406. ISSN 0921-5093. URL https://doi.org/10.1016/j.msea.2013.07.070.

[42] R. Alberdi, R. Dingreville, J. Robbins, T. Walsh, B. C. White, B. Jared, B.L. Boyce, Multi-morphology lattices lead to improved plastic energy absorption, Mater. Des. 194 (2020) 108883. ISSN 0264-1275. URL https://doi.org/10.1016/j.matdes.2020.108883.

[43] C. Li, H. Lei, Z. Zhang, X. Zhang, H. Zhou, P. Wang, and D. Fang. Architecture design of periodic truss-lattice cells for additive manufacturing. Addit. Manuf. 34 (2020) 101172. ISSN 2214-8604. URL https://doi.org/10.1016/j.addma.2020.101172.

[44] T. Maconachie, M. Leary, B. Lozanovski, X. Zhang, M. Qian, O. Faruque, M. Brandt. SLM lattice structures: properties, performance, applications and challenges, Mater. Des. 183:108137, 2019. ISSN 0264-1275. URL https://doi.org/10.1016/j.matdes.2019.108137.

[45] A.M. Torres, A.A. Trikanad, C.A. Aubin, F.M. Lambers, M. Luna, C.M. Rimnac, P. Zavattieri, C.J. Hernandez, Bone-inspired microarchitectures achieve enhanced fatigue life, Proc. Natl. Acad. Sci. U.S.A. 116 (2019) 0027–8424, https://doi.org/10.1073/pnas.1905814116.

[46] F. N. Habib, P. Iovenitti, S. H. Masood, M. Nikzad, Fabrication of polymeric lattice structures for optimum energy absorption using Multi Jet Fusion technology, Mater. Des. 155 (2018) 86–98. ISSN 0264-1275. URL https://doi.org/10.1016/j.matdes.2018.05.059.

[47] M. Leary, M. Mazur, H. Williams, E. Yang, A. Alghamdi, B. Lozanovski, X. Zhang, D. Shidid, L. Farahbod-Sternahl, G. Witt, I. Kelbassa, P. Choong, M. Qian, M. Brandt, Inconel 625 lattice structures manufactured by selective laser melting (SLM): Mechanical properties, deformation and failure modes, Mater. Des. 157 (2018) 179–199. ISSN 0264-1275. URL https://doi.org/10.1016/j.matdes.2018.06.010.

[48] L. Yang, O. Harrysson, D. Cormier, H. West, H. Gong, B. Stucker, Additive manufacturing of metal cellular structures: design and fabrication, Jom 67(3) (2015) 608–615, ISSN 1543-1851. URL https://doi.org/10.1007/s11837-015-1322-y.

[49] J. J. Andrew, H. Alhashmi, A. Schiffer, S. Kumar, V.S. Deshpande, Energy absorption and self-sensing performance of 3D printed CF/PEEK cellular composites, Mater. Des. 208 (2021) 109863. ISSN 0264-1275. URL https://doi.org/10.1016/j.matdes.2021.109863.

[50] S.M. Zaharia, L.A. Enescu, M.A. Pop, Mechanical performances of lightweight sandwich structures produced by material extrusion-based additive manufacturing, Polymers 12 (2020), https://doi.org/10.3390/polym12081740.

[51] Y. Tao, L. Pan, D. Liu, P. Li, A case study: Mechanical modeling optimization of cellular structure fabricated using wood flour-filled polylactic acid composites with fused deposition modelling, Compos. Struct. 216 (2019) 360–365. ISSN 0263-8223. URL https://doi.org/10.1016/j.compstruct.2019.03.010.

[52] A. Kumar, S. Verma, J.-Y. Jeng, Supportless lattice structures for energy absorption fabricated by fused deposition modelling, 3D Print Addit Manuf. 7 (2020) 2329–7662, https://doi.org/10.1089/3dp.2019.0089.

[53] J. D. Rossiter, A. A. Johnson, G.A. Bingham, Assessing the design and compressive performance of material extruded lattice structures, 3D Print Addit Manuf, 7(1) (2020) 19–27, ISSN 2329-7662, URL https://doi.org/10.1089/3dp.2019.0030.

[54] A. Forés-Garriga, G. Gómez-Gras, M. A. Pérez, Mechanical performance of additively manufactured lightweight cellular solids: influence of cell pattern and relative density on the printing time and compression behaviour, Mater. Design 215 (2022) 110474. ISSN 0264-1275. URL https://doi.org/10.1016/j.matdes.2022.110474.

[55] Y. Lu, W. Zhao, Z. Cui, H. Zhu, C. Wu, The anisotropic elastic behavior of the widely-used triply-periodic minimal surface based scaffolds, J. Mech. Behav. Biomed. Mater. 99(2) (2019) 56–65. ISSN 18780180. URL https://doi.org/10.1016/j.jmbbm.2019.07.012.

[56] W. Liu, H. Song, Z. Wang, J. Wang, C. Huang, Improving mechanical performance of fused deposition modeling lattice structures by a snap-fitting method, Mater. Des. 181 (2019) 108065, ISSN 0264-1275, URL https://doi.org/10.1016/j.matdes.2019.108065.

[57] G. Dong, G. Wijaya, Y. Tang, Y. F. Zhao, Optimizing process parameters of fused deposition modeling by Taguchi method for the fabrication of lattice structures, Addit. Manuf., 19 (2018) 62–72, ISSN 2214-8604, URL https://doi.org/10.1016/j.addma.2017.11.004.

[58] R. Gautam, S. Idapalapati, S. Feih, Printing and characterisation of Kagome lattice structures by fused deposition modelling, Mater. Design, 137 (2018) 266–275, ISSN 0264-1275, URL https://doi.org/10.1016/j.matdes.2017.10.022.

[59] N. Sreedhar, N. Thomas, O. Al-Ketan, R. Rowshan, H.H. Hernandez, R.K. Abu Al-Rub, H.A. Arafat. Mass transfer analysis of ultrafiltration using spacers based

on triply periodic minimal surfaces: Effects of spacer design, directionality and voidage, J. Membr. Sci., 561 (2018) 89–98, ISSN 0376-7388, URL https://doi.org/10.1016/j.memsci.2018.05.028.
[60] O. Al-Ketan, R. Rezgui, R. Rowshan, H. Du, N. X. Fang, R.K. Abu Al-Rub, Microarchitected stretching-dominated mechanical metamaterials with minimal surface topologies, Adv. Eng. Mater. 20(9) (2018) 1800029, ISSN 15272648. URL https://doi.org/10.1002/adem.201800029.
[61] O. Al-Ketan, D. W. Lee, R. Rowshan, R. K. Abu Al-Rub, Functionally graded and multi-morphology sheet TPMS lattices: Design, manufacturing, and mechanical properties, J. Mech. Behav. Biomed. Mater., 102 (2020) 103520, ISSN 1751-6161, URL https://doi.org/10.1016/j.jmbbm.2019.103520.
[62] N. Sathishkumar, N. Vivekanandan, L.Balamurugan, N. Arunkumar, I. Ahamed, Mechanical properties of triply periodic minimal surface based lattices made by polyjet printing, Mater. Today: Proc., 22(4) (2020) 2934–2940, ISSN 2214-7853, URL https://doi.org/10.1016/j.matpr.2020.03.427.
[63] H. Jia, H. Lei, P. Wang, J. Meng, C. Li, H. Zhou, X. Zhang, D. Fang, An experimental and numerical investigation of compressive response of designed Schwarz Primitive triply periodic minimal surface with non-uniform shell thickness, Extreme Mech. Lett. 37 (2020) 100671, ISSN 2352-4316, URL https://doi.org/10.1016/j.eml.2020.100671.
[64] A. Kumar, L. Collini, A. Daurel, J.Y. Jeng, Design and additive manufacturing of closed cells from supportless lattice structure, Addit. Manuf., 33(January) (2020) 101168, ISSN 2214-8604. URL https://doi.org/10.1016/j.addma.2020.101168.
[65] D. Downing, A. Jones, M. Brandt, M. Leary, Increased efficiency gyroid structures by tailored material distribution, Mater. Des. 197 (2021) 109096, ISSN 0264-1275. URL https://doi.org/10.1016/j.matdes.2020.109096.
[66] I. Maskery, N. T. Aboulkhair, A. O. Aremu, C.J. Tuck, I.A. Ashcroft, Compressive failure modes and energy absorption in additively manufactured double gyroid lattices, Addit. Manuf 16 (2017) 24–29, ISSN 2214-8604, URL https://doi.org/10.1016/j.addma.2017.04.003.
[67] A. Forés-Garriga, H. García de la Torre, R. Lado-Roigé, G. Gómez- Gras, and M.A. Pérez. Triply Periodic Minimal Surfaces Generator - TPMSgen (2023). URL https://github.com/albertforesg/TPMSgen.
[68] A. Forés-Garriga, M. A. Pérez, G. Gómez-Gras, G. Reyes-Pozo. Role of infill parameters on the mechanical performance and weight reduction of PEI Ultem processed by FFF, Mater. Des. 193 (2020) 108810, ISSN 1873-4197, URL https://doi.org/10.1016/j.matdes.2020.108810.
[69] A. Chueca de Bruijn, G. Gómez-Gras, M. A. Pérez, Selective dissolution of polysulfone support material of fused filament fabricated Ultem 9085 parts, Polym. Test., 108 (2022) 107495, ISSN 01429418, URL https://doi.org/10.1016/j.polymertesting.2022.107495.
[70] A. Chueca de Bruijn, G. Gómez-Gras, M.A. Pérez, Mechanical study on the impact of an efective solvent support-removal methodology for FDM Ultem 9085 parts, Polym. Test., page 106702, 2020. ISSN 0893-9659. URL https://doi.org/10.1016/j.polymertesting.2020.106433.
[71] ASTM C365: Standard Test Method for Flatwise Compressive Properties of Sandwich Cores. Technical report, ASTM International, 2016. URL https://doi.org/10.1520/C0365_C0365M-16.
[72] M.M. Pastor-Artigues, F. Roure-Fernández, X. Ayneto-Gubert, J. Bonada-Bo, E. Pérez-Guindal, I. Buj-Corral, Elastic asymmetry of PLA material in FDM-printed parts: Considerations concerning experimental characterisation for use in numerical simulations, Materials 13(15) (2020) 1–24, ISSN 1996-1944, URL https://doi.org/10.3390/ma13010015.
[73] O. Fashanu, D. Murphy, M. Spratt, J. Newkirk, K. Chandrashekhara, B. Brown, J. Porter, Effective elastic properties of additively manufactured metallic cellular structures using numerical unit-cell homogenization, Prog. Addit. Manuf., 5 (2020) 355–366, ISSN 2363-9520, URL https://doi.org/10.1007/s40964-020-00141-7.
[74] D. V. Grinevich, N.O. Yakovlev, P.B. Mazalov, Linear homogenization in the analysis of cellular structures produced by additive technology, Russ. Eng. Res. 41 (2021) 423–427, ISSN 1068-798X, URL https://doi.org/10.3103/S1068798X2105004X.
[75] C.M. Zener, S. Siegel, Elasticity and anelasticity of metals, J. Phys. Chem. 53 (9) (1949) 1468, https://doi.org/10.1021/j150474a017.
[76] S.I. Ranganathan, M. Ostoja-Starzewski, Universal elastic anisotropy index, Phys. Rev. Lett., 101(5) (2008) 055504, ISSN 0031-9007, URL https://doi.org/10.1103/PhysRevLett.101.055504.
[77] J. Fu, P. Sun, Y. Du, H. Li, X. Zhou, Q. Tian, Isotropic design and mechanical characterization of TPMS-based hollow cellular structures, Compos. Struct., 279:114818, 2022. ISSN 0263-8223, URL https://doi.org/10.1016/j.compstruct.2021.114818.
[78] C. Lubombo, M.A. Huneault, Effect of infill patterns on the mechanical performance of lightweight 3D-printed cellular PLA parts, Mater. Today Commun. 17 (2018) 214–228, ISSN 2352-4928, URL https://doi.org/10.1016/j.mtcomm.2018.09.017.
[79] J. M. Chacón, M. A. Caminero, E. García-Plaza, P.J. Núñez, Additive manufacturing of PLA structures using fused deposition modelling: effect of process parameters on mechanical properties and their optimal selection, Mater. Des. 124 (2017) 143–157, ISSN 0264-1275, doi: 10.1016/j.matdes.2017.03.065.
[80] ASTM D790-17, Standard Test Methods for Flexural Properties of Unreinforced and Reinforced Plastics and Electrical Insulating Materials. Technical report, ASTM International, 2017. URL https://doi.org/10.1520/D0790-17.
[81] Stratasys. ULTEM™ 9085 Resin FDM Thermoplastic Filament Fit for High-Performance Applications. Technical report; 2021. URL https://support.stratasys.com/en/materials/fdm/ultem-9085.

Publication IV:

Lightweight hybrid composite sandwich structures with additively manufactured cellular cores

Preprint submitted to Thin-Walled Structures (May 2023)

Lightweight hybrid composite sandwich structures with additively manufactured cellular cores

Albert Forés-Garriga[a], Giovanni Gómez-Gras[a], Marco A. Pérez[a,*]

[a]*IQS School of Engineering, Universitat Ramon Llull, Via Augusta 390, 08017 Barcelona, Spain*

Abstract

This study focuses on advancing sandwich structures by designing and fabricating complex two- and three-dimensional cellular cores combined with Carbon Fiber Reinforced Polymer (CFRP) skins. Numerical analysis is used to investigate the impact of core design and density on the bending performance. Optimal configurations are identified and experimentally validated. Professional Fused Filament Fabrication (FFF) equipment with a heating chamber is employed for manufacturing the core samples to enhance layer cohesion and material joint stiffness. A high-performance technical polymer with a superior strength-to-weight ratio is employed to maximize structural capabilities. Hybrid sandwich structures with PEI Ultem cellular cores demonstrate stiffness and strength comparable to reference materials, outperforming foam cores while slightly trailing behind Nomex® and aluminum honeycombs. In addition, the results demonstrate more efficient cell morphologies achievable through additive manufacturing technologies, surpassing the hexagonal design. This work provides valuable insights into hybrid composite materials and the potential of additive manufacturing in creating lightweight, high-performance sandwich panels.

Keywords: Sandwich structures, Cellular solids, 3D printing, Fused Filament Fabrication, Mechanical performance, Ultem

1. Introduction

Over the years, significant advancements in materials and manufacturing techniques have improved structures' performance and functionality. One notable innovation was sandwich composites, which consist of two thin, rigid faces and a lightweight, thick core. This configuration offers exceptional specific stiffness and impressive flexural strength [1], making sandwich structures versatile solutions with widespread applications in land, maritime, aeronautical, and aerospace transportation sectors [2, 3]. However, the proper arrangement is vital for achieving the desired panel performance [4]. The core's material and structure play a crucial role, providing increased inertia, supporting shear stresses, and reducing the density of the composite panel [5]. Strategically choosing the core material optimizes properties such as rigidity, impact resistance, and thermal conductivity, allowing the sandwich structure to be tailored to specific application requirements.

Nature has served as a source of inspiration for developing sandwich core materials, resulting in innovative designs and enhanced performance [6–8]. For instance, open and closed-celled foams, inspired by the intricate network of trabecular bone, have found widespread use in construction for their excellent insulation properties [9–13]. Furthermore, patented manufacturing processes have enabled the replication of bees' hexagonal honeycombs, featuring thin walls composed of lightweight materials like Nomex® (meta-aramid fiber) or aluminum. These honeycombs exhibit exceptional heat and flame resistance and high strength-to-weight ratios [14–18], making them ideal for aerospace applications [19, 20]. Nevertheless, the limitations of conventional manufacturing methods have hindered the advancement of bio-inspired core designs.

The current decade has witnessed a remarkable breakthrough, primarily attributed to the rapid advancements in additive manufacturing (AM) technologies. These techniques have undoubtedly pushed the boundaries of fabrication, enabling the creation of intricate and highly complex structures with unparalleled precision and efficiency [21, 22]. As a result, bio-inspired cellular solids have found feasible means of materialization through AM technologies [23–28].

In recent studies, several authors have explored the mechanical behavior of AM sandwich structures utilizing cellular cores and faces composed of a single material [29–34]. This innovative approach eliminates the need for assembly and consolidation during fabrication, allowing the entire panel to be produced using the same equipment. Such a streamlined production process offers significant time and cost savings. These investigations have demonstrated the efficient distribution of material within cellular designs, leading to substantial mass reduction while maintaining structural functionality under compression [35], flexural [36–40], and impact [41–43] loads. However, the current state of AM technologies limits the ability to directly produce hybrid sandwich structures by combining different materials in the same fabrication process [44–46]. An optimal combination would enable the utilization of the desirable properties of both components, such as the rigidity and strength of the face material and the lightweight nature of the cellular core.

*Corresponding author.
Email address: marcoantonio.perez@iqs.edu (Marco A. Pérez)

Anticipating future advancements, some researchers have begun to explore the benefits of combining stiffer and denser faces with AM cellular cores [47–49]. However, these studies have primarily focused on a limited number of cellular designs with outer skin reinforcement using alternative materials. Further analysis is required to fully comprehend the potential revolution that these arrangements can bring to the development and fabrication of lightweight sandwich panels. This analysis should delve into the structural capabilities of each pattern, considering unexplored designs and additional factors like unit cell size, the volume fraction occupied by the faces, and other manufacturing considerations.

This work aims to advance the field by focusing on designing and fabricating a wide range of two- and three-dimensional cellular cores with increased geometric complexity. These cores are combined with Carbon Fiber Reinforced Polymer (CFRP) skins to create hybrid sandwich structures. A numerical approach is utilized to assess the impact of core design and density on the bending performance of the panels. Furthermore, optimal configurations are identified and manufactured, in order to experimentally validate the developed FE model.

In contrast to some prior research, this study utilizes professional Fused Filament Fabrication (FFF) equipment with a heating chamber, enhancing the cohesion between printing layers and improving the stiffness of the melted material joints. Additionally, a high-performance technical polymer with an exceptional strength-to-weight ratio is employed to maximize the structural capabilities of each cellular design.

The results are compared with the performance of reference foam (polyurethane) and honeycomb (aluminum and Nomex®) panels, contributing to the development of innovative design-for-manufacturing strategies for lightweight cores in sandwich structures.

2. Methodology

2.1. Cellular core designs

A comprehensive analysis was conducted considering multiple cellular designs to investigate the impact of cell geometry and density on the bending performance of hybrid sandwich panels. Twelve two-dimensional patterns and seven three-dimensional Triple Periodic Minimal Surface (TPMS) designs, consisting of four Shell and three Skeletal structures (see Fig. 2), were inspected. Careful selection of these designs was based on prior research [50, 51], ensuring a wide range of cell shape, arrangement, and density variations without the need for support structures during FFF manufacturing.

Two-dimensional patterns, resembling extruded shapes, were parametrically generated using SolidWorks. The intricate TPMS cellular designs were derived from their mathematical equations [51] using TPMSgen [52], an in-house open-source software. Different CAD files for each cellular design were implemented for the numerical analysis, as summarized in Fig. 3 and explained in subsequent sections. Furthermore, optimal configurations were exported to STL file format and fabricated for experimental testing to validate the simulation results.

A Stratasys Fortus 400mc 3D printer was used to prepare the core specimens for conducting the bending tests on the hybrid structures. This professional FFF equipment features a thermal chamber that maintains controlled ambient temperature throughout the printing process, improving inter-layer adherence between adjacent building layers and ultimately enhancing the overall strength [53]. Ultem™ 9085 (PEI Ultem) material was chosen for manufacturing the cellular samples [54]. This high-performance technical polyetherimide offers exceptional stiffness- and strength-to-weight ratio, as well as high-temperature and chemical resistance. Its FST (flame, smoke, and toxicity) certification also makes it particularly suitable for industrial sectors like aerospace. The manufacturing of the core samples was conducted with an oven temperature of 195 °C,

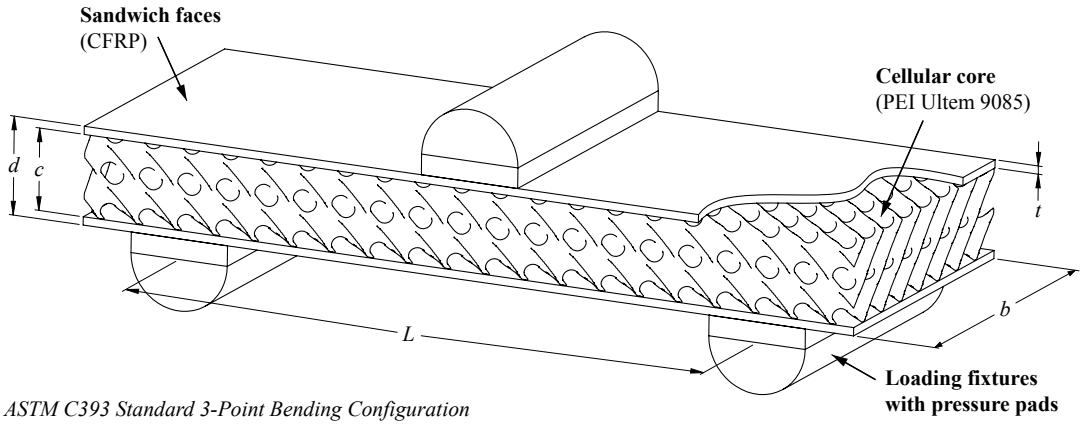

Figure 1: Dimensional diagram of a hybrid sandwich panel for the 3-Point bending test according to ASTM C393 Standard. The core pattern corresponds to the Diamond three-dimensional cellular design.

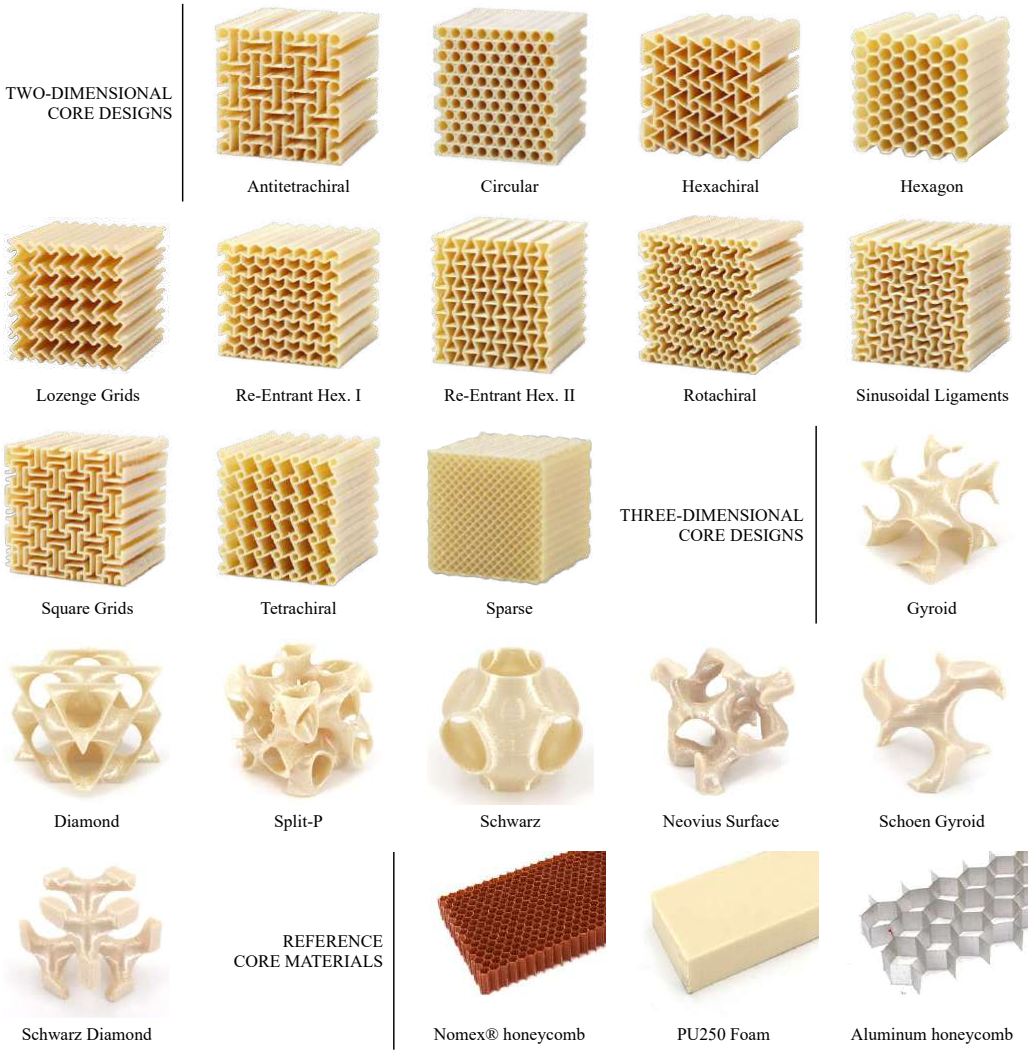

Figure 2: FFF two- and three-dimensional cellular core designs considered for hybrid sandwich panels. Classical core materials were included as reference configurations.

while the model extrusion temperature was set at 380 °C, according to the technical specifications.

Two-dimensional patterns and Shell-TPMS designs were printed with the minimum achievable wall thickness using the AM equipment to explore the maximum potential for fabricating lightweight cellular cores. This resulted in a single contour thickness of 0.508 mm for the two-dimensional patterns and two contours (1.016 mm) for the Shell-TPMS designs. A layer height of 0.254 mm was used for manufacturing all the specimens.

2.2. *Numerical approach*

An Ansys FE implicit model was developed to assess the impact of cellular design, density and sandwich arrangement on the bending performance of the hybrid structure. Six relative density levels were examined for each core design, ranging from 5% to 30% based on the cellular solid criterion [6] (see Table 1). Due to their geometric complexity and the FFF manufacturing process, cellular solids can exhibit different degrees of anisotropy [51]. Therefore, a Representative Volume Element (RVE) orthotropic approach was employed to mitigate

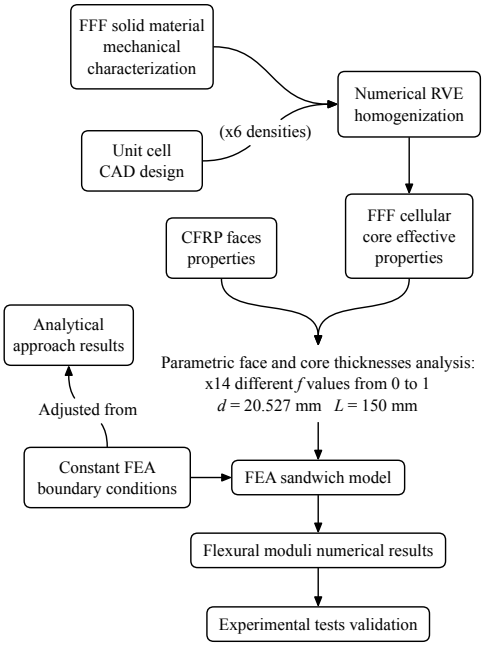

Figure 3: Flowchart of the methodological approach.

mesh generation issues and reduce the computational resources required for simulating the flexural performance of the intricate core designs. Numerical homogenization of the elastic properties was performed on each cellular core using the Ansys Material Designer module, considering periodic boundary conditions, to obtain the effective orthotropic properties of each pattern's RVE. Additionally, the mechanical properties of the sandwich faces were extracted from the manufacturer's datasheet [55], as outlined in Table 2.

A parametric static structural FE model was developed based on the dimensions of the hybrid structure, including the core thickness (c) and face thickness (t). The flexural behavior of the composite panel was simulated, considering multiple sandwich arrangements for each core design and density. Fourteen[1] different f values (see Eq. 1) were analyzed, ranging from an isolated core ($f = 0$) to a full CFRP panel ($f = 1$), while maintaining a constant total panel height (d) of 20.572 mm, a width (b) of 75 mm, and a support span (L) of 150 mm, thus resulting in a total of 1596 simulated models. The FE model was simplified to a quarter of the sandwich panel to optimize computational efficiency. Therefore, two frictionless support boundary conditions were introduced to designate the xz and yz symmetry planes (see Fig. 4). The SOLID186 element type was used to create meshes for both the core and faces, with divisions of 50, 40, and 8 elements along the x, y, and z-axis, respectively.

$$f = 2t/d \tag{1}$$

Perfectly bonded unions between sandwich faces and core were assumed. Round bending test supports were employed, imposing a frictionless contact between them and the bottom

[1] Considered values of volume fraction of the nominal cross-section occupied by sandwich faces (f): 0, 0.028, 0.056, 0.083, 0.139, 0.195, 0.278, 0.389, 0.473, 0.584, 0.667, 0.751, 0.862, 1.

Table 1: Relative density values of each two-dimensional and three-dimensional (Shell-TPMS and Skeletal-TPMS) cellular core design considered for conducting the numerical approach and the experimental validation tests.

Cellular Core Design (see Fig. 2)	**Typology**	**Core Relative Density (%)** [a]								
		Numerical Approach						Experimental Tests		
		1	2	3	4	5	6	1	2	3
Antitetrachiral	Two-dimensional	29.99	25.11	20.02	15.14	9.90	5.40	28.75	22.99	18.39
Circular	Two-dimensional	29.67	25.11	20.02	15.14	9.90	5.40	28.73	18.10	9.14
Hexachiral	Two-dimensional	29.58	24.69	20.11	15.14	9.95	5.38	28.50	24.45	21.71
Hexagon	Two-dimensional	29.32	25.34	19.90	14.81	9.59	5.07	32.42	18.94	9.37
Lozenge Grids	Two-dimensional	29.12	25.29	19.91	14.81	9.59	5.07	33.16	22.56	13.49
Re-Entrant Hexagon I	Two-dimensional	29.61	25.03	19.54	15.12	10.68	4.98	32.74	18.39	9.46
Re-Entrant Hexagon II	Two-dimensional	30.08	25.05	19.39	15.04	10.02	5.01	30.14	20.29	9.64
Rotachiral	Two-dimensional	30.20	24.90	20.20	14.93	10.22	5.07	29.31	25.05	20.79
Sinusoidal Ligaments	Two-dimensional	30.00	24.92	20.06	15.06	10.05	5.08	33.35	28.84	22.56
Square Grids	Two-dimensional	30.02	25.23	20.32	15.07	10.13	5.13	33.90	28.92	20.56
Tetrachiral	Two-dimensional	29.91	25.04	20.09	15.03	10.31	5.05	30.56	20.51	9.68
Sparse	Two-dimensional	32.85	23.23	20.04	13.74	10.01	5.05	30.19	21.26	12.54
Gyroid	Shell-TPMS	29.57	24.59	19.66	14.74	9.81	5.36	15.56	-	-
Diamond	Shell-TPMS	29.48	25.26	19.64	14.74	10.39	5.43	19.30	-	-
Split-P	Shell-TPMS	29.13	24.98	20.14	15.42	10.42	5.81	18.05	-	-
Schwarz	Shell-TPMS	30.03	25.60	19.17	15.68	9.59	5.75	11.84	-	-
Neovius Surface	Skeletal-TPMS	29.27	25.42	19.77	14.75	10.51	8.79	23.52	-	-
Schoen Gyroid	Skeletal-TPMS	29.67	25.17	19.70	15.05	9.74	5.29	23.64	-	-
Schwarz Diamond	Skeletal-TPMS	29.43	25.24	20.67	14.86	10.29	5.62	24.39	-	-

[a] Experimental density measurement of Solid ±45º Ultem processed by FFF: 1.1457 g/cm^3 (equivalent to 100% of core relative density).

Table 2: CFRP PrePreg elastic properties used for the sandwich faces in the FE model [55]. PEI Ultem solid ±45° infill elastic properties employed for calibrating the FE model are included [53].

Orthotropic Elasticity		
Description	CFRP PrePreg	PEI Ultem
Young's Modulus *x*-direction (MPa)	119300	2121
Young's Modulus *y*-direction (MPa)	8200	2121
Young's Modulus *z*-direction (MPa)	8200	2126
Poisson's Ratio *xy*	0.100	0.344
Poisson's Ratio *yz*	0.340	0.392
Poisson's Ratio *xz*	0.100	0.392
Shear Modulus *xy* (MPa)	59059	630
Shear Modulus *yz* (MPa)	3600	741
Shear Modulus *xz* (MPa)	59059	741

sandwich CFRP face. The Augmented Lagrange formulation was activated with a penetration tolerance of $1 \cdot 10^{-5}$ mm and a Normal Stiffness Factor (FKN) of 0.01, as recommended for bending test simulations. Lastly, a remote displacement of 1 mm was applied at the center of the top face of the sandwich panel, coinciding with the *yz*-symmetry plane. The *z* component of the reaction force on this boundary condition was evaluated to determine the stiffness of each sandwich structure.

2.3. Manufacturing of sandwich structures

Cores with various relative densities (see Table 1) were fabricated and assembled with CFRP skins to experimentally verify the hybrid sandwich structures' bending performance. The outer dimensions of the sandwich samples were set at $200 \times 75 \times 20.572$ mm. The numerical results indicated an optimal arrangement with a f value of 0.028, which was selected for implementation. Accordingly, the core thickness was set to 20 mm, while the faces were fabricated using a single layer of Carbon Fiber Prepreg MTC510UD300-HS-33%RW 24K with a thickness of 0.286 mm [56].

Sandwich skins were prepared in an OV301 Precision Benchtop Curing oven following the manufacturer's specifications[2]. A vacuum bag was utilized to apply back pressure during the process. Then, the additively manufactured cellular cores and CFRP faces were assembled, and the hybrid sandwich structures were consolidated. To achieve this, adhesive film MTFA500 [57] was placed between the cellular core and each CFRP face, following the appropriate curing procedure[3]. A rectangular polytetrafluoroethylene (PTFE) plate, slightly wider than the specimen dimensions, was positioned over each sandwich panel to ensure uniform compression and prevent the CFRP skins from puncturing the vacuum bag. Finally, the quality of the consolidated bond between the CFRP skins and the FFF cellular core of each fabricated sandwich panel was inspected using an Evident Olympus BondMaster 600 Multimode Bond Tester, ensuring that no skin-to-core debonding had occurred.

2.4. 3-Point bending tests

The mechanical performance of the manufactured sandwich panels was validated through experimental testing following the ASTM C393 standard [58]. The 3-Point bending test configuration was utilized, with a support span (L) of 150 mm (see Fig. 1) and a crosshead speed of 6 mm/min, ensuring failure occurred within 3 to 6 minutes for all specimens. Experimental tests were conducted using ZwickRoell Z030 (30 kN) equipment. The deflection at the center of the specimen was measured using a laser displacement sensor (see Fig. 5). To guarantee the accuracy of the experimental results, two specimens per sandwich core design and density were fabricated and evaluated, thus resulting in a total of 86 tested samples.

[2]Curing pressure: -0.90 bar. Curing conditions: 60 min at 120 ºC. Post-curing conditions (Tg=130 ºC): 60 min dwell at 120 ºC.

[3]Curing pressure: -0.45 bar. Curing conditions: 60 min at 120 ºC. Post-curing conditions (Tg=120 ºC): 60 min dwell at 120 ºC.

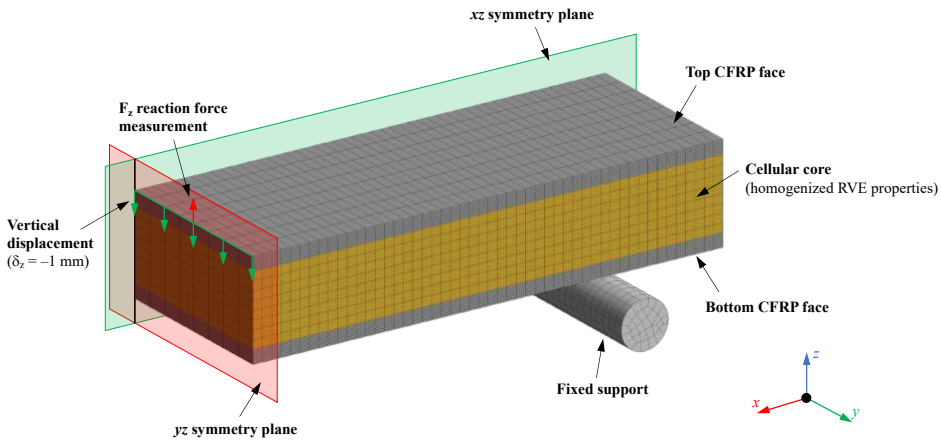

Figure 4: Representative FE model employed for simulating the bending performance of hybrid sandwich panels. Geometry corresponds to $f = 0.278$ arrangement.

Table 3: Ultimate failure modes for sandwich panels tested under 3-Point bending.

Failure Identification Codes					
First Character		Second Character		Third Character	
Failure Type	Code	Failure Area	Code	Failure Location	Code
Core crushing	C	At load bar	A	Core	C
Skin to core delamination	D	Gage	G	Core-facing bond	A
Facing failure	F	Multiple areas	M	Bottom facing	B
Multi-mode	M(*xyz*)	Outside gage	O	Top facing	T
Transverse shear	S	Various	V	Both facings	F
Explosive	X	Unknown	U	Various	V
Other	O			Unknown	U

Nominal external dimensions of the specimens were considered to calculate effective stress and strain data. The results for flexural modulus and maximum stress prior to first failure (FF) were reported. Flexural moduli were determined by linear regression, extracting data from the test results between 0.1% and 0.3% bending strain. The ultimate failure mode was also identified and reported for each test, following the standard identification codes presented in Table 3.

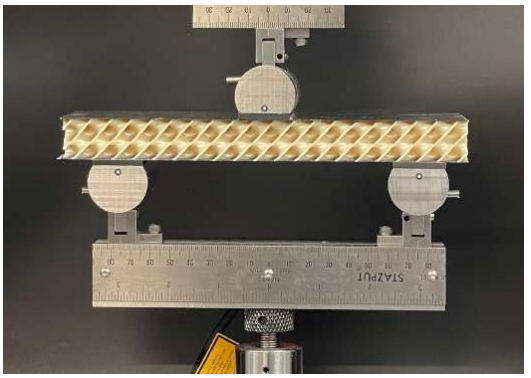

Figure 5: Experimental setup for conducting the bending tests of the hybrid sandwich structures, corresponding to the sample with the Diamond Shell-TPMS core design.

3. Results and discussion

3.1. Performance of hybrid sandwich structures

M.F. Ashby [59] introduced analytical expressions to estimate the mechanical performance of sandwich panels. Specifically, Eq. 2 evaluates the equivalent flexural modulus ($\tilde{E}_{flex}$) based on the loading mode[4], dimensions, and elastic properties of its constituent materials (E_f, E_c and G_c)[5].

$$\frac{1}{\tilde{E}_{flex}} = \frac{1}{E_f\left[\left(1-(1-f)^3\right)+\frac{E_c}{E_f}(1-f)^3\right]} + \frac{B_1}{B_2}\left(\frac{d}{L}\right)^2\frac{(1-f)}{12G_c} \quad (2)$$

Similarly, different failure modes should be considered to determine the equivalent flexural strength of the sandwich structure ($\tilde{\sigma}_{flex}$) according to the compression and shear strengths of its components (σ_f, σ_c and τ_c). Therefore, multiple stress values can be calculated for different failure modes, such as face yield (Eq. 3), face buckling (Eq. 4), core shear (Eq. 5), or face indentation. These failure mechanisms compete, meaning the one with the lowest load dominates.

$$\tilde{\sigma}^{FY}_{flex} = \left(1-(1-f)^2\right)\sigma_f + (1-f)^2\sigma_c \quad (3)$$

$$\tilde{\sigma}^{FB}_{flex} = 1.14 f\left(E_f \cdot E_c^2\right)^{1/3} \quad (4)$$

$$\tilde{\sigma}^{CS}_{flex} = \frac{B_4}{B_3}\left[4\frac{L}{d}(1-f)\tau_c + f^2\sigma_f\right] \quad (5)$$

$$\tilde{\sigma}_{flex} = min(\tilde{\sigma}^{FY}_{flex}, \tilde{\sigma}^{FB}_{flex}, \tilde{\sigma}^{CS}_{flex}) \quad (6)$$

Furthermore, the equivalent density of the sandwich structure $\tilde{\rho}$ can be determined regarding the respective densities of its constituent materials (ρ_f and ρ_c) and the value of f as:

$$\tilde{\rho} = f\rho_f + (1-f)\rho_c \quad (7)$$

Fig. 6 illustrates the different trends of analytical values for flexural modulus (*top*) and strength (*bottom*) with respect to the density of various sandwich panels under a 3-Point bending load case. Depicted points correspond to sandwich arrangements with multiple f values ranging from 0 to 1, regarding three different material combinations (see Table 4): a single-material arrangement (*A*) and two hybrid structures (*B* and *C*). In all cases, the effective properties of a FFF Diamond three-dimensional cellular design fabricated in PEI Ultem [51] were considered for the core. However, the properties of the same material printed in the ±45º solid configuration were employed in the skins of the single-material arrangement. Meanwhile, the two hybrid compositions involved faces additively

[4] In three-point bending with central load configuration, $B_1 = 48$, $B_2 = 4$, $B_3 = 4$, and $B_4 = 2$.

[5] Subscripts c and f correspond to core and face materials, respectively.

Table 4: Core and face material properties of the different sandwich configurations considered in the analytical preliminary approach.

Core Material Properties						Face Material Properties			
Description	ρ_c (kg/m^3)	E_c (MPa)	G_c (MPa)	σ_c (MPa)	τ_c (MPa)	Description	ρ_f (kg/m^3)	E_f (MPa)	σ_f (MPa)
PEI Ultem Diamond Shell-TPMS [51]	222.3	154	59	6.9	2.6	(A) PEI Ultem [53]	1145.7	2121	24.5
						(B) AM Continuous CF [60]	1400.0	60000	420.0
						(C) CFRP PrePreg [55]	119300	1435.6	2282.0

manufactured with Continuous Carbon Fiber [60] or a standard unidirectional Carbon Fiber Reinforced Polymer (CFRP) PrePreg [55], respectively. The total height of the sandwich structure (d = 20.572 mm) and the support span (L = 150 mm) remained constant for all calculations.

As observed, while single-material arrangements simplify the manufacturing process, they significantly limit the potential of cellular core designs in terms of stiffness and strength. On the other hand, the direct production of the faces using the same AM technology and new polymeric materials combined with long fiber has great fabrication potential. However, despite the continuous advancements in this field, the current technology still exhibits certain limitations, particularly in terms of material compatibility and mechanical strength of the printed parts. Consequently, the hybrid combination of a FFF cellular core and CFRP PrePreg skins emerges as the optimal alternative, maximizing the structural capabilities of these highly complex designs for developing advanced sandwich composites.

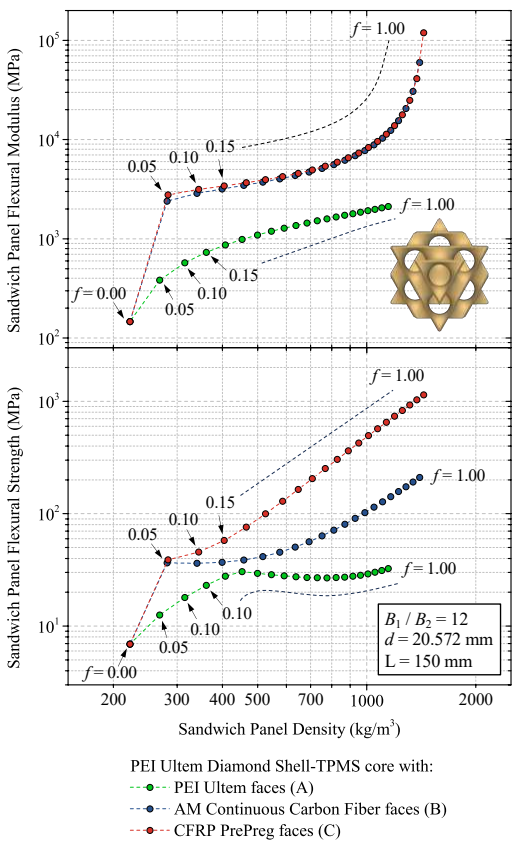

Figure 6: Comparison of the flexural modulus (*top*) and strength (*bottom*) of single-material and hybrid sandwich structures.

3.2. FE model accuracy

The developed FE model was carefully adjusted to ensure accuracy, considering the orthotropic elastic properties of a solid PEI Ultem core processed by FFF with the ±45° infill configuration and CFRP PrePreg skins (see Table 2). A parametric approach was employed to simulate the bending performance of 14 sandwich arrangements, varying the thicknesses of the skins and the core. The numerical results of flexural modulus were compared with the theoretical values calculated using the analytical expression Eq. 2.

Figure 7 depicts the relationship between the numerical and analytical flexural moduli and the density of the different considered sandwich arrangements. The curves demonstrate excellent agreement between each sandwich arrangement's theoretical and simulated bending stiffness values. The corresponding

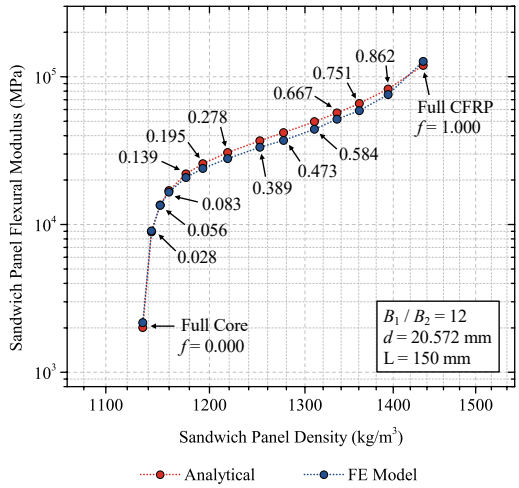

Figure 7: Accuracy of the FE model developed to simulate the flexural modulus of hybrid sandwich panels for different arrangements.

f value is indicated next to each calculated point, ranging from the PEI Ultem full core ($f = 0$) to a full CFRP panel ($f = 1$). Hence, these results validate the computational capability of the developed numerical model to accurately simulate the bending performance of any hybrid sandwich structure investigated in this study, utilizing the RVE homogenized properties of the FFF cellular design as the core material definition.

3.3. Performance of PEI Ultem cellular cores

The trend lines presented in Figure 8 quantify the importance that the unit cell design and density play on the individual flexural elastic modulus of the FFF cellular cores. The represented values have been simulated employing the calibrated FE model, considering skins of zero thickness.

Comparing the two-dimensional patterns (*left*) with the three-dimensional designs (*right*), it is evident that the latter exhibit higher flexural moduli within the same range of relative density. This difference becomes particularly pronounced at very low-density values, where the three-dimensional designs can offer a stiffness of up to three orders of magnitude greater than the two-dimensional patterns. Furthermore, the trends observed for the three-dimensional cellular cores confirm that the Shell-TPMS designs (Gyroid, Diamond, Split-P, and Schwarz) outperform the Skeletal-TPMS ones (Neovius Surface, Schoen Gyroid, and Schwarz Diamond) in terms of flexural modulus.

Regarding the two-dimensional patterns, the trend lines demonstrate that certain designs (Circular and Re-Entrant Hexagon I) surpass the conventional honeycomb (Hexagonal) performance. This again highlights the potential of AM technologies to fabricate more efficient structures with enhanced mechanical properties.

3.4. Hybrid sandwich arrangement analysis

Fig. 9 and Fig. 10 show the correlation between the flexural moduli of hybrid sandwich structures with two- and three-dimensional FFF cellular cores, respectively, and the density of the entire composite panel. Each subfigure displays 72 colored circular points, representing data obtained from the previously calibrated FE model and Eq. 7. These points cover six relative density levels for each cellular core, ranging from 5% to 30%, and twelve hybrid sandwich arrangements. A second-degree polynomial curve has been fitted to each set of six points corresponding to the same sandwich arrangement, whose f value appears indicated. The color gradient reflects the relative density of the cellular core. A black circular symbol also represents a 100% CFRP PrePreg sample (f = 1), serving as a reference.

The variations among the different charts demonstrate the core's significant impact on the mechanical behavior and weight of the sandwich structure. For instance, a hybrid sandwich panel with a total thickness of 20.572 mm was considered, combining a cellular core made of FFF-processed PEI Ultem

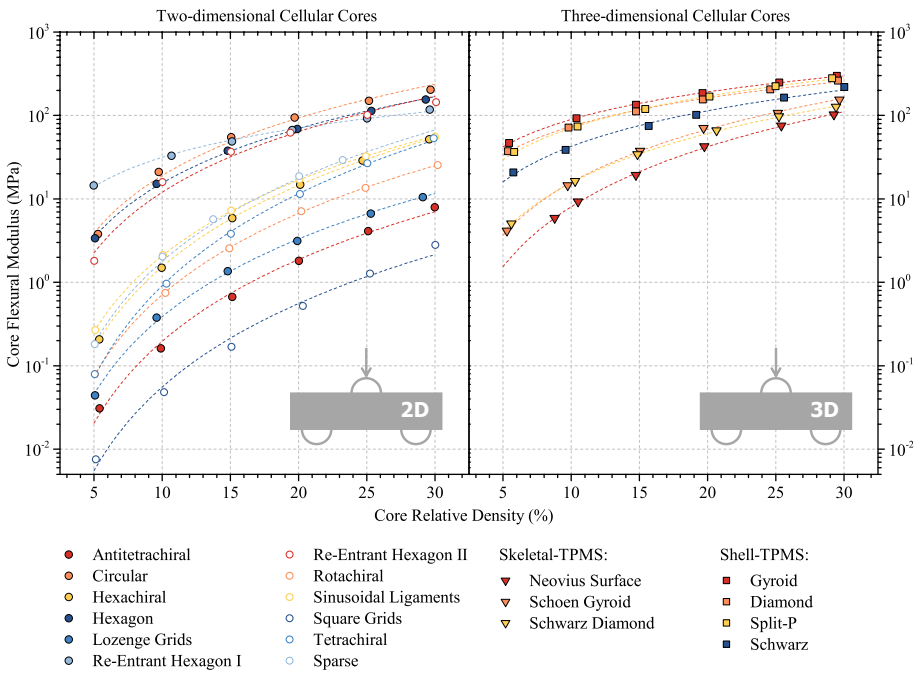

Figure 8: Flexural moduli results of two- (*left*) and three-dimensional (*right*) cellular cores at different values of relative density obtained by FE numerical simulation.

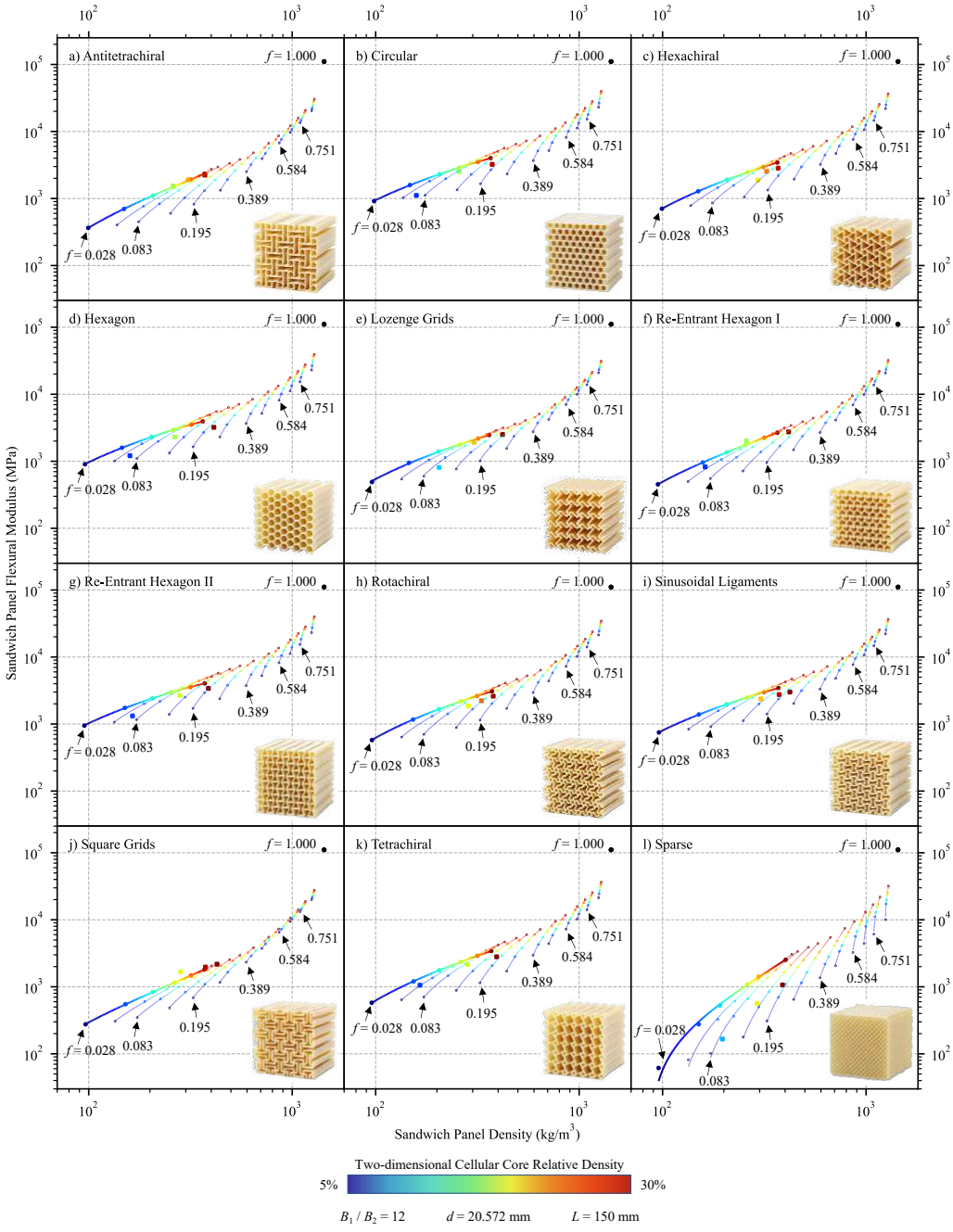

Figure 9: Numerically simulated flexural moduli of hybrid sandwich panels with two-dimensional FFF cellular cores considering multiple sandwich arrangements and core densities.

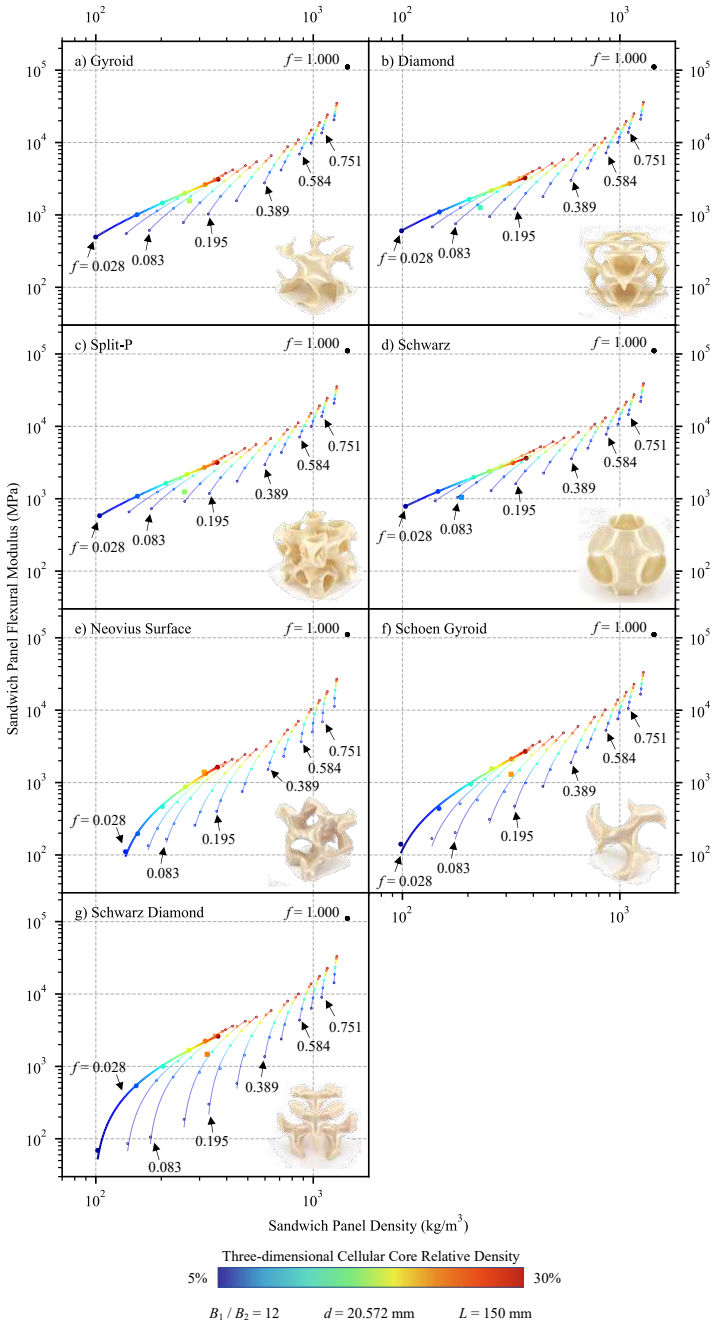

Figure 10: Numerically simulated flexural moduli of hybrid sandwich panels with three-dimensional FFF cellular cores considering multiple sandwich arrangements and core densities.

and PrePreg CFRP skins. The core's design, relative density, and dimensions enable tailoring the flexural modulus and density within the ranges of 61 MPa to 40019 MPa and 95 kg/m^3 to 1289 kg/m^3, respectively, to meet specific application requirements. In particular, utilizing thick cores with thin skins (low f values) allows for achieving a more than one order of magnitude reduction in the density of the composite assembly compared to the 100% full CFRP PrePreg. Moreover, in such cases where the core occupies a significant portion of the sandwich volume, the relative density of the cellular design plays an even more crucial role. Conversely, at high f values, the characteristics of the core material have minimal effect on the overall structure's performance.

When designing hybrid sandwich structures for most structural applications, one common challenge is achieving the lightest and stiffest configuration. Therefore, finding the right balance between mechanical performance and density is crucial. In this regard, cellular designs with shorter vertical widths in their charts demonstrate more significant structural potential. Specifically, the two-dimensional Circular, Hexachiral, Hexagon, Re-Entrant Hexagon II, and Sinusoidal Ligaments patterns, as well as the three-dimensional Shell-TPMS designs, appear to be the most efficient in terms of flexural stiffness and weight. Furthermore, the porosity of the Shell-TPMS cellular geometries is continuous, unlike the extruded-like two-dimensional shapes. This fact offers added value for applications that require a fluid flow through the cells or to avoid moisture accumulation in specific areas of the sandwich panel. On the other hand, Skeletal-TPMS and some two-dimensional designs compromise the stiffness of the sandwich panel to a greater extent when very low-density patterns are employed, thus limiting the feasibility of fabricating functional, lightweight components. However, the sandwich arrangement composed of CFRP PrePreg skins with a single-ply thickness of 0.286 mm (f = 0.028) consistently proves to be the optimal simulated curve in all cases, and therefore, it will be implemented for the experimental validation tests.

3.5. *Experimental validation*

Figure 11 compares the experimental-specific modulus and flexural strength values for the fabricated hybrid sandwich structures and the required time for manufacturing each FFF cellular core. Specific properties were calculated as the ratio of the flexural modulus or strength of the composite panel over the total weight of each tested specimen, respectively. Core manufacturing time data was estimated directly using the Insight software, the official slicer of the professional FFF equipment employed in this investigation.

As can be seen, both the cellular design and the core's density significantly influence the sandwich panel's mechanical performance and the printing process, as expected. In particular, the fabrication of the majority of two-dimensional designs, such as Hexachiral, Hexagon, Re-Entrant Hexagon II, Rotachiral, and Sinusoidal Ligaments, requires up to an order of magnitude more time compared to other cellular geometries, without significant advantages in terms of flexural modulus and strength. This occurs because the morphology of these patterns makes

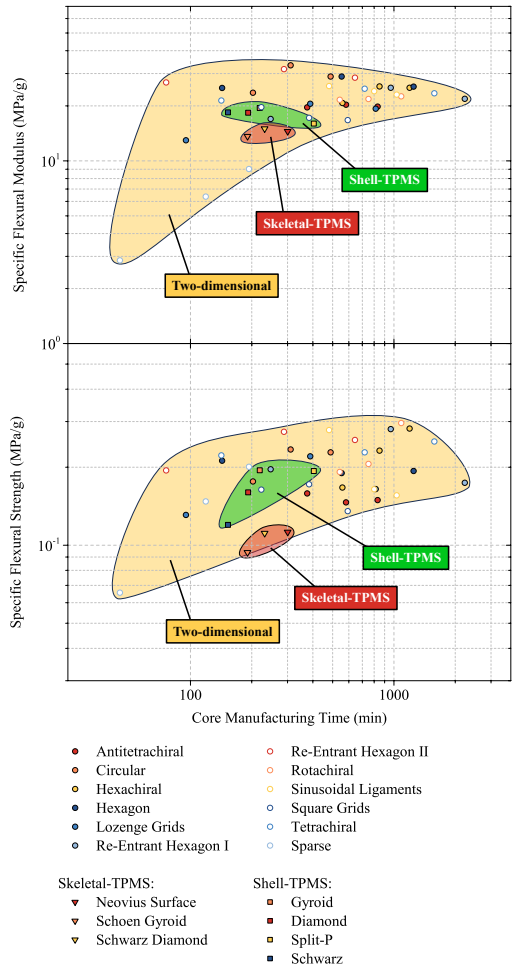

Figure 11: Analysis of the specific flexural modulus (*top*) and strength (*bottom*) of the hybrid sandwich structured versus the core manufacturing time considering each tested cellular design and density.

it challenging to implement continuous deposition paths during FFF manufacturing, resulting in considerable time losses due to extrusion head movements without material extrusion. On the other hand, the surface continuity of the Shell-TPMS and Skeletal-TPMS designs facilitates their construction without such interruptions. As a result, these three-dimensional patterns exhibit appealing specific mechanical properties while significantly reducing manufacturing time.

Table 5 summarizes the experimental results of flexural modulus and strength for the hybrid sandwich structures, considering every cellular design and core relative density examined in this study. For each case, the average value and standard de-

viation are presented. In addition, the experimental results of flexural modulus have been overlapped with the numerical values presented in Fig. 9 and Fig. 10 employing square symbols. The good agreement between both the experimental and the FE model results verifies the effectiveness of the developed simulation tool to evaluate the flexural behavior of hybrid sandwich structures prior to manufacturing with acceptable accuracy.

Additionally, the failure modes of the tested samples are identified using the character code presented in Table 3. All evaluated specimens failed at the load bar, specifically in the central zone of the composite panel, indicating the quality of the sandwich specimen fabrication and the proper execution of the 3-Point bending tests. The main failure types observed in samples with FFF cellular cores were delamination (both within the core or at the core-facing bond) and the breakage of the top skin due to a micro buckling effect. Only the two-dimensional Sparse design exhibited transverse shear failure in the core. Comparatively, the reference core materials (Nomex® and aluminum honeycombs) demonstrated core crushing effects, which were not observed either in AM core designs or in PU250 foam samples, which consistently exhibited brittle failures.

3.6. Comparative performance

Experimental results have been represented in Fig. 12 to compare the structural performance of the hybrid sandwich structures with FFF two- and three-dimensional cellular cores and CFRP PrePreg skins in terms of flexural modulus, flexural strength, and density. Additionally, results from sandwich composites with reference core materials (Nomex® and aluminum honeycombs and PU250 foam) are included in a grey-shaded area, along with the mechanical properties of PEI Ultem and other materials from the Ansys GRANTA EduPack database for comparison. It is worth noting that the flexural mechanical

Table 5: Flexural modulus, strength and failure mode of the hybrid sandwich structures with different FFF cellular core designs obtained from the 3-Point bending experimental tests. Mechanical properties of samples with reference core materials are included for comparison.

Cellular Core Design (see Fig. 2)	**Core Rel. Density** (%)	$\tilde{E}_{flex}$ (MPa)	$\tilde{\sigma}_{flex}$ (MPa)	**Failure Code**	**Cellular Core Design** (see Fig. 2)	**Core Rel. Density** (%)	$\tilde{E}_{flex}$ (MPa)	$\tilde{\sigma}_{flex}$ (MPa)	**Failure Code**
Antitetrachiral	28.75	2235 ± 6	16.9 ± 3.1	DAC	Circular	28.73	3233 ± 140	25.5 ± 0.4	FAT
	22.99	1894 ± 10	13.7 ± 2.6	DAC		18.10	2526 ± 0	17.8 ± 1.1	FAT
	18.39	1541 ± 11	12.5 ± 1.8	DAC		9.14	1112 ± 67	8.3 ± 0.2	FAT
Hexachiral	28.50	2841 ± 145	31.9 ± 0.5	FAT	Hexagon	32.42	3207 ± 79	24.3 ± 7.2	DAC
	24.45	2540 ± 117	23.1 ± 0.5	FAT		18.94	2308 ± 58	15.1 ± 2.7	DAC
	21.71	1875 ± 140	15.1 ± 3.0	FAT		9.37	1211 ± 5	10.3 ± 0.6	DAC
Lozenge Grids	33.16	2511 ± 251	21.5 ± 4.4	FAT	Re-Entrant Hexagon I	32.74	2748 ± 45	21.9 ± 1.2	DAA
	22.56	1922 ± 191	20.6 ± 5.4	FAT		18.39	2013 ± 21	22.5 ± 0.4	DAC
	13.49	808 ± 17	8.2 ± 3.1	DAC		9.46	825 ± 7	9.6 ± 1.0	DAC
Re-Entrant Hexagon II	30.14	3407 ± 126	30.4 ± 22.9	FAT	Rotachiral	29.31	2610 ± 155	34.3 ± 0.1	FAT
	20.29	2682 ± 79	23.2 ± 5.1	FAT		25.05	2225 ± 134	21.0 ± 13.7	DAC
	9.64	1323 ± 14	9.6 ± 0.3	DAA		20.79	1862 ± 98	16.5 ± 8.4	DAC
Sinusoidal Ligaments	33.35	3003 ± 421	20.4 ± 9.3	FAT	Square Grids	33.90	2177 ± 10	17.7 ± 0.3	DAA
	28.84	2755 ± 73	18.9 ± 1.8	FAT		28.92	1969 ± 79	19.7 ± 0.2	FAT
	22.56	2380 ± 168	25.8 ± 13.2	DAC		20.56	1679 ± 82	14.0 ± 0.0	DAC
Tetrachiral	30.56	2804 ± 89	30.1 ± 2.9	FAT	Sparse	30.19	1066 ± 12	23.8 ± 0.1	FAT
	20.51	2148 ± 71	19.8 ± 2.1	FAT		21.26	563 ± 11	13.0 ± 0.8	SAC
	9.68	1057 ± 12	11.0 ± 1.1	FAT		12.54	166 ± 2	3.8 ± 1.1	SAC
Gyroid	15.56	1266 ± 5	11.1 ± 0.6	FAT	Diamond	19.30	1564 ± 15	15.6 ± 0.3	FAT
Split-P	18.05	1242 ± 4	15.0 ± 1.1	FAT	Schwarz	11.84	1045 ± 6	6.8 ± 0.2	DAA
Neovius Surface	23.52	1389 ± 14	10.8 ± 0.3	FAT	Schoen Gyroid	23.64	1302 ± 18	9.0 ± 2.2	DAA
Schwarz Diamond	24.39	1468 ± 7	10.9 ± 3.6						
PU250 Foam	20.55	1475 ± 171	14.9 ± 0.8	FAT	Nomex® honeycomb	4.40	5320 ± 17	24.8 ± 1.6	CAC
Aluminum honeycomb	6.46	13097 ± 132	40.5 ± 2.3	CAC					
	2.19	5549 ± 3	9.4 ± 0.8	CAC					

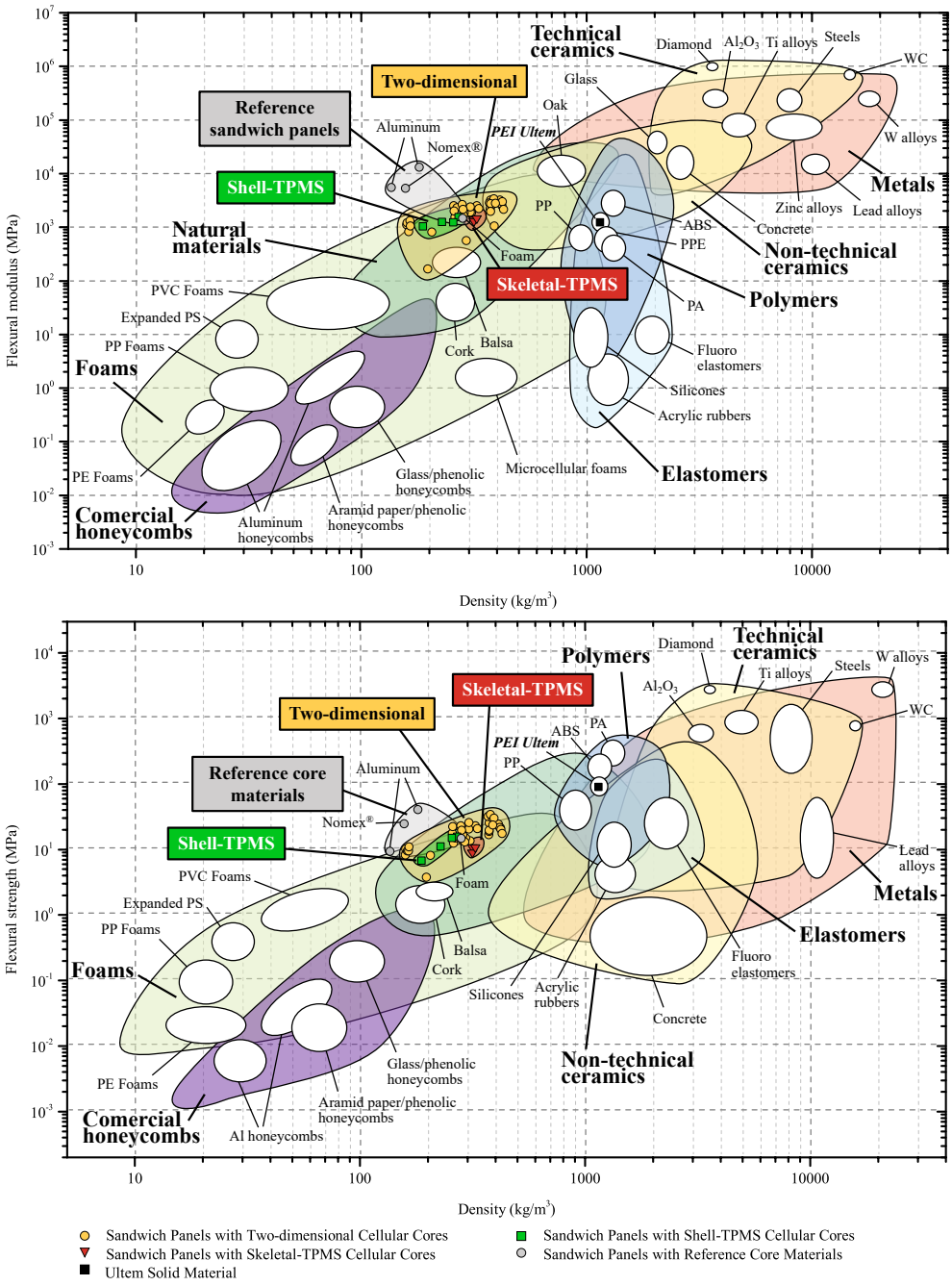

Figure 12: Comparison of the experimental performance of hybrid sandwich panels composed of two- and three-dimensional FFF cellular cores with materials database adapted from CES EduPack 2019, ANSYS Granta© 2020 Granta Design, with permission.

behavior of the tested sandwich panels closely approaches the upper limit of the range occupied by foams and natural materials.

Analyzing the *top* chart, it can be seen that the design and relative density of the cellular core significantly influence the mechanical properties and density of the hybrid structure, as intended to demonstrate. Specifically, the depicted trends confirm that a lower core density reduces the bending stiffness of the sandwich panel, as less material is utilized. Many sandwich structures with two-dimensional cellular designs and all Shell-TPMS configurations exhibit a higher flexural modulus than the PU250 foam core combination at the same density, which behaves similarly to the Skeletal-TPMS arrangements. However, the two reference honeycomb materials demonstrate greater efficiency in terms of flexural modulus, thanks to their extremely thin vertical walls[6]. The ability to achieve such thin thicknesses during their manufacturing process enables an extremely low core weight while maintaining the necessary shear stiffness, positioning them favorably in the presented property charts.

The *bottom* chart in Fig. 12 allows the comparison of the different materials in terms of flexural strength and density. Overall, the depicted trends are similar to the previous case. However, the differences in flexural strength between the reference honeycomb cores and the cellular designs manufactured by FFF are relatively minor. As extensively reported in previous investigations [53, 50, 51], it should be noted the importance of printing defects on the maximum load that components fabricated by this AM technology can withstand. Therefore, further improvements in this field to enhance the quality of fabricated parts, along with the implementation of optimized deposition trajectories for each cellular design with a thinner raster width, could have a positive effect on obtaining stiffer and stronger hybrid sandwich panels, thereby contributing to the development of more efficient lightweight composite structures.

4. Conclusions

This work presents a comprehensive research study on the mechanical performance of hybrid sandwich structures, combining CFRP skins with additively manufactured cellular cores. The study encompasses a diverse range of two- and three-dimensional patterns with different cell designs and densities. The paper provides numerical simulations and experimental findings to analyze and compare the flexural modulus and strength of different cellular designs and sandwich arrangements. The research also addresses important manufacturing aspects, such as core printing time.

The analysis of core-to-skin debonding confirms proper adhesion between the faces and the additively manufactured cellular core, as evident from the observed failure types in all tests. Forthcoming advancements in FFF technology hold the potential for further progress, enabling the complete fabrication of hybrid sandwich structures. These structures could incorporate multiple polymeric materials, including short or continuous fibers and metallic materials. Such advancements would significantly reduce fabrication time and costs associated with these structures.

From a manufacturing perspective, Shell-TPMS and Skeletal-TPMS three-dimensional designs are highly advantageous. These designs can be fabricated using continuous deposition paths, eliminating imperfections in the joints between unit cells. Moreover, their geometrical complexity eliminates the need for support structures. However, it should be noted that in this work, the minimum wall thickness required for Shell-TPMS cellular cores was 1.016 mm, whereas two-dimensional patterns could be achieved with a single contour of 0.508 mm. Consequently, two-dimensional patterns offer superior weight reduction for the same cell size compared to three-dimensional designs.

Hybrid sandwich structures with PEI Ultem cellular cores demonstrate stiffness and strength comparable to reference materials, outperforming foam cores while slightly trailing behind Nomex® and aluminum honeycombs. The analysis of various two- and three-dimensional cellular cores reveals the presence of more efficient morphologies than the traditional hexagonal design, which can only be fabricated thanks to AM technologies. The manufacturing of cells with thinner walls, as observed in reference honeycomb materials, has the potential to significantly reduce panel weight without compromising mechanical properties. This advancement could contribute to the development of more highly efficient sandwich structures.

Acknowledgements

This work has been supported by the grant RTI2018-099754-A-I00 funded by MCIN/AEI/10.13039/501100011033 and by ERDF A way of making Europe, and the grant PID2021-123876OB-I00 funded by MCIN/AEI/10.13039/501100011033 and by the European Union.

Data availability

The raw data required to reproduce these findings are available to download from Mendeley Data. Kindly cite this article and the dataset if utilizing or modifying the data in your work.

References

[1] H. G. Allen, Analysis and Design of Structural Sandwich Panels, Pergamon Press, 1969. doi:10.1016/C2013-0-02134-2.

[2] A. Kausar, I. Ahmad, S. A. Rakha, M. H. Eisa, A. Diallo, State-Of-The-Art of Sandwich Composite Structures: Manufacturing—to—High Performance Applications, J. Compos. Sci. 7 (2023) 102. doi:10.3390/jcs7030102.

[3] A. B. H. Kueh, S. H. Abo Sabah, D. N. Qader, S. H. Drahman, M. Amran, Single and repetitive low-velocity impact responses of sandwich composite structures with different skin and core considerations: A review, Case Stud. Constr. Mater. 18 (2023) e01908. doi:10.1016/j.cscm.2023.e01908.

[6] The Nomex® and aluminum tested honeycombs had a wall thickness of 0.10 mm and 0.15 mm, respectively.

[4] D. Zenkert, An intrroduction to sandwich structures, Chameleon Press Ltd., 1995.

[5] D. Zhang, G. Lu, D. Ruan, Q. Fei, W. Duan, Quasi-static combined compression-shear crushing of honeycombs: An experimental study, Mater. Design 167 (2019) 107632. doi:10.1016/j.matdes.2019.107632.

[6] L. J. Gibson, M. F. Ashby, Cellular solids - Structure and properties, 2n edition ed., Cambridge University Press, 1997. doi:10.1017/CBO9781139878326.

[7] M. M. Barak, M. A. Black, A novel use of 3D printing model demonstrates the effects of deteriorated trabecular bone structure on bone stiffness and strength, J Mech Behav Biomed Mater 78 (2018) 455–464. doi:10.1016/j.jmbbm.2017.12.010.

[8] T. N. Sullivan, B. Wang, H. D. Espinosa, M. A. Meyers, Extreme lightweight structures: avian feathers and bones, Mater. Today 20 (2017) 377–391. doi:10.1016/j.mattod.2017.02.004.

[9] F. Matalkah, H. Bharadwaj, P. Soroushian, W. Wu, A. Almalkawi, A. M. Balachandra, A. Peyvandi, Development of sandwich composites for building construction with locally available materials, Constr Build Mater. 147 (2017) 380–387. doi:10.1016/j.conbuildmat.2017.04.113.

[10] Z. Zhang, Z. Zhang, N. Liu, X. Xia, Z. Wang, J. Wang, L. Cui, Z. Qiu, J. Ding, Y. Wang, Y. Liu, Three-point bending performances of integral-forming aluminum foam sandwich, Mater. Design 229 (2023) 111889. doi:10.1016/j.matdes.2023.111889.

[11] E. Tang, H. Yin, C. Chen, Y. Han, M. Feng, Simulation of CFRP/aluminum foam sandwich structure under high velocity impact, J. Mater. Res. Technol. 9 (2020) 7273–7287. doi:10.1016/j.jmrt.2020.04.093.

[12] A. C. Balaban, M. E. Toygar, Investigation into Mechanical Properties and Failure Mechanisms of Novel Sandwich Composite Material with Carbon Fibre / Epoxy Facesheets and PVC Foam Core, Procedia Structural Integrity 42 (2022) 284–291. doi:10.1016/j.prostr.2022.12.035.

[13] X. Y. Miao, R. Lu, X. Chen, Fracture behaviour of foam core sandwich structures with manufacturing defects using phase-field modelling, Compos. Struct. 274 (2021) 114294. doi:10.1016/j.compstruct.2021.114294.

[14] M. Giglio, A. Gilioli, A. Manes, A numerical investigation on significant parameters influencing the flatwise compressive behaviour of a nomex™ honeycomb, Procedia Eng. 10 (2011) 3441–3446. doi:10.1016/j.proeng.2011.04.567.

[15] G. Sun, X. Huo, D. Chen, Q. Li, Experimental and numerical study on honeycomb sandwich panels under bending and in-panel compression, Mater. Design 133 (2017) 154–168. doi:10.1016/j.matdes.2017.07.057.

[16] L. L. Hu, T. X. Yu, Mechanical behavior of hexagonal honeycombs under low-velocity impact - Theory and simulations, Int J Solids Struct 50 (2013) 3152–3165. doi:10.1016/j.ijsolstr.2013.05.017.

[17] X. Li, F. Lu, Y. Zhang, Y. Lin, Y. Meng, Experimental study on out-of-plane mechanical and energy absorption properties of combined hexagonal aluminum honeycombs under dynamic impact, Mater. Design 194 (2020) 108900. doi:10.1016/j.matdes.2020.108900.

[18] Y. Duan, Z. Cui, X. Xie, Y. Tie, T. Zou, T. Wang, Mechanical characteristics of composite honeycomb sandwich structures under oblique impact, Theoretical and Applied Mechanics Letters 12 (2022) 100379. doi:10.1016/j.taml.2022.100379.

[19] D. Hara, G. O. Özgen, Investigation of Weight Reduction of Automotive Body Structures with the Use of Sandwich Materials, Transp. Res. Proc. 14 (2016) 1013–1020. doi:10.1016/j.trpro.2016.05.081.

[20] N. Baral, D. D. Cartié, I. K. Partridge, C. Baley, P. Davies, Improved impact performance of marine sandwich panels using through-thickness reinforcement: Experimental results, Compos. Part B. Eng. 41 (2010) 117–123. doi:10.1016/j.compositesb.2009.12.002.

[21] X. Fan, Q. Tang, Q. Feng, S. Ma, J. Song, M. Jin, F. Guo, P. Jin, Design, mechanical properties and energy absorption capability of graded-thickness triply periodic minimal surface structures fabricated by selective laser melting, Int. J. Mech. Sci. 204 (2021) 106586. doi:10.1016/j.ijmecsci.2021.106586.

[22] M. Dallago, B. Winiarski, F. Zanini, S. Carmignato, M. Benedetti, On the effect of geometrical imperfections and defects on the fatigue strength of cellular lattice structures additively manufactured via Selective Laser Melting, Int. J. Fatigue 124 (2019) 348–360. doi:10.1016/j.ijfatigue.2019.03.019.

[23] L. L. Hu, M. Z. Zhou, H. Deng, Dynamic crushing response of auxetic honeycombs under large deformation: Theoretical analysis and numerical simulation, Thin-Walled Struct. 131 (2018) 373–384. doi:10.1016/j.tws.2018.04.020.

[24] Z. Sun, Y. Guo, V. P. Shim, Deformation and energy absorption characteristics of additively-manufactured polymeric lattice structures — Effects of cell topology and material anisotropy, Thin-Walled Struct. 169 (2021). doi:10.1016/j.tws.2021.108420.

[25] H. Xia, Q. Sun, S. Wang, Influence of strain rate effect on energy absorption characteristics of bio-inspired honeycomb column thin-walled structure under impact loading, Case Stud. Constr. Mater. 18 (2023) e01761. doi:10.1016/j.cscm.2022.e01761.

[26] N. Novak, M. Borovinšek, O. Al-Ketan, Z. Ren, M. Vesenjak, Impact and blast resistance of uniform and graded sandwich panels with TPMS cellular structures, Compos. Struct. 300 (2022). doi:10.1016/j.compstruct.2022.116174.

[27] R. S. Ambekar, E. F. Oliveira, B. Kushwaha, V. Pal, P. M. Ajayan, A. K. Roy, D. S. Galvao, C. S. Tiwary, Flexure resistant 3D printed zeolite-inspired structures, Addit. Manuf. 47 (2021) 102297. doi:10.1016/j.addma.2021.102297.

[28] C. J. Ejeh, I. Barsoum, R. K. Abu Al-Rub, Flexural properties of functionally graded additively manufactured AlSi10Mg TPMS latticed-beams, Int. J. Mech. Sci. 223 (2022) 107293. doi:10.1016/j.ijmecsci.2022.107293.

[29] A. I. Indreș, D. M. Constantinescu, O. A. Mocian, Bending behavior of 3D printed sandwich beams with different core topologies, Mat. Design Process. Comm. 3 (2021) 1–8. doi:10.1002/mdp2.252.

[30] C. Peng, K. Fox, M. Qian, H. Nguyen-Xuan, P. Tran, 3D printed sandwich beams with bioinspired cores: Mechanical performance and modelling, Thin-Walled Struct. 161 (2021) 107471. doi:10.1016/j.tws.2021.107471.

[31] M. Spahic, N. Di Cesare, A. Le Duigou, V. Keryvin, Multi-scale analysis of the flexural behaviour of 3D printed cellular polymer materials: Comparison between morphing and sandwich beams, Compos. Struct. 273 (2021) 114249. doi:10.1016/j.compstruct.2021.114249.

[32] S. A. Ghannadpour, M. Mahmoudi, K. Hossein Nedjad, Structural behavior of 3D-printed sandwich beams with strut-based lattice core: Experimental and numerical study, Compos. Struct. 281 (2022) 115113. doi:10.1016/j.compstruct.2021.115113.

[33] M. H. Zamani, M. Heidari-Rarani, K. Torabi, Optimal design of a novel graded auxetic honeycomb core for sandwich beams under bending using digital image correlation (DIC), Compos. Struct. 286 (2022) 115310. doi:10.1016/j.compstruct.2022.115310.

[34] A. Y. Kanani, A. Kennedy, Experimental and numerical analysis of additively manufactured foamed sandwich beams, Compos. Struct. 312 (2023) 116866. doi:10.1016/j.compstruct.2023.116866.

[35] K. Zhang, T. Zeng, G. Xu, S. Cheng, S. Yu, Mechanical properties of SiCp/SiC composite lattice core sandwich panels fabricated by 3D printing combined with precursor impregnation and pyrolysis, Compos. Struct. 240 (2020) 112060. doi:10.1016/j.compstruct.2020.112060.

[36] P. Paczos, R. Wichniarek, K. Magnucki, Three-point bending of sandwich beam with special structure of the core, Compos. Struct. 201 (2018) 676–682. doi:10.1016/j.compstruct.2018.06.077.

[37] K. Essassi, J. luc Rebiere, A. El Mahi, M. A. Ben Souf, A. Bouguecha, M. Haddar, Experimental and analytical investigation of the bending behaviour of 3D-printed bio-based sandwich structures composites with auxetic core under cyclic fatigue tests, Compos. Part A Appl. Sci. Manuf. 131 (2020) 105775. doi:10.1016/j.compositesa.2020.105775.

[38] L. Meng, X. Qiu, T. Gao, Z. Li, W. Zhang, An inverse approach to the accurate modelling of 3D-printed sandwich panels with lattice core using beams of variable cross-section, Compos. Struct. 247 (2020) 112363. URL: https://doi.org/10.1016/j.compstruct.2020.112363. doi:10.1016/j.compstruct.2020.112363.

[39] S. Brischetto, R. Torre, Honeycomb Sandwich Specimens Made of PLA and Produced Via 3D FDM Printing Process: An Experimental Study, J. Aircr. Spacecr. Technol 4 (2020) 54–69. doi:10.3844/jastsp.2020.54.69.

[40] K. Essassi, J. L. Rebiere, A. El Mahi, M. A. B. Souf, A. Bouguecha, M. Haddar, Investigation of the Static Behavior and Failure Mechanisms of a 3D Printed Bio-Based Sandwich with Auxetic Core, Int. J. Appl. Mech. 12 (2020) 2050051. doi:10.1142/S1758825120500519.

[41] F. A. Santos, H. Rebelo, M. Coutinho, L. S. Sutherland, C. Cismasiu, I. Farina, F. Fraternali, Low velocity impact response of 3D printed structures formed by cellular metamaterials and stiffening plates: PLA vs. PETg, Compos. Struct. 256 (2021) 113128. doi:10.1016/j.compstruct.2020.113128.

[42] S. Sun, D. Liu, Y. Sheng, S. Feng, H. Zhu, T. Jian Lu, Out-of-plane compression of a novel hybrid corrugated core sandwich panel, Compos. Struct. 272 (2021) 114222. doi:10.1016/j.compstruct.2021.114222.

[43] H. Yazdani Sarvestani, A. H. Akbarzadeh, H. Niknam, K. Hermenean, 3D printed architected polymeric sandwich panels: Energy absorption and structural performance, Compos. Struct. 200 (2018) 886–909. doi:10.1016/j.compstruct.2018.04.002.

[44] D. Bonthu, H. S. Bharath, S. Gururaja, P. Prabhakar, M. Doddamani, 3D printing of syntactic foam cored sandwich composite, Compos. Part C. 3 (2020) 100068. doi:10.1016/j.jcomc.2020.100068.

[45] H. S. Bharath, D. Bonthu, S. Gururaja, P. Prabhakar, M. Doddamani, Flexural response of 3D printed sandwich composite, Compos. Struct. 263 (2021) 113732. doi:10.1016/j.compstruct.2021.113732.

[46] S. Brischetto, C. G. Ferro, R. Torre, P. Maggiore, 3D FDM production and mechanical behavior of polymeric sandwich specimens embedding classical and honeycomb cores, Curved Layer. Struct. 5 (2018) 80–94. doi:10.1515/cls-2018-0007.

[47] V. Acanfora, S. Saputo, A. Russo, A. Riccio, A feasibility study on additive manufactured hybrid metal/composite shock absorbers, Compos. Struct. 268 (2021) 113958. doi:10.1016/j.compstruct.2021.113958.

[48] D. Harland, A. W. Alshaer, H. Brooks, An experimental and numerical investigation of a novel 3D printed sandwich material for motorsport applications, Procedia Manuf. 36 (2019) 11–18. doi:10.1016/j.promfg.2019.08.003.

[49] T. Li, L. Wang, Bending behavior of sandwich composite structures with tunable 3D-printed core materials, Compos. Struct. 175 (2017) 46–57. doi:10.1016/j.compstruct.2017.05.001.

[50] A. Forés-Garriga, G. Gómez-Gras, M. A. Pérez, Mechanical performance of additively manufactured lightweight cellular solids: influence of cell pattern and relative density on the printing time and compression behavior, Mater. Design 215 (2022) 110474. doi:10.1016/j.matdes.2022.110474.

[51] A. Forés-Garriga, G. Gómez-Gras, M. A. Pérez, Additively manufactured three-dimensional lightweight cellular solids: Experimental and numerical analysis, Mater. Design 226 (2023). doi:10.1016/j.matdes.2023.111641.

[52] A. Forés-Garriga, H. García de la Torre, R. Lado-Roigé, G. Gómez-Gras, M. A. Pérez, Triply Periodic Minimal Surfaces Generator - TPMSgen, 2023. URL: https://github.com/albertforesg/TPMSgen. doi:10.1016/j.matdes.2023.111641.

[53] A. Forés-Garriga, M. A. Pérez, G. Gómez-Gras, G. Reyes-Pozo, Role of infill parameters on the mechanical performance and weight reduction of PEI Ultem processed by FFF, Mater. Design 193 (2020) 108810. doi:10.1016/j.matdes.2020.108810.

[54] Stratasys, ULTEM™ 9085 Resin - FDM® Thermoplastic Filament Fit for High-Performance Applications, Technical Report, 2021. URL: https://www.stratasys.com/en/materials/materials-catalog/fdm-materials/ultem-9085/.

[55] Castro Composites, MTC510 Unidirectional Epoxy Component Prepreg Mechanical Data, Technical Report, 2018. URL: https://www.castrocompositesshop.com.

[56] Castro Composites, MTC510 Unidirectional Epoxy Component Prepreg Technical Data Sheet, Technical Report, 2013. URL: https://www.castrocompositesshop.com.

[57] Castro Composites, MTFA500 (DF044) Adhesive Film, Technical Report, 2014.

[58] ASTM Standard C393/C393M-20, Standard Test Method for Core Shear Properties of Sandwich Constructions by Beam Flexure, ASTM International, West Conshohocken, PA (2006). URL: www.astm.org. doi:10.1520/C0393_C0393M-20.

[59] M. F. Ashby, Materials Selection in Mechanical Design, Elsevier Ltd., 2011. doi:10.1016/C2009-0-25539-5.

[60] Markforged, Composites - Material datasheet, Technical Report, 2022. URL: https://markforged.com/materials/continuous-fibers/continuous-carbon-fiber.

References

1. Forés-Garriga, A., García de la Torre, H., Lado-Roigé, R., Gómez-Gras, G. & Pérez, M. A. *Triply Periodic Minimal Surfaces Generator - TPMSgen* 2023. doi:10.1016/j.matdes.2023.111641. https://github.com/albertforesg/TPMSgen.
2. International Energy Agency. *Global energy-related CO2 emissions by sector* tech. rep. (International Energy Agency, Paris, 2022). https://www.iea.org/data-and-statistics/charts/global-energy-related-co2-emissions-by-sector.
3. Ashby, M. F. *Materials Selection in Mechanical Design* doi:10.1016/C2009-0-25539-5 (Elsevier Ltd., 2011).
4. Zenkert, D. *An intrroduction to sandwich structures* (ed Engineering Advisory Services Ltd) 454 (Chameleon Press Ltd., 1995).
5. Matalkah, F. *et al.* Development of sandwich composites for building construction with locally available materials. *Constr Build Mater.* **147,** 380–387. doi:10.1016/j.conbuildmat.2017.04.113 (2017).
6. Hara, D. & Özgen, G. O. Investigation of Weight Reduction of Automotive Body Structures with the Use of Sandwich Materials. *Transp. Res. Proc.* **14,** 1013–1020. doi:10.1016/j.trpro.2016.05.081 (2016).
7. Baral, N., Cartié, D. D., Partridge, I. K., Baley, C. & Davies, P. Improved impact performance of marine sandwich panels using through-thickness reinforcement: Experimental results. *Compos. Part B. Eng.* **41,** 117–123. doi:10.1016/j.compositesb.2009.12.002 (2010).
8. Barak, M. M. & Black, M. A. A novel use of 3D printing model demonstrates the effects of deteriorated trabecular bone structure on bone stiffness and strength. *J Mech Behav Biomed Mater* **78,** 455–464. doi:10.1016/j.jmbbm.2017.12.010 (2018).
9. Sullivan, T. N., Wang, B., Espinosa, H. D. & Meyers, M. A. Extreme lightweight structures: avian feathers and bones. *Mater. Today* **20,** 377–391. doi:10.1016/j.mattod.2017.02.004 (2017).
10. Chuaponpat, N. & Areerat, S. The Effects of Foaming Conditions on Plasticized Polyvinyl Chloride Foam Morphology by using Supercritical Carbon Dioxide. *Mater. Today: Proc.* **5,** 23526–23533. doi:10.1016/j.matpr.2018.10.140 (2018).
11. Papantoniou, I. G., Pantelis, D. I. & Manolakos, D. E. Powder metallurgy route aluminium foams: A study of the effect of powder morphology, compaction pressure and foaming temperature on the porous structure. *Procedia Struct. Integr.* **10,** 243–248. doi:10.1016/j.prostr.2018.09.034 (2018).
12. Mahadev, Sreenivasa, C. G. & Shivakumar, K. M. A Review on Prodution of Aluminium Metal Foams. *IOP Conf. Ser. Mater. Sci. Eng.* **376.** doi:10.1088/1757-899X/376/1/012081 (2018).

13. Redmann, A., Montoya-Ospina, M. C., Karl, R., Rudolph, N. & Osswald, T. A. High-force dynamic mechanical analysis of composite sandwich panels for aerospace structures. *Compos. Part C.* **5.** doi:10.1016/j.jcomc.2021.100136 (2021).
14. Fan, X. *et al.* Design, mechanical properties and energy absorption capability of graded-thickness triply periodic minimal surface structures fabricated by selective laser melting. *Int. J. Mech. Sci.* **204,** 106586. doi:10.1016/j.ijmecsci.2021.106586 (2021).
15. Dallago, M., Winiarski, B., Zanini, F., Carmignato, S. & Benedetti, M. On the effect of geometrical imperfections and defects on the fatigue strength of cellular lattice structures additively manufactured via Selective Laser Melting. *Int. J. Fatigue* **124,** 348–360. doi:10.1016/j.ijfatigue.2019.03.019 (2019).
16. Benedetti, M *et al.* Materials Science & Engineering R Architected cellular materials : A review on their mechanical properties towards fatigue-tolerant design and fabrication. *Mater. Sci. Eng. R* **144,** 100606. doi:10.1016/j.mser.2021.100606 (2021).
17. Choudhry, N. K., Panda, B. & Kumar, S. Enhanced energy absorption performance of 3D printed 2D auxetic lattices. *Thin-Walled Struct.* **186,** 110650. doi:10.1016/j.tws.2023.110650 (2023).
18. Schoen, A. H. *Infinite Periodic Minimal Surfaces Without Self-Intersections* tech. rep. (NASA, Washington, D.C., 1970). https://ntrs.nasa.gov/citations/19700020472.
19. Pelanconi, M. & Ortona, A. Gyroid Cores Produced by Additive Manufacturing and Reinforced by Unidirectional Carbon Fiber Ribs. *Materials* **12,** 1–14. doi:10.3390/ma12244134 (2019).
20. Dixit, T., Al-hajri, E., Paul, M. C., Nithiarasu, P. & Kumar, S. High performance , microarchitected , compact heat exchanger enabled by 3D printing. *Appl. Therm. Eng.* **210,** 118339. doi:10.1016/j.applthermaleng.2022.118339 (2022).
21. Li, L. *et al.* Gyroid Nanoporous Membranes with Tunable Permeability. *ACS Nano,* 7754–7766. doi:10.1021/nn200610r (2011).
22. Hull, D. & Clyne, T. *An introduction to composite materials* doi:https://doi.org/10.1017/CBO9781139170130 (Cambridge University Press, 1996).
23. Budiansky, B. & Flexk, N. Compressive Failure of Fibre Composites. *J. Mech. Phys. Solids* **41,** 183–211. doi:10.1016/0022-5096(93)90068-Q (1993).
24. Clyne, T. & Withers, P. *An introduction to metal matrix composites* doi:https://doi.org/10.1017/CBO9780511623080 (Cambridge University Press, 1993).
25. Allen, H. G. *Analysis and Design of Structural Sandwich Panels* doi:10.1016/C2013-0-02134-2 (Pergamon Press, 1969).
26. Murugan, S. & Friswell, M. I. Morphing wing flexible skins with curvilinear fiber composites. *Compos. Struct.* **99,** 69–75. doi:10.1016/j.compstruct.2012.11.026 (2013).
27. Mohamed, Y. S. & Abdelbary, A. Theoretical and experimental study on the influence of fiber orientation on the tensile properties of unidirectional carbon fiber/epoxy composite. *Alex. Eng. J.* **67,** 693–705. doi:10.1016/j.aej.2022.12.058 (2023).
28. Hassan, S. A. *et al.* Effect of fiber stacking sequence and orientation on quasi- static indentation properties of sustainable hybrid carbon/ramie fiber epoxy composites. *Curr. Res. Green Sustain. Chem.* **5,** 100284. doi:10.1016/j.crgsc.2022.100284 (2022).

29. Borrega, M., Ahvenainen, P., Serimaa, R. & Gibson, L. Composition and structure of balsa (Ochroma pyramidale) wood. *Wood Sci. Technol.* **49,** 403–420. doi:10.1007/s00226-015-0700-5 (2015).
30. Petel, O. E., Ouellet, S., Higgins, A. J. & Frost, D. L. The elastic-plastic behaviour of foam under shock loading. *Shock Waves* **23,** 55–67. doi:10.1007/s00193-012-0414-7 (2013).
31. Kausar, A., Ahmad, I., Rakha, S. A., Eisa, M. H. & Diallo, A. State-Of-The-Art of Sandwich Composite Structures: Manufacturing—to—High Performance Applications. *J. Compos. Sci.* **7,** 102. doi:10.3390/jcs7030102 (2023).
32. Kueh, A. B. H., Abo Sabah, S. H., Qader, D. N., Drahman, S. H. & Amran, M. Single and repetitive low-velocity impact responses of sandwich composite structures with different skin and core considerations: A review. *Case Stud. Constr. Mater.* **18,** e01908. doi:10.1016/j.cscm.2023.e01908 (2023).
33. Jaafar, M. *et al.* A 3D FE Modeling of Machining Process of Nomex® Honeycomb Core: Influence of the Cell Structure Behaviour and Specific Tool Geometry. *Procedia CIRP* **58,** 505–510. doi:10.1016/j.procir.2017.03.255 (2017).
34. Makich, H., Nouari, M. & Jaafar, M. Surface integrity quantification in machining of aluminum honeycomb structure. *Procedia CIRP* **108,** 693–697. doi:10.1016/j.procir.2022.03.107 (2022).
35. Zhang, D., Lu, G., Ruan, D., Fei, Q. & Duan, W. Quasi-static combined compression-shear crushing of honeycombs: An experimental study. *Mater. Design* **167,** 107632. doi:10.1016/j.matdes.2019.107632 (2019).
36. Giglio, M., Gilioli, A. & Manes, A. A numerical investigation on significant parameters influencing the flatwise compressive behaviour of a nomex™ honeycomb. *Procedia Eng.* **10,** 3441–3446. doi:10.1016/j.proeng.2011.04.567 (2011).
37. Sun, G., Huo, X., Chen, D. & Li, Q. Experimental and numerical study on honeycomb sandwich panels under bending and in-panel compression. *Mater. Design* **133,** 154–168. doi:10.1016/j.matdes.2017.07.057 (2017).
38. Hu, L. L. & Yu, T. X. Mechanical behavior of hexagonal honeycombs under low-velocity impact - Theory and simulations. *Int J Solids Struct* **50,** 3152–3165. doi:10.1016/j.ijsolstr.2013.05.017 (2013).
39. Li, X., Lu, F., Zhang, Y., Lin, Y. & Meng, Y. Experimental study on out-of-plane mechanical and energy absorption properties of combined hexagonal aluminum honeycombs under dynamic impact. *Mater. Design* **194,** 108900. doi:10.1016/j.matdes.2020.108900 (2020).
40. Duan, Y. *et al.* Mechanical characteristics of composite honeycomb sandwich structures under oblique impact. *Theoretical and Applied Mechanics Letters* **12,** 100379. doi:10.1016/j.taml.2022.100379 (2022).
41. Zhang, Z. *et al.* Three-point bending performances of integral-forming aluminum foam sandwich. *Mater. Design* **229,** 111889. doi:10.1016/j.matdes.2023.111889 (2023).
42. Tang, E., Yin, H., Chen, C., Han, Y. & Feng, M. Simulation of CFRP/aluminum foam sandwich structure under high velocity impact. *J. Mater. Res. Technol.* **9,** 7273–7287. doi:10.1016/j.jmrt.2020.04.093 (2020).

43. Balaban, A. C. & Toygar, M. E. Investigation into Mechanical Properties and Failure Mechanisms of Novel Sandwich Composite Material with Carbon Fibre / Epoxy Facesheets and PVC Foam Core. *Procedia Structural Integrity* **42,** 284–291. doi:10.1016/j.prostr.2022.12.035 (2022).
44. Wang, Z. *et al.* Compressive crushing of novel aluminum hexagonal honeycombs with perforations: Experimental and numerical investigations. *Int J Solids Struct* **126-127,** 187–195. doi:10.1016/j.ijsolstr.2017.08.005 (2017).
45. Miao, X. Y., Lu, R. & Chen, X. Fracture behaviour of foam core sandwich structures with manufacturing defects using phase-field modelling. *Compos. Struct.* **274,** 114294. doi:10.1016/j.compstruct.2021.114294 (2021).
46. Wang, H., Wang, W., Wang, B. & Fan, H. Foam-filling technique to improve low-velocity impact behaviors of woven lattice truss sandwich panels. *Polym. Test.* **114,** 107714. doi:10.1016/j.polymertesting.2022.107714 (2022).
47. Li, S. & Fan, H. Flexural behaviors and local failure analyses of EPS foam-filled GFRC truss-core sandwich panels. *Case Stud. Constr. Mater.* **15,** e00688. doi:10.1016/j.cscm.2021.e00688 (2021).
48. Pietras, D., Linul, E., Sadowski, T. & Rusinek, A. Out-of-plane crushing response of aluminum honeycombs in-situ filled with graphene-reinforced polyurethane foam. *Compos. Struct.* **249,** 112548. doi:10.1016/j.compstruct.2020.112548 (2020).
49. Xia, H., Sun, Q. & Wang, S. Influence of strain rate effect on energy absorption characteristics of bio-inspired honeycomb column thin-walled structure under impact loading. *Case Stud. Constr. Mater.* **18,** e01761. doi:10.1016/j.cscm.2022.e01761 (2023).
50. Novak, N., Borovinšek, M., Al-Ketan, O., Ren, Z. & Vesenjak, M. Impact and blast resistance of uniform and graded sandwich panels with TPMS cellular structures. *Compos. Struct.* **300.** doi:10.1016/j.compstruct.2022.116174 (2022).
51. Ambekar, R. S. *et al.* Flexure resistant 3D printed zeolite-inspired structures. *Addit. Manuf.* **47,** 102297. doi:10.1016/j.addma.2021.102297 (2021).
52. Ejeh, C. J., Barsoum, I. & Abu Al-Rub, R. K. Flexural properties of functionally graded additively manufactured AlSi10Mg TPMS latticed-beams. *Int. J. Mech. Sci.* **223,** 107293. doi:10.1016/j.ijmecsci.2022.107293 (2022).
53. Zhang, K., Zeng, T., Xu, G., Cheng, S. & Yu, S. Mechanical properties of SiCp/SiC composite lattice core sandwich panels fabricated by 3D printing combined with precursor impregnation and pyrolysis. *Compos. Struct.* **240,** 112060. doi:10.1016/j.compstruct.2020.112060 (2020).
54. Paczos, P., Wichniarek, R. & Magnucki, K. Three-point bending of sandwich beam with special structure of the core. *Compos. Struct.* **201,** 676–682. doi:10.1016/j.compstruct.2018.06.077 (2018).
55. Essassi, K. *et al.* Experimental and analytical investigation of the bending behaviour of 3D-printed bio-based sandwich structures composites with auxetic core under cyclic fatigue tests. *Compos. Part A Appl. Sci. Manuf.* **131,** 105775. doi:10.1016/j.compositesa.2020.105775 (2020).
56. Meng, L., Qiu, X., Gao, T., Li, Z. & Zhang, W. An inverse approach to the accurate modelling of 3D-printed sandwich panels with lattice core using beams of variable cross-section. *Compos. Struct.* **247,** 112363. doi:10.1016/j.compstruct.2020.112363. https://doi.org/10.1016/j.compstruct.2020.112363 (2020).

57. Brischetto, S. & Torre, R. Honeycomb Sandwich Specimens Made of PLA and Produced Via 3D FDM Printing Process: An Experimental Study. *J. Aircr. Spacecr. Technol* **4,** 54–69. doi:10.3844/jastsp.2020.54.69 (2020).
58. Essassi, K. *et al.* Investigation of the Static Behavior and Failure Mechanisms of a 3D Printed Bio-Based Sandwich with Auxetic Core. *Int. J. Appl. Mech.* **12,** 2050051. doi:10.1142/S1758825120500519 (2020).
59. Santos, F. A. *et al.* Low velocity impact response of 3D printed structures formed by cellular metamaterials and stiffening plates: PLA vs. PETg. *Compos. Struct.* **256,** 113128. doi:10.1016/j.compstruct.2020.113128 (2021).
60. Sun, S. *et al.* Out-of-plane compression of a novel hybrid corrugated core sandwich panel. *Compos. Struct.* **272,** 114222. doi:10.1016/j.compstruct.2021.114222 (2021).
61. Yazdani Sarvestani, H., Akbarzadeh, A. H., Niknam, H. & Hermenean, K. 3D printed architected polymeric sandwich panels: Energy absorption and structural performance. *Compos. Struct.* **200,** 886–909. doi:10.1016/j.compstruct.2018.04.002 (2018).
62. Indreș, A. I., Constantinescu, D. M. & Mocian, O. A. Bending behavior of 3D printed sandwich beams with different core topologies. *Mat. Design Process. Comm.* **3,** 1–8. doi:10.1002/mdp2.252 (2021).
63. Peng, C., Fox, K., Qian, M., Nguyen-Xuan, H. & Tran, P. 3D printed sandwich beams with bioinspired cores: Mechanical performance and modelling. *Thin-Walled Struct.* **161,** 107471. doi:10.1016/j.tws.2021.107471 (2021).
64. Spahic, M., Di Cesare, N., Le Duigou, A. & Keryvin, V. Multi-scale analysis of the flexural behaviour of 3D printed cellular polymer materials: Comparison between morphing and sandwich beams. *Compos. Struct.* **273,** 114249. doi:10.1016/j.compstruct.2021.114249 (2021).
65. Ghannadpour, S. A., Mahmoudi, M. & Hossein Nedjad, K. Structural behavior of 3D-printed sandwich beams with strut-based lattice core: Experimental and numerical study. *Compos. Struct.* **281,** 115113. doi:10.1016/j.compstruct.2021.115113 (2022).
66. Zamani, M. H., Heidari-Rarani, M. & Torabi, K. Optimal design of a novel graded auxetic honeycomb core for sandwich beams under bending using digital image correlation (DIC). *Compos. Struct.* **286,** 115310. doi:10.1016/j.compstruct.2022.115310 (2022).
67. Kanani, A. Y. & Kennedy, A. Experimental and numerical analysis of additively manufactured foamed sandwich beams. *Compos. Struct.* **312,** 116866. doi:10.1016/j.compstruct.2023.116866 (2023).
68. Bonthu, D., Bharath, H. S., Gururaja, S., Prabhakar, P. & Doddamani, M. 3D printing of syntactic foam cored sandwich composite. *Compos. Part C.* **3,** 100068. doi:10.1016/j.jcomc.2020.100068 (2020).
69. Bharath, H. S., Bonthu, D., Gururaja, S., Prabhakar, P. & Doddamani, M. Flexural response of 3D printed sandwich composite. *Compos. Struct.* **263,** 113732. doi:10.1016/j.compstruct.2021.113732 (2021).

70. Brischetto, S., Ferro, C. G., Torre, R. & Maggiore, P. 3D FDM production and mechanical behavior of polymeric sandwich specimens embedding classical and honeycomb cores. *Curved Layer. Struct.* **5,** 80–94. doi:10.1515/cls-2018-0007 (2018).
71. Acanfora, V., Saputo, S., Russo, A. & Riccio, A. A feasibility study on additive manufactured hybrid metal/composite shock absorbers. *Compos. Struct.* **268,** 113958. doi:10.1016/j.compstruct.2021.113958 (2021).
72. Harland, D., Alshaer, A. W. & Brooks, H. An experimental and numerical investigation of a novel 3D printed sandwich material for motorsport applications. *Procedia Manuf.* **36,** 11–18. doi:10.1016/j.promfg.2019.08.003 (2019).
73. Li, T. & Wang, L. Bending behavior of sandwich composite structures with tunable 3D-printed core materials. *Compos. Struct.* **175,** 46–57. doi:10.1016/j.compstruct.2017.05.001 (2017).
74. Gibson, L. J. & Ashby, M. F. *Cellular solids - Structure and properties* 2n Edition. doi:10.1017/CBO9781139878326 (Cambridge University Press, 1997).
75. Seharing, A., Azman, A. H. & Abdullah, S. A review on integration of lightweight gradient lattice structures in additive manufacturing parts. *Adv. Mech. Eng.* **12,** 1–21. doi:10.1177/1687814020916951 (2020).
76. Kaur, I. & Singh, P. State-of-the-art in heat exchanger additive manufacturing. *International Journal of Heat and Mass Transfer* **178,** 121600. doi:10.1016/j.ijheatmasstransfer.2021.121600 (2021).
77. Lubombo, C. & Huneault, M. A. Effect of infill patterns on the mechanical performance of lightweight 3D-printed cellular PLA parts. *Mater. Today Commun.* **17,** 214–228. doi:10.1016/j.mtcomm.2018.09.017 (2018).
78. Kumar, S., Ubaid, J., Abishera, R., Schiffer, A. & Deshpande, V. S. Tunable Energy Absorption Characteristics of Architected Honeycombs Enabled via Additive Manufacturing. *ACS Appl. Mater. Interfaces* **11,** 42549–42560. doi:10.1021/acsami.9b12880 (2019).
79. Refai, K., Montemurro, M., Brugger, C. & Saintier, N. Determination of the effective elastic properties of titanium lattice structures. *Mech. Adv. Mater. Struct.* **27,** 1966–1982. doi:10.1080/15376494.2018.1536816 (2020).
80. Liu, Q. *et al.* Metamaterials mapped lightweight structures by principal stress lines and topology optimization: Methodology, additive manufacturing, ductile failure and tests. *Mater. Design* **212,** 110192. doi:10.1016/j.matdes.2021.110192 (2021).
81. Cheng, L., Bai, J. & To, A. C. Functionally graded lattice structure topology optimization for the design of additive manufactured components with stress constraints. *Comput. Methods Appl. Mech. Eng.* **344,** 334–359. doi:10.1016/j.cma.2018.10.010 (2019).
82. Feng, Y., Huang, T., Gong, Y. & Jia, P. Stiffness optimization design for TPMS architected cellular materials. *Mater. Design* **222,** 111078. doi:10.1016/j.matdes.2022.111078 (2022).
83. Yang, N., Wei, H. & Mao, Z. Tuning surface curvatures and young's moduli of TPMS-based lattices independent of volume fraction. *Mater. Design* **216,** 110542. doi:10.1016/j.matdes.2022.110542 (2022).

84. Liu, Y. & Hu, H. A review on auxetic structures and polymeric materials. *Sci. Res. Essays* **5,** 1052–1063. doi:10.5897/SRE.9000104 (2010).
85. Álvarez-Elipe, J. C. & Díaz-Lantada, A. Comparative study of auxetic geometries by means of computer-aided design and engineering. *Smart Mater. Struct.* **21.** doi:10.1088/0964-1726/21/10/105004 (2012).
86. Fleck, N. A., Deshpande, V. S. & Ashby, M. F. Micro-architectured materials: Past, present and future. *Proc. R. Soc. A* **466,** 2495–2516. doi:10.1098/rspa.2010.0215 (2010).
87. Du Plessis, A. *et al.* Properties and applications of additively manufactured metallic cellular materials: A review. *Progress in Materials Science* **125,** 100918. doi:10.1016/j.pmatsci.2021.100918 (2022).
88. Lin, C. *et al.* Revealing the sound insulation capacities of TPMS sandwich panels. *J. Sound Vib.* **540,** 117303. doi:10.1016/j.jsv.2022.117303 (2022).
89. Zeng, C. & Wang, W. Modeling method for variable and isotropic permeability design of porous material based on TPMS lattices. *Tribol. Int.* **176,** 107913. doi:10.1016/j.triboint.2022.107913 (2022).
90. Andrew, J. J., Alhashmi, H., Schiffer, A., Kumar, S. & Deshpande, V. S. Energy absorption and self-sensing performance of 3D printed CF/PEEK cellular composites. *Mater. Design* **208,** 109863. doi:10.1016/j.matdes.2021.109863 (2021).
91. Zaharia, S. M., Enescu, L. A. & Pop, M. A. Mechanical performances of lightweight sandwich structures produced by material extrusion-based additive manufacturing. *Polymers* **12,** 1740. doi:10.3390/polym12081740 (2020).
92. Tao, Y., Pan, L., Liu, D. & Li, P. A case study: Mechanical modeling optimization of cellular structure fabricated using wood flour-filled polylactic acid composites with fused deposition modeling. *Compos. Struct.* **216,** 360–365. doi:10.1016/j.compstruct.2019.03.010 (2019).
93. Yang, X. *et al.* Effect of volume fraction and unit cell size on manufacturability and compressive behaviors of Ni-Ti triply periodic minimal surface lattices. *Addit. Manuf.* **54,** 102737. doi:10.1016/j.addma.2022.102737 (2022).
94. Jones, A., Leary, M., Bateman, S. & Easton, M. Parametric design and evaluation of TPMS-like cellular solids. *Mater. Design* **221,** 110908. doi:10.1016/j.matdes.2022.110908 (2022).
95. Alomar, Z. & Concli, F. Compressive behavior assessment of a newly developed circular cell-based lattice structure. *Mater. Design* **205,** 109716. doi:10.1016/j.matdes.2021.109716 (2021).
96. Ding, R., Yao, J., Du, B., Zhao, L. & Guo, Y. Mechanical Properties and Energy Absorption Capability of ARCH Lattice Structures Manufactured by Selective Laser Melting. *Adv. Eng. Mater.* **22,** 1901534. doi:10.1002/adem.201901534 (2020).
97. Li, C. *et al.* Crushing behavior of multi-layer metal lattice panel fabricated by selective laser melting. *Int. J. Mech. Sci.* **145,** 389–399. doi:10.1016/j.ijmecsci.2018.07.029 (2018).
98. Xiao, Z. *et al.* Evaluation of topology-optimized lattice structures manufactured via selective laser melting. *Mater. Design* **143,** 27–37. doi:10.1016/j.matdes.2018.01.023 (2018).

99. Cao, X., Duan, S., Liang, J., Wen, W. & Fang, D. Mechanical properties of an improved 3D-printed rhombic dodecahedron stainless steel lattice structure of variable cross section. *Int. J. Mech. Sci.* **145,** 53–63. doi:10.1016/j.ijmecsci.2018.07.006 (2018).
100. Gümrük, R., Mines, R. A. & Karadeniz, S. Static mechanical behaviours of stainless steel micro-lattice structures under different loading conditions. *Mater. Sci. Eng. A* **586,** 392–406. doi:10.1016/j.msea.2013.07.070 (2013).
101. Alberdi, R. *et al.* Multi-morphology lattices lead to improved plastic energy absorption. *Mater. Design* **194,** 108883. doi:10.1016/j.matdes.2020.108883 (2020).
102. Li, C. *et al.* Architecture design of periodic truss-lattice cells for additive manufacturing. *Addit. Manuf.* **34,** 101172. doi:10.1016/j.addma.2020.101172 (2020).
103. Maconachie, T. *et al.* SLM lattice structures: Properties, performance, applications and challenges. *Mater. Design* **183,** 108137. doi:10.1016/j.matdes.2019.108137 (2019).
104. Torres, A. M. *et al.* Bone-inspired microarchitectures achieve enhanced fatigue life. *Proc. Natl. Acad. Sci. U.S.A.* **116,** 24457–24462. doi:10.1073/pnas.1905814116 (2019).
105. Habib, F. N., Iovenitti, P., Masood, S. H. & Nikzad, M. Fabrication of polymeric lattice structures for optimum energy absorption using Multi Jet Fusion technology. *Mater. Design* **155,** 86–98. doi:10.1016/j.matdes.2018.05.059 (2018).
106. Leary, M. *et al.* Inconel 625 lattice structures manufactured by selective laser melting (SLM): Mechanical properties, deformation and failure modes. *Mater. Design* **157,** 179–199. doi:10.1016/j.matdes.2018.06.010 (2018).
107. Yang, L. *et al.* Additive Manufacturing of Metal Cellular Structures: Design and Fabrication. *Jom* **67,** 608–615. doi:10.1007/s11837-015-1322-y (2015).
108. Sreedhar, N. *et al.* Mass transfer analysis of ultrafiltration using spacers based on triply periodic minimal surfaces: Effects of spacer design, directionality and voidage. *J. Membr. Sci.* **561,** 89–98. doi:10.1016/j.memsci.2018.05.028 (2018).
109. Al-Ketan, O. *et al.* Microarchitected Stretching-Dominated Mechanical Metamaterials with Minimal Surface Topologies. *Adv. Eng. Mater.* **20,** 1800029. doi:10.1002/adem.201800029 (2018).
110. Al-Ketan, O., Lee, D. W., Rowshan, R. & Abu Al-Rub, R. K. Functionally graded and multi-morphology sheet TPMS lattices: Design, manufacturing, and mechanical properties. *J. Mech. Behav. Biomed. Mater.* **102,** 103520. doi:10.1016/j.jmbbm.2019.103520 (2020).
111. Sathishkumar, N., Vivekanandan, N., L.Balamurugan, Arunkumar, N. & Ahamed, I. Mechanical Properties of Triply Periodic Minimal Surface based lattices made by Polyjet Printing. *Mater. Today: Proc.* **22,** 2934–2940. doi:10.1016/j.matpr.2020.03.427 (2020).
112. Kumar, A., Verma, S. & Jeng, J.-Y. Supportless lattice structures for energy absorption fabricated by fused deposition modeling. *3D Print Addit. Manuf.* **7,** 85–96. doi:10.1089/3dp.2019.0089 (2020).
113. Jia, H. *et al.* An experimental and numerical investigation of compressive response of designed Schwarz Primitive triply periodic minimal surface with non-uniform shell thickness. *Extreme Mech. Lett.* **37,** 100671. doi:10.1016/j.eml.2020.100671 (2020).

114. Kumar, A., Collini, L., Daurel, A. & Jeng, J. Y. Design and additive manufacturing of closed cells from supportless lattice structure. *Addit. Manuf.* **33,** 101168. doi:10.1016/j.addma.2020.101168 (2020).
115. Downing, D., Jones, A., Brandt, M. & Leary, M. Increased efficiency gyroid structures by tailored material distribution. *Mater. Design* **197,** 109096. doi:10.1016/j.matdes.2020.109096 (2021).
116. Maskery, I., Aboulkhair, N. T., Aremu, A. O., Tuck, C. J. & Ashcroft, I. A. Compressive failure modes and energy absorption in additively manufactured double gyroid lattices. *Addit. Manuf.* **16,** 24–29. doi:10.1016/j.addma.2017.04.003 (2017).
117. Saleh, M., Anwar, S., Al-Ahmari, A. M. & Alfaify, A. Compression Performance and Failure Analysis of 3D-Printed Carbon Fiber/PLA Composite TPMS Lattice Structures. *Polymers* **14.** doi:10.3390/polym14214595 (2022).
118. Tanlak, N., De Lange, D. F. & Van Paepegem, W. Numerical prediction of the printable density range of lattice structures for additive manufacturing. *Mater. Design* **133,** 549–558. doi:10.1016/j.matdes.2017.08.007 (2017).
119. Gopsill, J. A., Shindler, J. & Hicks, B. J. Using finite element analysis to influence the infill design of fused deposition modelled parts. *Prog. Addit. Manuf.* **3,** 145–163. doi:10.1007/s40964-017-0034-y (2018).
120. Bates, S. R., Farrow, I. R. & Trask, R. S. 3D printed polyurethane honeycombs for repeated tailored energy absorption. *Mater. Design* **112,** 172–183. doi:10.1016/j.matdes.2016.08.062 (2016).
121. Bates, S. R., Farrow, I. R. & Trask, R. S. Compressive behaviour of 3D printed thermoplastic polyurethane honeycombs with graded densities. *Mater. Design* **162,** 130–142. doi:10.1016/j.matdes.2018.11.019 (2019).
122. Caccese, V., Ferguson, J. R. & Edgecomb, M. A. Optimal design of honeycomb material used to mitigate head impact. *Compos. Struct.* **100,** 404–412. doi:10.1016/j.compstruct.2012.12.034 (2013).
123. Ma, Q. *et al.* Effect of infill pattern, density and material type of 3D printed cubic structure under quasi-static loading. *Proc Inst Mech Eng C J Mech Eng Sci.* doi:10.1177/0954406220971667 (2020).
124. Alderson, A. *et al.* Elastic constants of 3-, 4- and 6-connected chiral and anti-chiral honeycombs subject to uniaxial in-plane loading. *Compos. Sci. Technol.* **70,** 1042–1048. doi:10.1016/j.compscitech.2009.07.009 (2010).
125. Scarpa, F. *et al.* Elastic buckling of hexagonal chiral cell honeycombs. *Compos. Part A Appl. Sci. Manuf.* **38,** 280–289. doi:10.1016/j.compositesa.2006.04.007 (2007).
126. Hu, L. L., Zhou, M. Z. & Deng, H. Dynamic crushing response of auxetic honeycombs under large deformation: Theoretical analysis and numerical simulation. *Thin-Walled Struct.* **131,** 373–384. doi:10.1016/j.tws.2018.04.020 (2018).
127. Hou, S., Li, T., Jia, Z. & Wang, L. Mechanical properties of sandwich composites with 3d-printed auxetic and non-auxetic lattice cores under low velocity impact. *Mater. Design* **160,** 1305–1321. doi:10.1016/j.matdes.2018.11.002 (2018).
128. Mir, M., Ali, M. N., Sami, J. & Ansari, U. Review of mechanics and applications of auxetic structures. *Adv. Mater. Sci. Eng.* doi:10.1155/2014/753496 (2014).

129. Prawoto, Y. Seeing auxetic materials from the mechanics point of view: A structural review on the negative Poisson's ratio. *Comput. Mater. Sci.* **58,** 140–153. doi:10.1016/j.commatsci.2012.02.012 (2012).

130. Grima, J. N., Gatt, R. & Farrugia, P. S. On the properties of auxetic meta-tetrachiral structures. *Phys. Status Solidi B* **245,** 511–520. doi:10.1002/pssb.200777704 (2008).

131. Gaspar, N., Ren, X. J., Smith, C. W., Grima, J. N. & Evans, K. E. Novel honeycombs with auxetic behaviour. *Acta Mater.* **53,** 2439–2445. doi:10.1016/j.actamat.2005.02.006 (2005).

132. Whitty, J. P. M., Alderson, A., Myler, P. & Kandola, B. Towards the design of sandwich panel composites with enhanced mechanical and thermal properties by variation of the in-plane Poisson's ratios. *Compos. Part A Appl. Sci. Manuf.* **34,** 525–534. doi:10.1016/S1359-835X(03)00058-7 (2003).

133. Scarpa, F. & Tomlin, P. J. On the transverse shear modulus of negative Poisson's ratio honeycomb structures. *Fatigue Fract. Eng. Mater. Struct.* **23,** 717–720. doi:10.1046/j.1460-2695.2000.00278.x (2000).

134. Ufodike, C. O., Wang, H., Ahmed, M. F., Dolzyk, G. & Jung, S. Design and modeling of bamboo biomorphic structure for in-plane energy absorption improvement. *Mater. Design* **205,** 109736. doi:10.1016/j.matdes.2021.109736 (2021).

135. Bai, L. *et al.* Improved mechanical properties and energy absorption of Ti6Al4V laser powder bed fusion lattice structures using curving lattice struts. *Mater. Design* **211,** 110140. doi:10.1016/j.matdes.2021.110140 (2021).

136. Ye, G., Bi, H. & Hu, Y. Compression behaviors of 3D printed pyramidal lattice truss composite structures. *Compos. Struct.* **233,** 111706. doi:10.1016/j.compstruct.2019.111706 (2020).

137. Arjunan, A., Singh, M., Baroutaji, A. & Wang, C. Additively manufactured AlSi10Mg inherently stable thin and thick-walled lattice with negative Poisson's ratio. *Compos. Struct.* **247,** 112469. doi:10.1016/j.compstruct.2020.112469 (2020).

138. Bahrami Babamiri, B., Askari, H. & Hazeli, K. Deformation mechanisms and post-yielding behavior of additively manufactured lattice structures. *Mater. Design* **188,** 108443. doi:10.1016/j.matdes.2019.108443 (2020).

139. Azzouz, L. *et al.* Mechanical properties of 3-D printed truss-like lattice biopolymer non-stochastic structures for sandwich panels with natural fibre composite skins. *Compos. Struct.* **213,** 220–230. doi:10.1016/j.compstruct.2019.01.103 (2019).

140. Zhang, X. Y., Fang, G., Xing, L. L., Liu, W. & Zhou, J. Effect of porosity variation strategy on the performance of functionally graded Ti-6Al-4V scaffolds for bone tissue engineering. *Mater. Design* **157,** 523–538. doi:10.1016/j.matdes.2018.07.064 (2018).

141. Yap, Y. L. & Yeong, W. Y. Shape recovery effect of 3D printed polymeric honeycomb: This paper studies the elastic behaviour of different honeycomb structures produced by PolyJet technology. *Virtual Phys. Prototyp.* **10,** 91–99. doi:10.1080/17452759.2015.1060350 (2015).

142. Chen, X. *et al.* Wide-range tuning of the mechanical properties of TPMS lattice structures through frequency variation. *Mater. Design* **224,** 111370. doi:10.1016/j.matdes.2022.111370 (2022).

143. Fu, J. *et al.* Isotropic design and mechanical characterization of TPMS-based hollow cellular structures. *Compos. Struct.* **279,** 114818. doi:10.1016/j.compstruct.2021.114818 (2022).
144. Montgomery-Liljeroth, E., Schievano, S. & Burriesci, G. Elastic properties of 2D auxetic honeycomb structures- a review. *Appl. Mater. Today* **30,** 101722. doi:10.1016/j.apmt.2022.101722 (2023).
145. Wei, K. *et al.* Additively manufactured bi-material metamaterial to program a wide range of thermal expansion. *Mater. Design* **198,** 109343. doi:10.1016/j.matdes.2020.109343 (2021).
146. Sun, Z., Guo, Y. & Shim, V. P. Deformation and energy absorption characteristics of additively-manufactured polymeric lattice structures — Effects of cell topology and material anisotropy. *Thin-Walled Struct.* **169.** doi:10.1016/j.tws.2021.108420 (2021).
147. Pramanik, S., Milaege, D., Hoyer, K.-P. & Schaper, M. Additively manufactured novel Ti6Al7Nb circular honeycomb cellular solid for energy absorbing applications. *Mater. Sci. Eng. A* **854,** 143887. doi:10.1016/j.msea.2022.143887 (2022).
148. Lee, J. W., Oh, S. H., Jeon, E., Kim, J. & Park, K. Functional gradation of the morphological properties of TPMS channel for enhanced flow performance. *Mater. Design* **224,** 111413. doi:10.1016/j.matdes.2022.111413 (2022).
149. Novak, N. *et al.* Compression behaviour of TPMS-filled stainless steel tubes. *Mater. Sci. Eng. A* **852,** 143680. doi:10.1016/j.msea.2022.143680 (2022).
150. Tee, Y. L. *et al.* From nature to additive manufacturing: Biomimicry of porcupine quill. *Mater. Design* **210,** 110041. doi:10.1016/j.matdes.2021.110041 (2021).
151. Ouda, M. *et al.* Novel static mixers based on triply periodic minimal surface (TPMS) architectures. *J. Environ. Chem. Eng.* **8,** 104289. doi:10.1016/j.jece.2020.104289 (2020).
152. Yang, C. & Li, Q. M. Advanced lattice material with high energy absorption based on topology optimisation. *Mech. Mater.* **148,** 103536. doi:10.1016/j.mechmat.2020.103536 (2020).
153. Xu, Y. *et al.* Mechanical properties tailoring of topology optimized and selective laser melting fabricated Ti6Al4V lattice structure. *J. Mech. Behav. Biomed. Mater.* **99,** 225–239. doi:10.1016/j.jmbbm.2019.06.021 (2019).
154. Zener, C. M. & Siegel, S. Elasticity and Anelasticity of Metals. *J. Phys. Chem.* **53,** 1468. doi:10.1021/j150474a017 (1949).
155. Ranganathan, S. I. & Ostoja-Starzewski, M. Universal Elastic Anisotropy Index. *Phys. Rev. Lett.* **101,** 055504 (2008).
156. Lee, J. W., Oh, S. H., Jeon, E., Kim, J. & Park, K. Functional gradation of the morphological properties of TPMS channel for enhanced flow performance. *Mater. Design* **224,** 111413. doi:10.1016/j.matdes.2022.111413 (2022).
157. Dong, Z. & Zhao, X. Application of TPMS structure in bone regeneration. *Eng. Regen.* **2,** 154–162. doi:10.1016/j.engreg.2021.09.004 (2021).
158. Attarzadeh, R., Attarzadeh-Niaki, S. H. & Duwig, C. Multi-objective optimization of TPMS-based heat exchangers for low-temperature waste heat recovery. *Appl. Therm. Eng.* **212,** 118448. doi:10.1016/j.applthermaleng.2022.118448 (2022).

159. Blakey-Milner, B. *et al.* Metal additive manufacturing in aerospace: A review. *Mater. Design* **209,** 110008. doi:10.1016/j.matdes.2021.110008 (2021).

160. Sola, A. *et al.* Open challenges in tensile testing of additively manufactured polymers: A literature survey and a case study in fused filament fabrication. *Polymer Testing* **117,** 107859. doi:10.1016/j.polymertesting.2022.107859 (2023).

161. Dey, A., Eagle, I. N. R. & Yodo, N. A review on filament materials for fused filament fabrication. *J. Manuf. Mater. Process.* **5.** doi:10.3390/jmmp5030069 (2021).

162. Popescu, D., Zapciu, A., Amza, C., Baciu, F. & Marinescu, R. FDM process parameters influence over the mechanical properties of polymer specimens: A review. *Polym. Test.* **69,** 157–166. doi:10.1016/j.polymertesting.2018.05.020 (2018).

163. Jandyal, A., Chaturvedi, I., Wazir, I., Raina, A. & Ul Haq, M. I. 3D printing – A review of processes, materials and applications in industry 4.0. *Sustain. Oper. Comput.* **3,** 33–42. doi:10.1016/j.susoc.2021.09.004 (2022).

164. Hsissou, R. *et al.* Polymer composite materials: A comprehensive review. *Compos. Struct.* **262,** 0–3. doi:10.1016/j.compstruct.2021.113640 (2021).

165. Ceruti, A., Marzocca, P., Liverani, A. & Bil, C. Maintenance in aeronautics in an Industry 4.0 context: The role of Augmented Reality and Additive Manufacturing. *J Comput Des Eng* **6,** 516–526. doi:10.1016/j.jcde.2019.02.001 (2019).

166. Byberg, K. I., Gebisa, A. W. & Lemu, H. G. Mechanical properties of ULTEM 9085 Material Processed by Fused Deposition Modeling. *Polym. Test.* **72,** 335–347. doi:10.1016/j.polymertesting.2018.10.040 (2018).

167. Melton, G. H., Peters, E. N. & Arisman, R. K. *Engineering Thermoplastics* (ed Kutz, M.) 7–21. doi:10.1016/B978-1-4377-3514-7.10002-9 (William Andrew Publishing, 2011).

168. Blanco, I., Cicala, G., Ognibene, G., Rapisarda, M. & Recca, A. Thermal properties of polyetherimide/polycarbonate blends for advanced applications. *Polym. Degrad. Stab* **154,** 234–238. doi:10.1016/j.polymdegradstab.2018.06.011 (2018).

169. Luchinsky, D. G., Hafiychuk, H., Hafiychuk, V. & Wheeler, K. R. *Molecular Dynamics of ULTEM 9085 for 3D Manufacturing: Spectra, Thermodynamic Properties, and Shear Viscosity.* tech. rep. 220213 (2018). https://ntrs.nasa.gov/citations/20190026629.

170. Lau, K. S. *High-Performance Polyimides and High Temperature Resistant Polymers* Third Edit (eds Dodiuk, H. & Goodman, S. H.) 297–424. doi:10.1016/B978-1-4557-3107-7.00010-5 (William Andrew Publishing, 2014).

171. Stratasys. *ULTEM™ 1010 Resin - FDM® Thermoplastic Filament* tech. rep. (2021). https://www.stratasys.com/en/materials/materials-catalog/fdm-materials/ultem-1010/.

172. Hooper, J. *et al.* Feasibility of single-use 3D-printed instruments for total knee arthroplasty. *Bone Joint J.* **101,** 115–120. doi:10.1302/0301-620X.101B7.BJJ-2018-1506.R1 (2019).

173. Stratasys. *ULTEM™ 9085 Resin - FDM® Thermoplastic Filament Fit for High-Performance Applications* tech. rep. (2021). https://www.stratasys.com/en/materials/materials-catalog/fdm-materials/ultem-9085/.

174. Najmon, J. C., Raeisi, S. & Tovar, A. *Review of additive manufacturing technologies and applications in the aerospace industry* (eds Froes, F. & Boyer, R.) 7–31. doi:10.1016/B978-0-12-814062-8.00002-9 (Elsevier Ltd, 2019).
175. Wu, H. *et al.* Additive manufacturing of thermal protection system materials. *2018 AIAA/ASCE/AHS/ASC Structures, Structural Dynamics, and Materials Conference,* 1–10. doi:10.2514/6.2018-0092 (2018).
176. Fard, S. H. & Hashemi, S. M. On the strain-life fatigue parameters of additive manufactured plastic materials through used filament fabrication process. *Addit. Manuf.* **32.** doi:10.1016/j.addma.2019.100973 (2020).
177. Roberson, D. A. *et al.* Comparison of Stress Concentrator Fabrication for 3D Printed Polymeric Izod Impact Test Specimens. *Addit. Manuf.* **7,** 1–11. doi:10.1016/j.addma.2015.05.002 (2015).
178. Dilberoglu, U. M., Gharehpapagh, B., Yaman, U. & Dolen, M. The role of additive manufacturing in the era of Industry 4.0. *Procedia Manuf.* **11,** 545–554. doi:10.1016/j.promfg.2017.07.148 (2017).
179. Dizon, J. R. C., Espera Jr., A. H., Chen, Q. & Advincula, R. C. Mechanical characterization of 3D-printed polymers. *Addit. Manuf.* **20,** 44–67. doi:10.1016/j.addma.2017.12.002 (2018).
180. Gabor, C. *et al.* The optimization of the production procedure in relation to the mechanical properties of additively manufactured parts. *Mater. Today* **19,** 1008–1013. doi:10.1016/j.matpr.2019.08.014 (2019).
181. McLouth, T. D., Severino, J. V., Adams, P. M., Patel, D. N. & Zaldivar, R. J. The impact of print orientation and raster pattern on fracture toughness in additively manufactured ABS. *Addit. Manuf.* **18,** 103–109. doi:10.1016/j.addma.2017.09.003 (2017).
182. Sood, A. K., Ohdar, R. K. & Mahapatra, S. S. Parametric appraisal of mechanical property of fused deposition modelling processed parts. *Mater. Design* **31,** 287–295. doi:10.1016/j.matdes.2009.06.016 (2010).
183. Ziemian, C. W. & Ziemian, R. D. Residual strength of additive manufactured ABS parts subjected to fatigue loading. *Int. J. Fatigue.* doi:10.1016/j.ijfatigue.2019.105455 (2019).
184. Ahn, S.-H., Montero, M., Odell, D., Roundy, S. & Wright, P. K. Anisotropic material properties of fused deposition modeling ABS. *Rapid Prototyp. J.* **8,** 248–257. doi:10.1108/13552540210441166 (2002).
185. Wittbrodt, B. & Pearce, J. M. The Effects of PLA Color on Material Properties of 3-D Printed Components. *Addit. Manuf.* **8,** 110–116. doi:10.1016/j.addma.2015.09.006 (2015).
186. Lee, C.-Y. & Liu, C.-Y. The Influence of Forced-Air Cooling on a 3D printed Part Manufactured by Fused Filament Fabrication. *Addit. Manuf.* **25,** 196–203. doi:10.1016/j.addma.2018.11.012 (2019).
187. Chacón, J. M., Caminero, M. A., García-Plaza, E. & Núñez, P. J. Additive manufacturing of PLA structures using fused deposition modelling: effect of process parameters on mechanical properties and their optimal selection. *Mater. Design* **124,** 143–157. doi:10.1016/j.matdes.2017.03.065 (2017).

188. Gomez-Gras, G., Jerez-Mesa, R., Travieso-Rodriguez, J. A. & Lluma-Fuentes, J. Fatigue performance of fused filament fabrication PLA specimens. *Mater. Design* **140,** 278–285. doi:10.1016/j.matdes.2017.11.072 (2018).

189. Smith, W. C. & Dean, R. W. Structural characteristics of fused deposition modeling polycarbonate material. *Polym. Test.* **32,** 1306–1312. doi:10.1016/j.polymertesting.2013.07.014 (2013).

190. Domingo-Espin, M. *et al.* Mechanical property characterization and simulation of fused deposition modeling Polycarbonate parts. *Mater. Design* **83,** 670–677. doi:10.1016/j.matdes.2015.06.074 (2015).

191. Sedighi, I., Ayatollahi, M. R., Bahrami, B., Pérez-Martínez, M. A. & Garcia-Granada, A. A. Mechanical behavior of an additively manufactured poly-carbonate specimen: tensile, flexural and mode I fracture properties. *Rapid Prototyp. J.* **26,** 267–277. doi:10.1108/RPJ-03-2019-0055 (2020).

192. Bahrami, B., Ayatollahi, M. R., Sedighi, I., Pérez, M. A. & Garcia-Granada, A. A. The effect of in-plane layer orientation on mixed-mode I-II fracture behavior of 3D-printed poly-carbonate specimens. *Eng. Fract. Mech.* **231,** 107018. doi:10.1016/j.engfracmech.2020.107018 (2020).

193. Salazar-Martín, A. G., Pérez, M. A., García-Granada, A.-A., Reyes, G. & Puigoriol-Forcada, J. M. A Study of Creep in Polycarbonate Fused Deposition Modelling parts. *Mater. Design* **141,** 414–425. doi:10.1016/j.matdes.2018.01.008 (2018).

194. Puigoriol-Forcada, J. M., Alsina, A., Salazar-Martín, A. G., Gomez-Gras, G. & Pérez, M. A. Flexural Fatigue Properties of Polycarbonate Fused-deposition Modelling Specimens. *Mater. Design* **155,** 414–421. doi:10.1016/j.matdes.2018.06.018 (2018).

195. Zaldivar, R. J. *et al.* Influence of Processing and Orientation Print Effects on the Mechanical and Thermal Behavior of 3D-Printed ULTEM® 9085 Material. *Addit. Manuf.* **13,** 71–80. doi:10.1016/j.addma.2016.11.007 (2017).

196. Bagsik, A. & Schöppner, V. *Mechanical Properties of Fused Deposition Modeling Pards with Ultem* 9085* in *ANTEC 2011 Plastics, Boston* (2011). doi:10.1016/j.polymertesting.2018.10.040.

197. Bagsik, A., Schöppner, V. & Klemp, E. *FDM Part Quality Manufactured with Ultem*9085* in *International Conference Polymeric Materials 2010 Halle, Saale* (2010).

198. Gebisa, A. W. & Lemu, H. G. Influence of 3D Printing FDM Process Parameters on Tensile Property of ULTEM 9085. *Procedia Manuf.* **30,** 331–338. doi:10.1016/j.promfg.2019.02.047 (2019).

199. Motaparti, K. P. *Effect of Build Parameters on Mechanical Properties of Ultem 9085 Parts By Fused Deposition Modeling* PhD thesis (Missouri University of Science and Technology, 2016), 75. https://scholarsmine.mst.edu/cgi/viewcontent.cgi?referer={\&}httpsredir=1{\&}article=8512{\&}context=masters{_}theses.

200. Gebisa, A. W. & Lemu, H. G. Investigating Effects of Fused-Deposition Modeling (FDM) Processing Parameters on Flexural Properties of ULTEM 9085 using Designed Experiment. *Materials* **11,** 1–23. doi:10.3390/ma11040500 (2018).

201. Zaldivar, R. J. *et al.* Effect of Initial Filament Moisture Content on the Microstructure and Mechanical Performance of ULTEM® 9085 3D Printed Parts. *Addit. Manuf.* **24,** 457–466. doi:10.1016/j.addma.2018.10.022 (2018).

202. Chueca de Bruijn, A., Gómez-Gras, G. & Pérez, M. A. Selective dissolution of polysulfone support material of fused filament fabricated Ultem 9085 parts. *Polym. Test.* **108,** 107495. doi:10.1016/j.polymertesting.2022.107495 (2022).
203. Chueca de Bruijn, A., Gómez-Gras, G. & Pérez, M. A. Mechanical study on the impact of an efective solvent support-removal methodology for FDM Ultem 9085 parts. *Polym. Test.* **85,** 106433. doi:10.1016/j.polymertesting.2020.106433 (2020).
204. ASTM Standard D638-14, Standard Test Method for Tensile Properties of Plastics. *ASTM International, West Conshohocken, PA.* doi:10.1520/D0638-14. www.astm.org (2014).
205. ASTM Standard D790-17, Standard Test Methods for Flexural Properties of Unreinforced and Reinforced Plastics and Electrical Insulating Materials. *ASTM International, West Conshohocken, PA.* doi:10.1520/D0790-17 (2017).
206. ASTM Standard D5379/D5379M-19, Standard Test Method for Shear Properties of Composite Materials by the V-Notched Beam Method. *ASTM International, West Conshohocken, PA.* doi:10.1520/D5379_D5379M-19E01. www.astm.org (2019).
207. ASTM Standard C365-22, Standard Test Method for Flatwise Compressive Properties of Sandwich Cores. *ASTM International, West Conshohocken, PA.* doi:10.1520/C0365_C0365M-22. www.astm.org (2022).
208. Forés-Garriga, A., Pérez, M. A., Gómez-Gras, G. & Reyes-Pozo, G. Role of infill parameters on the mechanical performance and weight reduction of PEI Ultem processed by FFF. *Mater. Design* **193,** 108810. doi:10.1016/j.matdes.2020.108810 (2020).
209. Pastor-Artigues, M. M. *et al.* Elastic asymmetry of PLA material in FDM-printed parts: Considerations concerning experimental characterisation for use in numerical simulations. *Materials* **13,** 15. doi:10.3390/ma13010015 (2020).
210. Perkowski, C. *Tensile-compressive asymmetry and anisotropy of fused deposition modeling PLA under monotonic conditions* PhD thesis (University of Central Florida, 2017), 125. https://stars.library.ucf.edu/cgi/viewcontent.cgi?referer={\&}httpsredir=1{\&}article=6576{\&}context=etd.
211. ASTM Standard C393/C393M-20, Standard Test Method for Core Shear Properties of Sandwich Constructions by Beam Flexure. *ASTM International, West Conshohocken, PA.* doi:10.1520/C0393_C0393M-20. www.astm.org (2006).
212. Castro Composites. *MTC510 Unidirectional Epoxy Component Prepreg Technical Data Sheet* tech. rep. (2013), 1–5. https://www.castrocompositesshop.com.
213. Castro Composites. *Waterclean - Limpiador para moldes en base acuosa ChemTrend* tech. rep. (2023), 1–2. https://www.castrocompositesshop.com.
214. Castro Composites. *Chemlease 15 Sealer EZ - Sellador de moldes ChemTrend* tech. rep. (2018), 1–2. https://www.castrocompositesshop.com.
215. Castro Composites. *Sistema Flex-Z - Desmoldeante semipermanente para aplicación manual o a pistola ChemTrend* tech. rep. (2023), 1–3. https://www.castrocompositesshop.com.
216. Castro Composites. *MTFA500 (DF044) Adhesive Film* tech. rep. (2014), 1–2. https://www.castrocompositesshop.com.